

Syracuse University

**SURFACE**

---

Dissertations - ALL

SURFACE

---

December 2014

## Evaluation of Non-Covalent Interaction Models in Molecular Crystals Using Terahertz Spectroscopy

Thomas Juliano  
*Syracuse University*

Follow this and additional works at: <https://surface.syr.edu/etd>



Part of the [Physical Sciences and Mathematics Commons](#)

---

### Recommended Citation

Juliano, Thomas, "Evaluation of Non-Covalent Interaction Models in Molecular Crystals Using Terahertz Spectroscopy" (2014). *Dissertations - ALL*. 168.

<https://surface.syr.edu/etd/168>

This Dissertation is brought to you for free and open access by the SURFACE at SURFACE. It has been accepted for inclusion in Dissertations - ALL by an authorized administrator of SURFACE. For more information, please contact [surface@syr.edu](mailto:surface@syr.edu).

## Abstract

Density functional theory (DFT) is a powerful tool that can be used to evaluate the low-frequency vibrational spectra of solid-state crystalline materials. Since THz spectroscopy is sensitive to both the intermolecular and intramolecular forces that govern the formation of crystalline materials, it is an ideal tool to investigate the accuracy of calculated DFT crystal structures and their vibrational spectra. When using solid-state DFT, non-covalent dispersion interactions are not fully treated in typical approaches. In order to account for these interactions, the addition of dispersion force correction terms are necessary. A number of methods exist to correct for this deficiency of DFT, and this work investigates the use of semi-empirical London dispersion force correction models. Through the investigation of several small organic molecules, amino acids and related compounds, the standard implementation (referred to as DFT-D) is examined, and the need to alter this standard approach has been identified. Modifications of the scaling factor and atomic parameters within this method have led to more accurate simulations, termed the DFT-DX model. In addition to this work on improving London dispersion force corrections, solid-state DFT calculations with these enhancements can be used to predict the crystal structures of previously unknown or difficult to synthesize materials, such as amino acid hydrates, and achieve detailed information about the internal and external forces in molecular crystals.

EVALUATION OF NON-COVALENT INTERACTION MODELS IN MOLECULAR  
CRYSTALS USING TERAHERTZ SPECTROSCOPY

by

Thomas R. Juliano Jr.

B.S. University at Buffalo, 2011  
M.Phil. Syracuse University, 2013

Dissertation

Submitted in partial fulfillment of the requirements for the degree of  
Doctor of Philosophy in Chemistry

Syracuse University  
December 2014

Copyright © Thomas R. Juliano Jr. 2014

All Rights Reserved

## Acknowledgments

This project would not have been possible without the help and support of a number of people. First and foremost, I would like to thank Dr. Timothy Korter. As my advisor, he assisted me through all of the work presented here. He worked with me daily, ensuring that everything was moving along smoothly, and when problems arose, he was there to help me figure them out.

I would like to thank Dr. Ari Chakraborty and Dr. Joe Chaiken who have been my main two committee members since my second year research proposal. I would also like to thank the rest of my committee members, Dr. Lisa Manning, Dr. Bruce Hudson, and Dr. Tara Kahan, for taking the time to read my thesis and be a part of my defense. I also need to thank the Chemistry department office staff, who was very helpful throughout my time here, especially while getting ready for my defense.

I also thank the friends that I have made here and especially the current and former members of the Korter group. Dr. Matt King, Dr. Ewelina Witko, and Dr. Sean Delaney assisted me when I joined the group and showed me what I would need to do to make it to this day, and Mike Ruggiero who is a current group member that played a large role in our international travels.

My family has supported me throughout this entire process since day one, and for this I thank them. No matter how things were going, I could always count on them to be behind me. I also would like to thank my wife, Stephanie. She moved out here with me with no questions asked and has been the main force behind me when I was less-than-motivated.

Finally I would like to thank the NSF and Syracuse University for their support which allows all of this research to take place.

## Table of Contents

Acknowledgments.....	iv
List of Illustrative Materials.....	viii
CHAPTER 1: Introduction .....	1
1.1 Research Objectives .....	1
1.2 Terahertz Spectroscopy .....	7
1.3 Solid-State Density Functional Theory .....	14
1.3.1 Quantum Theory .....	14
1.3.2 Density Functional Theory .....	16
1.3.2.1 Density Functionals .....	18
1.3.2.2 Local Density Approximations .....	19
1.3.2.3 Generalized Gradient Approximations .....	19
1.3.2.4 Hybrid Functionals.....	21
1.3.3 Basis Sets .....	22
1.3.3.1 Pople-style Basis Sets .....	23
1.3.3.2 Correlation-consistent Split-valence Basis Sets.....	24
1.3.4 Density Functional Theory in the Solid State.....	25
1.3.4.1 Reciprocal Space, the Brillouin Zone, and Bloch Functions .....	25
1.3.4.2 Periodic Boundary Conditions .....	28
1.3.4.3 Geometry Optimizations .....	31
1.3.4.4 Vibrational Mode Calculations .....	32
1.3.4.4.1 Vibrational Frequencies .....	32
1.3.4.4.2 Infrared Intensities.....	34
1.3.4.5 Dispersion Forces.....	34
1.4 References .....	41
CHAPTER 2: Terahertz Spectroscopy in the Korter Group.....	50
2.1 Time-Domain Terahertz Spectrometer.....	50
2.2 Terahertz Generation and Detection .....	52
2.2.1 Optical Rectification.....	52
2.2.2 Free-Space Electro-Optic Sampling .....	54
2.3 Sample Preparation .....	55
2.4 Data Acquisition and Processing.....	56
2.5 References .....	59
CHAPTER 3. Use of Solid-State Density Functional Theory in the Korter Group .....	60
3.1 CRYSTAL Software Package.....	60
3.2 Unit Cell Optimizations .....	62
3.3 Frequency Calculations .....	64
3.4 Energy Calculations .....	67

3.4.1 Total Electronic Energy .....	67
3.4.2 Conformational and Cohesive Energies .....	67
3.4.3 Basis Set Superposition Error .....	69
3.6 References .....	70
CHAPTER 4. London Force Correction Disparity in the Modeling of Crystalline Asparagine and Glutamine .....	72
4.1 Introduction .....	73
4.2 Methods .....	75
4.2.1 Experimental .....	75
4.2.2 Theoretical .....	79
4.3 Results and Discussion .....	80
4.3.1 Experimental Terahertz Spectra .....	80
4.3.2 Comparison of Calculated and Experimental Crystal Structures .....	82
4.3.3 Comparison of Calculated and Experimental Terahertz Spectra .....	87
4.3.4 Evaluation of Solid-State Cohesive Energies .....	92
4.4 Conclusions .....	94
4.5 Supporting Information .....	95
4.6 Acknowledgements .....	95
4.7 References .....	96
CHAPTER 5. Origins of Hydration Differences in Homochiral and Racemic Molecular Crystals .....	99
5.1 Introduction .....	100
5.2 Methods .....	102
5.2.1 Experimental .....	102
5.2.2 Theoretical .....	105
5.3 Results and Discussion .....	106
5.3.1 Terahertz Spectroscopy .....	106
5.3.2 Theoretical Analysis .....	109
5.3.2.1 Structural Analysis of Anhydrous L-ASP and DL-ASP .....	109
5.3.2.2 Simulated Terahertz Spectra of Anhydrous L-ASP and DL-ASP .....	111
5.3.2.3 Structural Analysis of L-ASP Monohydrate .....	114
5.3.2.4 Structural Predictions for DL-ASP Hydrates .....	116
5.3.2.5 Conformational, Cohesive, and Gibbs Free Energies of Aspartic Acid Crystals .....	120
5.4 Conclusions .....	122
5.5 Supporting Information .....	122
5.6 Acknowledgements .....	123
5.7 References .....	124
CHAPTER 6. Evaluating London Dispersion Force Corrections in Crystalline Nitroguanidine by Terahertz Spectroscopy .....	127
6.1 Introduction .....	128

6.2 Experimental .....	131
6.3 Theoretical.....	133
6.4 Results and Discussion.....	135
6.4.1 Experimental Section.....	135
6.4.2 Theoretical Section.....	138
6.4.2.1 Structural Analysis.....	139
6.4.2.2 Simulated Terahertz Spectra and Mode Assignments .....	143
6.5 Conclusions .....	147
6.6 Acknowledgements .....	148
6.7 References .....	149
CHAPTER 7. Terahertz Vibrations of Crystalline Acyclic and Cyclic Diglycine: Benchmarks for London Force Correction Models .....	152
7.1 Introduction .....	153
7.2 Methods.....	155
7.2.1 Experimental.....	155
7.2.2 Theoretical .....	158
7.3 Results and Discussion.....	160
7.3.1 Experimental.....	160
7.3.2 Theoretical .....	163
7.3.2.1 Structural Analysis.....	163
7.3.2.2 Simulated Terahertz Spectra .....	168
7.4 Conclusions .....	176
7.5 Supporting Information.....	177
7.6 Acknowledgements .....	177
7.7 References .....	178
CHAPTER 8. Applications to Future Work .....	181
8.1 Glutamic Acid .....	181
8.2 Serine and Proline .....	185
8.3 References .....	190
CHAPTER 9. Conclusions.....	191
Appendix A. Chapter 4 Supporting Information .....	195
Appendix B. Chapter 5 Supporting Information.....	198
Appendix C. Chapter 7 Supporting Information.....	200
Curriculum Vitae .....	202



## List of Illustrative Materials

Figure 1-1. Chart of the electromagnetic spectrum. Note the terahertz region located between the microwave and infrared regions. ....	7
Figure 1-2. The expanded view of a cubic simulation cell surrounded by 26 periodic images generated by periodic boundary conditions.....	29
Figure 1.3. Unit cell depictions of cyclodiglycine with (left) and without (right) London dispersion force corrections.....	34
Figure 2-1. Schematic of the terahertz spectrometer used in the Korter lab.....	50
Figure 2-2. Representation of the terahertz waveform (a), frequency spectrum from Fourier transform (b), and the final terahertz absorption spectrum (c).....	57
Figure 3-1. Step-by-step process for DFT calculations in the Korter Group.....	65
Figure 4-1. Labeled glutamine molecule and unit cell. ....	76
Figure 4-2. Labeled asparagine molecule and unit cell. ....	77
Figure 4-3. Terahertz spectra of glutamine (top panel) and asparagine (bottom panel) at 293 K (red) and 78 K (blue). ....	80
Figure 4-4. Terahertz spectrum of glutamine at 78 K compared to the theoretical spectrum generated using PBE/cc-pVTZ with DFT-D* dispersion corrections.....	87
Figure 4-5. Terahertz spectrum of asparagine at 78 K compared to the theoretical spectrum generated using PBE/cc-pVTZ with DFT-D* dispersion corrections.....	88
Figure 5-1. Labeled L-ASP asymmetric unit and full unit cell.....	102

Figure 5-2. Labeled DL-ASP asymmetric unit and full unit cell.....	103
Figure 5-3. Experimental THz spectra of L-ASP (top) and DL-ASP (bottom) at 78 K. ....	107
Figure 5-4. Terahertz spectra of L-ASP (top) and DL-ASP (bottom) compared to theoretically generated spectra (red traces) using B3LYP/6-31G (d,p). ....	112
Figure 5-5. Labeled L-ASP•H <sub>2</sub> O asymmetric unit and full unit cell. ....	114
Figure 5-6. DL-ASP•0.5H <sub>2</sub> O asymmetric unit and full unit cell. ....	116
Figure 5-7. DL-ASP•H <sub>2</sub> O asymmetric unit and full unit cell. ....	118
Figure 6-1. Labeled nitroguanidine molecule and nitroguanidine unit cell.....	131
Figure 6-2. Terahertz spectrum of solid nitroguanidine at 78 K.....	135
Figure 6-3. Terahertz spectra of solid nitroguanidine (black) and fully-deuterium substituted nitroguanidine (red) at 78 K. ....	137
Figure 6-4. 78 K terahertz spectrum of nitroguanidine compared to the theoretical spectra generated using PBE/cc-pVTZ with DFT-D2, DFT-D*, and DFT-DX London force corrections. ....	144
Figure 7-1. Labeled acyclic diglycine molecule and unit cell. ....	155
Figure 7-2. Labeled cyclic diglycine molecule and unit cell. ....	156
Figure 7-3. Terahertz spectra of acyclic diglycine (top panel) and cyclic diglycine (bottom panel) at 293 K (red) and 78 K (blue). ....	160
Figure 7-4. Terahertz spectrum of acyclic diglycine at 78 K compared to the theoretical spectra generated using PBE/cc-pVTZ with three different London force corrections applied. Note the differences in absorption unit scales.....	167

Figure 7-5. Terahertz spectrum of cyclic diglycine at 78 K compared to the theoretical spectra generated using PBE/cc-pVTZ with three different London force corrections applied. ....	168
Figure 7-6. Percent variation across the DFT-D2, DFT-D*, and DFT-DX models in the prediction of the frequencies of all normal modes of vibration for acyclic diglycine (bottom) and cyclic diglycine (top). ....	170
Figure 7-7. A portion of the 78 K terahertz spectrum of cyclic diglycine from 35 to 55 $\text{cm}^{-1}$ with baseline correction compared to the theoretical spectra generated using PBE/cc-pVTZ with three different London force corrections applied. ....	173
Figure 8-1. Images of molecules of L-GLU (extracted from L-GLU crystal) and D-GLU (extracted from DL-GLU crystal) to show the L- and DL- orientations. ....	181
Figure 8-2. Single molecule (molecule pairs for hydrates) for the crystalline amino acids L-PRO (I), L-SER (II), L-PRO monohydrate (III), and L-SER monohydrate (IV). All molecules were extracted from their respective crystal structures. ....	184
Figure A1. Experimental cryogenic terahertz spectrum of asparagine monohydrate from 10 to 100 $\text{cm}^{-1}$ . ....	194
Figure A2. Experimental powder X-ray diffraction data of room-temperature ASN (black). The best fit X-ray data is shown in red. The calculated pattern based on 90 K single-crystal X-ray data (gray) is shown for reference. <sup>3</sup> Data was collected on a Bruker KAPPA APEX DUO using Cu radiation. ....	195

## **CHAPTER 1: Introduction**

### **1.1 Research Objectives**

The main objective of the research presented in this thesis is the accurate modeling of the non-covalent intermolecular forces that exist between molecules in the solid state. In order to achieve this goal, the computational method known as solid-state density functional theory (DFT), with the incorporation of semi-empirical dispersion force corrections, and their modifications, was used and evaluated.<sup>1</sup> Terahertz (THz) spectroscopy was performed on several molecular solids, including amino acids, biologically relevant molecules, and derivatives of these molecules, in order to evaluate the accuracy of the DFT simulations. As is often the case with solid-state DFT, the strength of the non-covalent intermolecular forces present in the molecular systems studied was underestimated. To correct for this, semi-empirical dispersion force corrections, based on fixed theoretical data that represent the van der Waals radii, atomic ionization potentials, and static dipole polarizabilities of the atoms, in conjunction with an adjustable global scaling factor, were implemented. In the standard usage of these corrections, the suggested global scaling parameter only varies depending on the functional being used.<sup>2</sup> Through the extensive research into the aforementioned molecules, it was determined that the use of a standard global scaling parameter based on functionals does not reproduce the molecular structures well enough for investigations in the THz region. The overall result shows that the global scaling parameter of the semi-empirical corrections is not only functional specific, but is also specific to the molecule(s) under investigation.<sup>3-6</sup> Using this guideline, it became possible to predict the structures of hydrated species of amino acids. . Furthermore, this led to the development of a newly parameterized set of semi-empirical dispersion corrections based on

experimentally obtained values (when available) for the van der Waals radii,<sup>7</sup> the atomic ionization potentials,<sup>8</sup> and the static dipole polarizabilities.<sup>5,9</sup> The van der Waals radii were obtained from X-ray crystallographic data.<sup>10</sup> Atomic ionization potentials can be determined in a number of ways, including ionization induced by an electron impact, measuring the energy of photons during photoionization, and studying spectroscopic data on energy levels and their convergence toward the ionization limit.<sup>7</sup> The static dipole polarizabilities were obtained from measuring the capacitance of charge with and without the presence of the atomic/molecular gas.<sup>7</sup> The molecules investigated in this research include monomeric amino acids, racemic and homochiral amino acids and their hydrates, an explosive compound related to an amino acid, and dimeric cyclic and acyclic amino acids.

Two very similar amino acids, L-asparagine (ASN) and L-glutamine (GLN), were chosen as benchmark systems to determine the effect of non-covalent dispersion forces in solid-state DFT calculations. In both amino acids, the use of the functional-based global scaling value resulted in structures that were not acceptable when compared to X-ray crystallographic data. In order to simulate the best possible structures, the global scaling factor was individually adjusted for each molecule. This result was somewhat surprising given the similarities between the molecular structures of ASN and GLN. Once the molecule-based global scalar values were determined, the resulting theoretical structural and spectral data accurately represented the respective experimental data.

With the use of a system-dependent global scaling factor, interest in chiral amino acids led to the next investigation. The amino acid, aspartic acid, was chosen because known structures for both L-aspartic acid (L-ASP) and DL-aspartic acid (DL-ASP) exist. With these structures available, the effect of the global scalar was tested to see if chirality has any effect on the

intermolecular force contributions from the semi-empirical dispersion force correction method. After completing structural simulations using solid-state DFT with the semi-empirical dispersion force corrections, it was determined that in the case of L-ASP versus DL-ASP, the global scaling values were identical. From these accurate structural recreations, the THz spectra were simulated and compared to the experimental THz spectra to gauge the accuracy of the calculations. They were found to be in excellent agreement with one another. The investigation into ASP went even deeper with the inclusion of hydrates. The L-ASP monohydrate structure was known, however no known structures of a DL-ASP hydrate exist, sparking interest into the reasons behind hydrate formation in amino acids. In order to evaluate the L-ASP monohydrate, the global scaling factor from the anhydrous ASP was used in the solid-state DFT calculations. This resulted in an acceptable structure that was used to simulate the low-frequency vibrations. Unfortunately, experimental THz data could not be obtained for the L-ASP monohydrate, but the success of the structural simulations speaks towards the accuracy of the calculations. Furthermore, the absence of any DL-ASP hydrates led to the prediction and proposal of two DL-ASP hydrate structures, a hemihydrate and a monohydrate. These structures were proposed using the same global scaling factor as the other ASP calculations, which resulted in viable structures. The structures were further tested by simulating frequencies which proved to be successful as well.

The obvious need for a more accurate dispersion correction model, as seen in the results above, led to the development of a new parameterization of the standard Grimme model. In this new parameterization, the values used for the van der Waals radii, the atomic ionization potentials, and the static dipole polarizabilities were taken from experimental data, rather than theoretically calculated values.<sup>1,5</sup> With the use of experimentally determined values for physical

data, the hopes were to produce a more accurate representation of the non-covalent dispersion forces found in molecular solids.

To initially test this newly parameterized model, nitroguanidine (NG), an explosive closely related to amino acids, was chosen for its small size and low computational cost. It was also chosen due to interest in explosive compounds related to security purposes. The use of the new parameterization, termed DFT-DX,<sup>5</sup> was evaluated against the traditional approaches developed by Grimme (DFT-D2)<sup>2</sup> and modified for use in the solid-state by Civalleri (DFT-D\*<sup>8</sup>). The comparison process began with structural simulations based on the experimental X-ray structures. Once the best global scaling value was determined for each correction model, the resulting structures were compared to the experimental structures for accuracy. In the case of both the external parameters (unit cell volume and length of axes *a*, *b*, and *c*) and internal parameters (bond length, bond angle, dihedral angle, and heavy-atom hydrogen bond distance), DFT-DX proved to have the lowest overall errors. As is the standard procedure, the best structure for each dispersion model was subjected to frequency calculations to be compared to the experimental THz spectrum. Each of the three correction models provided acceptable representations of the experimental spectrum, however the DFT-DX spectrum was the most closely related of the three. The initial findings from the work on nitroguanidine opened the door for further investigations using the DFT-DX correction model.

This DFT-DX parameterization was then tested on the dimeric amino acid compounds glycine-glycine and cycloglycine-glycine. These molecular solids were chosen for both their similarities: both consisting of two glycine molecules linked together, and their differences: one is linear, and the other is cyclic. Once again, due to the unproven nature of the DFT-DX model, all solid-state DFT calculations were carried out using the two standard semi-empirical

dispersion force models, DFT-D2 and DFT-D\*, as well as the DFT-DX method. The simulated structures were compared to the experimental X-ray structures for both external and internal parameters (same criteria used for nitroguanidine). For the acyclic diglycine, the best representation of the external parameters was provided by the DFT-D2 correction model, while DFT-DX gave the best structure for the cyclic analogue. When the internal parameters were reviewed, all three parameterization models performed equally. The true test of the semi-empirical dispersion correction methods came down to the simulations of the low-frequency vibrational modes. When the calculated spectra for each method were compared to the experimental THz spectra, the superior parameterization became the DFT-DX method. This was especially true in the case of the cyclic diglycine molecule. The DFT-DX model was the only model of the three that accurately portrayed the ordering and intensity of the lowest frequencies absorptions seen in the experimental THz spectrum.

The research presented in this thesis provides insight into the use and transferability of semi-empirical dispersion corrections in solid-state DFT simulations. The focus of these studies was on amino acids and similar molecules as benchmarks for the care needed in evaluating all molecules when using semi-empirical correction methods. Using the knowledge gained from these small molecular systems, the hope is for transferability to the investigations of larger, more complex systems in future work. It will serve future research well to be aware of the limitations of the current semi-empirical dispersion correction models, until the ultimate goal of a globally transferable dispersion correction method is attained. In addition to these general findings, the use of DFT to predict the formation/non-formation of hydrates of molecular solids can be very useful in the studies of larger molecules, such as pharmaceuticals. Ultimately, this research has provided the THz and theoretical communities with much insight into the true nature of semi-



empirical corrections and the abilities of solid-state DFT to predict the hydration qualities of molecular crystals.

## 1.2 Terahertz Spectroscopy

Terahertz radiation (far-infrared) is located between the microwave and infrared regions of the electromagnetic spectrum and falls in the range of 0.3 THz to 10 THz ( $3\text{-}333\text{ cm}^{-1}$ ). Because of its location on the electromagnetic spectrum (**Figure 1-1**), THz radiation is both non-ionizing and non-destructive, which allows it to be used to investigate sample types from small organic molecules to sensitive biological samples.<sup>9</sup> In addition, THz is able to penetrate non-conducting materials such as paper, plastics, and fabrics; making it particularly interesting for security applications.<sup>10-12</sup> Terahertz spectroscopy also has practical applications in medical imaging,<sup>13-15</sup> pharmaceutical manufacturing,<sup>16-18</sup> and industrial diagnostics.<sup>19-21</sup> The origins of terahertz spectroscopy have roots in the 1960s investigations utilizing far-infrared spectroscopy,<sup>22</sup> however, these techniques were limited by the available THz sources at the time.<sup>23</sup> Terahertz spectroscopy has seen rapid advancement over the past few decades due to the advent of femtosecond laser systems. The late 1980s saw the first applications of ultrafast laser systems to the generation and detection of THz radiation using photoconductive antennas, developed by Auston and Grischkowsky.<sup>24,25</sup> Terahertz technology continued to evolve based on ultrafast laser systems and other generation/detection schemes.

Time-domain THz spectroscopic methods now typically use ultrafast femtosecond Ti:Sapphire laser systems. The femtosecond laser pulses are used to generate THz radiation through electro-optic methods in semiconductor crystals (GaAs, ZnTe, and others).<sup>23,26-28</sup> Using the same methods, detection of phase and amplitude information contained within the THz pulse can be achieved.<sup>23</sup> In addition to the pulsed THz systems, the use of continuous wave (cw) THz radiation can be achieved via photomixing of light sources at a photoconductive antenna. This method is, however, limited in practical applications as longer acquisition times are needed in

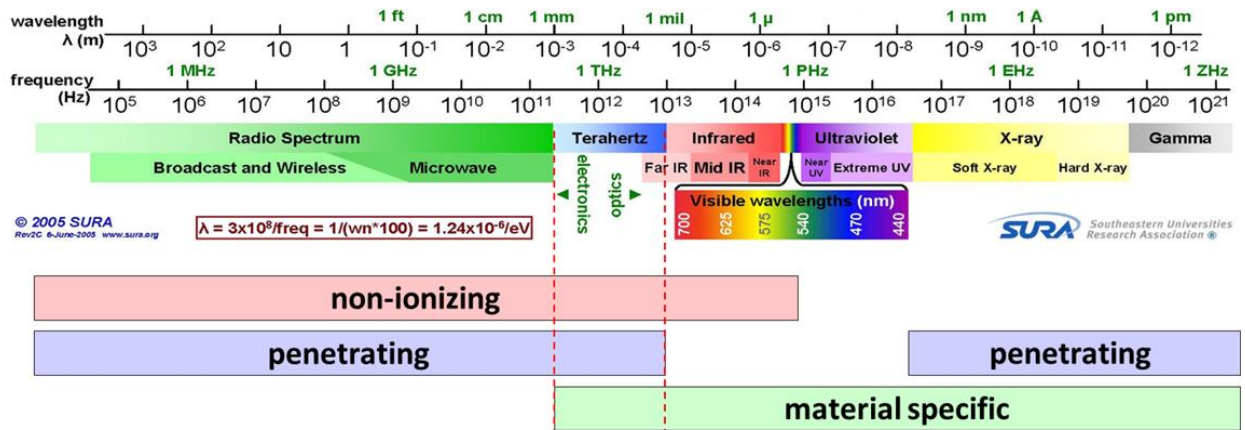


**Figure 1-1.** Chart of the electromagnetic spectrum.<sup>29</sup> Note the terahertz region located between the microwave and infrared regions.

order to detect the signals.<sup>30,31</sup> Terahertz technologies using cw radiation continue to advance with the development of electronic RF (radio-frequency) up-conversion, optical source down-conversion, new lasers, and backward-wave oscillators.<sup>23</sup> The interest in cw THz technology stems from the fact that it is the most likely technique to be practical in the development of small and reliable portable devices.<sup>23,32-34</sup>

Terahertz spectroscopy and imaging have potential applications across a wide variety of scientific, industrial, and government interests. This has led to numerous studies of chemicals and materials in the gas, liquid, and solid phases. Studies in the gas phase have been conducted primarily on small molecules, investigating the rotational transitions, such as those seen in water and ammonia.<sup>35-37</sup> The study of larger gas-phase molecules, those able to exhibit torsional vibrational motions, is of particular interest in the detection of explosive materials.<sup>38</sup> In terms of security and defense applications, this is a very promising and useful THz technique. The use of gas-phase THz spectroscopy is also present in the fields of atmospheric science and astronomy.<sup>39-41</sup> Free-space investigations are interesting; however, they are highly limited in practical applications due to the presence of water vapor. Outside of controlled laboratory settings, ambient water strongly absorbs THz radiation, thereby significantly decreasing signal-to-noise, making the collected data difficult to use. Condensed-phase materials have seen far more interest in the field of THz spectroscopy. Liquid-phase systems have gained interest in THz studies, mainly due to biological applications.

Terahertz spectroscopy has been used extensively to study water in hopes of transferability to biological systems.<sup>42-44</sup> Polar liquids, like water, produce THz spectra based on the reorientation of molecular dipoles. The timescale of the relaxation processes occur in the picosecond to femtosecond range, making THz an ideal detection method.<sup>45,46</sup> The solvation

shells of dissolved molecules have also been studied using THz spectroscopy, as the relaxation times can change based on the presence of solutes and/or multiple solvents.<sup>47-50</sup> Studies have also been conducted on non-polar liquids, such as benzene, *n*-alkanes, and cyclohexane, using THz spectroscopy.<sup>51</sup> The relaxations of collision-induced dipoles within the non-polar liquids are believed to be the root of the THz spectral features.<sup>52,53</sup> Although studies of liquid-phase materials are very interesting to future applications, by far the most widely studied materials using THz spectroscopy are those in the solid-phase.

Materials in the solid-state have drawn the most attention using THz spectroscopy. The THz research conducted on solid-state materials ranges from molecular crystals to nanoparticles.<sup>54-58</sup> A large majority of molecular crystals have lattice vibrations that are active in the THz region, since such vibrations are governed by the intermolecular forces that hold the molecules together. Each individual molecular crystal has a unique THz spectrum due to differences in the intermolecular forces present.<sup>59</sup> Terahertz spectra can, therefore, act as “fingerprints” in the detection and identification of solid-state substances, including harmful and illegal substances such as explosives and drugs.<sup>12,60-64</sup> Current research efforts are focusing on the development of small mobile THz scanner devices for use in these applications.<sup>65-67</sup> The sensitivity of THz spectroscopy to molecular packing and interactions has led to interest from the pharmaceutical industry in order to analyze crystallinity and polymorphism in drug molecules.<sup>16-18,68-70</sup> The use of THz spectroscopy can not only identify polymorphs within a sample, but can also relatively quantify the amount of each polymorph present.<sup>71</sup> The individual polymorph spectra form a linear combination that leads to the overall spectrum of a sample. By using a method to subtract each individual spectrum, the percent composition of the sample can be deduced. Terahertz spectroscopy has also been used to observe phase transition in molecular

crystal samples.<sup>72,73</sup> Carrier dynamics in nanoparticles and semiconductors have been studied using THz spectroscopy as an optical probe that measures the conductivity of the substance. This is particularly useful in cases where the use of conventional electrical connections is unable to be used reliably due to signal disruptions.<sup>74-78</sup>

In terms of real world applications, the use of THz systems is prevalent in a number of industrial settings including the food processing industry,<sup>79-82</sup> the plastics industry,<sup>83,84</sup> and the paper industry.<sup>85-87</sup> Terahertz systems are used as one of many quality control methods. In the food processing industry, THz is used in order to monitor water content and detect foreign objects within the products. The plastics industry uses THz spectroscopy to monitor a number of attributes of the products, including transition temperatures and fiber orientations, among other things.<sup>88-90</sup> The use of THz spectroscopy has even been applied to art. Art historians and conservationist use THz spectroscopy to investigate paintings,<sup>91-93</sup> since it is both non-destructive and can penetrate layers of paint. Terahertz spectroscopy is able to shed light onto the pigments used in paintings as well as provide imaging of layers of the art works that are unable to be seen by eye.

Beyond spectroscopy, there is much interest in T-ray imaging; which is the use of THz radiation to image various materials. The most important and largest interest in this technology is in the defense and security market, especially airport security. The use of a THz scanner would provide the security personnel with a means to non-invasively scan both persons and luggage. Since THz radiation can penetrate clothing and fabric, the potential presence of harmful materials can readily be detected on a person or in a luggage item.<sup>94,95</sup> And since THz radiation cannot penetrate human skin, it poses no threat to the individuals being scanned. In addition to these large-scale security instruments, the possibility of handheld THz devices is under

development.<sup>66</sup> Such devices would allow the users to analyze any suspicious substances. T-ray imaging is also of interest to the pharmaceutical industry, as it can be used to determine the thickness of and irregularities in tablet coatings.<sup>16,17</sup> These imaging methods are not currently in wide use. However, as the technology becomes more practical, there will be a large demand for these techniques. As THz technology progresses, its applications will continue to grow.

Terahertz technology continues to improve with the development of new optical sources and generation and detection methods. The ability to increase THz field strength and the sensitivity of detection will lead to new fields of interest and research paths. In its current form, THz spectroscopy can be better understood when coupled with the ability to interpret the physical meaning of THz spectra. The use of computational methods can be used to model the interactions within molecular crystals that are responsible for the observed THz absorptions. When determining the physical properties that give rise to THz absorptions, it is important to consider that both inter- and intra-molecular forces contribute to the vibrational motions in the THz region.<sup>5,6,14,60,61,99-104</sup> The current computational methods in use with THz spectroscopy primarily include molecular dynamics and solid-state density functional theory. A number of studies have been published using computational methods to interpret experimental THz data on molecules including biological molecules,<sup>6,97</sup> pharmaceuticals,<sup>68,70</sup> illicit drugs,<sup>63,64</sup> and explosive materials.<sup>5,62</sup> Of the computational methods used, solid-state DFT has proven to show the best results. Further improvements to the solid-state DFT simulations have been seen with the inclusion of semi-empirical dispersion force corrections added into the calculations. This method results in the accurate modeling of both the geometric properties of the molecular crystals, as well as the low-frequency lattice vibrations.<sup>5,6,97,99</sup> The research proposed in this thesis is primarily focused on the accurate modeling of the THz spectra of molecular crystals by

investigating the use and modification of the semi-empirical dispersion force correction terms. The knowledge gained from these evaluations led to the extension of solid-state DFT to the prediction of amino acid hydrates and ultimately to a newly parameterized semi-empirical dispersion force correction model.<sup>5,6,100</sup>



### 1.3 Solid-State Density Functional Theory

All of the computational work presented in this thesis was conducted using solid-state density functional theory. In order to gain a better understanding of this method, the origins of density functional theory, quantum theory, and its application in the solid state must be discussed. Several text books are available that go into deeper descriptions of this material.<sup>101-104</sup>

#### 1.3.1 Quantum Theory

When studying atomic-level systems, the electrons exhibit properties of both waves and particles, given their small mass, and require a quantum mechanical approach. Quantum mechanics does not permit an exact answer to the location of particles in time, instead it uses a probabilistic approach in which the probabilities of the locations of particles at specific times ( $t$ ) can be obtained. The Schrödinger equation (wave function,  $\Psi$ ),

$$H\Psi = i \frac{\partial \Psi}{\partial t}, \quad (1.1)$$

where  $H$  is the Hamiltonian operator corresponding to the total energy of the system under study,  $\Psi$  is the basis of the probability function. The probability function is simply the square of the wave function. The Hamiltonian represents the sum of the kinetic ( $T$ ) and the potential ( $V$ ) energy operators and is expressed as

$$H(\mathbf{r}, t) = T(\mathbf{r}) + V(\mathbf{r}, t), \quad (1.2)$$

where  $\mathbf{r}$  is the spatial coordinates of the electrons and  $t$  is time. In the case of a bound system, the potential energy part of the Hamiltonian becomes independent of time. The space and time variables can then be separated and a simple form of the Schrödinger equation can be expressed as

$$H\Psi = E\Psi. \quad (1.3)$$

This equation is known as the time-independent Schrödinger equation, where  $\Psi$  represents the set of solutions (eigenstates), and  $E$  represents the eigenvalues that satisfy the equation.

The definition of the Hamiltonian is not constant; it is dependent on the physical system under study. In order to simplify the Hamiltonian for atomic systems, the Born-Oppenheimer approximation is used. This approximation states that since the masses of atomic nuclei are so much larger than those of the electrons, the kinetic energy of the nuclei is negligible and is ignored in many-body systems. The removal of terms involving the kinetic energy of the nuclei results in the remaining terms that only involve the electrons. This leads to a simplified Hamiltonian which is represented as

$$\left[ -\frac{\hbar^2}{2m} \sum_{i=1}^N \nabla_i^2 + \sum_{i=1}^N V(\mathbf{r}_i) + \sum_{i=1}^N \sum_{j<i} U(\mathbf{r}_i, \mathbf{r}_j) \right] \Psi = E\Psi. \quad (1.4)$$

In this equation, the terms in the brackets are equal to the Hamiltonian operator. The first term represents the kinetic energy of the electrons, where  $m$  is the mass of an electron and  $\nabla$  is the Laplace operator, defined as

$$\nabla_i^2 = \frac{\partial^2}{\partial x_i^2} + \frac{\partial^2}{\partial y_i^2} + \frac{\partial^2}{\partial z_i^2}. \quad (1.5)$$

The second term corresponds to the energy that results from the interaction of each electron to the collective of atomic nuclei, and the third term represents to interaction energy between separate electrons. As part of the Schrödinger equation, the other variables,  $E$  and  $\Psi$  represent the ground state energy and the electronic wave function, respectively. The electronic wave function is represented as a function of the spatial coordinates of the individual electrons,  $\Psi = \Psi(\mathbf{r}_1, \mathbf{r}_2, \dots, \mathbf{r}_N)$ .

The solution of the Schrödinger equation becomes increasingly more difficult with the increasing size of the systems being studied. Each electron is defined by three parameters, making the total number of parameters equal to  $3N$ . The increased number of parameters is not the only prohibitive property of large systems. As defined in the Hamiltonian, the third term shows the interactions between individual electrons. It is not possible to solve the electronic wave function for any electron without considering the wave functions of all other electrons present. This limitation has led to the development of methods that can approximate the energies of large systems, such as density functional theory (DFT).<sup>102</sup> DFT is based on the premise that the probability of an electron being in a particular location in space determines the quantities of physical interest. The density of electrons,  $n(\mathbf{r})$ , at point  $\mathbf{r}$ , in terms of the individual wave functions,

$$n(\mathbf{r}) = 2 \sum_i \Psi_i^*(\mathbf{r}) \Psi_i(\mathbf{r}), \quad (1.6)$$

is used to estimate the probability of the electron location. When applying this method, the electron density is defined by a function of three coordinates, whereas, in the Schrödinger equation the number of parameters is equal to  $3N$  coordinates. Due to the reduction of parameters, DFT allows for calculations to be performed on large systems that would have otherwise been impossible.

### 1.3.2 Density Functional Theory

Density functional theory is based on the work of Kohn, Hohenberg, and Sham. Two fundamental mathematical theorems proven by Hohenberg and Kohn laid the groundwork for the development of DFT.<sup>105</sup> The first principle states that “The ground-state energy from Schrödinger’s equation is a unique functional of the electron density.”<sup>102</sup> This theorem states that the electron density can be used as a one-to-one correspondence to the ground-state wave

function. Knowing the electron density would allow for the determination of all properties, including the ground-state energy and wave function. The problem with this theorem is the unfortunate fact that the true functional is not known, and therefore the DFT approach can only use approximations. This leads to the second theorem from Hohenberg and Kohn that says, “The electron density that minimizes the energy of the overall functional is the true electron density corresponding to the full solution of the Schrödinger equation.”<sup>102</sup> The use of the true functional would allow for the variation of the electron density until the minimization was achieved, and the solution to the Schrödinger equation to be obtained.

The equation developed by Kohn and Sham in 1965 is the basis of most current DFT work.<sup>106</sup> They discovered that the inclusion of atomic orbitals into the calculations led to a better description of the kinetic energy of electrons. The set of equations developed by Kohn and Sham results in solutions that are single-electron wave functions. By separating each electron into its own equation, the number of variables is increased from 3 to  $3N$ , which can be a limiting factor in this formalism. The Kohn-Sham equations have the following form

$$\left[ -\frac{\hbar^2}{2m} \nabla^2 + V(\mathbf{r}) + V_H(\mathbf{r}) + V_{XC}(\mathbf{r}) \right] \Psi_i(\mathbf{r}) = \varepsilon_i \Psi_i(\mathbf{r}). \quad (1.7)$$

The variables in this equation are similar to those seen in the in Eq. 1.4. The main difference is the absence of the summations, due to the fact that this form of the equation is applied to single electrons as opposed to all electrons in a system. The first two terms are known from the full Schrödinger equation. The next term,  $V_H(\mathbf{r})$ , is known as the Hartree potential and represents the Coulomb repulsion between the electron under consideration and the total electron density of all electrons present, and has the form

$$V_H(\mathbf{r}) = e^2 \int \frac{n(\mathbf{r}')}{|\mathbf{r}-\mathbf{r}'|} d^3 \mathbf{r}'. \quad (1.8)$$

Inherent to this part of the equation is the self-interaction of the electron under consideration. This value has no physical meaning and is corrected by the fourth term in the equation. The fourth term is known as the exchange-correlation functional and is essentially a correction term used for numerous effects.

The development of new and more accurate functionals for use with DFT is an ongoing field of research.<sup>107-111</sup> Once new functionals are developed, they must be tested for accuracy. There is currently no proven computational method to unambiguously evaluate the performances of functionals, so the results must be compared to experimental data, such as molecular structures or ionization potentials. There are a number of different approaches in use and under development in an attempt to discover (or at least approach more closely) the true functional necessary for the full solution to the Schrödinger equation. The search for better correlation between experimental observations and DFT simulations has even led to the incorporation of empirical or semi-empirical parameters into the functionals to enhance their performance.<sup>107,112</sup>

### 1.3.2.1 Density Functionals

The ultimate goal of the exchange-correlation potential,  $V_{XC}$ , is to define the functional needed to exactly solve the Schrödinger equation. The form of this functional is not known, and therefore must be approximated in order to account for the energy contributions made by the other components of the Kohn-Sham equation. The exchange-correlation potential is critical in determining the nonphysical contributions made by the Hartree potential, including the self-interactions of electrons and a correction to the kinetic energy. The search for the best functional

has led to three classes of approximations: local density approximations (LDAs), generalized gradient approximations (GGAs), and hybrid functionals.

### 1.3.2.2 Local Density Approximations

Although its existence was proven by the theorem of Hohenberg and Sham, the true exchange-correlation functional is not known for any system. Using an approximation, the exact functional has been derived for one system, a uniform electron gas.<sup>113</sup> This definition makes the assumption that the electron density is uniform over all space,  $n(\mathbf{r}) = \text{constant}$ . In the formulation of LDAs, the energy is determined by the integration over all space with uniform electron density at each point. Only one electron spin polarization is considered in the original LDA form. In the case of open-shell systems, the inclusion of spin polarizations is necessary since there are two states that can be present. The use of spin polarizations in LDAs is known as local spin density approximations (LSDAs). Two of the most often used LSDA functionals are VWN and VWN5.<sup>114</sup>

The LDA exchange-correlation functionals are useful in cases where solid-state materials contain delocalized electrons, for examples, metallic solids. When a material with localized electrons is investigated, the shortcomings of LDAs become apparent.<sup>102,115,116</sup> Calculations of systems with delocalized electrons using LDAs often lead to underestimated bond lengths and overestimated binding energies.<sup>115</sup> With the general limitation to delocalized electron systems, LDAs have been expanded upon in order to better account for systems with localized electrons.

### 1.3.2.3 Generalized Gradient Approximations

The use of generalized gradient approximation functionals (GGAs) is widespread in current DFT calculations. As mentioned before, the majority of molecular systems do not have

uniform electron distribution and therefore can be evaluated by the changes in the local electron densities. With respect to the LDAs, GGAs add in a term to correct for the gradients in electron densities. There are many different forms of GGAs, as the added term has a number of different formulations. Different GGAs treat the exchange and correlation contributions in different ways, either together or separately. The use of empirical data is prevalent in the formulation of GGAs, leading to variations in the performance of such methods depending on the system being studied.<sup>107,117,118</sup>

There are a number of GGA exchange functionals in use, the most common being that developed by Becke (B) in 1988.<sup>112</sup> He based his exchange functional on empirical data taken from the known exchange energies of the six noble gases. Many functionals have since been developed that do not include the use of empirical data. Some examples of these exchange functionals include PBE (Perdew-Becke-Ernzerhof),<sup>107</sup> P (Perdew-Wang),<sup>119</sup> and B86 (Becke from 1986).<sup>120</sup> These exchange functionals were primarily optimized for gas-phase calculations, however, the development of exchange functionals for the solid-state has led to functionals such as PBEsol<sup>121</sup> and SOGGA (second-order expansion GGA).<sup>122</sup>

The other part of the exchange-correlation functional, correlation, has also seen numerous functional developments. This class of functionals includes PBE (Perdew-Becke-Ernzerhof in 1996),<sup>107</sup> PW91 (Perdew-Wang),<sup>123</sup> B95 (Becke in 1995),<sup>124</sup> and P86 (Perdew in 1986).<sup>125</sup> Other approaches have been developed for the correlation functionals, including that of LYP (Lee-Yang-Parr),<sup>108</sup> which calculates the full correlation energy and is capable of exactly cancelling the electron self-interaction energy of electrons that arises from the Hartree potential in the Hamiltonian. Much like the exchange functionals, many of these correlation functionals were

optimized for use in the gas-phase, but some solid-state functionals have been developed, including PBEsol<sup>121</sup> and WL (Wilson-Levy).<sup>126</sup>

Since the exchange and correlation functionals can be implemented independently, data on nearly all combinations exist in the literature. Some of these combinations have become more prevalent than others, including PBE (for both exchange and correlation), BLYP, and BPW91. In general, the results obtained using the most common GGAs are in good agreement with experimental data, however, it is not uncommon to see variation among the methods dependent on the system under study.<sup>102</sup> When choosing an exchange-correlation GGA to use for DFT calculations, it is advised to base the choice on previously reported performances on like systems.

#### 1.3.2.4 Hybrid Functionals

Combining exchange-correlation GGAs with a portion of exact HF exchange energy has shown an increase in accuracy for some systems.<sup>127,128</sup> The use of this combination of techniques is known as a hybrid method. Of this class of functionals, the most common and widely used is B3LYP.<sup>108,128</sup> This method takes the B exchange functional and the LYP correlation functional and combines them using a three parameter method that dictates the contribution of each term to the total energy. These parameters were optimized to experimental data and are represented by  $\alpha_1$ ,  $\alpha_2$ , and  $\alpha_3$  in the B3LYP equation,

$$V_{XC}^{B3LYP} = V_{XC}^{LDA} + \alpha_1(E^{exchange} - V_X^{LDA}) + \alpha_2(V_X^{GGA} - V_X^{LDA}) + \alpha_3(V_C^{GGA} - V_C^{LDA}). \quad (1.9)$$

The values of  $\alpha_1$ ,  $\alpha_2$ , and  $\alpha_3$  were empirically optimized to 0.20, 0.72, and 0.81, respectively. The term on the left of this equation is the Becke 88 exchange functional and the first term on the right is the Lee-Wang-Parr correlation functional. Several other hybrid functionals have also



been developed, including single parameter versions such as PBE0<sup>117,127</sup> and B1LYP.<sup>108,128</sup> These functionals use values for  $\alpha_1$ ,  $\alpha_2$ , and  $\alpha_3$  of 0.25, 0.75, and 1, respectively. When comparing the one- and three-parameter methods, the results are generally in agreement.

### 1.3.3 Basis Sets

Exactly solving a single-electron equation would require an infinite amount of functions that define the spin orbitals. In order to make these calculations viable, the number of functions must be made finite to allow for reasonable computations. The results of the approximate spin orbital functions can be added together in order to estimate the total single-electron energies using the equation

$$\chi_j(\mathbf{x}) = \sum_{i=1}^K \alpha_{i,j} \phi_i(\mathbf{x}). \quad (1.10)$$

It is important to acknowledge the electron spins when more than one electron populate an orbital. There are two different electron spins which must be included into the calculations due to the Pauli exclusion principle. When considering which basis set to implement, it is important to consider the number of functions within it. The more functions included in the basis set, the more accurate the results will be, but this comes at a cost to computational time as it increases as well. The ideal basis set choice is a compromise between the desired levels of chemical accuracy and the minimum number of basis functions. This compromise allows for calculations that can be completed in a reasonable amount of time with reasonable chemical accuracy when compared to experimental data. Two types of basis sets are primarily used in DFT calculations, Slater-type Orbitals (STOs) and Gaussian-type Orbitals (GTOs). When investigating molecular systems, the GTOs are highly computationally efficient and are therefore used almost exclusively.

The minimum basis set that can be used in DFT calculations is one that is large enough to contain the number of electrons present in the system. However, the use of a minimum basis set often proves to be insufficient for chemical flexibility.<sup>101,103</sup> This leads to the addition of more functions that provide greater chemical accuracy. When adding in functions, the number of valence functions is increased due to the fact that valence shells are the ones that contribute to bonding interactions. The addition of valence shell functions results in double-zeta, triple-zeta, and higher-zeta basis sets, with zeta referring to the exponents of the basis functions. The addition of valence shells only into basis sets is known as the split valence method. This method takes advantage of the fact that the core shells of atoms do not contribute to bonding interactions. Basis set accuracy can be improved further by the introduction of higher angular momentum functions, also known as polarization functions. The inclusion of polarization functions leads to a better representation of the molecular bonding environment. When using basis functions in practice, they can be systematically built up. By building up the basis functions, the accuracy of the results increases, but so does the computational cost. There are two types of basis set that are predominantly used in modern calculations, Pople-style sets and correlation-consistent split-valence sets.

### **1.3.3.1 Pople-style Basis Sets**

These types of basis sets, originally developed by Pople and his group, contract the number of functions used to describe the core electrons, a method that reduces computational cost.<sup>129,130</sup> The term primitive Gaussian-type orbitals (PGTOs) is applied to the contracted form basis sets. The contraction of the core electron functions is achieved by fixed linear combinations, which reduces the necessary number of calculations. The notation used for Pople basis sets is of the general form  $x\text{-}yz\text{G}$ , for the double-zeta sets. When triple-, quadruple-, or

higher-zeta sets are used the notation is expanded to  $x$ - $yzw$ G,  $x$ - $yzwv$ G, and so on. In this representation,  $x$  indicates the number of PGTOs used for the core electron orbitals, G stands for Gaussian, and the other coefficients  $y$ ,  $z$ , etc. represent the number of split valence orbitals and the number of PGTOs. A simple example of one of these functionals is 6-31G, where there are six PGTOs used for each core electron orbitals, and the split valence orbitals are represented by the linear combination of three and one PGTOs. Other functions can be added to these basis sets, such as polarization or diffuse functions. Adding in either polarization or diffuse functions (those of very large spatial extent) changes the representation of the basis set slightly. The polarization functions are represented in one of two ways, either by the use of asterisks, \*\*, or by explicitly including the orbital representations in parenthesis, (d,p). Building on the basis set example from above, the addition of polarization functions will give the form 6-31G\*\* or 6-31G(d,p). The use of (d,p) indicates that there has been the addition of p-type orbitals to hydrogen atoms and d-type orbitals to all non-hydrogen atoms. If diffuse functions are added to the basis set, they are represented by a '+' sign, for example 6-31+G.

### 1.3.3.2 Correlation-consistent Split-valence Basis Sets

This class of basis sets was developed by Dunning *et al.*<sup>131</sup> These basis sets are designed to systematically approach the complete basis set limit. Instead of adding polarization functions based on orbital type, they are added based on energy contribution. The notation for these basis sets is cc-pVNZ, where cc-p stands for correlation-consistent polarization, Z stands for zeta, and N can be equal to D (double), T (triple), Q (quadruple), 5, 6, ... So, the basis set denoted as cc-pVTZ would stand for correlation-consistent polarization triple zeta basis set. When adding in the successive polarizations, they are added in the following way: If the initial basis set is the cc-pVDZ basis set, it consists of one  $d$ -type orbital. When moving up the cc-pVTZ, a second  $d$ -type

orbital is added, as well as a simultaneously added  $f$ -type orbital. These two orbitals are added simultaneously because they both influence the energy similarly. If the cc-pVDZ basis set is evaluated, it consists of three  $d$ -type, two  $f$ -type, and one  $g$ -type orbitals. This build-up of orbitals continues based on the value of  $N$  in the general notation of the basis sets.

### 1.3.4 Density Functional Theory in the Solid State

When considering performing DFT calculations on solid-state materials, the basic assumption is that they are periodic or crystalline. Although this assumption eliminates the possibilities of imperfections (defects) in the crystal structures, it must be made in order to use solid-state DFT in a practical way. The structures of crystalline solids are infinite systems of repeating units. This characteristic is very important to solid-state DFT as it significantly simplifies the calculations. Using the symmetry present in crystalline systems allows for much smaller and more manageable units to be calculated and repeated in order to describe the entire bulk system. The most basic unit of a periodic solid is known as the Brillouin zone. The Brillouin zone exists in reciprocal space and can be used to calculate the periodic electronic structure. Through the exploitation of symmetry, the electronic structure is repeated over the infinite crystalline material.

#### 1.3.4.1 Reciprocal Space, the Brillouin Zone, and Bloch Functions

The use of reciprocal space, or  $\mathbf{k}$  space, is essential to solid-state DFT calculations as it allows for the more effective evaluation of Bloch functions and the use of the Brillouin zone.<sup>102</sup> Periodic structures with lattice dimension  $\mathbf{a}_1$ ,  $\mathbf{a}_2$ , and  $\mathbf{a}_3$  are converted to reciprocal space following the vector conversion,  $\overline{\mathbf{a}}_i \cdot \overline{\mathbf{b}}_j = 2\pi\delta_{ij}$ , where  $\delta_{ij} = 1$  for  $i = j$  and zero for all other

values and  $\vec{\mathbf{b}}_j$  represents the lattice vectors in reciprocal space. Expanding the reciprocal lattice vectors  $\mathbf{b}_1$ ,  $\mathbf{b}_2$ , and  $\mathbf{b}_3$  gives the following

$$\mathbf{b}_1 = 2\pi \frac{\mathbf{a}_2 \times \mathbf{a}_3}{\mathbf{a}_1 \cdot (\mathbf{a}_2 \times \mathbf{a}_3)} \quad (1.11)$$

$$\mathbf{b}_2 = 2\pi \frac{\mathbf{a}_1 \times \mathbf{a}_3}{\mathbf{a}_2 \cdot (\mathbf{a}_1 \times \mathbf{a}_3)} \quad (1.12)$$

$$\mathbf{b}_3 = 2\pi \frac{\mathbf{a}_1 \times \mathbf{a}_2}{\mathbf{a}_3 \cdot (\mathbf{a}_1 \times \mathbf{a}_2)} \quad (1.13)$$

These reciprocal lattice vectors define the unit cell in  $\mathbf{k}$  space, which is known as the Brillouin zone. The Brillouin zone can be defined as the set of points in reciprocal space that are closer to the origin of the reciprocal lattice than any other points in the reciprocal lattice. The origin of the Brillouin zone, (0,0,0), is defined as the special point,  $\Gamma$ . The use of the Brillouin zone makes only the points within it the necessary points to evaluate the Bloch functions. All  $\mathbf{k}$  points outside of the first Brillouin zone are simply replications of those contained within the first Brillouin zone, and therefore become redundancies.

A finite number of  $\mathbf{k}$  points, as defined by the Pack-Monkhorst net,<sup>132</sup> must be used in DFT calculations. The number of  $\mathbf{k}$  points used must be large enough to allow the calculations to converge to a specific energy tolerance. The shrinking factors are responsible for generating the number of  $\mathbf{k}$  points to be sampled. They are related to the lattice in the that,  $\mathbf{b}/s$ , where  $\mathbf{b}$  represents the lattice vectors and  $s$  represents the shrinking factor. The use of larger shrinking values results in the sampling of more  $\mathbf{k}$  points.

The use of reciprocal space and the Brillouin zone is primarily due to the effectiveness of Bloch functions with these methods. Bloch functions describe periodic crystalline orbitals as

linear combinations of atomic orbitals. The periodicity of the wave function,  $R$ , is exploited by Bloch functions of the form  $V(r) = V(r + R)$ , in periodic systems.

In order to calculate the electron density in real space, it is necessary to determine both the Kohn-Sham Hamiltonian and the set of orbitals simultaneously. An iterative procedure, known as the self-consistent field (SCF) cycle, must be used in order to fulfill these requirements. The SCF equation,

$$F^k A^k = S^k A^k E^k, \quad (1.14)$$

where  $F^k$  is the Kohn-Sham Hamiltonian matrix in reciprocal space,  $A^k$  are the orbital coefficients,  $S^k$  is the overlap matrix of the Bloch functions, and  $E^k$  is the diagonal energy matrix. The Kohn-Sham Hamiltonian matrix,  $F^k$ , is a term that includes the electronic kinetic energy, the electron-nuclear attraction, the electron-electron repulsion, and the DFT exchange-correlation term. The steps of the SCF cycle are as follows: Step 1, an initial guess for the electron density is defined,  $n(\mathbf{r})$ ; Step 2, find the single particle wave functions,  $\psi_i(\mathbf{r})$ , by solving the Kohn-Sham equations using the trial electron density from Step 1; Step 3, the electron density is calculated by the Kohn-Sham single-particle wave functions from Step 2,  $n_{\text{KS}}(\mathbf{r}) = 2 \sum_i \psi_i^*(\mathbf{r}) \psi_i(\mathbf{r})$ ; Step 4, the calculated electron density,  $n_{\text{KS}}(\mathbf{r})$ , is compared to the electron density used to solve the Kohn-Sham equation,  $n(\mathbf{r})$ . If the both densities are equal, the ground-state electron density has been determined and can be used to compute the energy of the system. If the two densities differ, the trial electron density,  $n(\mathbf{r})$ , must be updated. After the trial electron density is changed, Steps 2-4 are repeated until the electron densities become equal. Once the electron densities are equal, or at least within a user-defined specific tolerance, the total energy of the system can be determined.<sup>102</sup>

### 1.3.4.2 Periodic Boundary Conditions

When studying solid-state molecular systems that are crystalline, the bulk is composed of multiple repeating unit cells, collectively known as supercells. A general rule for DFT is, the larger the system, the longer the DFT computation. With this in mind, the use of a supercell to represent the bulk in a calculation would make computations take a very long time to complete. In order to reduce the computational cost of such systems, the crystal symmetry of the systems under study can be exploited. The use of periodic boundary condition (PBC) methods lowers the computational cost of calculations on crystalline solids (**Figure 1-2**).

The consideration of all important data when using PBCs is preserved by the use of a cut-off distance in order to allow molecules to be fully simulated. The simulation cell for each calculation is different, depending on the symmetry present in the molecular solids. The use of this smaller simulation cell is then replicated using symmetry and allows for shorter computation times. For example, if a unit cell contains four molecules, but only one is symmetrically unique, the simulation cell will only consist of the single unique molecule. During some molecular vibrations, the molecule in the simulation cell may move enough so that part of that molecule moves outside of the cell. If this occurs, the PBC function will preserve the mass, particle number, and total energy of the cell by having the part of the molecule that has moved out of the cell reenter the cell on the opposing side of the cell (it is the same as accounting for the part of the molecule that would enter the simulation cell from the symmetry created cell next to it). Essentially, the part of the molecule that exits in the cell is replaced by the same part of a different molecule which enters the cell due to the motion it is undergoing. Because of this ability, the use of PBCs is central to the determination of the translations and rotations seen in

the THz region. When a periodic system such as a solid is considered, the cut-off distances for the PBCs are defined by the primitive unit cell dimensions in reciprocal space.



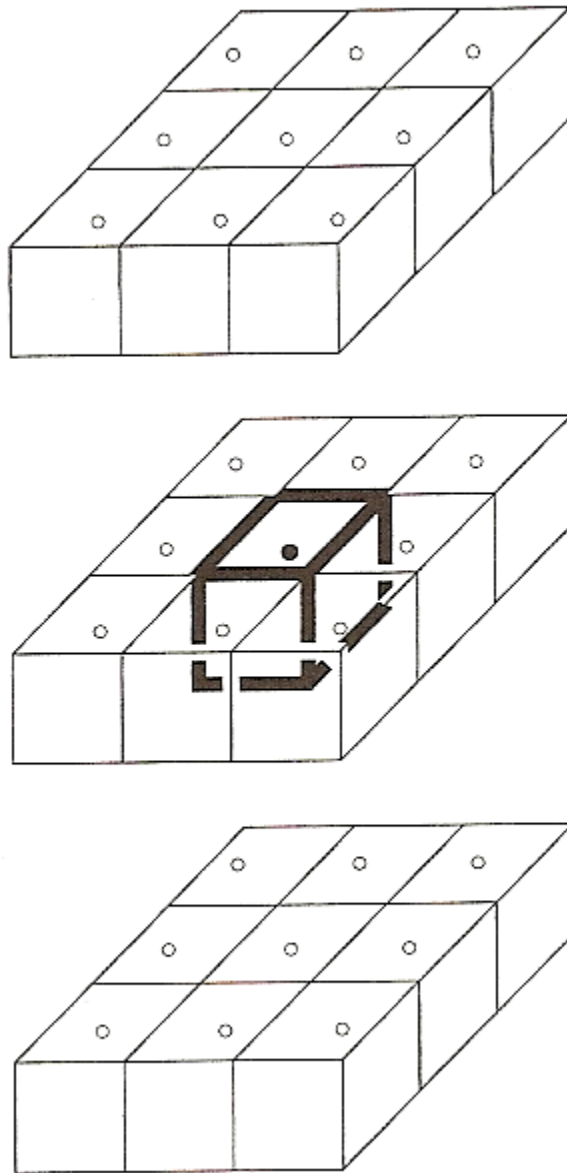


**Figure 1-2.** The expanded view of a cubic simulation cell surrounded by 26 periodic images generated by periodic boundary conditions.<sup>133</sup>

### 1.3.4.3 Geometry Optimizations

In order to reach a realistic structural prediction, the potential energy minimum of a system must be obtained. To achieve this, both the lattice parameters and the atomic positions must be iteratively optimized. Both the potential energy and its derivatives with respect to geometric changes are calculated at each step of the process. The first partial derivatives of the potential energy lead to a vector that is known as the gradient. When the gradient is equal to zero, the point that has been found can be a minimum, maximum or saddle point on the potential energy surface. To ensure that the gradient equals zero point is a minimum, the Hessian (force-constant matrix) must also be considered. The Hessian consists of the second derivatives of the potential energy. Since this function contains multiple variables, one of two approximations are often used, either the Newton-Raphson method or the quasi-Newton method. The approximation made by the Newton-Raphson method is a Taylor-series truncated after the quadratic terms, which are analytically calculated. The Newton-Raphson method is very costly in computational time and, due to this, the quasi-Newton method can be used to reduce the amount of computational time required (Hessian computed numerically). When using the quasi-Newton approach, the Hessian is not directly calculated. It is instead approximated and then gradually updated through each optimization step. To determine a true minimum, the Hessian should be a positive value.

Each geometry step consists of an SCF cycle to determine the electron density. For each atomic position, the gradients are evaluated and the Hessian updated. This process continues until the gradient equals zero (or a specified tolerance) and the Hessian becomes positive. As the optimization approaches completion, the differences in displacements and gradients approach

zero between optimization steps. Once the process is complete, the equilibrium position (potential energy minimum) has been found.

#### 1.3.4.4 Vibrational Mode Calculations

Accurate reproductions of low-frequency vibrational spectra are central to this research. The THz vibrational spectra measured here at Syracuse are interpreted using the results from solid-state DFT calculations. An accurately calculated molecular structure, simulated as previously described, is critical to the accuracy of the subsequent frequency simulations. For the complete analysis of the low-energy vibrational modes to be achieved, it is necessary to simulate both the frequencies and intensities of the IR-active absorptions in the THz region.

##### 1.3.4.4.1 Vibrational Frequencies

The Born-Oppenheimer potential energy surface consists of the number of atoms,  $N$ , with each atom defined by  $3N$  coordinates. Using the harmonic oscillator approximation, the potential energy equation takes the form

$$V(0) = \frac{1}{2} \sum_{ij} u_i H_{ij} u_j \equiv \frac{1}{2} \langle u | H | u \rangle, \quad (1.15)$$

where  $H$  is the Hessian matrix of the second derivatives with respect to the atomic displacements and  $u_i$  represents a displacement from the equilibrium value of the  $i$ -th Cartesian coordinate. The displacement coordinates of the Hessian are represented by

$$H_{ij} = \frac{1}{2} \left[ \frac{\partial^2 V(\mathbf{x})}{\partial u_i \partial u_j} \right]_0. \quad (1.16)$$

Using mass-weighted coordinates,  $q_i = \sqrt{M_i} u_i$ , with  $M$  equal to the atomic mass, the vibrational potential becomes

$$V(0) = \frac{1}{2} \langle q | W | q \rangle, \quad (1.17)$$

where  $W$  is the mass-weighted Hessian (hermitian matrix) and  $W_{ij} = H_{ij} / \sqrt{M_i M_j}$ . By diagonalizing the hermitian matrix, the force constants are obtained from the eigenvalues,  $\kappa_j$ .

The vibrational frequencies are computed using the eigenvalues in such a way that  $\omega = \sqrt{\kappa_j} / 2\pi$ .

In order to perform frequency calculations in the solid-state (an infinite periodic system), the approach must be modified. The use of generalized coordinates,  $q_i(\mathbf{k})$ , reduces the set of problems to be  $3N$ -dimensional, one for each  $\mathbf{k}$  point in the Brillouin zone. The new  $W$  matrix has the form

$$W_{ij}(\mathbf{k}) = \sum_{\mathbf{G}} \exp[i\mathbf{k} \cdot \mathbf{G}] \frac{H_{ij}^{0\mathbf{G}}}{\sqrt{M_i M_j}}, \quad (1.18)$$

where  $H$  is the Hessian with respect to atom  $i$  in cell  $\mathbf{0}$  and atom  $j$  in the  $\mathbf{G}$  cell. When evaluating the special point,  $\Gamma$  (0,0,0), the equation is reduced to

$$W_{ij}(0) = \sum_{\mathbf{G}} \frac{H_{ij}^{0\mathbf{G}}}{\sqrt{M_i M_j}}. \quad (1.19)$$

The frequencies at point  $\Gamma$  are evaluated using the procedure above, which is the same as the method used for single molecules. The atoms present are each displaced along the three Cartesian coordinates, and the energy derivatives evaluated using SCF cycles. The first order derivatives are analytically calculated and the second order derivatives are numerically calculated, similarly to the geometry optimization procedure. The hermitian is then diagonalized, which generates the force constants that are used to compute the vibrational frequencies.

#### 1.3.4.4.2 Infrared Intensities

The calculated intensities are computed as the dipole moment derivatives with respect to the atomic displacements (Born Charges). The Berry phase method, which uses the polarization difference between the equilibrium and distorted geometries of the atomic displacements, is used for these calculations.<sup>134,135</sup> The following general equation is used to calculate the intensities of active modes:

$$I \propto \left( \frac{\partial \mu}{\partial Q} \right)^2. \quad (1.20)$$

It is important to note that the use of the Berry phase method is limited to calculating the IR intensities of insulating systems. Since this method is used in reciprocal space, it has been suggested that the accuracy of IR intensities could be influenced by the number of  $\mathbf{k}$  used.

#### 1.3.4.5 Dispersion Forces

Typical functionals used in DFT lack the ability to account for the presence of weak non-covalent London dispersion interactions. This is of particular importance when studying condensed-phase systems as these forces can dominate the binding schemes between molecules. Dispersion forces play an integral role in the binding of biomolecules from DNA to proteins.<sup>136,137</sup> They also have been found to drive the formation of polymorphs of molecular solids.<sup>70</sup> The inability of most DFT simulations to describe these forces is due to their neglect of electron correlation. In order to accurately represent these forces, the exact exchange energy would need to be obtainable, but currently, it is not practical to carry out this type of calculation. This area of DFT is currently being studied by a number of researchers. Since this approach is not feasible at this point, correction models have been developed that can be added on to

standard DFT calculations in order to address the shortcomings of weak long-range interactions (Figure 1-3).

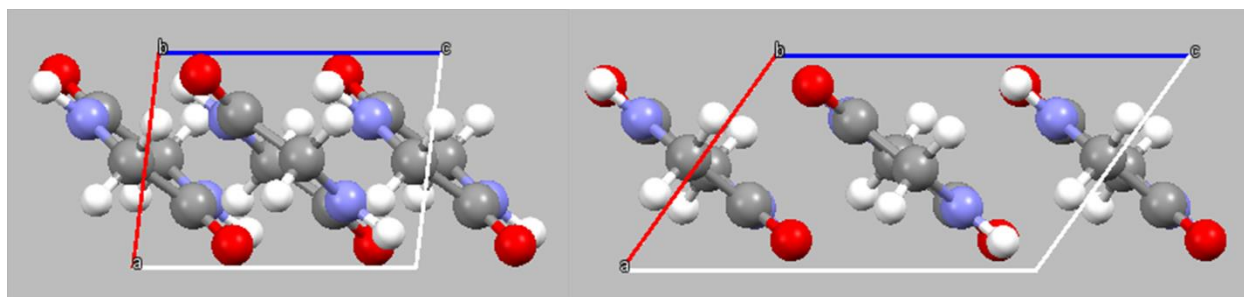


**Figure 1-3.** Unit cell depictions of cyclodiglycine with (left) and without (right) London dispersion force corrections.

Until the work of London in the 1930s, the idea of uniform electron density in atoms and nonpolar molecules was a commonly held misconception. London's work proved that even in systems with no apparent dipole moment, there were, in fact, disruptions to the electron densities.<sup>138</sup> These disruptions create a transient dipole moment in all materials. The transient dipole moment is able to affect, not only the atom or molecule it is located on, but the surrounding atoms and molecules. This phenomenon leads to the group of weak non-covalent intermolecular forces known as van der Waals forces. The strength of these forces is approximated by

$$V^{disp} = -\frac{C}{r^6}, \quad (1.21)$$

where  $C$  is a physical constant and  $r$  is the distance between two atoms.

In order to account for these interactions in DFT calculations, the addition of a dispersion-like energy contribution is necessary. The most relevant correction method to the research presented here is that devised by Grimme.<sup>139</sup> Grimme's first correction method, DFT-D1, uses an empirical correction method that accounts for all pair-wise atomic interactions and uses a damping function to limit the distance over which the interactions are considered. The equation of Grimme's DFT-D1 correction is

$$E_{disp} = -s_6 \sum_{i=1}^{N_{at}-1} \sum_{j=i+1}^{N_{at}} \frac{C_6^{ij}}{R_{ij}^6} f_{damp}(R_{ij}), \quad (1.22)$$

where  $N_{at}$  is the number of atoms present in the system,  $C_6^{ij}$  is the dispersion coefficient for the atom pair  $ij$ ,  $s_6$  is the global scalar, and  $R_{ij}$  is the distance between two atoms. The damping function used in DFT-D1 is

$$f_{damp}(R) = \frac{1}{1 + e^{-\alpha(\frac{R}{R_0} - 1)}} \quad (1.23)$$

where  $R_0$  is the sum of the atomic van der Waals radii and  $\alpha = 23$ , which determines the steepness of the damping function. This method was developed in 2004 and was optimized for use in gas-phase calculations. DFT-D1 suffered from several setbacks, including only having  $C_6$  values available for H and C-Ne, tests of third-row elements showed systematic errors and inconsistencies in ‘normal’ thermochemical properties. In his work on DFT-D1, Grimme states that the energy calculated as dispersion energy is, in fact, “a model-dependent quantity with no real physical meaning.” In calculations using the Grimme method, the energies generated are simply filling in for missing energy, and are not the real dispersion energy of the system.

In 2006, Grimme released a new correction model known as DFT-D2.<sup>2</sup> This model is a semi-empirical approach to the dispersion correction problem. The equations of this model are the same ones used in DFT-D1. The differences are found in the values used for the steepness of the damping function (23 in DFT-D1 and 20 in DFT-D2) and the  $C_6$  coefficients used in the calculations. The new  $C_6$  coefficients were determined from

$$C_6^a = 0.05NI_p^a\alpha^a. \quad (1.24)$$

In this equation, the  $N$  has values of 2, 10, 18, 36, and 54 for atoms from rows one through five of the periodic table, respectively,  $I_p$  are the atomic ionization potentials, and  $\alpha$  are the static dipole polarizabilities. The values for these variables were taken from DFT/PBE0 calculations. Grimme has also released an updated version of his correction known as DFT-D3.<sup>140</sup>

The goal of the Grimme parameterization was one of high transferability. In order to provide a single scheme that could be used for all systems, Grimme performed numerous studies



using multiple density functionals and systems. By studying the various combinations, functional-dependent values for the global scaling factor,  $s_6$ , were obtained. The numerical value of this parameter changes only depending on the functional being used. It was designed to be applied across all varieties of systems.

The development of a method for use with DFT that can account for the presence of non-covalent intermolecular forces is the topic of much research. There are several different approaches being taken to address this shortcoming of DFT. The three main approaches involve either pairwise atomic corrections, many-body corrections, or seamless density functionals.

Since the central method to this thesis is a pairwise atomic correction that is added into the calculation, the first class that will be considered will be those that use pairwise corrections. The principle of electron holes is used in several of these approaches. The use of the exchange dipole moment is the central point of the XDM class of dispersion corrections. With the XDM class of corrections, two prevalent models, XDM6 and XDM10, have risen to popular use.<sup>141,142</sup> The difference between the two models is the highest order term in the central expression (represented by 6 or 10). Building on the work of XDMs, Corminboeuf developed a method known as dDsC.<sup>142,143</sup> This method attempts to improve the XDM method by using a more sophisticated damping function that has an electron density dependence (Tang and Toennies).<sup>144</sup> Another type of pairwise approach, devised by Tkatchenko, is known as TS-vdW.<sup>142,145</sup> This approach uses a homostatic  $C_6$  coefficient which can account for the effects of the chemical environment of the atoms as part of molecules. Many of these approaches use the  $C_6/R^6$  formulation to account for the medium-to-long range interactions, however, the implication of  $C_8/R^8$  and  $C_{10}/R^{10}$  formulations have been proposed to better interpret the short-to-medium range interactions.<sup>146</sup>

The many-body approach to dispersion corrections (MBD)<sup>147</sup> is one that is not limited to a pairwise atomic scheme. It is capable of treating the full range of exchange and correlation effects. MBD is capable of suppressing the short-range interactions that are already accounted for in DFT calculations. Another important difference in this method is the absence of the traditional damping function. Instead, this method uses range-separated Coulomb potentials.

The last class of dispersion correction methods involves the development of seamless functionals, that is, functionals that are able to treat the covalent and non-covalent interactions on the same level. There are several examples of these functionals and the work of three main groups will be considered here. Non-local functionals have been developed by Langreth<sup>148</sup> and Andersson *et al.*<sup>149</sup> These methods combine the use of a GGA exchange functional, an LSDA correlation functional, and a non-local term that can account for the dispersion energy. Another class of seamless functionals has been developed by Vydrov and van Voorhis, known as DFT-NL.<sup>150,151</sup> These functionals have a term added to the exchange-correlation energy that is based on the electron density and dipole polarizability at an implicit fragment of a system. The final class of functionals is known as the Minnesota class of functionals, developed by Zhao and Truhlar.<sup>110,152</sup> These functions consist of more than thirty fitting parameters. They assign significant weight to non-covalent interactions and recover nearly all of the short-range dispersion energy.

The selection of a damping function is also a topic of active research when referencing its use with non-covalent dispersion corrections. The examples of corrections provided above also include the use of varying damping functions. Damping functions affect the distance at which the dispersion effects are considered. By varying parameters within or the structure of the damping function; the effects on the dispersion correction energies can be modified. Examples of different

damping functions include the rational damping formula developed by Becke and Johnson<sup>153</sup> and the zero-damping formula developed by Grimme.<sup>154</sup>

It should also be mentioned that functionals exist that have been tailored for use in the solid state. When using these functionals, the inclusion of a separate dispersion energy term is not necessary. Two such functionals are PBEsol (PBE solid)<sup>121</sup> and SOGGA.<sup>122</sup> These functionals can be used with no modification when applied to solid-state systems. In practice, it has been determined that these functionals often overestimate the size of unit cells, although not as drastically as PBE or B3LYP, suggesting that they do not fully consider the dispersion energy of systems.

## 1.4 References

- (1) Grimme, S. Density Functional Theory with London Dispersion Corrections. *WIREs: Comp. Mole. Sci.* **2011**, *1*, 211-228.
- (2) Grimme, S. Semiempirical GGA-Type Density Functional Constructed with a Long-Range Dispersion Correction. *J. Comput. Chem.* **2006**, *27*, 1787-1799.
- (3) King, M. D.; Korter, T. M. Modified Corrections for London Forces in Solid-State Density Functional Theory Calculations of Structure and Lattice Dynamics of Molecular Crystals. *J. Phys. Chem. A* **2012**, *116*, 6927-6934.
- (4) Witko, E. M.; Buchanan, W. D.; Korter, T. M. The Importance of London Dispersion Forces in Crystalline Magnesium Nitrate Hexahydrate. *Inorg. Chim. Acta* **2012**, *389*, 176-182.
- (5) Juliano, T. R., Jr.; King, M. D.; Korter, T. M. Evaluating London Dispersion Force Corrections in Crystalline Nitroguanidine by Terahertz Spectroscopy. *IEEE Trans. on THz. Sci. and Tech.* **2013**, *3*, 281-287.
- (6) Juliano, T. R.; Korter, T. M. Terahertz Vibrations of Crystalline Acyclic and Cyclic Diglycine: Benchmarks for London Force Correction Models. *J. Phys. Chem. A* **2013**, *117*, 10504-10512.
- (7) *Crc Handbook of Chemistry and Physics*, 93 ed.; CRC Press/Taylor and Francis: Boca Raton, FL.
- (8) Sansonetti, J. E.; Martin, W. C. Handbook of Basic Atomic Spectroscopic Data. *J. Phys. Chem. Ref. Data* **2005**, *34*, 1559-2259.
- (9) Miller, T. M.; Bederson, B. Atomic and Molecular Polarizabilities-A Review of Recent Advances. In *Advances in Atomic and Molecular Physics*; Bates, D. R., Benjamin, B., Eds.; Academic Press, 1978; Vol. Volume 13; pp 1-55.
- (10) Bondi, A. Van Der Waals Volumes and Radii. *J. Phys. Chem.* **1964**, *68*, 441-451.
- (11) Civalleri, B.; Zicovich-Wilson, C. M.; Valenzano, L.; Ugliengo, P. B3LYP Augmented with an Empirical Dispersion Term (B3LYP-D\*) as Applied to Molecular Crystals. *CrystEngComm* **2008**, *10*, 405-410.
- (12) Mernea, M.; Calborean, O.; Grigore, O.; Dascalu, T.; Mihailescu, D. Validation of Protein Structural Models Using THz Spectroscopy: A Promising Approach to Solve Three-Dimensional Structures. *Opt Quant Electron* **2014**, *46*, 505-514.
- (13) Allis, D. G.; Prokhorova, D. A.; Korter, T. M. Solid-State Modeling of the Terahertz Spectrum of the High Explosive HMX. *J. Phys. Chem. A* **2006**, *110*, 1951-1959.
- (14) Allis, D. G.; Zeitler, J. A.; Taday, P. F.; Korter, T. M. Theoretical Analysis of the Solid-State Terahertz Spectrum of the High Explosive RDX. *Chem. Phys. Lett.* **2008**, *463*, 84-89.
- (15) Trofimov, V. A. "Effective Criteria for the Detection and Identification of Explosive Using the Spectral Dynamics Analysis of THz Reflected Signal in Real Time", 2013.
- (16) Harris, J. J. S.; Gu, A.; Kim, S. M. "New THz Sources for Bio-Medical Imaging", 2007.
- (17) Jung, E.; Park, H.; Moon, K.; Lim, M.; Do, Y.; Han, H.; Choi, H.; Min, B.-H.; Kim, S.; Park, I.; Lim, H. THz Time-Domain Spectroscopic Imaging of Human Articular Cartilage. *J. Infrared Millim. Terahertz Waves* **2012**, *33*, 593-598.
- (18) Koch, M. Bio-Medical Applications of THz Imaging. *Springer series in optical sciences* **2003**, *85*, 295.

- (19) Ajito, K. Nondestructive Multicomponent Terahertz Chemical Imaging of Medicine in Tablets. *J. Electrochem. Soc.* **2014**, *161*, B171-B175.
- (20) Ajito, K.; Ueno, Y.; Song, H.-J.; Kim, J.-Y.; Tamechika, E.; Kukutsu, N.; Limwikrant, W.; Yamamoto, K.; Moribe, K. Terahertz Chemical Imaging of a Multicomponent Tablet in Pharmaceutical Applications. *ECS Transactions* **2013**, *50*, 109-116.
- (21) Woodward, R. M. Terahertz Technology in the Medical and Pharmaceutical Industry. *Preclinica* **2004**, *2*, 328.
- (22) Nagai, N. Analysis of the Industrial Materials by THz Spectroscopy. *Rēzā kenkyū* **2005**, *33*, 848-854.
- (23) Nishizawa, S. Industrial Application of Terahertz Waves. New Quality Inspection by Using Terahertz Time-Domain Spectroscopy (THz-TDS). *Kurin Tekunoroji* **2009**, *19*, 31.
- (24) Shen, F. Applications of Terahertz Spectroscopy and Imaging Techniques in Food Safety Inspection. *Guangpuxue Yu Guangpu Fenxi* **2009**, *29*, 1445-1449.
- (25) Rothschild, W. G.; Moller, K. D. Far-Infrared Spectroscopy. *Physics Today* **1970**, *23*, 44.
- (26) Zhang, X.-C.; Xu, J. *Introduction to THz Wave Photonics*; Springer: New York, 2010.
- (27) Auston, D. H.; Nuss, M. C. Electrooptical Generation and Detection of Femtosecond Electrical Transients. *IEEE J. Quant. Elec.* **1988**, *24*, 184-197.
- (28) Krökel, D.; Grischkowsky, D.; Ketchen, M. B. Subpicosecond Electrical Pulse Generation Using Photoconductive Switches with Long Carrier Lifetimes. *Appl. Phys. Lett.* **1989**, *54*, 1046-1047.
- (29) Rice, A.; Jin, Y.; Ma, X. F.; Zhang, X. C.; Bliss, D.; Larkin, J.; Alexander, M. Terahertz Optical Rectification from <110> Zinc-Blende Crystals. *Appl. Phys. Lett.* **1994**, *64*, 1324-1326.
- (30) Wu, Q.; Litz, M.; Zhang, X. C. Broadband Detection Capability of ZnTe Electro-Optic Field Detectors. *Appl. Phys. Lett.* **1996**, *68*, 2924-2926.
- (31) Erschens, D.; Turchinovich, D.; Jepsen, P. Optimized Optical Rectification and Electro-Optic Sampling in ZnTe Crystals with Chirped Femtosecond Laser Pulses. *J. Infrared Millim. Terahertz Waves* **2011**, *32*, 1371-1381.
- (32) Chart of the Electromagnetic Spectrum; SURF, Ed., 2006.
- (33) Karpowicz, N.; Zhong, H.; Xu, J.; Lin, K. I.; Hwang, J.-S.; Zhang, X. C. Comparison between Pulsed Terahertz Time-Domain Imaging and Continuous Wave Terahertz Imaging. *Semicond. Sci. Technol.* **2005**, *20*, S293.
- (34) Matsuura, S. Generation of cw Terahertz Radiation with Photomixing. *Top. Appl. Phys.* **2005**, *97*, 157.
- (35) Jepsen, P. U.; Cooke, D. G.; Koch, M. Terahertz Spectroscopy and Imaging – Modern Techniques and Applications. *Laser Photonics Rev* **2011**, *5*, 124-166.
- (36) Kim, J.-Y.; Nishi, H.; Song, H.-J.; Fukuda, H.; Yaita, M.; Hirata, A.; Ajito, K. Compact and Stable THz Vector Spectroscopy Using Silicon Photonics Technology. *Opt. Express* **2014**, *22*, 7178-7185.
- (37) Park, K. H.; Kim, N.; Moon, K.; Ko, H.; Park, J.-W.; Lee, E. S.; Lee, I.-M.; Han, S.-P. “Photonic Devices for Tunable Continuous-Wave Terahertz Generation and Detection”; Proceedings of SPIE, 2014.

- (38) Penkov, N. V.; Yashin, V. A.; Shvirst, N. E.; Fesenko, E. E., Jr.; Fesenko, E. E. On Peculiarities of Temperature Dependences of Water Spectra in the Terahertz Frequency Domain. *BIOPHYSICS* **2014**, *59*, 220-222.
- (39) Chen, P.; Pearson, J. C.; Pickett, H. M.; Matsuura, S.; Blake, G. A. Measurements of 14nh<sub>3</sub> in the V<sub>2</sub>=1 State by a Solid-State, Photomixing, THz Spectrometer, and a Simultaneous Analysis of the Microwave, Terahertz, and Infrared Transitions between the Ground and N<sub>2</sub> Inversion–Rotation Levels. *J. Mol. Spectrosc.* **2006**, *236*, 116-126.
- (40) Liu, H.; Chen, Y.; Yuan, T.; Al-Douseri, F.; Xu, J.; Zhang, X.-C. “Quantitative Analysis of Ammonia by THz Time-Domain Spectroscopy”, 2004.
- (41) Foltynowicz, R. J.; Allman, R. E.; Zuckerman, E. Terahertz Absorption Measurement for Gas-Phase 2,4-Dinitrotoluene from 0.05 THz to 2.7 THz. *Chem. Phys. Lett.* **2006**, *431*, 34-38.
- (42) Drouin, B. J.; Yu, S.; Pearson, J. C.; Gupta, H. Terahertz Spectroscopy for Space Applications: 2.5–2.7 Thz Spectra of Hd, H<sub>2</sub>O and NH<sub>3</sub>. *J. Mol. Struct.* **2011**, *1006*, 2-12.
- (43) Ioppolo, S.; McGuire, B. A.; Allodi, M. A.; Blake, G. A. THz and Mid-IR Spectroscopy of Interstellar Ice Analogs: Methyl and Carboxylic Acid Groups. *Faraday Discuss.* **2014**, *168*, 461-484.
- (44) Kawano, Y. Terahertz Waves: A Tool for Condensed Matter, the Life Sciences and Astronomy. *Contemp. Phys.* **2013**, *54*, 143-165.
- (45) Turton, D.; Harwood, T.; Laphorn, A.; Ellis, E.; Wynne, K. “Ultrabroadband Terahertz Spectroscopies of Biomolecules and Water”; Proceedings of SPIE, 2013.
- (46) Torii, H. Cooperative Contributions of the Intermolecular Charge Fluxes and Intramolecular Polarizations in the Far-Infrared Spectral Intensities of Liquid Water. *J. Chem. Theor. and Comp.* **2014**, *10*, 1219-1227.
- (47) Murakami, H. Chapter Six - Protein and Water Confined in Nanometer-Scale Reverse Micelles Studied by near Infrared, Terahertz, and Ultrafast Visible Spectroscopies. In *Advan. In Protein Chem. And Struct. Bio.*; Christo, Z. C., Ed.; Academic Press, 2013; Vol. Volume 93; pp 183-211.
- (48) Kindt, J. T.; Schmuttenmaer, C. A. Far-Infrared Dielectric Properties of Polar Liquids Probed by Femtosecond Terahertz Pulse Spectroscopy†. *J. Phys. Chem.* **1996**, *100*, 10373-10379.
- (49) Kindt, J. T.; Schmuttenmaer, C. A. Theory for Determination of the Low-Frequency Time-Dependent Response Function in Liquids Using Time-Resolved Terahertz Pulse Spectroscopy. *J. Chem. Phys.* **1999**, *110*, 8589-8596.
- (50) Conti Nibali, V.; Havenith, M. New Insights into the Role of Water in Biological Function: Studying Solvated Biomolecules Using Terahertz Absorption Spectroscopy in Conjunction with Molecular Dynamics Simulations. *J. Am. Chem. Soc.* **2014**, *136*, 12800-12807.
- (51) Sun, J.; Niehues, G.; Forbert, H.; Decka, D.; Schwaab, G.; Marx, D.; Havenith, M. Understanding THz Spectra of Aqueous Solutions: Glycine in Light and Heavy Water. *J. Am. Chem. Soc.* **2014**, *136*, 5031-5038.
- (52) Sharma, V.; Bohm, F.; Seitz, M.; Schwaab, G.; Havenith, M. From Solvated Ions to Ion-Pairing: A THz Study of Lanthanum(III) Hydration. *PCCP* **2013**, *15*, 8383-8391.
- (53) Funkner, S.; Havenith, M.; Schwaab, G. Urea, a Structure Breaker? Answers from THz Absorption Spectroscopy. *J. Phys. Chem. B* **2012**, *116*, 13374-13380.
- (54) Liu, C. Accurate Optical Parameters Extracting of Non-Polar Organic Solvents in the Terahertz Range. *Guangpuxue Yu Guangpu Fenxi* **2011**, *31*, 2886-2890.

- (55) Liu, C. Accurate Optical Parameters Extracting of Non-Polar Organic Solvents in the Terahertz Range. *Guangpuxue Yu Guangpu Fenxi* **2011**, *31*, 2886.
- (56) Zhou, L.; Xu, W.; Hua, T.; Lu, X.; Chen, J.; Jin, B.; Kang, L.; Wu, P. Transmission of THz Wave by Liquid Dielectric Waveguide. *Sci. China Technol. Sci.* **2010**, *53*, 1594-1597.
- (57) Kadlec, F.; Kadlec, C.; Kužel, P.; Petzelt, J. Study of the Ferroelectric Phase Transition in Germanium Telluride Using Time-Domain Terahertz Spectroscopy. *Phys. Rev. B* **2011**, *84*, 205209.
- (58) Ortolani, M.; Stehr, D.; Wagner, M.; Helm, M.; Pizzi, G.; Virgilio, M.; Grosso, G.; Capellini, G.; De Seta, M. Long Intersubband Relaxation Times in N-Type Germanium Quantum Wells. *Appl. Phys. Lett.* **2011**, *99*, -.
- (59) Walther, M.; Fischer, B. M.; Uhd Jepsen, P. Noncovalent Intermolecular Forces in Polycrystalline and Amorphous Saccharides in the Far Infrared. *Chem. Phys.* **2003**, *288*, 261-268.
- (60) Williams, M. R. C.; True, A. B.; Izmaylov, A. F.; French, T. A.; Schroeck, K.; Schmuttenmaer, C. A. Terahertz Spectroscopy of Enantiopure and Racemic Polycrystalline Valine. *PCCP* **2011**, *13*, 11719.
- (61) True, A.; Schroeck, K.; French, T.; Schmuttenmaer, C. Terahertz Spectroscopy of Histidine Enantiomers and Polymorphs. *J. Infrared Millim. Terahertz Waves* **2011**, *32*, 691-698.
- (62) Beard, M. C.; Turner, G. M.; Schmuttenmaer, C. A. Terahertz Spectroscopy. *J. Phys. Chem. B* **2002**, *106*, 7146-7159.
- (63) Federici, J. F. F. Thz Imaging and Sensing for Security Applications—Explosives, Weapons and Drugs. *Semicond. Sci. Technol.* **2005**, *20*, S266-S280.
- (64) He, T. Applications of Terahertz Spectroscopy in Illicit Drugs Detection. *Guangpuxue Yu Guangpu Fenxi* **2013**, *33*, 2348.
- (65) Witko, E. M.; Korter, T. M. Terahertz Spectroscopy of the Explosive Taggant 2,3-Dimethyl-2,3-Dinitrobutane. *J. Phys. Chem. A* **2012**, *116*, 6879-6884.
- (66) Hakey, P. M.; Allis, D. G.; Hudson, M. R.; Ouellette, W.; Korter, T. M. Investigation of (1R,2S)-(-)-Ephedrine by Cryogenic Terahertz Spectroscopy and Solid-State Density Functional Theory. *ChemPhysChem* **2009**, *10*, 2434-2444.
- (67) Hakey, P. M.; Allis, D. G.; Ouellette, W.; Korter, T. M. Cryogenic Terahertz Spectrum of (+)-Methamphetamine Hydrochloride and Assignment Using Solid-State Density Functional Theory. *J. Phys. Chem. A* **2009**, *113*, 5119-5127.
- (68) Schulkin, B. J.; Tondue, T. D.; St-James, J. G. Terahertz Spectrometer; USPTO, Ed.; Zomega Terahertz Corporation: USA, 2012.
- (69) Duling, I.; Zimdars, D. Compact TD-THz Systems Offer Flexible, Turnkey Imaging Solutions. In *Laser Focus World*, 2007; Vol. 43; pp 63+.
- (70) Zimdars, D.; White, J.; Stuk, G.; Sucha, G.; Fichter, G.; Williamson, S. L. Time Domain Terahertz Imaging of Threats in Luggage and Personnel. *Int. J. of High Speed Elect. and Sys.* **2007**, *17*, 271-281.
- (71) King, M. D.; Buchanan, W. D.; Korter, T. M. Identification and Quantification of Polymorphism in the Pharmaceutical Compound Diclofenac Acid by Terahertz Spectroscopy and Solid-State Density Functional Theory. *Anal. Chem.* **2011**, *83*, 3786-3792.
- (72) King, M. D.; Buchanan, W. D.; Korter, T. M. Understanding the Terahertz Spectra of Crystalline Pharmaceuticals: Terahertz Spectroscopy and Solid-State Density

Functional Theory Study of (S)-(+)-Ibuprofen and (R<sub>s</sub>)-Ibuprofen. *J. Pharm. Sci.* **2011**, *100*, 1116-1129.

(73) Delaney, S. P.; Pan, D.; Yin, S. X.; Smith, T. M.; Korter, T. M. Evaluating the Roles of Conformational Strain and Cohesive Binding in Crystalline Polymorphs of Aripiprazole. *Cryst. Growth Des.* **2013**, *13*, 2943-2952.

(74) Delaney, S. P.; Pan, D.; Galella, M.; Yin, S. X.; Korter, T. M. Understanding the Origins of Conformational Disorder in the Crystalline Polymorphs of Irbesartan. *Cryst. Growth Des.* **2012**, *12*, 5017-5024.

(75) Zeitler, J. A.; Taday, P. F.; Gordon, K. C.; Pepper, M.; Rades, T. Solid-State Transition Mechanism in Carbamazepine Polymorphs by Time-Resolved Terahertz Spectroscopy. *ChemPhysChem* **2007**, *8*, 1924-1927.

(76) Rades, T. Terahertz Pulsed Spectroscopy: Potential for Analysis of Pharmaceutical Ingredients. *G.I.T. Lab. Jour. Euro.* **2006**, *10*, 10.

(77) Baxter, J. B. Time-Resolved Terahertz Spectroscopy and Terahertz Emission Spectroscopy. *Opt. Sci. and Engin.* **2008**, *131*, 73.

(78) Harrel, S. M.; Milot, R. L.; Schleicher, J. M.; Schmuttenmaer, C. A. Influence of Free-Carrier Absorption on Terahertz Generation from ZnTe(110). *J. Appl. Phys.* **2010**, *107*.

(79) Baxter, J. B. Carrier Dynamics in Bulk ZnO. Part 2. Transient Photoconductivity Measured by Time-Resolved Terahertz Spectroscopy. *Phys. Rev. B* **2009**, *80*.

(80) Talbayev. Dynamic Investigations of Multiferroics: Terahertz and Beyond. *J. Phys.: Conf. Ser.* **2009**, *148*.

(81) Kubler. Coherent Structural Dynamics and Electronic Correlations During an Ultrafast Insulator-Metal Phase Transition in Vo<sub>2</sub>. *Phys. Rev. Lett.* **2007**, *99*.

(82) Redo-Sanchez, A.; Salvatella, G.; Galceran, R.; Roldos, E.; Garcia-Reguero, J. A.; Castellari, M.; Tejada, J. Assessment of Terahertz Spectroscopy to Detect Antibiotic Residues in Food and Feed Matrices. *The Analyst* **2011**, *136*, 1733-1738.

(83) Qin, J.; Xie, L.; Ying, Y. Determination of Tetracycline Hydrochloride by Terahertz Spectroscopy with Plsr Model. *Food Chem.* **2015**, *170*, 415-422.

(84) Kawase, M. Application of Terahertz Waves to Food Science. *Food Sci. and Tech. Res.* **2012**, *18*, 601-609.

(85) Gowen, A. A.; O'Sullivan, C.; O'Donnell, C. P. Terahertz Time Domain Spectroscopy and Imaging: Emerging Techniques for Food Process Monitoring and Quality Control. *Trends Food Sci. and Tech.* **2012**, *25*, 40-46.

(86) Jansen, C.; Wietzke, S.; Peters, O.; Scheller, M.; Vieweg, N.; Salhi, M.; Krumbholz, N.; Jördens, C.; Hochrein, T.; Koch, M. Terahertz Imaging: Applications and Perspectives. *Appl. Opt.* **2010**, *49*, E48-E57.

(87) Wietzke, S.; Jansen, C.; Scheller, M.; Krumbholz, N.; Peters, O.; Jördens, C.; Hochrein, T.; Jung, T.; Chatterjee, S.; Koch, M. Anwendungen Für Terahertz-Systeme: Märkte Und Perspektiven Einer Innovativen Technik. *Chem. Ing. Tech.* **2010**, *82*, 467-476.

(88) Banerjee, D.; von Spiegel, W.; Thomson, M. D.; Schabel, S.; Roskos, H. G. Diagnosing Water Content in Paper by Terahertz Radiation. *Opt. Express* **2008**, *16*, 9060-9066.

(89) Mousavi, P.; Haran, F.; Jez, D.; Santosa, F.; Dodge, J. S. Simultaneous Composition and Thickness Measurement of Paper Using Terahertz Time-Domain Spectroscopy. *Appl. Opt.* **2009**, *48*, 6541-6546.

(90) Reid, M.; Fedosejevs, R. Terahertz Birefringence and Attenuation Properties of Wood and Paper. *Appl. Opt.* **2006**, *45*, 2766-2772.



- (91) Wietzke, S.; Jansen, C.; Jung, T.; Reuter, M.; Baudrit, B.; Bastian, M.; Chatterjee, S.; Koch, M. Terahertz Time-Domain Spectroscopy as a Tool to Monitor the Glass Transition in Polymers. *Opt. Express* **2009**, *17*, 19006-19014.
- (92) Jansen, C.; Wietzke, S.; Koch, M. Terahertz Spectroscopy of Polymers. In *Terahertz Spectroscopy and Imaging*; Peiponen, K.-E., Zeitler, A., Kuwata-Gonokami, M., Eds.; Springer Berlin Heidelberg, 2013; Vol. 171; pp 327-353.
- (93) Fischer, B. M.; Wietzke, S.; Reuter, M.; Peters, O.; Gente, R.; Jansen, C.; Vieweg, N.; Koch, M. Investigating Material Characteristics and Morphology of Polymers Using Terahertz Technologies. *IEEE Trans. on THz. Sci. and Tech.* **2013**, *3*, 259-268.
- (94) Bodnar, J.-L. Non Destructive Testing of Works of Art by Terahertz Analysis. *Euro. Phys. Jour.:Appl. Phys.* **2013**, *64*.
- (95) Fukunaga, K.; Picollo, M. Characterisation of Works of Art. In *Terahertz Spectroscopy and Imaging*; Peiponen, K.-E., Zeitler, A., Kuwata-Gonokami, M., Eds.; Springer Berlin Heidelberg, 2013; Vol. 171; pp 521-538.
- (96) Fukunaga, K.; Hosako, I. Innovative Non-Invasive Analysis Techniques for Cultural Heritage Using Terahertz Technology. *Comptes Rendus Physique* **2010**, *11*, 519-526.
- (97) Morf, T.; Klein, B.; Despont, M.; Drechsler, U.; Kull, L.; Corcos, D.; Elad, D.; Kaminski, N.; Pfeiffer, U. R.; Al Hadi, R.; Keller, H. M.; Braendli, M.; Menolfi, C.; Kossel, M.; Francese, P. A.; Toifl, T.; Plettemeier, D. Wide Bandwidth Room-Temperature THz Imaging Array Based on Antenna-Coupled Mosfet Bolometer. *Sensors and Actuators A: Physical* **2014**, *215*, 96-104.
- (98) Burdette, D. J.; Alverbro, J.; Zhang, Z.; Fay, P.; Ni, Y.; Potet, P.; Sertel, K.; Trichopoulos, G.; Topalli, K.; Volakis, J.; Mosbacher, H. L. "Development of an 80 X 64 Pixel, Broadband, Real-Time THz Imager", 2011.
- (99) King, M. D.; Buchanan, W. D.; Korter, T. M. Investigating the Anharmonicity of Lattice Vibrations in Water-Containing Molecular Crystals through the Terahertz Spectroscopy of L-Serine Monohydrate. *J. Phys. Chem. A* **2010**, *114*, 9570-9578.
- (100) King, M. D.; Ouellette, W.; Korter, T. M. Noncovalent Interactions in Paired DNA Nucleobases Investigated by Terahertz Spectroscopy and Solid-State Density Functional Theory. *J. Phys. Chem. A* **2011**, *115*, 9467-9478.
- (101) Nickel, D. V.; Delaney, S. P.; Bian, H.; Zheng, J.; Korter, T. M.; Mittleman, D. M. Terahertz Vibrational Modes of the Rigid Crystal Phase of Succinonitrile. *J. Phys. Chem. A* **2014**, *118*, 2442-2446.
- (102) Delaney, S. P.; Smith, T. M.; Korter, T. M. Conformational Origins of Polymorphism in Two Forms of Flufenamic Acid. *J. Mol. Struct.* **2014**, *1078*, 83-89.
- (103) Jepsen, P. U.; Clark, S. J. Precise Ab-Initio Prediction of Terahertz Vibrational Modes in Crystalline Systems. *Chem. Phys. Lett.* **2007**, *442*, 275-280.
- (104) Williams, M. R. C.; Aschaffenburg, D. J.; Ofori-Okai, B. K.; Schmuttenmaer, C. A. Intermolecular Vibrations in Hydrophobic Amino Acid Crystals: Experiments and Calculations. *J. Phys. Chem. B* **2013**, *117*, 10444-10461.
- (105) Juliano, T. R.; Korter, T. M. London Force Correction Disparity in the Modeling of Crystalline Asparagine and Glutamine. *J. Phys. Chem. A* **2014**, *Submitted*.
- (106) Levine, I. N. *Quantum Chemistry*, Sixth ed.; Pearson Prentice Hall: Upper Saddle River, NJ, 2009.
- (107) Sholl, D. S.; Steckel, J. A. *Density Functional Theory: A Practical Introduction*; John Wiley and Sons, Inc.: Hoboken, NJ, 2009.

- (108) Foresman, J. B.; Frisch, A. *Exploring Chemistry with Electronic Structure Methods*, Second ed.; Gaussian, Inc.: Pittsburgh, PA, 1996.
- (109) Leach, A. R. *Molecular Modelling: Principles and Applications*, Second ed.; Pearson Prentice Hall: Edinburgh Gate, UK, 2001.
- (110) Hohenberg, P.; Kohn, W. Inhomogeneous Electron Gas. *Phys. Rev.* **1964**, *136*, B864-B871.
- (111) Sham, L. J.; Kohn, W. One-Particle Properties of an Inhomogeneous Interacting Electron Gas. *Phys. Rev.* **1966**, *145*, 561-567.
- (112) Perdew, J. P.; Burke, K.; Ernzerhof, M. Generalized Gradient Approximation Made Simple [Phys. Rev. Lett. 77, 3865 (1996)]. *Phys. Rev. Lett.* **1997**, *78*, 1396-1396.
- (113) Lee, C.; Yang, W.; Parr, R. G. Development of the Colle-Salvetti Correlation-Energy Formula into a Functional of the Electron Density. *Phys. Rev. B* **1988**, *37*, 785-789.
- (114) Becke, A. D. Density-Functional Exchange-Energy Approximation with Correct Asymptotic Behavior. *Phys. Rev. A* **1988**, *38*, 3098.
- (115) Zhao, Y.; Truhlar, D. G. Density Functionals with Broad Applicability in Chemistry. *Acc. Chem. Res.* **2008**, *41*, 157-167.
- (116) Sun, J.; Marsman, M.; Csonka, G. I.; Ruzsinszky, A.; Hao, P.; Kim, Y.-S.; Kresse, G.; Perdew, J. P. Self-Consistent Meta-Generalized Gradient Approximation within the Projector-Augmented-Wave Method. *Phys. Rev. B* **2011**, *84*, 035117.
- (117) Becke, A. D. Correlation Energy of an Inhomogeneous Electron Gas: A Coordinate-Space Model. *J. Chem. Phys.* **1988**, *88*, 1053-1062.
- (118) Ortiz, G.; Ballone, P. Correlation Energy, Structure Factor, Radial Distribution Function, and Momentum Distribution of the Spin-Polarized Uniform Electron Gas. *Phys. Rev. B* **1994**, *50*, 1391-1405.
- (119) Vosko, S. H.; Wilk, L.; Nusair, M. Accurate Spin-Dependent Electron Liquid Correlation Energies for Local Spin Density Calculations: A Critical Analysis. *Can. J. Phys.* **1980**, *58*, 1200-1211.
- (120) Jones, R. O.; Gunnarsson, O. The Density Functional Formalism, Its Applications and Prospects. *Rev. Mod. Phys.* **1989**, *61*, 689-746.
- (121) Gunnarsson, O.; Jones, R. O. Self-Interaction Corrections in the Density Functional Formalism. *Solid State Commun.* **1981**, *37*, 249-252.
- (122) Ernzerhof, M.; Scuseria, G. E. Assessment of the Perdew–Burke–Ernzerhof Exchange–Correlation Functional. *J. Chem. Phys.* **1999**, *110*, 5029-5036.
- (123) Boese, A. D.; Handy, N. C. A New Parametrization of Exchange–Correlation Generalized Gradient Approximation Functionals. *J. Chem. Phys.* **2001**, *114*, 5497-5503.
- (124) Perdew, J. P.; Chevary, J. A.; Vosko, S. H.; Jackson, K. A.; Pederson, M. R.; Singh, D. J.; Fiolhais, C. Atoms, Molecules, Solids, and Surfaces: Applications of the Generalized Gradient Approximation for Exchange and Correlation. *Phys. Rev. B* **1992**, *46*, 6671-6687.
- (125) Becke, A. D. On the Large-Gradient Behavior of the Density Functional Exchange Energy. *J. Chem. Phys.* **1986**, *85*, 7184-7187.
- (126) Perdew, J. P.; Ruzsinszky, A.; Csonka, G. I.; Vydrov, O. A.; Scuseria, G. E.; Constantin, L. A.; Zhou, X.; Burke, K. Restoring the Density-Gradient Expansion for Exchange in Solids and Surfaces. *Phys. Rev. Lett.* **2008**, *100*, 136406.

- (127) Zhao, Y.; Truhlar, D. G. Construction of a Generalized Gradient Approximation by Restoring the Density-Gradient Expansion and Enforcing a Tight Lieb–Oxford Bound. *J. Chem. Phys.* **2008**, *128*, -.
- (128) Burke, K.; Perdew, J. P.; Wang, Y. Derivation of a Generalized Gradient Approximation: The PW91 Density Functional. *Electronic Density Functional Theory: Recent Progress and New Directions, [Proceedings of the International Workshop on Electronic Density Functional Theory: Recent Progress and New Directions]*, Nathan, Australia, July 14-19, 1996 **1998**, 81.
- (129) Becke, A. D. Current-Density Dependent Exchange-Correlation Functionals. *Can. J. Chem.* **1996**, *74*, 995-997.
- (130) Perdew, J. P. Density-Functional Approximation for the Correlation-Energy of the Inhomogeneous Electron-Gas. *Phys. Rev. B* **1986**, *33*, 8822-8824.
- (131) Wilson, L. C.; Levy, M. Nonlocal Wigner-Like Correlation-Energy Density Functional through Coordinate Scaling. *Phys. Rev. B* **1990**, *41*, 12930-12932.
- (132) Adamo, C.; Barone, V. Toward Reliable Density Functional Methods without Adjustable Parameters: The PBE0 Model. *J. Chem. Phys.* **1999**, *110*, 6158-6170.
- (133) Becke, A. D. A New Mixing of Hartree–Fock and Local Density-Functional Theories. *J. Chem. Phys.* **1993**, *98*, 1372-1377.
- (134) Hehre, W. J.; Ditchfield, R.; Pople, J. A. Self—Consistent Molecular Orbital Methods. XII. Further Extensions of Gaussian—Type Basis Sets for Use in Molecular Orbital Studies of Organic Molecules. *J. Chem. Phys.* **1972**, *56*, 2257-2261.
- (135) Francl, M. M.; Pietro, W. J.; Hehre, W. J.; Binkley, J. S.; Gordon, M. S.; DeFrees, D. J.; Pople, J. A. Self-Consistent Molecular Orbital Methods. XXIII. A Polarization-Type Basis Set for Second-Row Elements. *J. Chem. Phys.* **1982**, *77*, 3654-3665.
- (136) Dunning, T. H. Gaussian Basis Sets for Use in Correlated Molecular Calculations. I. The Atoms Boron through Neon and Hydrogen. *J. Chem. Phys.* **1989**, *90*, 1007-1024.
- (137) Monkhorst, H. J.; Pack, J. D. Special Points for Brillouin-Zone Integrations. *Phys. Rev. B: Condens. Matter* **1976**, *13*, 5188-5192.
- (138) Cramer, C. J. *Essentials of Computational Chemistry: Theories and Models*; Wiley, 2005.
- (139) Dall’Olio, S.; Dovesi, R.; Resta, R. Spontaneous Polarization as a Berry Phase of the Hartree-Fock Wave Function: The Case of KNbO<sub>3</sub>. *Phys. Rev. B: Condens. Matter* **1997**, *56*, 10105-10114.
- (140) Dovesi, R.; Saunders, V. R.; Roetti, C.; Orlando, R.; Zicovich-Wilson, C. M.; Pascale, F.; Civalleri, B.; Doll, K.; Harrison, N. M.; Bush, I. J.; D’Arco, P.; Llunell, M.; Torino, U. o. T. *CRYSTAL09 User's Manual* **2009**.
- (141) Nick Pace, C.; Scholtz, J. M.; Grimsley, G. R. Forces Stabilizing Proteins. *FEBS Lett* **2014**, *588*, 2177-2184.
- (142) Kolar, M.; Kubar, T.; Hobza, P. On the Role of London Dispersion Forces in Biomolecular Structure Determination. *J. Phys. Chem. B* **2011**, *115*, 8038-8046.
- (143) London, F. The General Theory of Molecular Forces. *Trans. Faraday Soc.* **1937**, *33*, 8b-26.
- (144) Grimme, S. Accurate Description of van der Waals Complexes by Density Functional Theory Including Empirical Corrections. *J. Comput. Chem.* **2004**, *25*, 1463-1473.

- (145) Grimme, S.; Antony, J.; Ehrlich, S.; Krieg, H. A Consistent and Accurate Ab Initio Parametrization of Density Functional Dispersion Correction (DFT-D) for the 94 Elements H-Pu. *J. Chem. Phys.* **2010**, *132*, 154104-154119.
- (146) Johnson, E. R.; Becke, A. D. van der Waals Interactions from the Exchange Hole Dipole Moment: Application to Bio-Organic Benchmark Systems. *Chem. Phys. Lett.* **2006**, *432*, 600-603.
- (147) Risthaus, T.; Grimme, S. Benchmarking of London Dispersion-Accounting Density Functional Theory Methods on Very Large Molecular Complexes. *J. Chem. Theor. and Comp.* **2013**, *9*, 1580-1591.
- (148) Steinmann, S. N.; Corminboeuf, C. Comprehensive Benchmarking of a Density-Dependent Dispersion Correction. *J. Chem. Theor. and Comp.* **2011**, *7*, 3567-3577.
- (149) Tang, K. T.; Toennies, J. P. An Improved Simple Model for the van der Waals Potential Based on Universal Damping Functions for the Dispersion Coefficients. *J. Chem. Phys.* **1984**, *80*, 3726-3741.
- (150) Tkatchenko, A.; Scheffler, M. Accurate Molecular van der Waals Interactions from Ground-State Electron Density and Free-Atom Reference Data. *Phys. Rev. Lett.* **2009**, *102*, 073005.
- (151) Johnson, E. R.; Becke, A. D. A Post-Hartree-Fock Model of Intermolecular Interactions: Inclusion of Higher-Order Corrections. *J. Chem. Phys.* **2006**, *124*.
- (152) DiStasio, R. A., Jr.; Gobre, V. V.; Tkatchenko, A. Many-Body van der Waals Interactions in Molecules and Condensed Matter. *J. Phys. Condens. Matter* **2014**, *26*, 213202.
- (153) Lee, K.; Murray, É. D.; Kong, L.; Lundqvist, B. I.; Langreth, D. C. Higher-Accuracy van der Waals Density Functional. *Phys. Rev. B: Condens. Matter* **2010**, *82*, 081101.
- (154) Lundqvist, B. I.; Andersson, Y.; Shao, H.; Chan, S.; Langreth, D. C. Density Functional Theory Including van der Waals Forces. *Int. J. Quantum Chem* **1995**, *56*, 247-255.
- (155) Vydrov, O. A.; Van Voorhis, T. Nonlocal van der Waals Density Functional: The Simpler the Better. *The Journal of Chemical Physics* **2010**, *133*.
- (156) Hujo, W.; Grimme, S. Performance of the van der Waals Density Functional VV10 and (Hybrid)GGA Variants for Thermochemistry and Noncovalent Interactions. *J. Chem. Theor. and Comp.* **2011**, *7*, 3866-3871.
- (157) Zhao, Y.; Truhlar, D. G. A New Local Density Functional for Main-Group Thermochemistry, Transition Metal Bonding, Thermochemical Kinetics, and Noncovalent Interactions. *J. Chem. Phys.* **2006**, *125*.
- (158) Becke, A. D.; Johnson, E. R. Exchange-Hole Dipole Moment and the Dispersion Interaction. *J. Chem. Phys.* **2005**, *122*.
- (159) Grimme, S.; Ehrlich, S.; Goerigk, L. Effect of the Damping Function in Dispersion Corrected Density Functional Theory. *J. Comput. Chem.* **2011**, *32*, 1456-1465.

## CHAPTER 2: Terahertz Spectroscopy in the Korter Group

### 2.1 Time-Domain Terahertz Spectrometer

The Korter group uses a home-built time-domain terahertz spectrometer based on an amplified Titanium:Sapphire (Ti:Sa) laser system (**Figure 2-1**). The THz radiation that is generated and detected is produced using a four-component laser system. The system consists of two pump lasers, a seed laser, and an amplifier. The output of this system is high-intensity near-IR radiation. The Ti:Sa regenerative amplifier is seeded by the pulsed output centered at 800 nm from the Ti:Sa oscillator. The oscillator is pumped by a continuous wave neodymium-doped yttrium orthovanadate (Nd:YVO<sub>4</sub>) laser. The gain medium of the amplifier (Ti:Sa) is pumped by a high-intensity neodymium-doped yttrium lithium fluoride (Nd:YVF<sub>4</sub>) laser. Laser pulses of ~35 fs centered at ~800 nm are generated by this system. With a peak output power of 2.5 W, the amplifier creates a pulse with an energy of 2.5 mJ with a 1 kHz repetition rate.

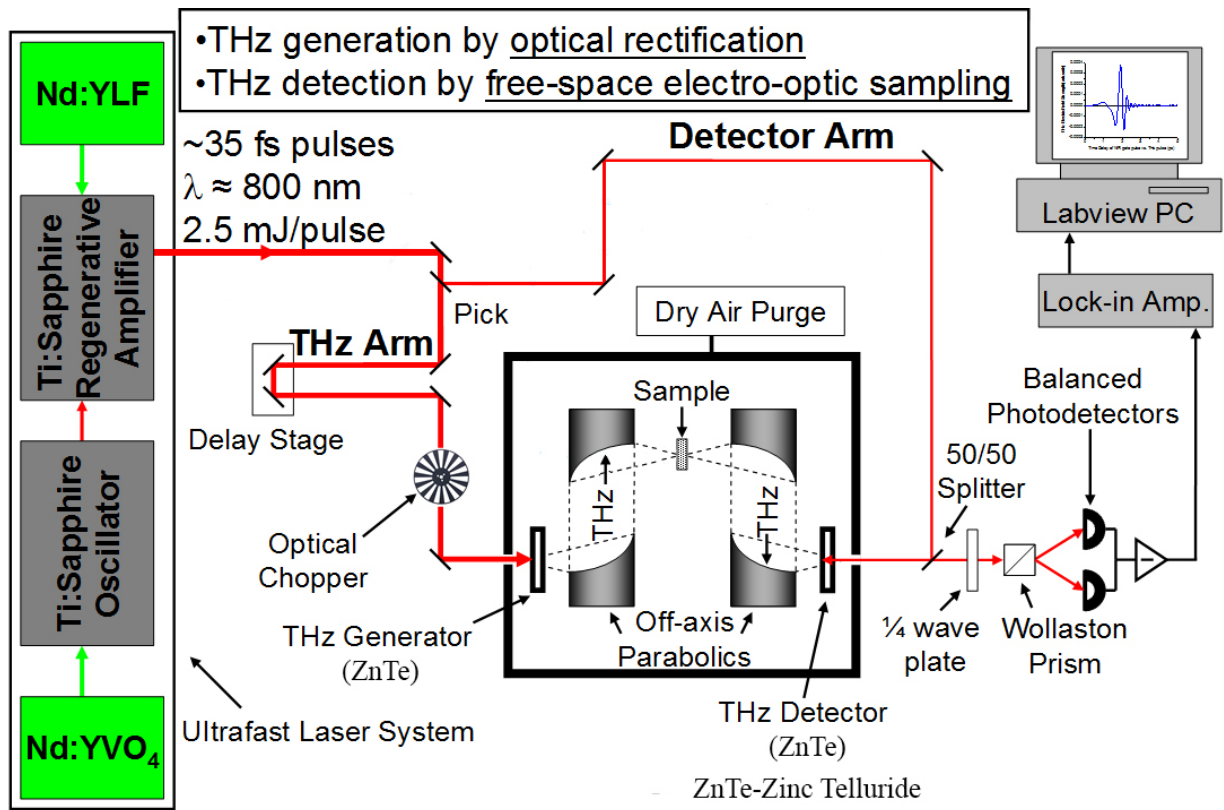


Figure 2-1. Schematic of the terahertz spectrometer used in the Korter lab.

## 2.2 Terahertz Generation and Detection

There are two prevalent methods for the generation of terahertz radiation, photoconductive switching and optical rectification. Photoconductive switching generates THz radiation by exciting the switch that is placed on a semiconductor substrate with a femtosecond laser pulse.<sup>1</sup> In the Korter group, optical rectification is used to generate THz radiation. This is achieved by using a non-linear medium (electro-optic crystal) and the high electric field of a femtosecond near-IR pulse to induce polarization changes.<sup>2</sup>

The detection of THz electric fields uses similar methods. Like the photoconductive switch for generation, photoconductive sampling uses a similar semiconductor set-up operating in reverse to detect THz pulses. The Korter group uses free-space electro-optic sampling, a method that uses a second-order nonlinear effect, known as the Pockels effect,<sup>3</sup> in semiconductor crystals to detect the radiation used in the THz experiments.

### 2.2.1 Optical Rectification

A noncentrosymmetric crystal is used to generate THz radiation via the second-order nonlinear process known as optical rectification.<sup>4</sup> The high intensity pulse generated from the four component laser system induces a second-order polarization within the crystal, which is represented by a Taylor expansion series,

$$P(t) = \chi^{(1)}E(t) + \chi^{(2)}E(t)^{(2)} + \dots \quad (2.1)$$

where  $\chi^{(1)}$  and  $\chi^{(2)}$  are the first and second order susceptibility tensors, respectively.<sup>4,5</sup> With respect to the terms of the equation, the first term describes the linear optical effects and the second term (and higher terms) represents the nonlinear effects within the material. Since optical rectification is a non-linear process, the second and higher terms of the Taylor expansion are

responsible for it, as well as other effects including second harmonic generation, sum and difference frequency mixing, and the Pockels effect.

In order to describe the electric field of a short laser pulse, the following equation can be used

$$E(t) = A(t) \cos \omega_0 t, \quad (2.2)$$

where  $A(t)$  is the pulse amplitude as a function of time and  $\omega_0$  is the central frequency. The second term for Eq. 2.1 is responsible for the optical rectification process and, when combined with Eq. 2.2, the nonlinear polarization,  $P^{(2)}(t)$ , can be broken into two terms,

$$P^{(2)}(t) = \chi^{(2)} E(t)^{(2)} = \frac{\chi^{(2)} A(t)^2}{2} + \frac{\chi^{(2)} A(t)^2}{2} \cos 2\omega_0 t. \quad (2.3)$$

The first term of this equation is responsible for optical rectification, which generates THz radiation. This term is directly proportional to the pulse intensity, as it is frequency independent. Due to the use of a noncentrosymmetric crystal, the average polarization induced by the oscillating pulse does not go to zero, and lasts the duration of the pulse. If the crystal is excited by a CW light source, the voltage across the crystal is increased, but does not result in a practical application. When a pulsed light source is used, specifically one that is sub-ps in timescale, a transient polarization occurs which generates pulsed THz radiation.<sup>6</sup> A more commonly encountered phenomenon in spectroscopy is found in the second term that produces radiation with frequencies that are twice that of the incident pulse, using the process of second-harmonic generation.

A number of materials, mainly semiconductors and organic crystals, have shown optical rectification ability. Each material generates a different THz pulse bandwidth, which is



dependent on the polarizability of the crystal, as well as the pulse power and bandwidth of the light source. The Korter lab uses a zinc telluride (ZnTe) inorganic crystal in order to generate THz radiation by optical rectification.<sup>4,7</sup> ZnTe is used for its superior spectral resolution and peak efficiency. Another popular choice for an inorganic crystal is gallium phosphide (GaP) which results in a higher spectral bandwidth, but lower resolution.<sup>8</sup>

### 2.2.2 Free-Space Electro-Optic Sampling

The electro-optic effect known as the Pockels effect, is a second-order nonlinear process that is used in the detection method known as free-space electro-optic sampling (FSEOS).<sup>3</sup> The Pockels effect is the induction of birefringence in a material as a response to a static electric field or the electric field of a laser pulse. The time-dependent polarization at a laser frequency is expressed as

$$P(t) = \chi^{(1)}E(t) + \chi^{(2)}E_0E(t) = (\chi^{(1)} + \chi^{(2)}E_0)E(t), \quad (2.4)$$

where  $E_0$  is the static electric field and  $(E(t))$  is the electric field of the laser pulse. By this relationship, the refractive index of the material changes when a static electric field,  $E_0$ , is introduced. The THz field is taken to be the static electric field in the above equation due to the fact that its oscillation is much slower than the duration of the detector pulse. The co-propagation of the THz beam with a linearly polarized near-IR probe beam occurs within the crystal. The polarization of the near-IR probe pulse is altered by the change in the refractive index of the crystal induced by the introduction of THz radiation.<sup>5</sup> Both the amplitude of the THz pulse and the variation of the refractive index can be measured using the rotation of the polarization of the detector pulse. Using a Wollaston prism and a pair of balanced photodetectors, the amplitude of the THz field can be measured because of its linear relation to the amount of rotation. By

introducing a time delay for the THz pulse, the measurements of the phase and amplitude of the THz pulse can be directly obtained. The Korter lab uses a ZnTe crystal for the detection of THz, as it is common to use similar types of crystals for both generation and detection.<sup>9</sup>

### **2.3 Sample Preparation**

In order to obtain the THz spectrum of a sample, the sample must be in microcrystalline form and mixed into a non-absorbing matrix. In most cases, a very small amount of the sample needs to be used (5-15 mg). The amount of sample necessary is, however, dependent on the absorption strength of the material, which in some cases leads to the use of 50 mg or more of sample for weakly absorbing species. When preparing a sample for investigation, it is important to consider the thickness of the sample pellet. The use of samples that are too thin lead to internal Fresnel reflections that will appear in the acquired waveform. As the sample thickness is increased, the distance between the first Fresnel reflection and the desired THz signal increases. This reflection can also be avoided by adjusting the distance over which the data are collected (time-delay).

There are several options for sample matrices that can be used to make the sample pellets. The most commonly used matrices are polytetrafluoroethylene (PTFE), polyethylene (PE), and adamantane (C<sub>10</sub>H<sub>16</sub>). All of these materials are suitable due to their weak low-frequency absorptions in the THz region. These absorptions are removed from the sample data by subtraction of the measurements of a blank made solely out of the matrix material. In the studies that follow, PTFE was chosen as the sample matrix due to its low water retention and high density. In addition, the use of PTFE allows for the sample pellets to be formed under lower pressure than some of the other matrices, which can become important when considering pressure induced polymorphism in molecular crystals. Any interaction between the samples and

matrix are of no concern in the acquisition of THz data due to the fact that they are not ordered and, therefore, do not show absorptions.

When mixing the sample into the PTFE matrix, an even distribution of the sample and small particle size are obtained by pulverization in a stainless-steel ball mill. Both the sample and matrix were placed in a stainless-steel vial along with a stainless-steel ball bearing and were pulverized for approximately two minutes total. In order to avoid heating of the mixture, the total pulverization time was broken into four 30 second intervals. After each 30 second interval, the sample was mixed manually in order to prevent the mixture from clumping in the vial.

After pulverization, the sample/matrix mixture was pressed into sample pellets using a hydraulic press with a 13-mm stainless-steel die. In order to make a pellet of the appropriate thickness (2.2 mm), approximately 0.55 g of the sample/matrix mixture was placed into the die. Using an applied pressure of 2000 psi, the samples were pressed into the pellet form with dimensions 13 mm (diameter) x 2.2 mm (thickness). The reference blank pellets were made in the same manner, using pure PTFE.

## **2.4 Data Acquisition and Processing**

A cryostat with 3-mm thick TPX (polymethylpentene) windows was used to hold the samples and blanks during measurements. Data sets were acquired under vacuum at temperatures of 293 K and 78 K (liquid nitrogen cooled). The THz waveform was captured using a 32 ps scan window consisting of 3200 data points. Before data transforms were applied, the THz waveform was symmetrically zero-padded using 6000 data points. The increased number of data points allowed for the increased apparent resolution of the transformed spectra. An effective instrument resolution of approximately  $1.0 \text{ cm}^{-1}$  was observed using the 32 ps scan window. The individual data set was comprised of the average of 32 scans.

The collected time-domain data were subjected to a Fourier transform in order to produce frequency-domain power spectra (**Figure 2-2**). The data were symmetrically weighted at the center of the number set by using a Hanning window applied to the transform. The use of this method aided in the prevention of higher frequency features becoming indistinguishable from one another. The THz absorption spectra were obtained from the ratio of the Fourier-transformed data sets of the samples and blanks. The presented THz spectra are the result of the averaging of four individual data sets, in order to reduce the effects of laser drift, power fluctuations, and baseline noise.

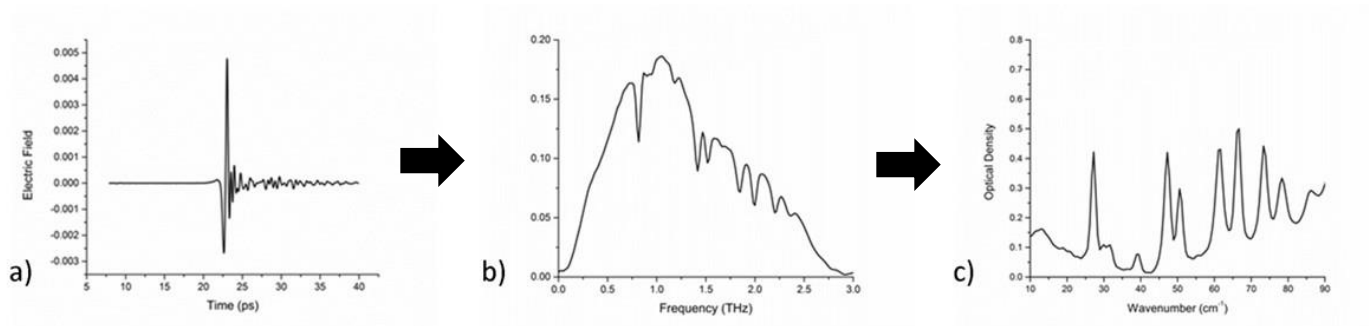


**Figure 2-2.** Representation of the terahertz waveform (a), frequency spectrum from Fourier transform (b), and the final terahertz absorption spectrum (c).

## 2.5 References

- (1) Auston, D. H. Picosecond Optoelectronic Switching and Gating in Silicon. *Appl. Phys. Lett.* **1975**, *26*, 101-103.
- (2) Jepsen, P. U.; Cooke, D. G.; Koch, M. Terahertz Spectroscopy and Imaging – Modern Techniques and Applications. *Laser Photonics Rev* **2011**, *5*, 124-166.
- (3) Wu, Q.; Zhang, X. C. Free-Space Electro-Optic Sampling of Terahertz Beams. *Appl. Phys. Lett.* **1995**, *67*, 3523-3525.
- (4) Rice, A.; Jin, Y.; Ma, X. F.; Zhang, X. C.; Bliss, D.; Larkin, J.; Alexander, M. Terahertz Optical Rectification from <110> Zinc-Blende Crystals. *Appl. Phys. Lett.* **1994**, *64*, 1324-1326.
- (5) Rulliere, C.; Editor *Femtosecond Laser Pulses: Principles and Experiments*, Second ed.; Springer: New York, NY, 2005.
- (6) Bonvalet, A.; Joffre, M. Terahertz Femtosecond Pulses. In *Femtosecond Laser Pulses*; Rullière, C., Ed.; Springer Berlin Heidelberg, 1998; pp 285-305.
- (7) Harrel, S. M.; Milot, R. L.; Schleicher, J. M.; Schmittenmaer, C. A. Influence of Free-Carrier Absorption on Terahertz Generation from ZnTe(110). *J. Appl. Phys.* **2010**, *107*, -.
- (8) Nishizawa, J.; Sasaki, T.; Suto, K.; Tanabe, T.; Yoshida, T.; Kimura, T.; Saito, K. Frequency-Tunable Terahertz-Wave Generation from Gap Using Cr:Forsterite Lasers. *Int J Infrared Milli Waves* **2006**, *27*, 923-929.
- (9) Wu, Q.; Litz, M.; Zhang, X. C. Broadband Detection Capability of ZnTe Electro-Optic Field Detectors. *Appl. Phys. Lett.* **1996**, *68*, 2924-2926.

## CHAPTER 3. Use of Solid-State Density Functional Theory in the Korter Group

Solid-state density functional theory is capable of simulating both geometric and spectroscopic data of crystalline solid materials. The geometry calculations provide energetically minimized structures that are then used to generate simulated low-frequency spectra. The theoretical spectra not only contain absorption positions, but the infrared intensities as well. Using the full simulated THz spectra allow for direct comparison to experimental data that provides insight into the nature of features in the THz region.

### 3.1 CRYSTAL Software Package

The CRYSTAL software package (2009 and 2014 release versions) was used to conduct all solid-state DFT calculations presented in this research.<sup>1,2</sup> This *ab initio* software package can use either Hartree-Fock or DFT approximations to calculate the electronic structures of periodic systems in 1, 2 or 3 dimensions. It can also be used on single molecules in order to obtain molecular information in the solid-state. Many physical and chemical properties can be determined using the CRYSTAL software package, this includes, but is not limited to, structural and vibrational properties, the two most important factors in the research that follows. This software can also be used to compute dielectric, magnetic and elastic properties. Although the work that follows focuses on infrared intensities, the most recent version of the software is able to calculate Raman intensities, as well. The use of a number of different exchange and correlation functionals is permitted in CRYSTAL; this includes both GGAs and hybrids. In the case of most of these functionals, the addition of a semi-empirical dispersion correction term is available. It is based on the Grimme DFTD-D2 parameterization and is dependent on a  $1/R^6$  term.<sup>3</sup>

The CRYSTAL program is used, rather than other DFT software (Gaussian,<sup>4</sup> dmol<sup>5</sup>), due to its ability to calculate solid-state vibrational normal modes, as well as their infrared intensities.<sup>1,6</sup> Since the vibrations of interest occur in the THz region, and are highly sensitive to the intermolecular interactions that occur in the solid-state, the use of a specifically solid-state DFT program is desirable. The majority of the work presented in this thesis used the CRYSTAL09 version of the software (CRYSTAL14 was released in early 2014). The range of calculations performed includes single-point energies, geometry optimizations, normal-mode simulations, and thermodynamic data calculations. CRYSTAL uses atom-centered GTOs and periodic boundary conditions which reduce computational cost. All of the calculations were carried out using desktop computers with the number of parallel processors ranging from eight to twelve.

There are several input parameters in these calculations that are variable-dependent upon the system under study. For example, commonly varying parameters include the shrinking factors and the truncation criteria of the Coulomb and exchange infinite sums. The truncation criteria for the Coulomb and exchange infinite sums can be adjusted (made larger) in cases when the calculation is having difficulty with convergence during the SCF cycles. The radial and angular distribution of grid points were defined by a pruned (75,974) DFT integration grid. Numerical differentiation of the analytical gradient of the potential energy with respect to atomic positions within the harmonic limit was used in the calculations of the normal mode frequencies. The IR intensities of the normal modes were obtained using the Berry phase method.<sup>1</sup>

The process of THz spectral simulations contains a number of subsequent steps. In most cases, the initial starting point for a simulation set is X-ray diffraction data, ideally cryogenic, which provides the starting atomic positions. In order to execute any successful calculations, the



appropriate functional and basis set must be chosen. Once the atomic positions are obtained and the parameters are chosen, the input file, which contains the initial atomic positions and program keywords and tolerances, can be created.

### 3.2 Unit Cell Optimizations

The first step to a geometry optimization involves the determination of the number of  $\mathbf{k}$  points needed, which is a system dependent factor. In CRYSTAL, the number of  $\mathbf{k}$  points is inputted with the keyword SHRINK. This parameter consists of two numbers, the first of which determines the number of  $\mathbf{k}$  points that diagonalize the Fock/KS matrix.<sup>1</sup> The result of this number is the creation of the Pack-Monkhorst net, or the proportional grid of  $\mathbf{k}$  point in reciprocal space.<sup>7</sup> The second number used in the SHRINK input is used to calculate the Fermi energy and density matrix.<sup>8,9</sup> The second number is important in cases of non-insulating solids, so it is often not needed in the calculations conducted. It does, however, become a factor in the cases where a conducting state is encountered during a calculation.

In order to optimize the shrink value, single point energy calculations are used. The single point calculations allow the system to converge in the SCF cycles, but do not proceed after that. The tolerance for these calculations is set to  $10^{-10}$  Hartree, and for each single point the shrink value is manually changed until the difference in energy between two single point energies is less than or equal to  $10^{-10}$ . Once this is achieved, the smallest shrink value that meets the criteria is chosen to proceed with the rest of the calculations.

Once the shrinking factor is established, the geometry optimizations can proceed. Two variations of geometry optimizations can be carried out. The first type, a faster option, optimizes the atomic positions with fixed unit cell dimensions. This is a preliminary calculation that is used to check systems for unexpected complications. Due to the constraints applied (fixed unit cell

dimensions), these calculations do not result in the lowest energy structure. In order to obtain the best energetic results, a full optimization must be used. In this type of geometry optimization, both the atomic positions and the unit cell dimensions are allowed to relax. When executing a full optimization, the unit cell axes and volume often expands as much as 20-30%. This expansion is due to the underestimation of the intermolecular forces within the molecular solids. To correct for this, the semi-empirical DFT-D\* dispersion correction method<sup>10</sup> is implemented, with the customization of the global scaling factor,  $s_6$ , based on the system under study.

In order to ensure the accuracy of geometry optimizations, a number of convergence criteria must be met before the calculation can finish. The typical convergence criteria and their values are (keywords provided in parentheses): overall energy convergence set to  $\Delta E < 10^{-8}$ , root-mean-squares (RMS) of the gradient (TOLDEG) set to 0.000010 a.u., largest component of the gradient set to 0.000015 a.u., RMS of the largest displacements (TOLDEX) set to 0.000040 a.u., and the absolute value of the largest displacements set to 0.000060 a.u. Convergence with all of these parameters signifies the completion of a geometry optimization which provides the final energy of the optimized cell, and the optimized atomic positions and unit cell dimensions. When using the CRYSTAL09 version of the software, the addition of the keyword FINALRUN allows for the optimization to restart repeatedly until the convergence criteria are met on all fronts. This is instated by default in CRYSTAL14. Another parameter set that often requires manual changes are the truncation tolerances for the Coulomb and HF exchange integrals (keyword TOLINTEG<sup>1,6</sup>). By default, these values are set to  $10^{-6}$ ,  $10^{-6}$ ,  $10^{-6}$ ,  $10^{-6}$ ,  $10^{-12}$  hartree, however, if a conducting state is encountered during the optimization, these values can be increased, which usually results in the convergence of the calculation due to enhanced mathematical accuracy.

With the final optimized structures in hand, a comparison to the experimental X-ray data is carried out to ensure the accuracy of the calculations. The primary criteria of evaluation are the percent differences in the unit cell parameters ( $a$ ,  $b$ ,  $c$ , and volume). If these values are found to be acceptable (usually within 1%), the structure is considered to be in good agreement. If this is not the case, the unit cell structure can be improved by altering the global scaling factor ( $s_6$ ) of the DFT-D\* dispersion correction model. Once a reasonable structure is obtained, it is subjected to more rigorous comparisons to experiment. This includes the evaluation of the root-mean-squared deviations (RMSDs) of the bond lengths, bond angles, torsional angles, and, in some cases, the hydrogen-bond heavy atom separations. When the fully optimized structures have completed the evaluation process and have been determined as acceptable, they are used in the next step of the process, frequency calculations.

### 3.3 Frequency Calculations

Now that the highest possible quality structure has been obtained, the simulation of the vibrational frequencies can be carried out. The sensitivity of the low-frequency vibrations requires the use of a more accurate convergence energy, in this case,  $10^{-11}$  Hartree. The CRYSTAL software package is not only capable of determining the frequencies of the THz region vibrations, but by the Berry phase method<sup>1,11</sup>, it is also capable of determining the infrared intensities of these vibrations. It should be mentioned that another method for the determination of intensities is available in CRYSTAL, the Wannier functions method<sup>1,12</sup>, but is not used in the work presented in this thesis.

Frequency calculations calculate the gradient numerical derivatives of the symmetrically unique atoms. The frequencies and normal modes are calculated using the eigenvalues that are determined by the diagonalization of the mass weighted full Hessian matrix. This matrix is

generated when symmetry is applied to the irreducible atoms within the unit cell. To calculate the intensities of the normal modes, the Berry phase method is used. The Berry phase method evaluates the dipole moment derivatives with respect to the atomic displacements (Born charges) as polarization differences between the equilibrium and distorted geometries. The time-integral transient current that flows through the insulating sample during the vibrations is equal to the differences in the polarization from above.<sup>11,13</sup> The Berry phase method is limited to the calculation of IR intensities in insulating systems. As in the geometry optimization section, the calculations of frequencies takes place in reciprocal space and is therefore sensitive to the number of  $\mathbf{k}$  points (Pack-Monkhorst net) used.<sup>1</sup>

The results of these simulations are used to simulate the full THz spectra of molecular solids. Although the output values of the simulations are not directly usable, they can be changed into actual experimental units using the experimental full-width half-maximum (fwhm) values and Lorentzian line shapes. Occasionally, the spectrum will not match acceptably with the experimental spectrum. In these cases, changing the functional or basis set may be able to correct the problem. This is not uncommon, and leads to restarting the whole process. The steps used during the entire process, from X-ray data to final frequency simulations are shown in **Figure 3-1**.

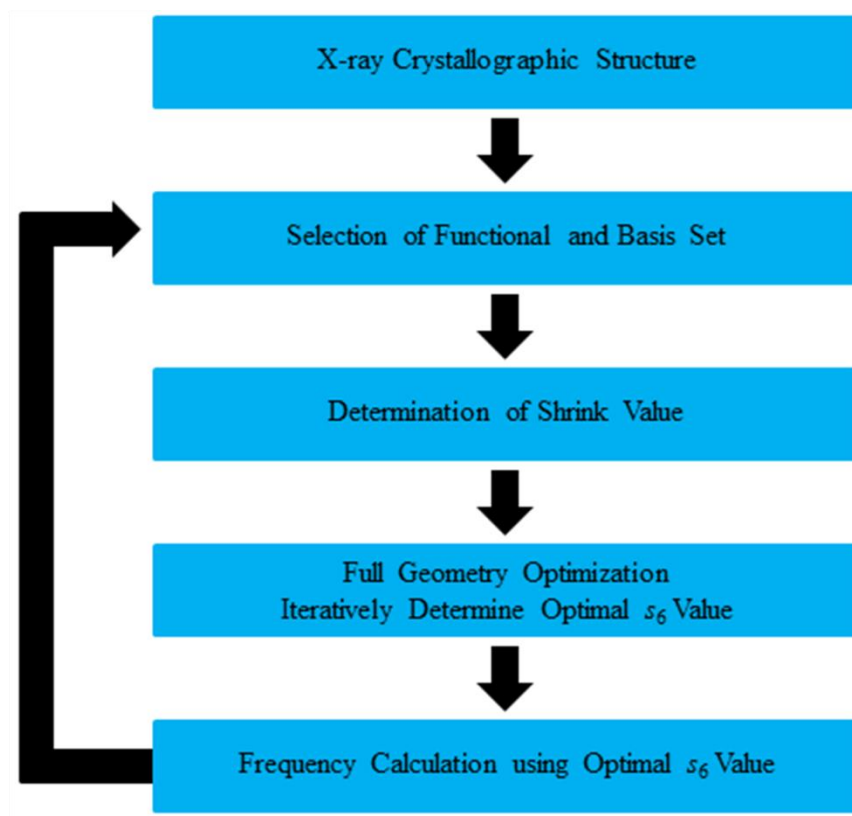


**Figure 3-1.** Step-by-step process for DFT calculations in the Korter Group.

### **3.4 Energy Calculations**

In addition to geometry optimizations and frequency/intensity simulations, solid-state DFT can be used to extract energetic data about the molecule under study. Examples of important energetic data to this thesis include the total electronic energy, the cohesive binding energy, and the basis set superposition energy correction.

#### **3.4.1 Total Electronic Energy**

The total amount of electronic energy in a system is included as part of the geometry optimizations. As mentioned before, these calculations allow the molecular systems to fully relax both the atomic positions and the lattice parameters. When establishing these energies, especially between similar molecules (L- and DL-amino acids and amino acid hydrates), it is essential to use the exact same input parameters for all calculations to ensure direct comparability. The electronic energy that comes out of these simulations is that of the entire unit cell. In order to make the numbers more manageable and comparable, they are divided by the crystallographic Z value to provide the energy per molecule. When comparing the per molecule energies, the results are often reported as relative energies in order to make the numbers more practical. These values can be compared to determine the relative stabilities of the different structures or even shed light onto the likelihood of hydrate formation.

#### **3.4.2 Conformational and Cohesive Energies**

The conformational energy of individual molecules can be obtained by executing calculations on a single molecule taken out of the unit cell. These are normally evaluated as a rigid single point energy calculation since we are concerned with the molecules conformational energy in the solid, not after it has relaxed in the gas phase. The energies between compounds such as L- and DL-amino acids and amino acids hydrates differ based on the conformation of

said molecules. As with the total electronic energies, the conformational energies are taken in relative terms to compare the similar molecular solids and determine which conformation is more favorable. It should be noted that conformational energies obtained from these calculations also contain a small amount of residual energy from the dispersion force corrections (due to limitations of the model).

With both the total electronic energy of the unit cell and conformational energy of the individual molecules known, the cohesive energy of molecular solids can be determined. In order to evaluate the cohesive energy, the energies of the single molecules are subtracted from the total energy of the crystalline solid. The most important components of the cohesive energy are the dispersion force, hydrogen bonding, and dipole-dipole contributions. These values of the cohesive energies are taken in absolute, not relative, terms, which allow for the direct calculations of the magnitudes of the hydrogens bonds, dipole-dipole contributions, and dispersion forces. The dispersion force contribution is part of the output from the calculations mentioned above, and when subtracted from the cohesive energy, the hydrogen bond contribution remains. It is important to keep track of these energies per molecule because both the output values of the calculations (per unit cell for total energy and per molecule for conformational energy) and the Z values of the unit cell can differ.

The CRYSTAL software package can also be used to obtain thermodynamic data. By adding the TEMPSCAN keyword to frequency calculations, the output of thermodynamic data over a range of temperatures is generated. This information can, for example, be used to determine the Gibbs free energy of molecular systems.

### 3.4.3 Basis Set Superposition Error

As previously mentioned, one of the issues that arises from using finite basis sets in DFT is an artificial energy, known as basis set superposition error (BSSE), introduced into the calculations. This energy lowers the total energy of the systems under study, and therefore must be removed to obtain the most accurate energy values possible. The value of the BSSE differs between systems and therefore must be calculated separately for each molecular solid. As a general rule, the larger the basis set, the smaller the BSSE, but even with the use of large basis sets, the artificial energy can be of significant magnitude. If the BSSE is not accounted for, the relative stabilities of molecules can be incorrectly ordered.

The CRYSTAL software package uses the counterpoise method<sup>14</sup> to determine the amount of BSSE present in simulations. This method completes single point energy calculations with ghost atoms surrounding the molecule of interest within a user defined distance. The number of ghost atoms used is dependent on the number of atoms in the molecule, as well as the user defined radius. The standard values for number of atoms and the distance cutoff are 300 atoms and 5 angstroms, respectively.



### 3.6 References

- (1) Dovesi, R.; Saunders, V. R.; Roetti, C.; Orlando, R.; Zicovich-Wilson, C. M.; Pascale, F.; Civalleri, B.; Doll, K.; Harrison, N. M.; Bush, I. J.; D'Arco, P.; Llunell, M.; Torino, U. o. T. *CRYSTAL09 User's Manual* **2009**.
- (2) Dovesi, R.; Saunders, V. R.; Roetti, C.; Orlando, R.; Zicovich-Wilson, C. M.; Pascale, F.; Civalleri, B.; Doll, K.; Harrison, N. M.; Bush, I. J.; D'Arco, P.; Llunell, M.; Torino, U. o. T. *CRYSTAL14 User's Manual* **2014**.
- (3) Grimme, S. Semiempirical GGA-Type Density Functional Constructed with a Long-Range Dispersion Correction. *J. Comput. Chem.* **2006**, *27*, 1787-1799.
- (4) Frisch, M. J.; Trucks, G. W.; Schlegel, H. B.; Scuseria, G. E.; Robb, M. A.; Cheeseman, J. R.; Scalmani, G.; Barone, V.; Mennucci, B.; Petersson, G. A.; Nakatsuji, H.; Caricato, M.; Li, X.; Hratchian, H. P.; Izmaylov, A. F.; Bloino, J.; G. Zheng; Sonnenberg, J. L.; Hada, M.; Ehara, M.; Toyota, K.; Fukuda, R.; Hasegawa, J.; Ishida, M.; Nakajima, T.; Honda, Y.; Kitao, O.; Nakai, H.; Vreven, T.; J. A. Montgomery, J.; Peralta, J. E.; Ogliaro, F.; Bearpark, M.; Heyd, J. J.; Brothers, E.; Kudin, K. N.; Staroverov, V. N.; Kobayashi, R.; Normand, J.; Raghavachari, K.; Rendell, A.; Burant, J. C.; Iyengar, S. S.; Tomasi, J.; Cossi, M.; Rega, N.; Millam, J. M.; Klene, M.; Knox, J. E.; Cross, J. B.; Bakken, V.; Adamo, C.; Jaramillo, J.; Gomperts, R.; Stratmann, R. E.; Yazyev, O.; Austin, A. J.; Cammi, R.; Pomelli, C.; Ochterski, J.; Martin, R. L.; Morokuma, K.; Zakrzewski, V. G.; Voth, G. A.; Salvador, P.; Dannenberg, J. J.; Dapprich, S.; Daniels, A. D.; Farkas, O.; Foresman, J. B.; Ortiz, J. V.; Cioslowski, J.; Fox, D. J. *GAUSSIAN 09* **2009**, *Guassian, Inc., Wallingford, CT*.
- (5) Sholl, D. S.; Steckel, J. A. *Density Functional Theory: A Practical Introduction*; John Wiley and Sons, Inc.: Hoboken, NJ, 2009.
- (6) Pascale, F.; Zicovich-Wilson, C. M.; López Gejo, F.; Civalleri, B.; Orlando, R.; Dovesi, R. The Calculation of the Vibrational Frequencies of Crystalline Compounds and Its Implementation in the Crystal Code. *J. Comput. Chem.* **2004**, *25*, 888-897.
- (7) Monkhorst, H. J.; Pack, J. D. Special Points for Brillouin-Zone Integrations. *Phys. Rev. B: Condens. Matter* **1976**, *13*, 5188-5192.
- (8) Gilat, G. Analysis of Methods for Calculating Spectral Properties in Solids. *Journal of Computational Physics* **1972**, *10*, 432-465.
- (9) Gilat, G.; Raubenheimer, L. J. Accurate Numerical Method for Calculating Frequency-Distribution Functions in Solids. *Phys. Rev.* **1966**, *144*, 390-395.
- (10) Civalleri, B.; Zicovich-Wilson, C. M.; Valenzano, L.; Ugliengo, P. B3LYP Augmented with an Empirical Dispersion Term (B3LYP-D\*) as Applied to Molecular Crystals. *CrystEngComm* **2008**, *10*, 405-410.
- (11) Dall'Olivo, S.; Dovesi, R.; Resta, R. Spontaneous Polarization as a Berry Phase of the Hartree-Fock Wave Function: The Case of KNbO<sub>3</sub>. *Phys. Rev. B: Condens. Matter* **1997**, *56*, 10105-10114.
- (12) Zicovich-Wilson, C. M.; Dovesi, R.; Saunders, V. R. A General Method to Obtain Well Localized Wannier Functions for Composite Energy Bands in Linear Combination of Atomic Orbital Periodic Calculations. *J. Chem. Phys.* **2001**, *115*, 9708-9719.
- (13) Evarestov, R. A. *Quantum Chemistry of Solids: The Lcao First Principles Treatment of Crystals*; Springer, 2007.

(14) Boys, S. F.; Bernardi, F. The Calculation of Small Molecular Interactions by the Differences of Separate Total Energies. Some Procedures with Reduced Errors. *Mol. Phys.* **1970**, *19*, 553-566.

## CHAPTER 4. London Force Correction Disparity in the Modeling of Crystalline Asparagine and Glutamine

The material contained within this chapter has been submitted to *The Journal of Physical Chemistry A*. (Juliano, T. R.; Korter, T. M. *J. Phys. Chem. A*. **2014**. Submitted.)

### Abstract

Solid-state density functional theory is a powerful computational method used to provide insight into the low-frequency vibrations of crystalline solids. A known limitation of this method is its general underestimation of weak intermolecular forces. Semi-empirical London force corrections have been developed to augment density functional theory calculations with the ultimate goal being corrections that are applicable to a range compounds. In this study, two structurally similar amino acids, asparagine and glutamine, were chosen to gauge the proximity of the widely used DFT-D2 approach to this goal. Despite their chemical similarities, it was determined that the two molecular solids required considerably different semi-empirical correction magnitudes, with asparagine requiring a 42% greater London force correction factor when compared to glutamine. To validate these findings, terahertz spectroscopy was used to investigate the intermolecular vibrations of both amino acids in the low-frequency, sub-100  $\text{cm}^{-1}$  region. The excellent correlation between the experimental and theoretical spectra demonstrates that the non-covalent interactions are well represented by the applied model despite the correction disparity. These results have highlighted a practical shortcoming of a common semi-empirical method for the modeling of weak forces and emphasizes that care must be exercised for effective use of such corrections in crystalline solids.

**Keywords:** van der Waals forces, low-frequency spectroscopy, far-infrared, crystal packing

## 4.1 Introduction

The intermolecular forces within molecular solids can be investigated by utilizing low-frequency ( $\leq 100 \text{ cm}^{-1}$ ) vibrational spectroscopies such as Raman,<sup>1</sup> terahertz,<sup>2-5</sup> and inelastic neutron scattering.<sup>6</sup> Measurement of the low-frequency motions (e.g. translations and librations) of molecules in crystalline lattices enables the potential energy surfaces governing the molecule-molecule interactions to be mapped since these motions are highly sensitive to the molecular environment in the solid state.<sup>7,8</sup> Knowledge of the vibrational frequencies in this spectral region, and indirectly the force constants associated with the intermolecular forces, positions low-frequency vibrational spectroscopy as an excellent test of computational models for the treatment of weak, non-covalent interactions.<sup>9-12</sup>

In this work, time-domain terahertz spectroscopy has been used to measure the sub-100  $\text{cm}^{-1}$  vibrational spectra of two solid-state amino acids, L-asparagine (ASN) and L-glutamine (GLN), which are then compared to simulated spectra based on solid-state density functional theory (DFT) calculations with semi-empirical London force corrections. These compounds were chosen for their general interest as small biologically-relevant molecules and also for their chemical similarity, with GLN differing from ASN only by the addition of a single methylene group. Given the structural similarities between the molecules, and ability to achieve the same types of intermolecular interactions, the computational requirements for the accurate simulations of the crystalline structures and the vibrational spectra would be anticipated to be the same. However, despite expectations, significant differences were found in the necessary London force corrections for ASN and GLN. The validity and possible origins of this unexpected difference are explored here through a careful investigation of the cohesive energies of the solids.

The use of DFT provides a very powerful method for the investigation of low-frequency motions in molecular solids, yet shortcomings do exist. The most common functionals used in DFT are unable to accurately account for weak non-covalent intermolecular forces.<sup>13</sup> To correct for this, new functionals are always under development<sup>14</sup>, but also explicit electron correlation methods such as periodic MP2 in solids have been reported.<sup>15</sup> While such methods are compelling solutions and show promise for future investigations, they are generally not readily available or they are prohibitively resource intensive (especially explicit correlation methods). The widespread availability and computational efficiency of well-established density functionals, such as that devised by Perdew, Burke, and Ernzerhof (PBE),<sup>16</sup> makes their use common. Semi-empirical London dispersion force corrections, as proposed by Grimme,<sup>17</sup> are an efficient and effective method (though clearly an approximation) for incorporating weak intermolecular forces into calculations utilizing traditional functionals. Such correction models are being actively developed with changes ranging from damping function modifications<sup>18</sup> to the construction of completely different approaches such as XDM<sup>19</sup>, TS-vdW<sup>20</sup>, and dDsC.<sup>21</sup> Yet even with these recent advances, the DFT-D2 approach remains one of the most commonly used formulations due to its availability in common software packages and therefore is the focus of this study.<sup>17</sup>

The use of semi-empirical corrections provides a solution to the deficiency within certain density functionals; however, there are still inconsistencies when it is applied.<sup>11,12</sup> The most commonly altered parameter within the equation for the DFT-D2 correction model<sup>17</sup> is the global scalar ( $s_6$ ),

$$E_{disp} = -s_6 \sum_{i=1}^{N_{at}-1} \sum_{j=i+1}^{N_{at}} \frac{C_6^{ij}}{R_{ij}^6} f_{damp}(R_{ij}), \quad (4.1)$$

which is responsible for scaling the magnitude of the entire correction (all other variables are as defined in Reference 22). The value of the global scalar varies, changing with functional, but is suggested to be 0.75 when using the PBE functional in gas-phase molecular clusters.<sup>17</sup> In practice, this is rarely the optimum value found in solid-state calculations. The exact value is dependent on the functional as expected, but also varies significantly between molecular species and the types of intermolecular forces present in the solids. Examples of this variation can be found in the solid-state DFT simulations of magnesium nitrate hexahydrate ( $s_6 = 0.07$ )<sup>22</sup> compared to naphthalene ( $s_6 = 0.73$ ).<sup>23</sup> The current work explores the use of semi-empirical London force corrections for two structurally similar amino acids, glutamine (GLN) and asparagine (ASN), where such disparity in required London force corrections is not expected. Thus, these molecules serve as an excellent test of the transferability of the semi-empirical London force model between chemically similar solids.

## 4.2 Methods

### 4.2.1 Experimental

Glutamine and asparagine were both purchased from Alfa Aesar and used without further purification beyond being desiccator dried to minimize residual water content. Low-temperature X-ray diffraction data for both amino acids have been previously reported and used for all structural comparisons. The structure of GLN at 130 K by Wagner and Luger indicates that the space group is P 21 21 21, with unit cell dimensions of  $a = 5.1028 \text{ \AA}$ ,  $b = 7.7641 \text{ \AA}$ ,  $c = 15.9878 \text{ \AA}$ , volume =  $633.415 \text{ \AA}^3$ , and  $Z = 4$ .<sup>24</sup> The space group of ASN at 100 K is P 21 with unit cell dimensions of  $a = 5.0622 \text{ \AA}$ ,  $b = 6.7001 \text{ \AA}$ ,  $c = 8.0543 \text{ \AA}$ ,  $\beta = 91.706^\circ$ , volume =  $273.059 \text{ \AA}^3$ , and  $Z = 2$ , as reported by Yamada *et. al.*<sup>25</sup> The single molecules and the crystallographic unit cells of GLN and ASN are shown in **Figures 4-1** and **4-2**, respectively.

A time-domain pulsed terahertz spectrometer based on an amplified Ti:Sapphire femtosecond laser system was used to collect all terahertz experimental data, and has been reported in detail elsewhere.<sup>26</sup> Terahertz radiation was generated by optical rectification and detected using free-space electro-optic sampling, both in zinc telluride crystals.<sup>27,28</sup> Samples of GLN and ASN were mixed with polytetrafluoroethylene (PTFE) powder to concentrations of 1.5% and 1.6% by mass, respectively. To reduce terahertz radiation scattering, the mixtures were pulverized in a stainless steel ball mill to ensure small particle size.<sup>29</sup> The pulverized mixtures were then pressed into pellets (13 mm diameter and 2.2 mm thickness) using approximately 0.55 g of each under a pressure of 2000 psi using a hydraulic press. The blank reference used for the measurements was a pure PTFE pellet of the same dimensions. Samples were held under vacuum in a variable temperature cryostat for room-temperature (293 K) and cryogenic (78 K) data collection. The time-domain terahertz waveforms were captured using a 32 ps scan window consisting of 3200 data points and symmetrically zero-padded to 6000 points. Each individual data set consists of 32 scans averaged to make up the complete set. The waveforms were subjected to Fourier transform using a Hanning window to give a spectral resolution of approximately  $1.0 \text{ cm}^{-1}$ . Taking the ratio of the sample to blank power spectra (Fourier transformed data) result in the terahertz absorption spectra. All terahertz spectra presented here are an average of four individual terahertz absorption spectra. Cubic spline interpolation has been applied for visual clarity, but does not influence the reported peak centers or intensities.

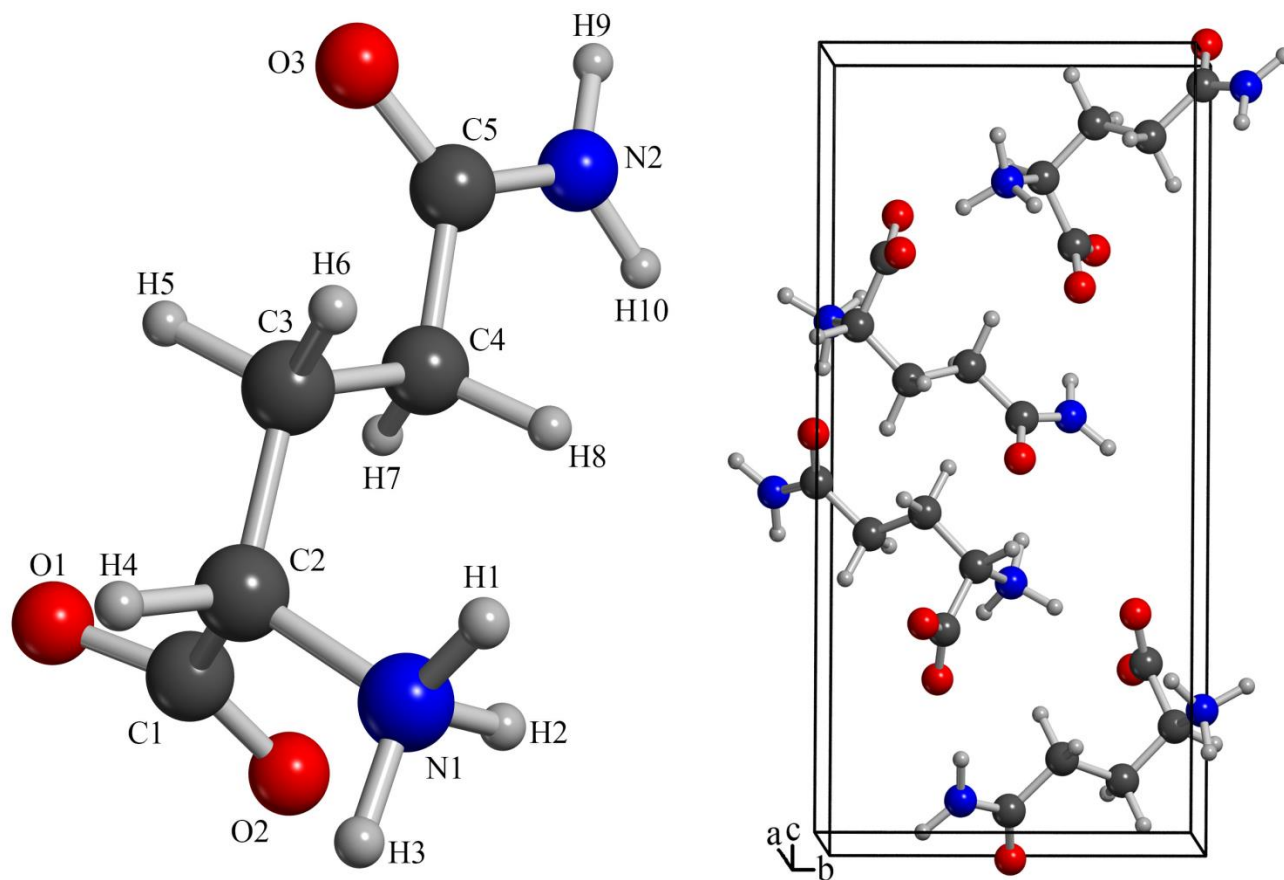


**Figure 4-1.** Labeled glutamine molecule and unit cell.



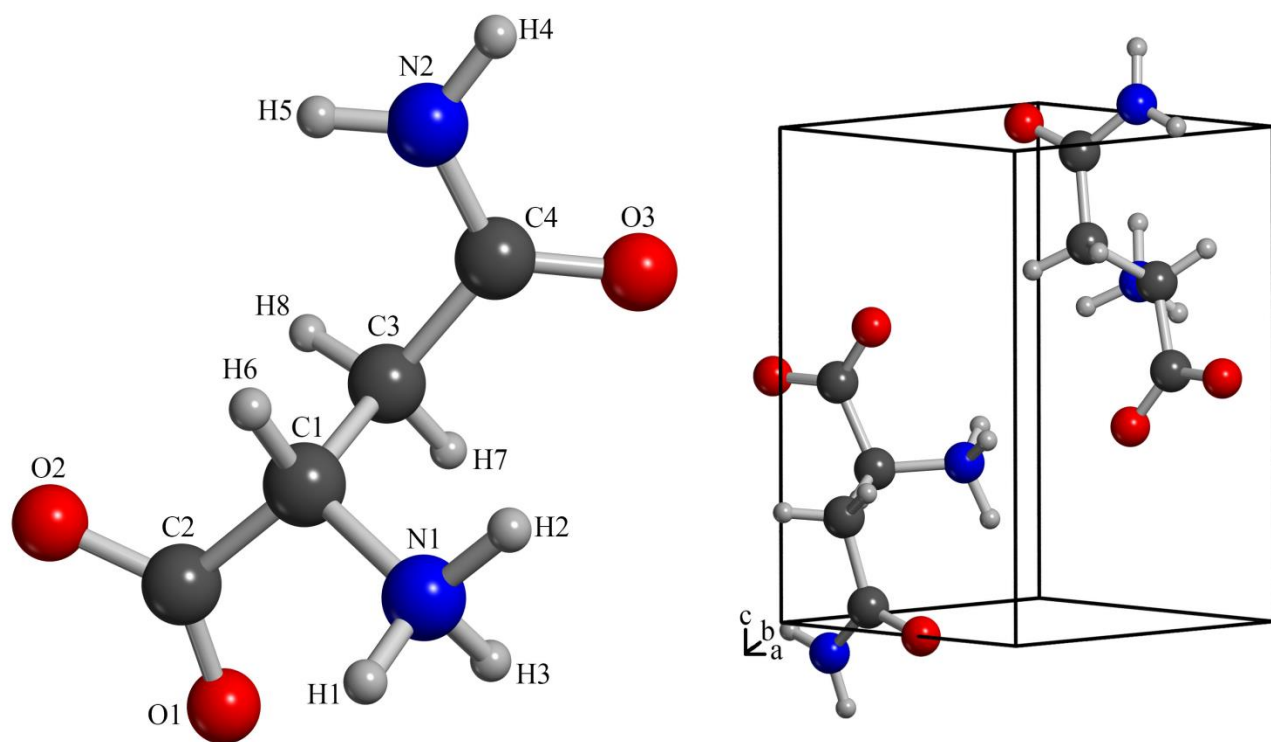


**Figure 4-2.** Labeled asparagine molecule and unit cell.

### 4.2.2 Theoretical

All solid-state DFT calculations were performed using the CRYSTAL09 software package<sup>30</sup> and utilized the PBE density functional<sup>16</sup> with the cc-pVTZ basis set.<sup>31</sup> Corrections for neglect of non-covalent interactions by the PBE functional were applied using the DFT-D2 semi-empirical method<sup>17</sup> with its modification (DFT-D\*) for use in the solid state.<sup>32</sup> As noted, the DFT-D2 method requires the application of a global scalar ( $s_6$ ) to modify the magnitude of the correction based on the particular density functional used.<sup>17</sup> For PBE this is 0.75,<sup>17</sup> but given its observed variability between compounds<sup>11,12</sup> it has been optimized here separately for both ASN and GLN to best reproduce the low-temperature (~100 K) crystallographic unit cell dimensions.

Experimental X-ray crystallographic data was used to create the initial starting geometries in all structural calculations, but all lattice dimensions and atomic positions (with symmetry constraints) were allowed to fully relax during the optimizations. The total energy convergence criterion for geometry optimizations was set to  $\Delta E < 10^{-8}$  hartree. A shrinking factor of 8 (125  $k$  points in the irreducible Brillouin zone) was used in all calculations, based on the sampling and monitoring of the total energy convergence as a function of  $k$ -point count in reciprocal space according to the Pack-Monkhorst method.<sup>33</sup> Truncation tolerances used for Coulomb and HF exchange integral series were set to values of  $10^{-8}$ ,  $10^{-8}$ ,  $10^{-8}$ ,  $10^{-8}$ , and  $10^{-16}$  hartree. The radial and angular distributions were defined by a (75,794) DFT integration grid. Binding energies were calculated using the differences in the total solid-state energy as compared to isolated molecule energies extracted from the bulk. All energies were corrected for basis set superposition error using the counterpoise method.<sup>34</sup>

Normal mode frequencies were calculated within the harmonic approximation by numerical differentiation of the potential energy gradient with respect to atomic position. For

frequency analyses, total energy convergence was set to  $\Delta E < 10^{-10}$  hartree. Infrared intensities were calculated from the dipole moment derivatives ( $d\mu/dQ$ ) determined using the Berry phase approach to calculate the Born charge tensor.<sup>30,35</sup> Spectral intensities are reported in units of  $\epsilon$  ( $M^{-1} \text{ cm}^{-1}$ ) where molarity is expressed in terms of the concentration of crystallographic unit cells.

## 4.3 Results and Discussion

### 4.3.1 Experimental Terahertz Spectra

Experimental terahertz spectra (10 to 95  $\text{cm}^{-1}$ ) of GLN and ASN at both 78 K and 298 K are shown in **Figure 4-3** with the observed frequencies listed in **Table 4-1**.

**Table 4-1.** Experimentally observed frequencies ( $\text{cm}^{-1}$ ) and peak intensities ( $M^{-1} \text{ cm}^{-1}$ ) of GLN and ASN.

GLN				ASN			
298 K		78 K		298 K		78 K	
freq	$\epsilon$	freq	$\epsilon$	freq	$\epsilon$	freq	$\epsilon$
56.7	83.81	59.5	109.27	62.4	32.70	56.8	16.22
75.7	108.58	76.1	131.77	68.7	25.38	64.6	33.31
83.4	104.22	85.2	126.02	87.3	43.34	72.5	24.07
-	-	-	-	-	-	83.9	32.62
-	-	-	-	-	-	90.3	60.04

Both amino acids exhibit terahertz spectra with multiple absorption features that are characteristic of the compound, demonstrating that while they are chemically similar, the

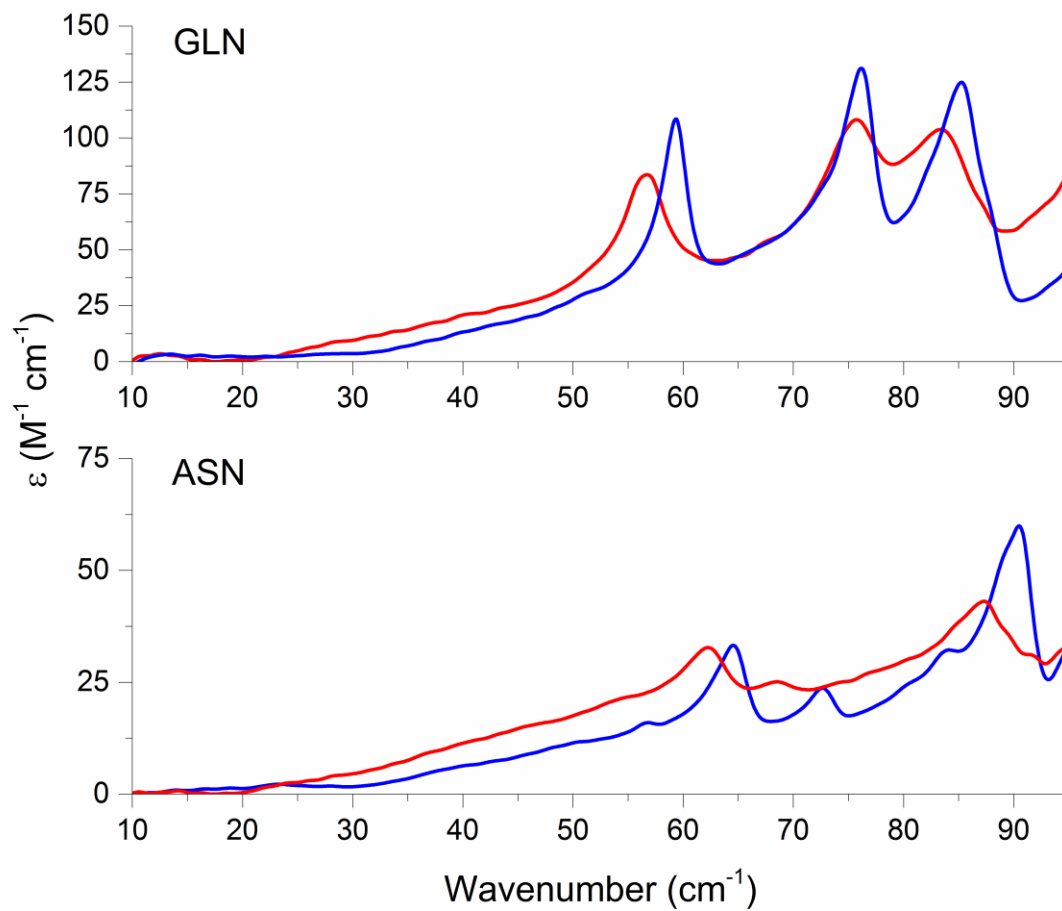


**Figure 4-3.** Terahertz spectra of glutamine (top panel) and asparagine (bottom panel) at 293 K (red) and 78 K (blue).

interactions of the molecules in each solid are unique and thus result in “signature” spectra. The GLN spectrum is consistent with previously reported THz data.<sup>5,36</sup> The 293 K GLN spectrum exhibits three clear absorptions. Upon cooling to 78 K, these features shifted to higher frequency and narrowed, as is common in such spectra. The ASN spectrum, however, is very different from other reported spectra.<sup>5,37</sup> The origin of this discrepancy is that previously reported terahertz spectra are that of the *monohydrate* version of ASN ( $\text{ASN}\cdot\text{H}_2\text{O}$ ),<sup>37</sup> not the anhydrous as studied here. For reference, the  $\text{ASN}\cdot\text{H}_2\text{O}$  THz spectrum is provided in the Supporting Information (**Figure A1**). The 293 K ASN spectrum contains three clear absorptions as well, however once cooled to 78 K, two additional absorptions become apparent. The first is seen as a weak feature at  $56.8\text{ cm}^{-1}$  and the second peak is located at  $83.9\text{ cm}^{-1}$ , appearing as a small feature on the shoulder of the strongest and highest-energy peak in the spectrum. The  $56.8\text{ cm}^{-1}$  absorption in the 78 K ASN spectrum was determined by drying studies to come from a small amount ( $< 2\%$ ) of  $\text{ASN}\cdot\text{H}_2\text{O}$  contamination in the ASN sample and matches the results of Nishizawa, *et al.*<sup>37</sup> Oven drying of the sample reduced its intensity, but the feature could not be entirely eliminated.

The well-resolved features in these terahertz spectra permit the vibrational frequencies to be precisely defined for the motions in the ASN and GLN crystals, facilitating their comparison to DFT-based simulations. The first step in the simulation of the spectra is the accurate calculation of the internal structure of the molecules, as well as their three-dimensional crystal packing.

### 4.3.2 Comparison of Calculated and Experimental Crystal Structures

The global  $s_6$  scalar for the semi-empirical London-type dispersion corrections was optimized separately for both GLN and ASN, with the aim being to minimize the absolute differences in the calculated lattice dimensions ( $a$ ,  $b$ ,  $c$ , and volume) as compared to the

cryogenic X-ray crystallographic data (90 K for ASN and 130 K for GLN). It is important to note that the goal was not simply to use the  $s_6=0.75$  standard, which is based on average performance, but to find the best  $s_6$  for each unique solid. The optimization process was a simple linear search, systematically varying the  $s_6$  value until the minimum average deviation in the lattice parameters between theory and experiment was found. The optimal  $s_6$  values found for GLN and ASN were 0.60 and 0.85, respectively. Investigations of other molecular solids generally have yielded  $s_6$  values close to 0.60, consistently smaller than the standard 0.75 value.<sup>11,38</sup> Thus, the GLN  $s_6$  value is consistent with previous solid-state studies, and the ASN  $s_6$  value is unusually large.

**Table 4-2** lists the signed percent errors in the unit cell dimensions and the overall absolute average percent error in both molecular solids using the optimized  $s_6$  values.

**Table 4-2.** Percent errors in the unit cell parameters of the calculated structures of GLN and ASN using different  $s_6$  values as compared to the experimental X-ray data.

$s_6$	GLN			ASN		
	0.85	0.60	0.00	0.85	0.60	0.00
Volume	-1.841	0.040	5.457	0.003	2.379	8.790
<i>a</i>	-0.838	-0.374	0.849	0.041	0.493	1.548
<i>b</i>	0.422	0.761	1.376	-0.119	1.526	5.989
<i>c</i>	-1.427	-0.342	3.149	0.064	0.312	1.035
$\beta$				-0.394	-0.943	-2.214
Absolute Average Error	1.132	0.379	2.708	0.057	1.177	4.340

In order to test the importance of the differing  $s_6$  values, GLN and ASN were evaluated not only at their own optimal  $s_6$  values, but also were subjected to geometry optimizations at the other's  $s_6$  value. Inspection of these errors, listed in **Table 4-2**, indicates that the crystal structures of the molecular solids are highly dependent on the amount of dispersion force correction applied in the calculations. The overall absolute average error seen in GLN, by using the 0.60 and 0.85 scalars, change by a factor of  $\sim 3$ . An even larger difference ( $\sim x21$ ) was

observed for ASN, with the only change being the  $s_6$  value used. Extrapolating these calculations to no London force correction at all (an effective  $s_6$  of 0.00) shows that both solids do need this additional attractive interaction to arrive at reasonable simulated structures, but ASN (volume increase of 8.789%) is more sensitive than GLN (volume increase of 5.457%).

The external unit cell parameters of the two molecular solids clearly indicate the ability of the simulations to accurately recreate the general packing of the materials. That noted, it is also important to evaluate the atomic-level accuracy of the DFT-derived crystal structures. To assess this, root-mean-squared deviations (RMSDs) of the bond lengths, bond angles, and dihedral angles were determined by comparison to experimental X-ray crystallographic data (**Table 4-3**).

**Table 4-3.** Evaluation of RMSDs in bond lengths, bond angles, and bond dihedral angles in the calculated structures of GLN<sup>1</sup> and ASN<sup>2</sup> as compared to X-ray diffraction data, at different  $s_6$  values. .

	GLN		ASN	
$s_6$	0.85	0.60	0.85	0.60
Bond Length (Å)	0.002	0.002	0.003	0.003
Bond Angles (°)	0.15	0.15	0.18	0.23
Dihedral Angles (°)	0.64	0.64	0.489	0.74

The RMSD values are based only on non-hydrogen atoms and were calculated for each molecule at both of the optimal  $s_6$  values. In both GLN and ASN, the bond length RMSDs were equal for the different  $s_6$  values revealing it had no effect on the reproduction of the internal bond lengths. This is expected based on the distance dependence of the semi-empirical correction. For GLN, there is essentially no variation in the RMSDs for bond angles or dihedral angles. While the internal structure of GLN is independent of applied  $s_6$ , the ASN bond angle and dihedral angle RMSDs show a small change between the two  $s_6$  values, but the differences are negligible. The

structures of both GLN and ASN are well modeled, regardless of the magnitude of the London force correction. The fact that ASN shows any changes at all in internal structure is likely related to its requirement for an unusually large dispersion correction.

In addition to these internal parameters, the heavy-atom hydrogen bond separations were also evaluated (**Table 4-4**). In the case of GLN, the hydrogen bond distances are well represented with the absolute average error (0.399%) being the lowest when using the optimal  $s_6$  value (0.60). However when ASN is considered, a different error pattern is encountered. The lowest error is seen in the  $s_6 = 0.60$  structure (0.810%), which is closely followed by the  $s_6 = 0.00$  structure (0.875%). At the optimal  $s_6$  value (0.85), the error in the hydrogen bond distances is noticeably higher (1.176%) than the other two structures. This unexpected trend originates from one poorly represented hydrogen bond (N1-H2•••O3) within the structure that is predicted to be much shorter (by 0.077 Å or 2.65%) than the X-ray crystallographic value. Ignoring this one bond drops the error by a factor of two, to normal levels (0.646%). The origin of this behavior in only one of the many hydrogen bonds in these solids is likely due to an error in the crystallographic data file.



**Table 4-4.** Heavy-atom hydrogen bond separations (Å), signed percent errors in separations (%), and absolute average percent errors (%) of the heavy-atom hydrogen bond separations at varying  $s_6$  values for GLN and ASN. Experimental data for GLN and ASN used for comparison.

GLN H-bond	Exp distance	$s_6=0.00$		$s_6=0.60$		$s_6=0.85$	
		distance	% error	distance	% error	distance	% error
O1•••N1	2.768	2.783	0.542	2.750	-0.650	2.733	-1.264
O1•••N1	2.846	2.889	1.511	2.833	-0.457	2.812	-1.195
O2•••N2	2.898	2.971	2.519	2.898	0.000	2.874	-0.828
N1•••O1	2.768	2.783	0.542	2.750	-0.650	2.733	-1.264
N1•••O1	2.846	2.889	1.511	2.833	-0.457	2.812	-1.195
N1•••O3	2.919	3.104	6.338	2.922	0.103	2.879	-1.370
O3•••N1	2.919	3.104	6.338	2.922	0.103	2.879	-1.370
O3•••N2	2.931	2.918	-0.444	2.908	-0.785	2.899	-1.092
N2•••O3	2.931	2.918	-0.444	2.908	-0.785	2.899	-1.092
N2•••O2	2.898	2.971	2.519	2.898	0.000	2.874	-0.828
Absolute Average Percent Error			2.271		0.399		1.150

ASN H-bond	Exp distance	$s_6=0.00$		$s_6=0.60$		$s_6=0.85$	
		distance	% error	distance	% error	distance	% error
O1•••N1	2.807	2.816	0.321	2.796	-0.392	2.780	-0.962
O1•••N1	2.741	2.772	1.131	2.724	-0.620	2.714	-0.985
O2•••N2	2.846	2.856	0.351	2.831	-0.527	2.826	-0.703
N1•••O1	2.741	2.772	1.131	2.724	-0.620	2.714	-0.985
N1•••O1	2.807	2.816	0.321	2.796	-0.392	2.780	-0.962
N1•••O3	2.908	2.879	-0.997	2.839	-2.373	2.831	-2.648
O3•••N2	2.921	2.967	1.575	2.917	-0.137	2.904	-0.582
O3•••N1	2.908	2.879	-0.997	2.839	-2.373	2.831	-2.648
N2•••O2	2.846	2.856	0.351	2.831	-0.527	2.826	-0.703
N2•••O3	2.921	2.967	1.575	2.917	-0.137	2.904	-0.582
Absolute Average Error			0.875		0.810		1.176

### 4.3.3 Comparison of Calculated and Experimental Terahertz Spectra

For both GLN and ASN, the use of solid-state DFT calculations with the DFT-D\* semi-empirical London-type dispersion force corrections and appropriate  $s_6$  scalars, provided reliable structures and simulated THz spectra. Simulated THz spectra for both GLN and ASN were compared to the 78 K experimental data and are shown in **Figures 4-4** and **4-5**, respectively.

**Table 4-5** lists the IR-active mode frequencies, intensities, and symmetries for GLN and ASN in the  $\leq 100 \text{ cm}^{-1}$  region.

**Table 4-5.** Calculated IR-active mode frequencies ( $\text{cm}^{-1}$ ), intensities ( $\text{km mol}^{-1}$ ) and symmetries for GLN and ASN below  $100 \text{ cm}^{-1}$ . No frequency scalars have been applied.

GLN			ASN		
freq	intens	symm	freq	intens	symm
60.1	8.78	B1	68.7	1.78	A
70.1	0.17	B3	75.7	1.64	A
76.5	11.26	B2	90.0	1.96	B
77.0	19.13	B1	99.0	6.29	A
82.7	0.17	B3	-	-	-
83.4	12.31	B2	-	-	-
85.1	0.45	B2	-	-	-
89.2	4.74	B1	-	-	-
100.1	4.39	B1	-	-	-

Spectral absorption units ( $\text{M}^{-1} \text{ cm}^{-1}$ ) are calculated from the theoretical units ( $\text{km mol}^{-1}$ ) using Lorentzian line shapes with full width half-maximum (FWHM) values empirically determined by least-squares fitting of the experimental spectra. The FWHM values were  $3.7 \text{ cm}^{-1}$  for GLN and  $4.4 \text{ cm}^{-1}$  for ASN. Specific assignment and mode descriptions are provided in **Table 4-6**.

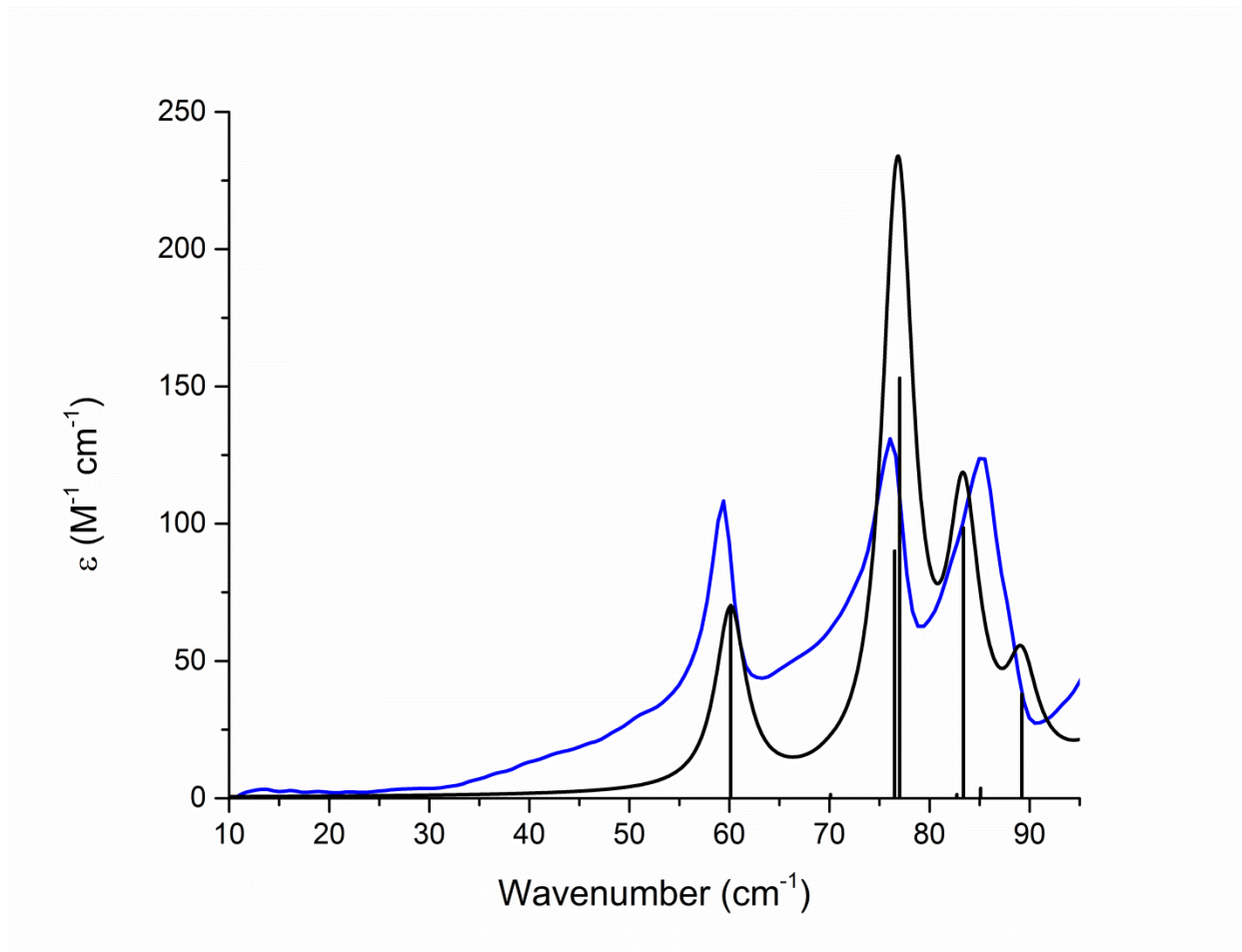


**Figure 4-4.** Terahertz spectrum of glutamine at 78 K compared to the theoretical spectrum generated using PBE/cc-pVTZ with DFT-D\* dispersion corrections.

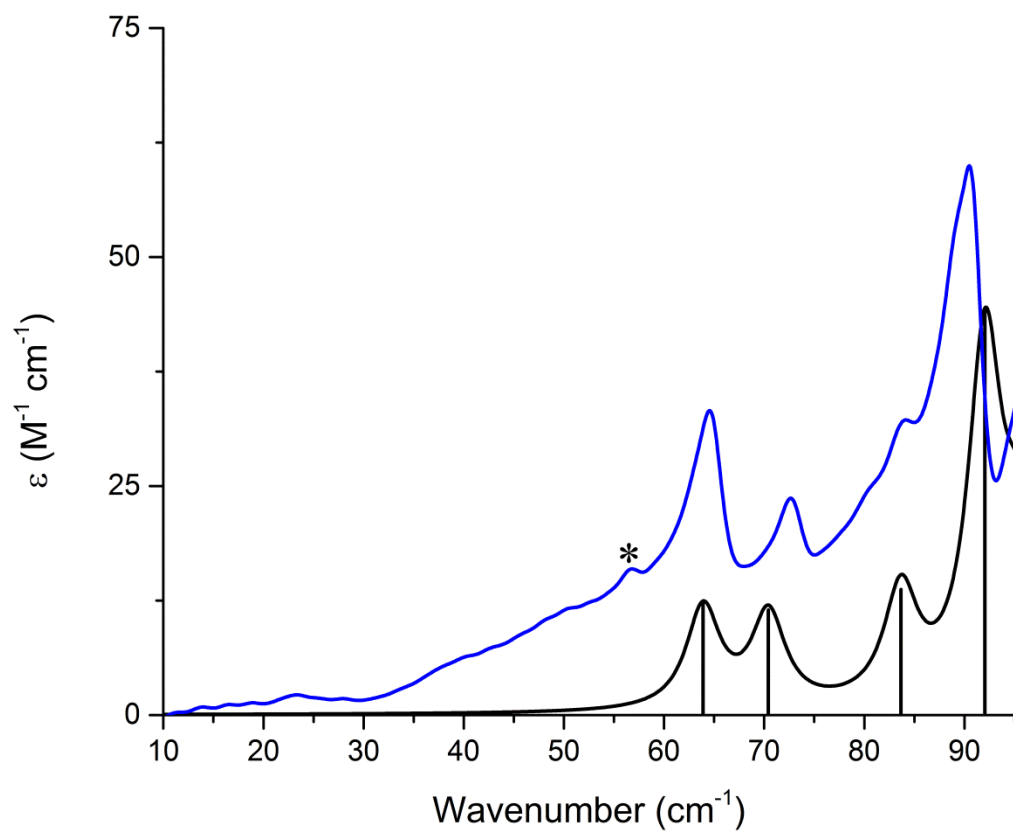


**Figure 4-5.** Terahertz spectrum of asparagine at 78 K compared to the theoretical spectrum generated using PBE/cc-pVTZ with DFT-D\* dispersion corrections.

**Table 4-6.** Assignment of the experimental THz absorptions and descriptions of the motions in GLN and ASN. The ASN frequencies have been scaled by 0.93. See text for details.

GLN				ASN			
exp freq	calc freq	symm	mode description	exp freq	calc freq	symm	mode description
59.5	60.1	B1	ET along <i>a</i>	64.6	63.9	A	ER along <i>c</i>
76.1	76.5	B2	ER about <i>a</i>	72.5	70.4	A	ER along <i>a</i>
76.1	77.0	B1	ET along <i>b</i>	83.9	83.7	B	torsion
85.2	83.4	B2	ET along <i>c</i>	90.3	92.0	A	ER along <i>b</i>

\* ET = external translation, ER = external rotation

The GLN simulation yields eight absorptions in the  $\leq 90 \text{ cm}^{-1}$  region, five of which are sufficiently intense to be readily detected experimentally. However, there are only three distinct absorptions seen in the measured GLN spectrum. The calculated absorption at  $60.1 \text{ cm}^{-1}$  corresponds to the experimental peak at  $59.5 \text{ cm}^{-1}$ , matching in both position and intensity. The strongest feature in the experimental spectrum at  $76.1 \text{ cm}^{-1}$  consists of a combination of two peaks in the simulated spectrum at  $76.5 \text{ cm}^{-1}$  and  $77.0 \text{ cm}^{-1}$ . The overlap of the two absorptions causes the predicted intensity of that frequency to become much larger than the experimentally observed intensity (though it is not clear if one or both normal mode infrared intensities are overestimated). The final peak seen in the experimental spectrum is located at  $85.2 \text{ cm}^{-1}$  and has a corresponding peak in the theoretical spectrum at  $83.4 \text{ cm}^{-1}$ , with good intensity agreement. This third experimental peak is rather broad, suggesting the possibility of an underlying unresolved absorption that could arise from the predicted peak at  $89.2 \text{ cm}^{-1}$ .

In the case of ASN, an initial comparison of the experiment and simulation lead to the conclusion that the raw calculated spectrum provided a relatively poor reproduction of the experimental data. Application of a frequency scalar (0.93) to the predicted vibrational spectrum greatly improved the correlation between theory and experiment. A scalar of 0.93 suggests that the ASN calculation has produced potential energy surfaces for the low-frequency motions with too steep a curvature, since such surfaces will result in overestimated vibrational frequencies. So

while the ASN structure is well done with the large  $s_6 = 0.85$ , the curvature of the potential energy surfaces are not well simulated. In contrast, the GLN simulation has both accurate potential energy minima and surface curvature, yielding good structure and frequencies.

A scalar of less than 1.0 suggests that the vibrations found in crystalline ASN are significantly more anharmonic than those of GLN. The anharmonicity of solid-state ASN is supported by the unit cell volume contraction (related to the Grüneisen parameter<sup>39</sup>) observed between X-ray diffraction measurements of the crystallographic unit cell parameters performed at 293 K and 100 K (**Figure A2**). Difficulties in the crystallization of large single crystals of ASN prevented single-crystal X-ray data to be collected, so room-temperature powder X-ray diffraction was utilized to determine its unit cell dimensions at 293 K. The GSAS-II program<sup>40</sup> was used to analyze the powder data and produced unit cell dimensions of  $a = 5.06406 \text{ \AA}$ ,  $b = 6.79640 \text{ \AA}$ ,  $c = 8.08960 \text{ \AA}$ ,  $\beta = 91.279^\circ$ , and volume =  $278.35 \text{ \AA}^3$ . Given these values, the volume shrink for ASN from room temperature to 100 K<sup>25</sup> was found to be 1.9%. This reduction in unit cell volume indicates that the ASN crystal does indeed exhibit greater anharmonicity as compared to GLN, which only shows a 0.49% contraction over nearly the same temperature interval.<sup>24,41</sup>

Five distinct features were seen in the ASN experimental spectrum, but only four infrared-active vibrations were simulated in this region. As noted, the first small peak observed at  $56.8 \text{ cm}^{-1}$  arises from  $\text{ASN}\cdot\text{H}_2\text{O}$  contamination and therefore can be ignored (**Figure A1**). The theoretical peak positions discussed here are those scaled by the 0.93 frequency scalar. The first peak seen in the experimental spectrum of ASN is located at  $64.6 \text{ cm}^{-1}$  and its corresponding theoretical peak is predicted at  $63.9 \text{ cm}^{-1}$ . The next absorption is located at  $72.5 \text{ cm}^{-1}$  in the experiment and is assigned to the  $70.4 \text{ cm}^{-1}$  mode in the simulation. The final two peaks, are

located at 83.9 cm<sup>-1</sup> (shoulder) and 90.3 cm<sup>-1</sup>, with the theoretical assigned peaks found at 83.7 cm<sup>-1</sup> and 92.0 cm<sup>-1</sup>.

#### 4.3.4 Evaluation of Solid-State Cohesive Energies

Due to the unexpectedly large difference in the  $s_6$  values between ASN and GLN, the energies associated with the molecular solids were investigated in more detail. **Table 4-7** lists the semi-empirical dispersion correction energies and total cohesive (binding) energies per molecule in both GLN and ASN, at each  $s_6$  value used.

**Table 4-7.** Calculated (kJ mol<sup>-1</sup>, per molecule) dispersion correction energy and cohesive energy for crystalline GLN and ASN, using different  $s_6$  values for the semi-empirical London force correction.

$s_6$	GLN		ASN	
	0.85	0.60	0.85	0.60
Dispersion Correction Energy	-89.74	-61.10	-76.72	-51.87
Cohesive Energy	-339.58	-312.99	-333.40	-311.66

The cohesive energies have been corrected for basis set superposition errors. Comparing the energetic results for these solids, each at the same  $s_6$  value, shows that the cohesive energies are consistent. At an  $s_6$  value of 0.85 for both GLN and ASN, the cohesive energy difference is 6.18 kJ mol<sup>-1</sup> (1.84% of the average cohesive energy) and with  $s_6 = 0.60$ , the difference is even smaller at only 1.33 kJ mol<sup>-1</sup> (0.43% of the average cohesive energy). The results at each molecule's optimal  $s_6$  values resulted in a difference of 20.41 kJ mol<sup>-1</sup> (6.32% of the average cohesive energy). This relatively small difference was somewhat surprising, especially considering the large difference in  $s_6$  value that was needed to generate the optimized structures. However, based on the ten hydrogen found in each molecular solid (likely the driving forces in

determining the packing arrangement), the small cohesive energy difference between these crystalline amino acids is reasonable.

To aid in evaluating the validity of the total (including the semi-empirical corrections) solid-state cohesive energies, MP2/cc-pVTZ calculations<sup>31,42</sup> were carried out on both ASN and GLN gas-phase clusters utilizing rigid structures extracted from the geometry-optimized solid-state simulations for each. These clusters consisted of one central molecule completely surrounded by the minimum number of neighboring molecules within van der Waals radii contact. For both ASN and GLN, this was 13 (1+12) total molecules. The MP2 and DFT-D\* results are remarkably consistent. For ASN (based on  $s_6 = 0.85$ ), the DFT and MP2 cohesive energies are -333.40 kJ/mol and -335.14 kJ/mol, respectively. Similar results were found for GLN (based on  $s_6 = 0.60$ ) with cohesive energies of -312.99 kJ/mol (DFT) and -317.27 kJ/mol (MP2). The excellent agreement between the two fundamentally different intermolecular energy calculations reveals that the disparate  $s_6$  values determined in the DFT-D\* model tuning are in fact correct and meaningful. While it may be expected that the  $s_6$  values would be the same for the chemically similar ASN and GLN samples, these results have demonstrated that the actual best performing  $s_6$  is unique to each solid.

The chemical origins of this significant deviation in  $s_6$  are likely tied to the packing efficiency differences between the two species, with ASN having a density of 1.606 g/cm<sup>3</sup> and GLN being lower at 1.531 g/cm<sup>3</sup>, providing greater opportunity for stronger non-covalent intermolecular interactions to occur in ASN. The greater density may also lead to a situation where exact exchange plays a greater role in the calculations. This possibility was tested using the hybrid PBE0 density functional,<sup>43</sup> but the same trend in London force corrections was found, indicating that exchange treatment is not the source of this observed disparity. Other potential



sources for the differences could be the lack of higher-order pairwise dispersion corrections<sup>44</sup> or many-body dispersion (MBD) effects such as those that have been reported in polymorphs of glycine.<sup>45</sup> Regardless of the origins of this variation in  $s_6$  parameter between similar molecular solids, it highlights a potential problem in the application of semi-empirical London force corrections. Care should be taken when comparing energetic data of different solids and may even be an issue when comparing the relative energies of crystalline polymorphs of a single substance.<sup>46</sup>

#### 4.4 Conclusions

The standard implementation of the DFT-D2 (DFT-D\* in solids) semi-empirical correction method for accounting for London-type dispersion forces was tested through comparison of the structurally similar ASN and GLN molecules in the crystalline solid state. Terahertz spectra (10 to 95  $\text{cm}^{-1}$ ) and X-ray crystallographically determined structures of GLN and ASN were used as benchmarks for the evaluation of the correction model to accurately determine both the minima and the curvature of the potential energy surfaces governing the intermolecular interactions. Initial expectations suggested that the same global London force scalar ( $s_6$ ) would be applicable to both molecules. The investigation proved that specific customizations of the correction model to each molecule were necessary in the solid-state DFT simulations in order to successfully recreate the experimental observations. For each of the compounds, a unique  $s_6$  value was determined and used to generate high-quality crystal structures and terahertz spectra. The results reveal that while ASN and GLN are chemically similar, the required London force correction needed was 42% greater in ASN versus GLN, a value supported by explicit electron correlation calculations. Overall, these findings show that semi-empirical corrections to solid-state DFT simulations are valuable and enable accurate

simulations of molecular crystals to be achieved. However, when utilizing such models, their performance must be carefully evaluated for each individual crystalline system being considered.

#### **4.5 Supporting Information**

Structural RMSDs as compared to experimental values at different  $s_6$  values, hydrogen bond distances and errors, and powder X-ray diffraction data of ASN. This material is available free of charge via the Internet at <http://pubs.acs.org>. This information is located in Appendix A.

#### **4.6 Acknowledgements**

This research was funded by a grant from the National Science Foundation CAREER Program (CHE-0847405). They also thank Syracuse University for its continued support.

## 4.7 References

- (1) Hédoux, A.; Paccou, L.; Guinet, Y.; Willart, J.-F.; Descamps, M. Using the Low-Frequency Raman Spectroscopy to Analyze the Crystallization of Amorphous Indomethacin. *Eur. J. Pharm. Sci.* **2009**, *38*, 156-164.
- (2) Ueno, Y.; Rungsawang, R.; Tomita, I.; Ajito, K. Quantitative Measurements of Amino Acids by Terahertz Time-Domain Transmission Spectroscopy. *Anal. Chem.* **2006**, *78*, 5424-5428.
- (3) Shen, Y.-C. Terahertz Pulsed Spectroscopy and Imaging for Pharmaceutical Applications: A Review. *Int. J. Pharm.* **2011**, *417*, 48-60.
- (4) Leahy-Hoppa, M.; Fitch, M.; Osiander, R. Terahertz Spectroscopy Techniques for Explosives Detection. *Anal. Bioanal. Chem.* **2009**, *395*, 247-257.
- (5) Nishizawa, J.; Sasaki, T.; Suto, K.; Tanabe, T.; Yoshida, T.; Kimura, T.; Saito, K. Frequency-Tunable Terahertz-Wave Generation from Gap Using Cr:Forsterite Lasers. *Int J Infrared Milli Waves* **2006**, *27*, 923-929.
- (6) Parker, S. F.; Haris, P. I. Inelastic Neutron Scattering Spectroscopy of Amino Acids. *Spectrosc-Int. J.* **2008**, *22*, 297-307.
- (7) Beard, M. C.; Turner, G. M.; Schmuttenmaer, C. A. Terahertz Spectroscopy. *J. Phys. Chem. B* **2002**, *106*, 7146-7159.
- (8) Jepsen, P. U.; Cooke, D. G.; Koch, M. Terahertz Spectroscopy and Imaging – Modern Techniques and Applications. *Laser Photonics Rev* **2011**, *5*, 124-166.
- (9) Klimeš, J.; Bowler, D. R.; Angelos, M. Chemical Accuracy for the Van Der Waals Density Functional. *J. Phys.: Condens. Matter* **2010**, *22*, 022201/022201-022205.
- (10) Vydrov, O. A.; Van Voorhis, T. Nonlocal Van Der Waals Density Functional Made Simple. *Phys. Rev. Lett.* **2009**, *103*, 063004/063001-063004.
- (11) Juliano, T. R., Jr.; King, M. D.; Korter, T. M. Evaluating London Dispersion Force Corrections in Crystalline Nitroguanidine by Terahertz Spectroscopy. *IEEE Trans. on THz. Sci. and Tech.* **2013**, *3*, 281-287.
- (12) Juliano, T. R.; Korter, T. M. Terahertz Vibrations of Crystalline Acyclic and Cyclic Diglycine: Benchmarks for London Force Correction Models. *J. Phys. Chem. A* **2013**, *117*, 10504-10512.
- (13) Grimme, S. Density Functional Theory with London Dispersion Corrections. *WIREs: Comp. Mole. Sci.* **2011**, *1*, 211-228.
- (14) Zhao, Y.; Truhlar, D. G. Density Functionals with Broad Applicability in Chemistry. *Acc. Chem. Res.* **2008**, *41*, 157-167.
- (15) Pisani, C.; Schutz, M.; Casassa, S.; Usvyat, D.; Maschio, L.; Lorenz, M.; Erba, A. Cryscor: A Program for the Post-Hartree-Fock Treatment of Periodic Systems. *PCCP* **2012**, *14*, 7615-7628.
- (16) Perdew, J. P.; Burke, K.; Ernzerhof, M. Generalized Gradient Approximation Made Simple [Phys. Rev. Lett. 77, 3865 (1996)]. *Phys. Rev. Lett.* **1997**, *78*, 1396-1396.
- (17) Grimme, S. Semiempirical Gga-Type Density Functional Constructed with a Long-Range Dispersion Correction. *J. Comput. Chem.* **2006**, *27*, 1787-1799.
- (18) Grimme, S.; Ehrlich, S.; Goerigk, L. Effect of the Damping Function in Dispersion Corrected Density Functional Theory. *J. Comput. Chem.* **2011**, *32*, 1456-1465.

- (19) Becke, A. D.; Johnson, E. R. A Density-Functional Model of the Dispersion Interaction. *J. Chem. Phys.* **2005**, *123*, -.
- (20) Tkatchenko, A.; Scheffler, M. Accurate Molecular van der Waals Interactions from Ground-State Electron Density and Free-Atom Reference Data. *Phys. Rev. Lett.* **2009**, *102*, 073005.
- (21) Steinmann, S. N.; Corminboeuf, C. Comprehensive Benchmarking of a Density-Dependent Dispersion Correction. *J. Chem. Theor. and Comp.* **2011**, *7*, 3567-3577.
- (22) Witko, E. M.; Buchanan, W. D.; Korter, T. M. The Importance of London Dispersion Forces in Crystalline Magnesium Nitrate Hexahydrate. *Inorg. Chim. Acta* **2012**, *389*, 176-182.
- (23) King, M. D.; Korter, T. M. Modified Corrections for London Forces in Solid-State Density Functional Theory Calculations of Structure and Lattice Dynamics of Molecular Crystals. *J. Phys. Chem. A* **2012**, *116*, 6927-6934.
- (24) Wagner, A.; Luger, P. Charge Density and Topological Analysis of L-Glutamine. *J. Mol. Struct.* **2001**, *595*, 39-46.
- (25) Yamada, K.; Hashizume, D.; Shimizu, T.; Yokoyama, S. L-Asparagine. *Acta Crystallogr. Sect. E* **2007**, *63*, o3802-o3803.
- (26) Hakey, P. M.; Allis, D. G.; Ouellette, W.; Korter, T. M. Cryogenic Terahertz Spectrum of (+)-Methamphetamine Hydrochloride and Assignment Using Solid-State Density Functional Theory. *J. Phys. Chem. A* **2009**, *113*, 5119-5127.
- (27) Wu, Q.; Litz, M.; Zhang, X. C. Broadband Detection Capability of ZnTe Electro-Optic Field Detectors. *Appl. Phys. Lett.* **1996**, *68*, 2924-2926.
- (28) Rice, A.; Jin, Y.; Ma, X. F.; Zhang, X. C.; Bliss, D.; Larkin, J.; Alexander, M. Terahertz Optical Rectification from <110> Zinc-Blende Crystals. *Appl. Phys. Lett.* **1994**, *64*, 1324-1326.
- (29) Shen, Y. C.; Taday, P. F.; Pepper, M. Elimination of Scattering Effects in Spectral Measurement of Granulated Materials Using Terahertz Pulsed Spectroscopy. *Appl. Phys. Lett.* **2008**, *92*, 051103-051103.
- (30) Dovesi, R.; Saunders, V. R.; Roetti, C.; Orlando, R.; Zicovich-Wilson, C. M.; Pascale, F.; Civalleri, B.; Doll, K.; Harrison, N. M.; Bush, I. J.; D'Arco, P.; Llunell, M.; Torino, U. o. T. *CRYSTAL09 User's Manual* **2009**.
- (31) Dunning, T. H. Gaussian Basis Sets for Use in Correlated Molecular Calculations. I. The Atoms Boron through Neon and Hydrogen. *J. Chem. Phys.* **1989**, *90*, 1007-1024.
- (32) Civalleri, B.; Zicovich-Wilson, C. M.; Valenzano, L.; Ugliengo, P. B3LYP Augmented with an Empirical Dispersion Term (B3LYP-D\*) as Applied to Molecular Crystals. *CrystEngComm* **2008**, *10*, 405-410.
- (33) Monkhorst, H. J.; Pack, J. D. Special Points for Brillouin-Zone Integrations. *Phys. Rev. B: Condens. Matter* **1976**, *13*, 5188-5192.
- (34) Boys, S. F.; Bernardi, F. The Calculation of Small Molecular Interactions by the Differences of Separate Total Energies. Some Procedures with Reduced Errors. *Mol. Phys.* **1970**, *19*, 553-566.
- (35) Dall'Olivo, S.; Dovesi, R.; Resta, R. Spontaneous Polarization as a Berry Phase of the Hartree-Fock Wave Function: The Case of KNbO<sub>3</sub>. *Phys. Rev. B: Condens. Matter* **1997**, *56*, 10105-10114.
- (36) Wang, W.-N.; Wang, G.; Zhang, Y. Low-Frequency Vibrational Modes of Glutamine. *Chin. Phys. B* **2011**, *20*, 123301.

- (37) Nishizawa, J.-i.; Tanno, T.; Yoshida, T.; Suto, K. Consequence of a Defect on the Terahertz Spectra of L-Asparagine Monohydrate. *Chem. Lett.* **2007**, *36*, 134-135.
- (38) King, M. D.; Ouellette, W.; Korter, T. M. Noncovalent Interactions in Paired DNA Nucleobases Investigated by Terahertz Spectroscopy and Solid-State Density Functional Theory. *J. Phys. Chem. A* **2011**, *115*, 9467-9478.
- (39) Barron, T. H. K. Vibrational Effects in the Thermal Expansion of Noncubic Solids. *J. Appl. Phys.* **1970**, *41*, 5044-5050.
- (40) Toby, B. H.; Von Dreele, R. B. GSAS-II: The Genesis of a Modern Open-Source All Purpose Crystallography Software Package. *J. Appl. Crystallogr.* **2013**, *46*, 544-549.
- (41) Koetzle, T. F.; Frey, M. N.; Lehmann, M. S.; Hamilton, W. C. Precision Neutron Diffraction Structure Determination of Protein and Nucleic Acid Components. XIII. Molecular and Crystal Structure of the Amino Acid L-Glutamine. *Acta Crystallogr. Sect. B* **1973**, *29*, 2571-2575.
- (42) Frisch, M. J.; Trucks, G. W.; Schlegel, H. B.; Scuseria, G. E.; Robb, M. A.; Cheeseman, J. R.; Scalmani, G.; Barone, V.; Mennucci, B.; Petersson, G. A.; Nakatsuji, H.; Caricato, M.; Li, X.; Hratchian, H. P.; Izmaylov, A. F.; Bloino, J.; G. Zheng; Sonnenberg, J. L.; Hada, M.; Ehara, M.; Toyota, K.; Fukuda, R.; Hasegawa, J.; Ishida, M.; Nakajima, T.; Honda, Y.; Kitao, O.; Nakai, H.; Vreven, T.; J. A. Montgomery, J.; Peralta, J. E.; Ogliaro, F.; Bearpark, M.; Heyd, J. J.; Brothers, E.; Kudin, K. N.; Staroverov, V. N.; Kobayashi, R.; Normand, J.; Raghavachari, K.; Rendell, A.; Burant, J. C.; Iyengar, S. S.; Tomasi, J.; Cossi, M.; Rega, N.; Millam, J. M.; Klene, M.; Knox, J. E.; Cross, J. B.; Bakken, V.; Adamo, C.; Jaramillo, J.; Gomperts, R.; Stratmann, R. E.; Yazyev, O.; Austin, A. J.; Cammi, R.; Pomelli, C.; Ochterski, J.; Martin, R. L.; Morokuma, K.; Zakrzewski, V. G.; Voth, G. A.; Salvador, P.; Dannenberg, J. J.; Dapprich, S.; Daniels, A. D.; Farkas, O.; Foresman, J. B.; Ortiz, J. V.; Cioslowski, J.; Fox, D. J. *GAUSSIAN 09* **2009**, *Guassian, Inc., Wallingford, CT.*
- (43) Adamo, C.; Barone, V. Toward Reliable Density Functional Methods without Adjustable Parameters: The PBE0 Model. *J. Chem. Phys.* **1999**, *110*, 6158-6170.
- (44) Johnson, E. R.; Becke, A. D. A Post-Hartree-Fock Model of Intermolecular Interactions: Inclusion of Higher-Order Corrections. *J. Chem. Phys.* **2006**, *124*.
- (45) Marom, N.; DiStasio, R. A.; Atalla, V.; Levchenko, S.; Reilly, A. M.; Chelikowsky, J. R.; Leiserowitz, L.; Tkatchenko, A. Many-Body Dispersion Interactions in Molecular Crystal Polymorphism. *Angew. Chem. Int. Ed.* **2013**, *52*, 6629-6632.
- (46) Delaney, S. P.; Pan, D.; Yin, S. X.; Smith, T. M.; Korter, T. M. Evaluating the Roles of Conformational Strain and Cohesive Binding in Crystalline Polymorphs of Aripiprazole. *Cryst. Growth Des.* **2013**, *13*, 2943-2952.

## CHAPTER 5. Origins of Hydration Differences in Homochiral and Racemic Molecular Crystals

The material contained within this chapter has been formatted for submission to *The Journal of Physical Chemistry A*. (Juliano, T. R.; Korter, T. M. J. *Phys. Chem.* **2014**. In Preparation.)

### Abstract

The propensity for crystalline hydrates of organic molecules to form is related to the strength of the interactions between molecules, including the chiral composition of the molecular solids. Specifically, homochiral versus racemic crystalline samples can exhibit distinct differences in their ability to form energetically stable hydrates. The focus of the current study is a comparison of the crystal structures and intermolecular forces found in solid-state L-aspartic acid, DL-aspartic acid, and L-aspartic acid monohydrate. The absence of experimental evidence for the DL-aspartic acid monohydrate is considered here in terms of the enhanced thermodynamic stability of the DL-aspartic acid anhydrate crystal as compared to the L-aspartic acid anhydrate as revealed through solid-state density functional theory calculations and terahertz spectroscopic measurements. The results indicate that anhydrous DL-aspartic acid is the more stable solid, not due to intermolecular forces alone, but also due to the improved conformations of the molecules within the racemic solid. A hemihydrated and monohydrated form of DL-aspartic acid have been computationally evaluated and in each case the hydrates produce destabilized aspartic acid conformations that prevent DL-aspartic acid hydrate formation.

**Keywords:** far-infrared, London dispersion, hydrogen bonding, solvatomorphs

## 5.1 Introduction

Organic crystals often incorporate solvent molecules, such as water, into their crystal structures.<sup>1</sup> The ability to determine if and how solvates are formed is crucial in understanding the overall properties of a molecular crystal. This hydration phenomenon is widespread and has been singled out as a potential pitfall in the crystal engineering of optimized solid-state pharmaceuticals.<sup>2</sup> Many techniques exist that are able to determine the presence of a solvate, such as X-ray diffraction, thermogravimetric analysis, and vibrational spectroscopies (infrared and Raman), however gaining insight into the solvate forming mechanism is a more difficult task. Detailed knowledge of the structures and energies of hydrated organic molecular solids enables enhanced understanding of the crystalline solvates themselves to be achieved, but also how these hydrated substances interact with their environments, as in the case of active pharmaceutical ingredients and excipients.<sup>3</sup>

For a crystalline hydrate of a molecular solid to exist, there must be a net energetic advantage in terms of enthalpy and entropy (collectively, Gibbs free energy). The incorporation of one or more water molecules will disrupt the existing crystal packing arrangement of the anhydrous species, but this modification can ultimately yield enhanced intermolecular interactions or ease conformational strain, leading to a more energetically favorable system. The existence or absence of hydrate crystal forms of various molecules is typically interpreted by variations in the types of intermolecular forces (and their strengths) displayed by different compounds. This may be exemplified by considering extreme differences such as polar versus non-polar molecules, but the disparity in intermolecular interactions do not need to be so obvious to still be relevant. A more subtle difference in the interaction of molecules is found in chiral

solids where the molecules are identical except for their optical isomerism, yet this still leads to significant changes in the physical properties of the solids. This is observed as solubility and melting point variations, where the racemic solid is typically more stable.<sup>4,5</sup>

The amino acid aspartic acid has been the subject of numerous studies of its hydration properties, both alone and in proteins.<sup>6-14</sup> Aspartic acid is a chiral molecule that can be crystallized in the homochiral L-aspartic acid form (L-ASP) or in the racemic DL-aspartic acid form (DL-ASP), both with known crystal structures.<sup>15,16</sup> The two crystalline forms differ only by the chirality of the component molecules, but they exhibit marked differences in their propensities for hydrate formation. The pure L-ASP system forms a stable monohydrate (L-ASP•H<sub>2</sub>O) from evaporation of a mildly acidic aqueous solution,<sup>17</sup> while racemic DL-ASP has no known crystalline hydrates.

In this work, solid-state density functional theory (DFT) has been used to evaluate the energetic factors that help determine the likelihood of the hydrate formation in these two chiral solids. The conformational and cohesive energies within L-ASP, DL-ASP, and L-ASP•H<sub>2</sub>O are calculated and compared to each other as well as two proposed theoretical structures of DL-ASP hydrates, DL-ASP•0.5H<sub>2</sub>O and DL-ASP•H<sub>2</sub>O. The accurate reproduction of intermolecular forces is a key issue in this study and experimental terahertz spectroscopy of the low-frequency lattice vibrations has been utilized to test the validity of the applied computational methods. The results of this work reveal that the difficulty encountered in the creation of a DL-ASP hydrate is not due to the intermolecular forces alone, but depends strongly on the conformational stabilities of the aspartic acid molecules found in the homochiral and racemic solids.



## 5.2 Methods

### 5.2.1 Experimental

L-aspartic acid (98%) and DL-aspartic acid (99%) were purchased from Sigma-Aldrich and used with no further purification. Low-temperature crystallographic measurements are available for both molecular solids and were used for all structural comparisons and evaluations. Single-crystal X-ray diffraction data for L-ASP at 100 K has been reported by Bendeif and Jelsch,<sup>15</sup> showing L-ASP to adopt P 21 space group symmetry with unit cell dimensions of  $a = 5.1135 \text{ \AA}$ ,  $b = 6.9059 \text{ \AA}$ ,  $c = 7.5925 \text{ \AA}$ , volume =  $263.488 \text{ \AA}^3$ , and  $Z = 2$ . The crystal structure of DL-aspartic acid has been reported at 20 K by Flaig, *et al.*<sup>16</sup> The space group for DL-ASP is C 2/c with unit cell dimensions of  $a = 18.881 \text{ \AA}$ ,  $b = 7.325 \text{ \AA}$ ,  $c = 9.129 \text{ \AA}$ , volume  $1053.448 \text{ \AA}^3$ , and  $Z = 8$  (primitive cell  $Z=4$ ). Single asymmetric units and complete unit cells for both compounds are shown in **Figures 5-1** and **5-2**, respectively.

The time-domain pulsed THz spectrometer, based on an amplified Ti:Sapphire femtosecond laser system, has been previously reported in detail elsewhere.<sup>18</sup> Terahertz radiation is both generated (optical rectification) and detected (free-space electro-optic sampling) using ZnTe crystals.<sup>19,20</sup> The samples of L-ASP and DL-ASP were mixed with polytetrafluoroethylene (PTFE) powder to dilute the samples to 2.2% and 2.3% by mass, respectively. The particle size within these mixtures was minimized by pulverization in a stainless steel ball mill in order to reduce THz scattering.<sup>21</sup> After pulverization, approximately 0.55 g of each mixture was pressed into 13 mm diameter by 2 mm thickness pellets under 2000 psi using a hydraulic press. The blank used for THz measurements was one of pure PTFE, made under the same conditions. The samples and blank are held under vacuum in a variable-temperature cryostat that allows for data collection at both 293 K and 78 K. Each individual data set consisted of an average of 32 scans.

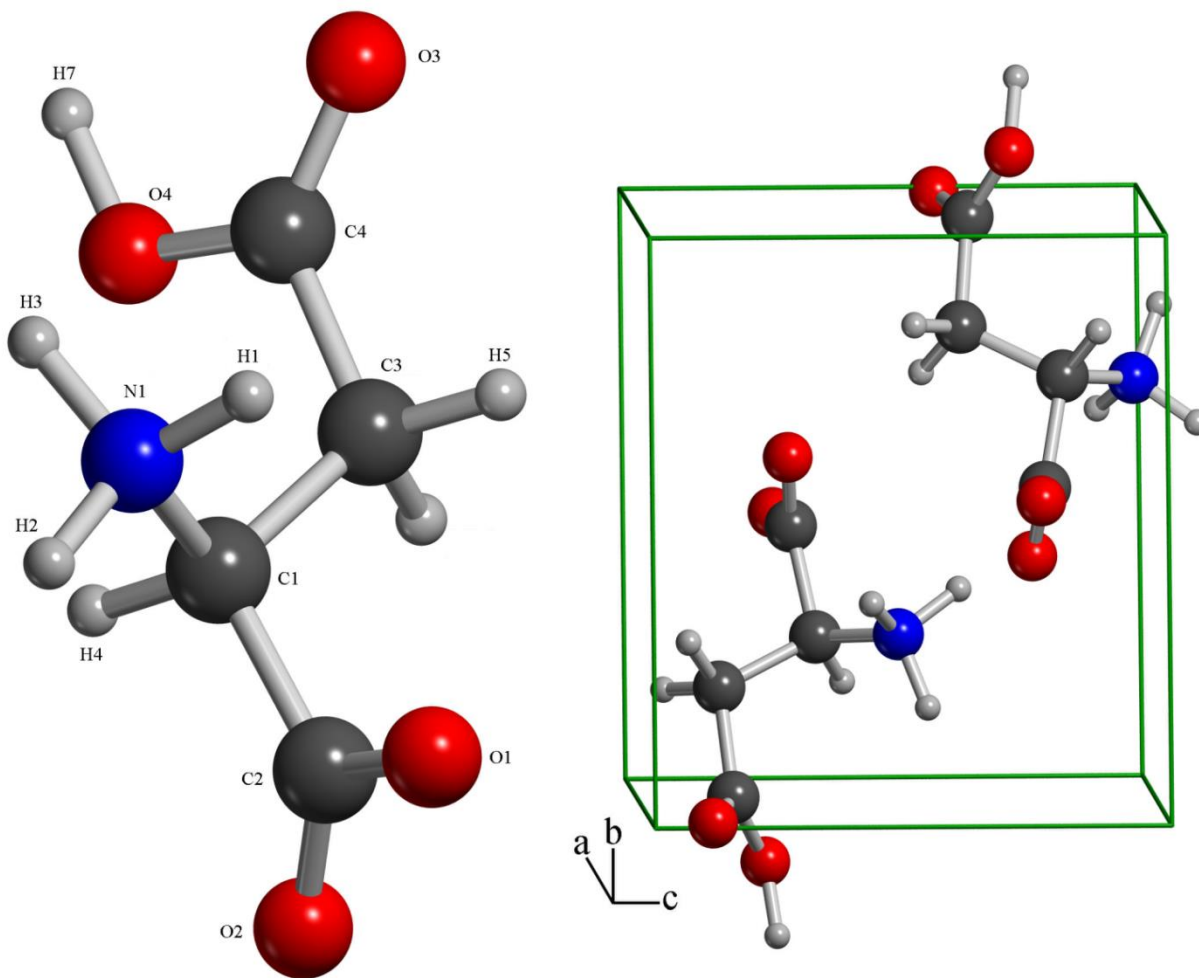


**Figure 5-1.** Labeled L-ASP asymmetric unit and full unit cell.

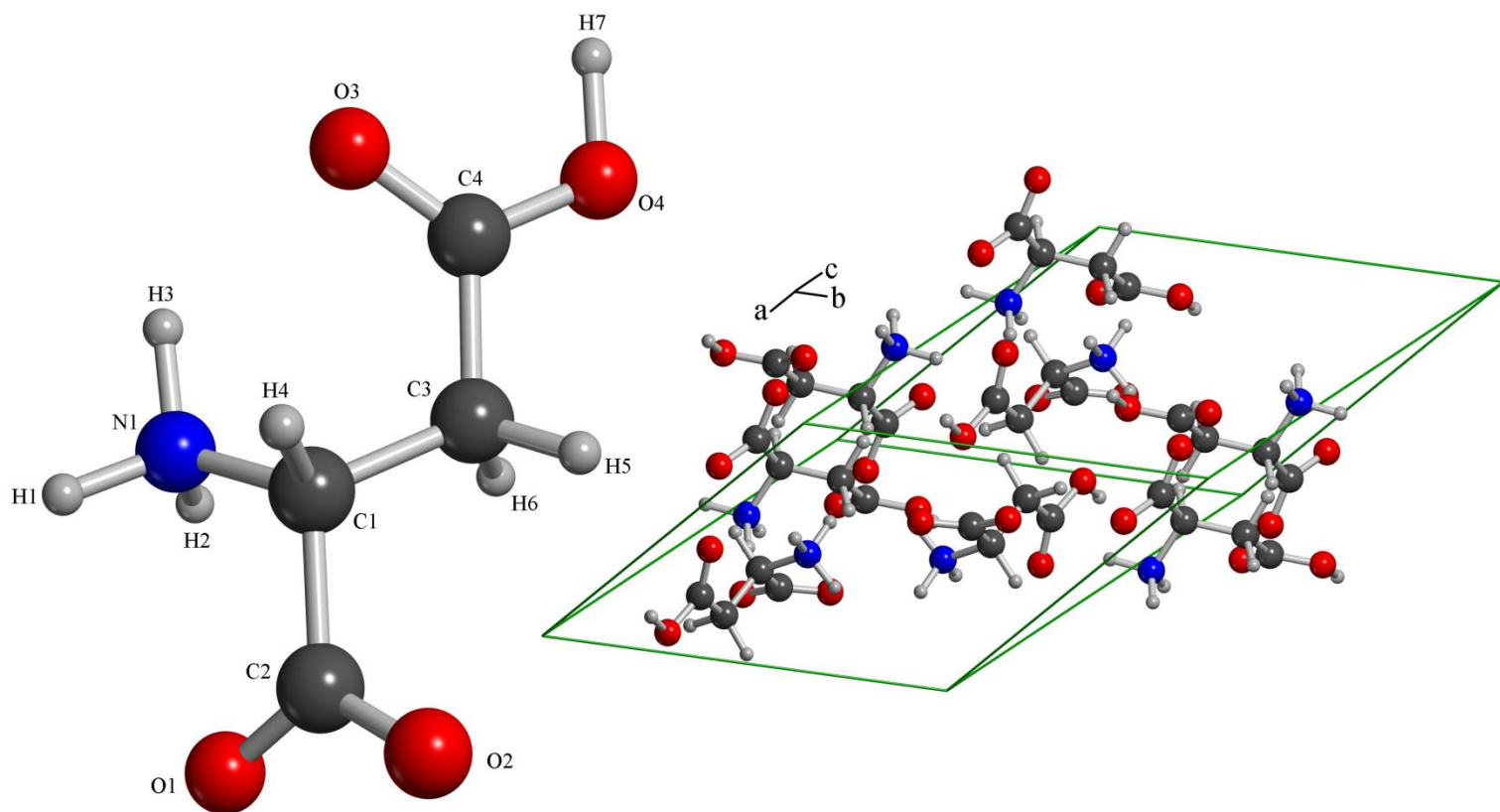


**Figure 5-2.** Labeled DL-ASP asymmetric unit and full unit cell.

The THz waveform was captured using a 32 ps scan window consisting of 3200 data points, which was then symmetrically zero-padded to 6000 points. Spectral resolution of approximately  $1.0 \text{ cm}^{-1}$  was achieved using a Hanning window to perform Fourier transforms on the waveforms. The ratio of the power spectra (Fourier transformed data) of the sample and blank produced the THz absorption spectra. Terahertz spectra shown here are the averages of four separate THz absorption spectra, each representing a complete set of sample and blank measurements. Cubic spline interpolation has been applied for visual clarity.

### 5.2.2 Theoretical

All solid-state DFT calculations were performed using the CRYSTAL09<sup>22</sup> software package. The B3LYP hybrid density functional<sup>23</sup> and 6-31G(d,p) atom-centered basis set<sup>24</sup> were used for all calculations. Semi-empirical London-type dispersion corrections (DFT-D\*) were included in the calculations in order to better account for weak non-covalent intermolecular forces.<sup>25</sup> The global scale factor ( $s_6$ ) for the dispersion correction was determined specifically for the aspartic acid solids considered here.

Atomic positions and lattice parameters were allowed to fully relax within the condition of preserved space group symmetries. Total energy convergence criteria were set to  $\Delta E < 10^{-8}$  hartree for geometry optimizations and  $\Delta E < 10^{-11}$  hartree for normal mode calculations. Truncation tolerances for Coulomb and HF exchange integral series were set to  $10^{-6}$ ,  $10^{-6}$ ,  $10^{-6}$ ,  $10^{-6}$ ,  $10^{-12}$  hartree. A shrinking factor of 8 (125  $k$  points in the irreducible Brillouin zone) was used in all calculations, based on the total energy convergence as a function of  $k$ -point count in reciprocal space according to the Pack-Monkhorst method.<sup>26</sup> The radial and angular distributions were defined by a (75 794) DFT integration grid. The harmonic approximation was used to calculate the normal modes of vibration by numerical differentiation of the potential energy

gradient with respect to atomic position. The Berry phase approach was used to calculate the Born charge tensor,<sup>22,27</sup> which enables the calculation of the infrared intensities of the normal modes. To facilitate comparison with experiment, spectral intensities are reported in units of  $\epsilon$  ( $\text{M}^{-1} \text{cm}^{-1}$ ) where molarity is expressed in terms of the concentration of the crystallographic unit cells ( $Z$ ).

## 5.3 Results and Discussion

### 5.3.1 Terahertz Spectroscopy

Terahertz spectra of L-ASP and DL-ASP, from 10 to 100  $\text{cm}^{-1}$ , are shown in **Figure 5-3** at 78 K. The experimentally determined absorptions are listed in **Table 5-1**. Room-temperature experimental THz data has been previously reported for both L-ASP<sup>28</sup> and DL-ASP<sup>29</sup> and the initial room-temperature THz spectra collected here (not shown) were consistent with those data. When cooled to 78 K, the absorptions narrow and shift to higher energy as is typical for such solids in this spectral region.

**Table 5-1.** Experimental frequencies ( $\text{cm}^{-1}$ ) and intensities ( $\text{M}^{-1} \text{cm}^{-1}$ ) of L-ASP and DL-ASP

L-ASP		DL-ASP	
freq.	$\epsilon$	freq.	$\epsilon$
42.8	2.66	52.6	84.30
83.9	15.61	67.2	153.95
90.2	20.88	83.3	64.41

The 78 K spectrum for L-ASP shows three distinct peaks at 42.8, 83.9, and 90.2  $\text{cm}^{-1}$ . The highest-energy peak also contains a shoulder near the edge of the spectral range at approximately 94.2  $\text{cm}^{-1}$ . In the DL-ASP spectrum there are also three distinct peaks at 52.6,

67.2, and 83.3  $\text{cm}^{-1}$ . Near the edge of the spectral bandwidth there is the possibility of a fourth peak at approximately 98  $\text{cm}^{-1}$ .

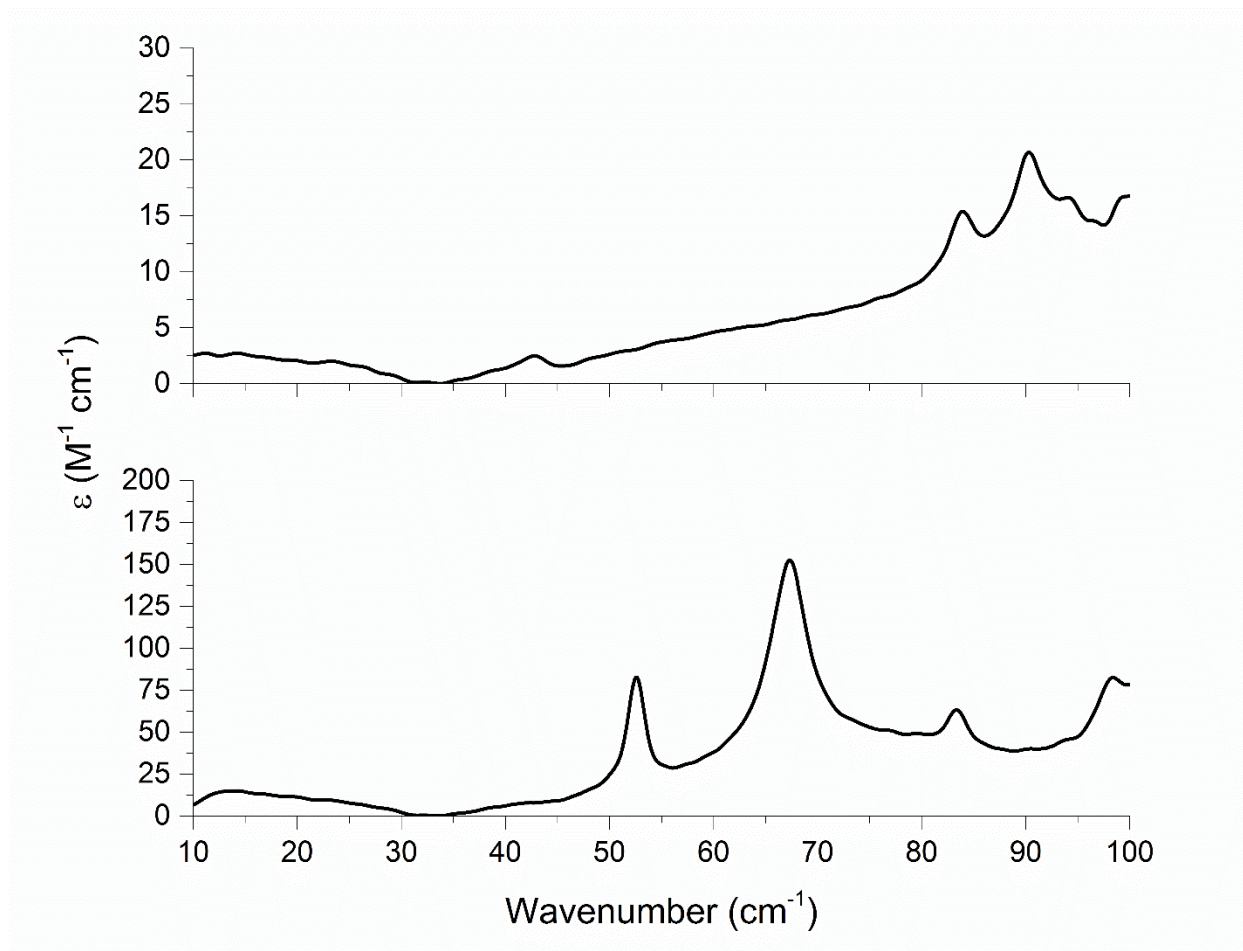


**Figure 5-3.** Experimental THz spectra of L-ASP (top) and DL-ASP (bottom) at 78 K.

## 5.3.2 Theoretical Analysis

### 5.3.2.1 Structural Analysis of Anhydrous L-ASP and DL-ASP

Previous work has demonstrated that the inclusion of semi-empirical London dispersion force corrections is essential to the success of simulations of crystalline organic molecules.<sup>30,31</sup> The DFT-D\* correction parameterization was chosen for these simulations due to its parameterization for solid-state use.<sup>25</sup> The first step to arriving at an acceptable structural reproduction is determining the global scaling factor,  $s_6$ , for L-ASP. In order to obtain the appropriate scaling factor value, the simulated lattice dimensions ( $a$ ,  $b$ ,  $c$ ,  $\beta$ , and volume) from calculations performed with varying  $s_6$  magnitudes were compared to the dimensions from the experimental X-ray crystal structures with the goal being the minimum deviation between the two data sets. The suggested  $s_6$  for B3LYP using DFT-D\* is 1.00,<sup>25</sup> but the L-ASP results indicated that the optimum  $s_6$  was significantly smaller at only 0.52. Once the  $s_6$  value for L-ASP was determined, it was applied in all subsequent calculations for DL-ASP and the hydrated solids. The signed percent errors in the unit cell dimensions and the overall absolute average percent error (not including the  $\beta$  angle) for L-ASP and DL-ASP are listed in **Table 5-2**. It should be noted that the structural simulations for L-ASP and DL-ASP were compared to 100 K<sup>15</sup> and 20 K<sup>16</sup> X-ray crystallographic structures, respectively, and that the performance of the applied theory is essentially the same for both.



**Table 5-2.** Percent errors in unit cell parameters of L-ASP, DL-ASP, and L-AS•H<sub>2</sub>O as compared to experimental X-ray diffraction data

Parameter	L-ASP	DL-ASP	L-ASP H <sub>2</sub> O
<i>a</i>	0.31	0.56	1.98
<i>b</i>	-1.06	0.55	-2.12
<i>c</i>	0.68	-0.25	-2.18
$\beta$	-0.02	0.12	-
Volume	-0.07	0.70	-2.36
Abs. Ave. Error	0.53	0.52	2.16

The overall success of these calculations (low errors in lattice dimensions) was only part of the necessary evaluation needed to determine their accuracy. Each simulated structure was also subjected to evaluation of both the intramolecular (bond lengths, bond angles, and dihedral angles) and intermolecular (hydrogen-bond heavy-atom distances) structural parameters. Hydrogen atoms were ignored in these comparisons due to their unreliable positions as determined by X-ray diffraction. The root-mean-squared deviations (RMSD) of each parameter for both anhydrous solids are provided in **Table 5-3**. The average RMSDs between these two solids were 0.0020 Å in bond lengths, 0.1197° in bond angles, 0.7689° in dihedral angles, and 0.0049 Å in hydrogen-bond heavy-atom distances. The greatest difference in the simulated structures was seen in the dihedral angle RMSDs, arising from only two poorly reproduced angles involving the carboxylate end of the L-ASP molecule. It is not clear if the origin of these outliers is computational or experimental. Overall, the two simulated structures were in excellent agreement with the experimental crystal data.

**Table 5-3.** Root-mean-squared deviations (RMSDs) of calculated bond lengths, bond angles, dihedral angles, and heavy-atom hydrogen bond lengths for L-ASP, DL-ASP, and L-ASP•H<sub>2</sub>O

	Bond Length (Å)	Bond Angle (°)	Dihedral Angle (°)	H Bond Length (Å)
L-ASP	0.0020	0.1352	1.1314	0.0069
DL-ASP	0.0020	0.1043	0.4065	0.0028
L-ASP H <sub>2</sub> O	0.0051	0.3890	2.1144	0.0476

### 5.3.2.2 Simulated Terahertz Spectra of Anhydrous L-ASP and DL-ASP

The calculated frequencies and intensities of the IR-active modes of L-ASP and DL-ASP are listed in **Table 5-4**. These results are plotted in **Figure 5-4** with convolved Lorentzian line shapes utilizing full width half-maximum (fwhm) values that have been empirically determined by least-squares fitting of the experimental data. The fwhm values were found to be 2.6 cm<sup>-1</sup> and 3.7 cm<sup>-1</sup> for L-ASP and DL-ASP, respectively.

**Table 5-4.** Calculated IR-active mode frequencies (cm<sup>-1</sup>), intensities (km mol<sup>-1</sup>), and symmetries for L-ASP and DL-ASP

L-ASP			DL-ASP		
freq.	intens.	symm.	freq.	intens.	symm.
49.8	0.07	A	60.8	5.19	B <sub>U</sub>
83.4	1.36	A	71.0	24.30	B <sub>U</sub>
92.4	2.50	B	93.8	0.54	A <sub>U</sub>

The simulated THz spectrum for L-ASP (**Figure 5-4, top**) has three peaks in the sub-100 cm<sup>-1</sup> area of interest. The two highest intensity peaks in the experimental spectrum at 83.9 and 92.4 cm<sup>-1</sup> are very well reproduced by the simulation which generated absorptions at 83.4 and 90.2 cm<sup>-1</sup>. The relative intensities of the simulated peaks agree well with the experimental data although the absolute intensities appear to be overestimated. This is somewhat difficult to judge

given the rising baseline of the L-ASP spectrum. The lowest-energy peak ( $42.8\text{ cm}^{-1}$  in the experimental spectrum) is reproduced by the simulations, but at a significantly higher energy ( $49.8\text{ cm}^{-1}$ ) which may indicate significant anharmonicity in that mode. The very low intensity of this absorption is common to both the experimental and simulated spectra.

The DL-aspartic acid crystal yielded a simulated THz spectrum also containing three absorptions features (**Figure 5-4, bottom**), but at  $60.8$ ,  $71.0$ , and  $93.8\text{ cm}^{-1}$ . The intensities of these peaks agree with the order of intensities seen in the experimental spectrum, however the peak positions are all slightly overestimated. For both L-ASP and DL-ASP, the use of the B3LYP/631G(d,p) solid-state DFT calculations resulted in simulated THz spectra in very good agreement with the experimental THz data. The determination of the  $s_6$  scaling factor, based off of the L-ASP geometry calculations, proved to be equally effective for the DL-ASP solid, and the same  $s_6$  value of  $0.52$  was subsequently applied to the hydrated versions aspartic acid.

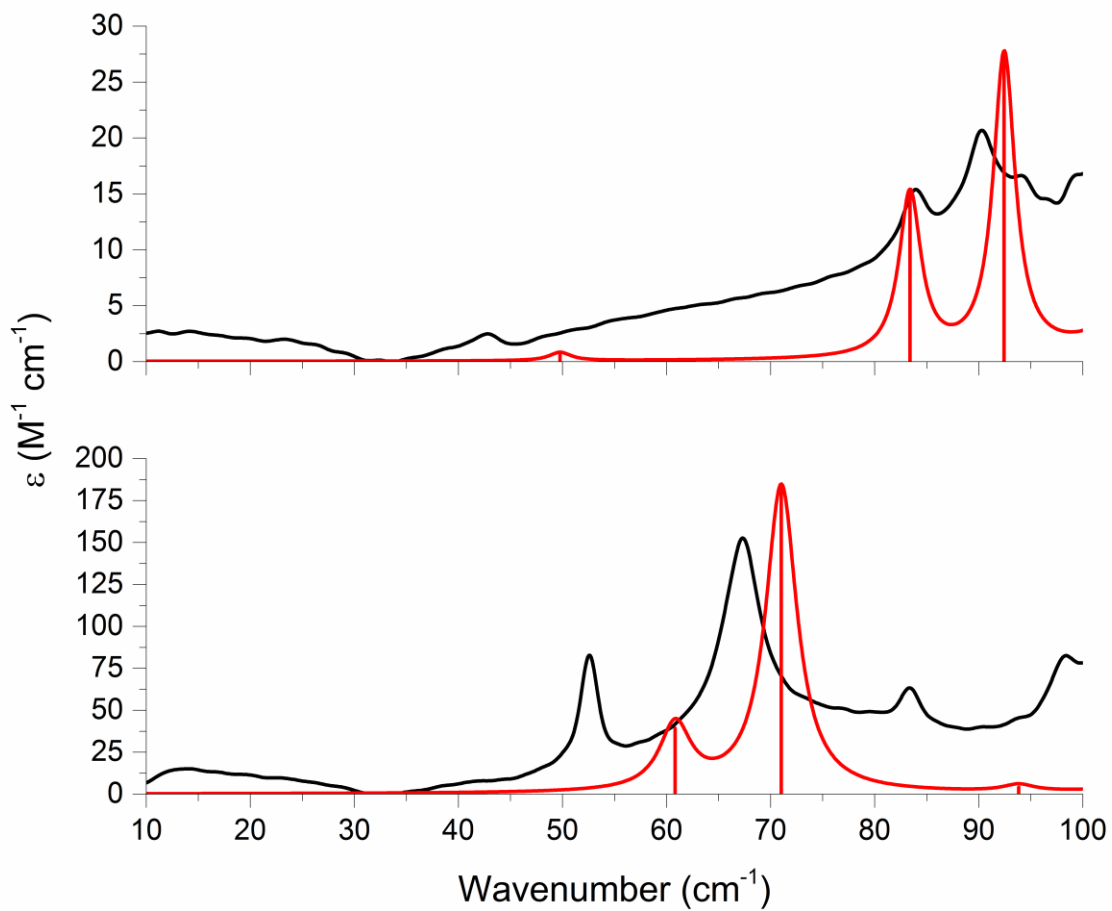


**Figure 4.** Terahertz spectra of L-ASP (top) and DL-ASP (bottom) compared to theoretically generated spectra (red traces) using B3LYP/6-31G (d,p).

### 5.3.2.3 Structural Analysis of L-ASP Monohydrate

L-ASP•H<sub>2</sub>O has only one available X-ray crystallographic structure, and this was determined at room temperature (**Figure 5-5**). Although room-temperature structures are not ideal, all attempts to recrystallize the monohydrate form in order to solve the cold structure resulted in anhydrous material. Therefore, for L-ASP•H<sub>2</sub>O, all structural comparisons will be made to the room-temperature crystallographic data. Comparison of the theoretical results to the room temperature L-ASP•H<sub>2</sub>O structure shows greater errors in the calculated unit cell parameters (**Table 5-2**) as was seen in the anhydrous analysis. This is expected since the solid-state DFT calculation is done without temperature effects (0 K) and therefore will tend to match better crystal structures measured at low temperature. For example, the percent error in the volume for the theoretical structure versus the 293 K structure was -2.36%. The volume discrepancy can be put into perspective by considering the well-studied L-serine monohydrate crystal system for comparison for which there exists two X-ray crystallographic structures, 293 K and 97 K.<sup>32,33</sup> The difference seen in the volume between these two L-serine monohydrate structures is -2.12%, similar to what has been predicted here for the L-ASP•H<sub>2</sub>O crystal. Taking into account the temperature issues, the geometry simulation for L-ASP•H<sub>2</sub>O is considered to be, at the very least, a reasonable representation of a low-temperature structure.

As was conducted on the anhydrous amino acids, L-ASP H<sub>2</sub>O was subjected to the same intramolecular and intermolecular comparisons. **Table 5-3** shows the RMSDs of the bond lengths, bond angles, dihedral angles, and hydrogen-bond heavy-atom distances. The RMSDs are 0.0051 Å, 0.3890°, 2.1144°, and 0.0476 Å, respectively. As with the anhydrous amino acids, there is low error in the bond lengths and bond angles, but a larger error is seen in the dihedral angles due to the comparison of the theoretical data to room-temperature experimental X-ray

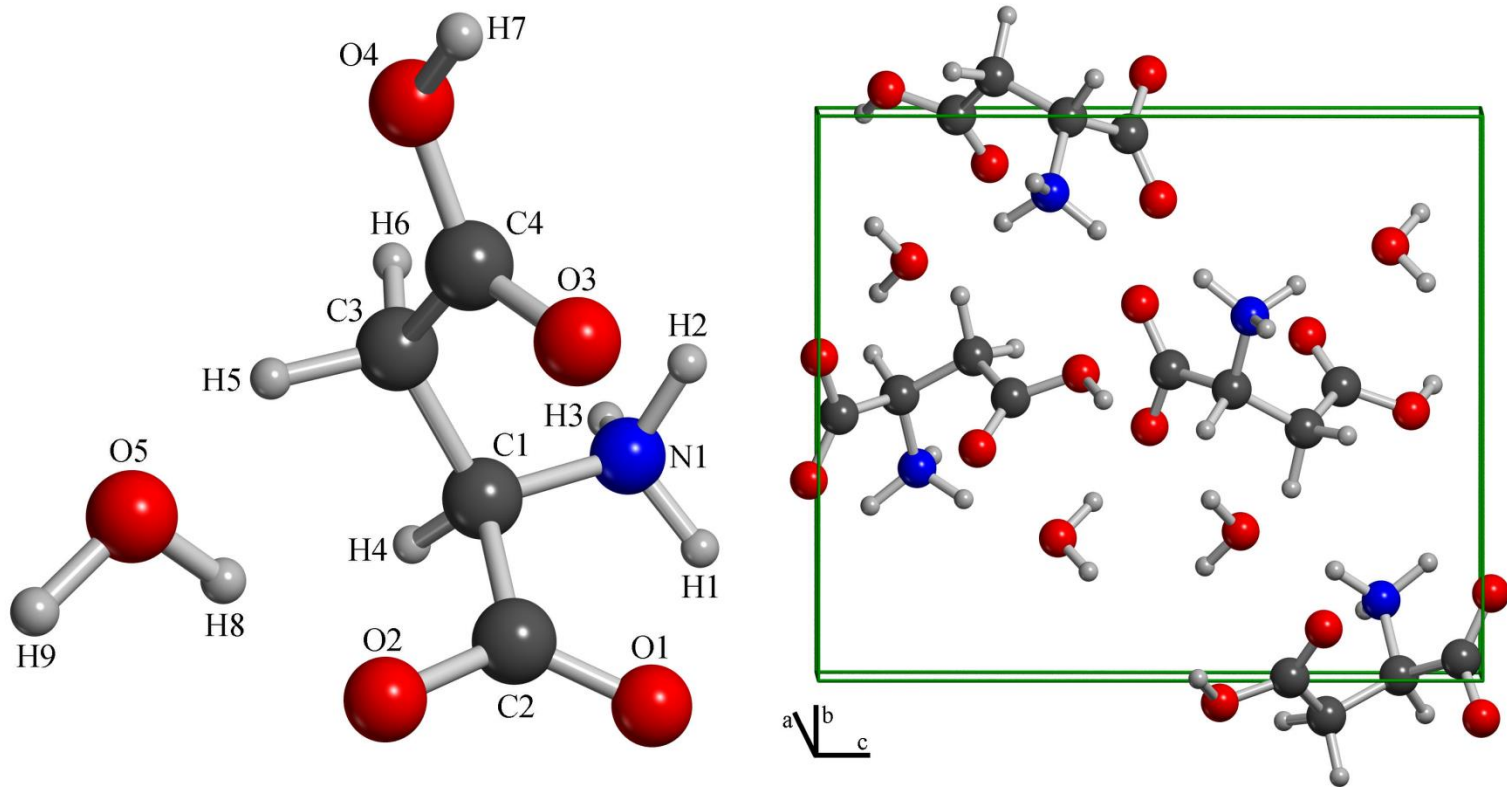


**Figure 5-5.** Labeled L-ASP•H<sub>2</sub>O asymmetric unit and full unit cell.

crystallographic data. The error in the hydrogen bond distances is very small, indicating that the intermolecular hydrogen bonds are well modeled for the water/aspartic acid interactions..

After the geometry optimization of L-ASP•H<sub>2</sub>O was completed, a frequency analysis was performed on the structure. No negative displacements (or imaginary frequencies) were seen in the vibrational calculations, proving that the optimized structure was located at a true minimum on the potential energy surface. The lack of experimental data prevents a detailed evaluation of the spectrum to be presented; however the results are listed in the **Appendix B, Table B1**.

#### 5.3.2.4 Structural Predictions for DL-ASP Hydrates

Based on the results obtained for the anhydrates and L-ASP•H<sub>2</sub>O, two possible structures for hydrated DL-ASP were found using the same calculation methodology. The initial step to predicting these structures was to determine the most probable positions for the water molecules to interact with the amino acid molecules in the DL-ASP crystallographic unit cell. Anhydrous DL-ASP was used as the basis for constructing the proposed DL-ASP hydrated crystal.

In the first prediction, two water molecules were inserted into the unit cell based on a hydrogen-bonding scheme similar to that seen in L-ASP•H<sub>2</sub>O. Once the water molecules were placed into the crystal following this pattern, the entire structure was allowed to relax with full unit cell and atomic positions optimization being performed with P 1 space group symmetry. After completion of the full optimization, inversion symmetry was found and the DL-ASP•0.5H<sub>2</sub>O structure placed in the P-1 space group for all subsequent calculations. This first simulation yielded a hemihydrate form (**Figure 5-6**) of DL-ASP (DL-ASP•0.5H<sub>2</sub>O) with unit cell dimensions of  $a = 8.15947017 \text{ \AA}$ ,  $b = 9.07693249 \text{ \AA}$ ,  $c = 9.49322074$ ,  $\alpha = 69.100418^\circ$ ,  $\beta = 63.954633^\circ$ ,  $\gamma = 91.576228^\circ$ , volume =  $575.756050 \text{ \AA}^3$ , and  $Z = 2$ .

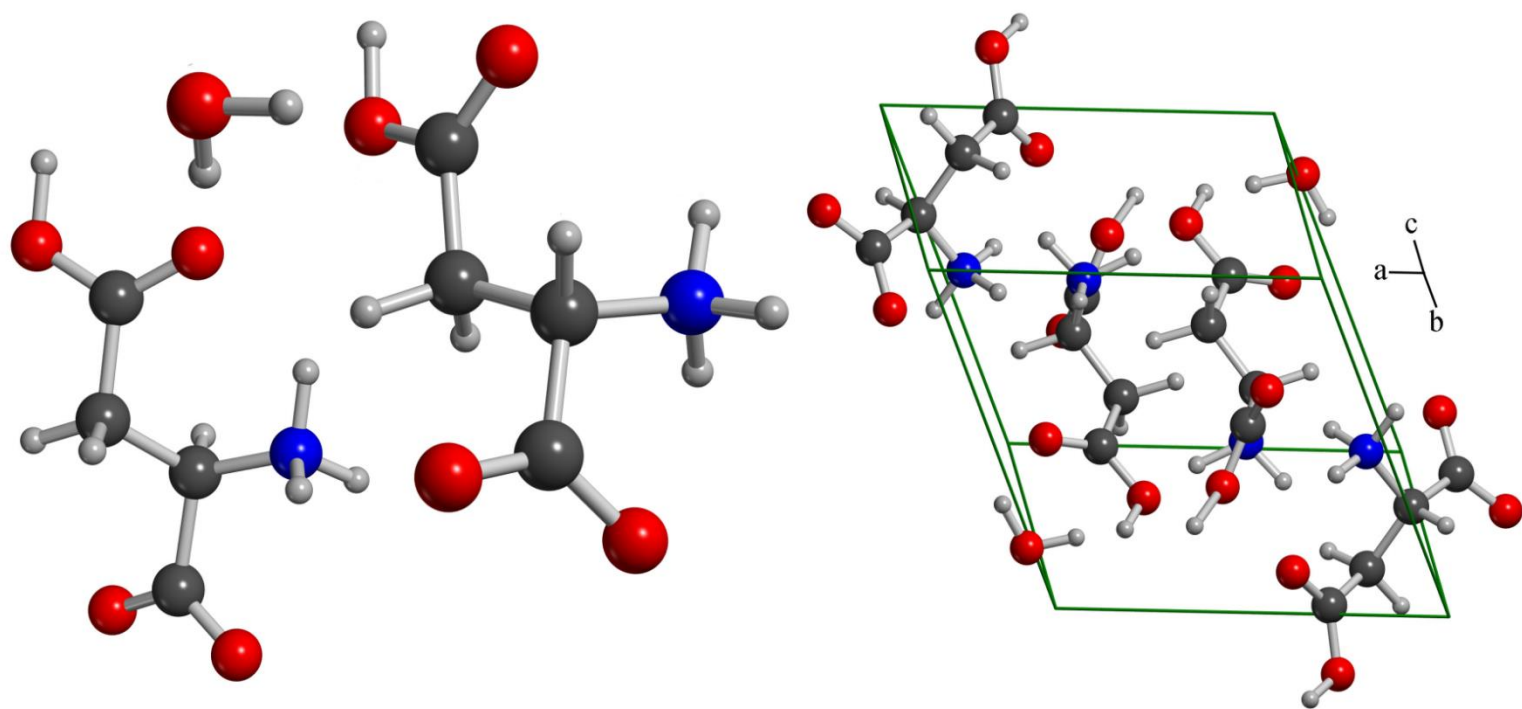


**Figure 5-6.** DL-ASP·0.5H<sub>2</sub>O asymmetric unit and full unit cell.



Despite the successfully converged simulation of DL-ASP•0.5H<sub>2</sub>O, none of the reported amino acid hydrate structures currently appearing in the Cambridge Structural Database<sup>34</sup> contain fractional waters in their unit cells. The same procedure was followed as for DL-ASP•0.5H<sub>2</sub>O, except that four waters were added to the DL-ASP unit cell (one per amino acid). In order to incorporate four water molecules, some small rotations of the terminal groups of the amino acids were necessary to promote the desired hydrogen bonding scheme. The initial structure was then fully optimized in the P 1 space group. Upon completion of the optimization, new space group symmetry of P-1 was found. The simulation yielded a DL-ASP•1H<sub>2</sub>O species (**Figure 5-7**) with unit cell dimensions of  $a = 8.69412473 \text{ \AA}$ ,  $b = 9.44524101 \text{ \AA}$ ,  $c = 10.02247791 \text{ \AA}$ ,  $\alpha = 67.287813^\circ$ ,  $\beta = 60.118818^\circ$ ,  $\gamma = 91.864362^\circ$ , volume =  $631.720324 \text{ \AA}^3$ , and  $Z = 2$ .

Although the geometry optimizations were successful, the testing of the proposed structures was not complete without normal mode calculations confirming their quality. Vibrational analysis of fully-optimized P-1 structures of both proposed DL-ASP hydrates were performed and no negative displacements or imaginary modes were generated. The frequency and infrared intensity results for DL-ASP•0.5H<sub>2</sub>O and DL-ASP•H<sub>2</sub>O are shown in **Appendix B, Tables B2** and **B3**, respectively. Based on the results of the geometry optimizations and normal mode calculations, it is confirmed that both structures correspond to minima on the potential energy hypersurface governing the interactions of the molecules in the solid state. Thus, the existence of DL-ASP hydrates with such structures is possible, but not necessarily probable. To better understand this, the energies involved with the hydrate formation must be investigated.

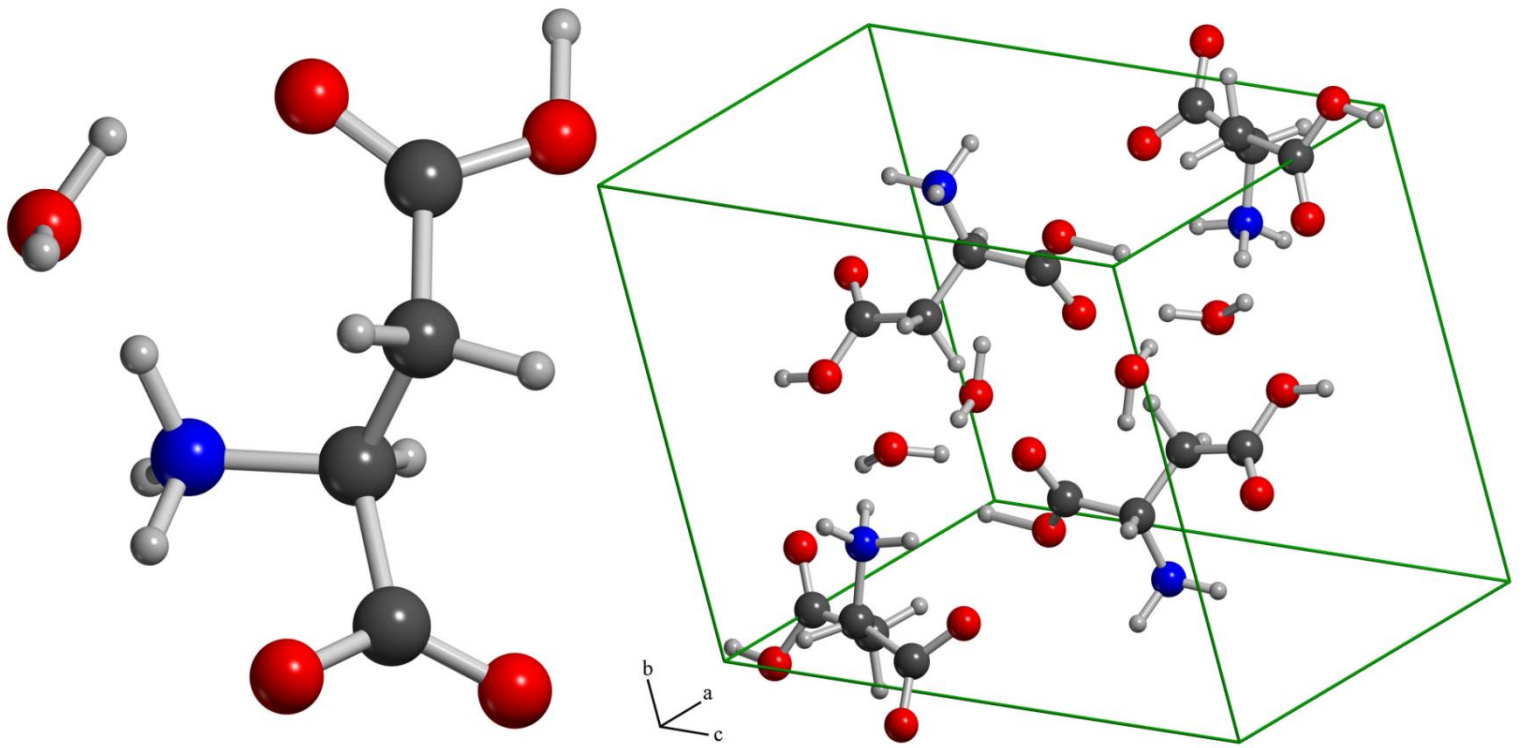


**Figure 5-7.** DL-ASP·H<sub>2</sub>O asymmetric unit and full unit cell.

### 5.3.2.5 Conformational, Cohesive, and Gibbs Free Energies of Aspartic Acid Crystals

Solid-state DFT calculations provide the information needed to evaluate the energies important to the formation of the DL-ASP hydrates, and all of the aspartic acid solids considered here, including conformational, cohesive, and Gibbs free energies. The results of these calculations on the aspartic acid anhydrates are listed in **Tables 5-5**. Of primary consideration is the cohesive energies found in L-ASP versus DL-ASP, since the expectation is that the solid that more readily forms a hydrate crystal would have weaker binding forces as an anhydrate. However, the cohesive energy of L-ASP is about 45.7 kJ/mol better than DL-ASP, suggesting that L-ASP should be less willing to incorporate co-crystallized waters, in contrast to experiment.

**Table 5-5.** Conformational, cohesive, total electronic, and Gibbs energies of L-ASP and DL-ASP. Units are in hartree.

	Conformational	Cohesive	Total Electronic	Gibbs (298 K)
L-ASP	-511.9932	-0.1486	-512.1418	-2048.0833
DL-ASP	-512.0114	-0.1312	-512.1426	-2048.0861

Considering the conformational energies of the aspartic acid molecules in the crystals helps to explain the observed behavior. The conformation of the DL-ASP molecules is considerably lower in energy (-47.8 kJ/mol) than those of L-ASP. Taking the conformational and cohesive energies together, it is seen that the total electronic energy of DL-ASP is actually slightly lower than L-ASP (-2.1 kJ/mol), now in agreement with the observation that the L-ASP•H<sub>2</sub>O crystal does form more easily than any DL-ASP hydrate. Furthermore, DL-ASP shows a lower Gibbs energy at room temperature than L-ASP (-7.4 kJ/mol).

Given the importance of molecular conformation on the formation of crystalline aspartic acid hydrates, it was evaluated in the known L-ASP•H<sub>2</sub>O solids and the proposed DL-

ASP•0.5H<sub>2</sub>O and DL-ASP•H<sub>2</sub>O forms (**Table 5-6**). An interesting pattern appears between the homochiral and racemic solids. The addition of water to L-ASP actually improves (-1.52 kJ/mol) the conformational energy of the ASP molecules, but the water molecules negatively impact (+6.87 kJ/mol) the internal energies of the ASP molecules in both the DL-ASP hemihydrate and monohydrate proposed in this work.

**Table 5-6.** Conformational energies of ASP molecules from crystalline hydrates as compared to those in anhydrous crystals. DL-ASP energies in the hydrates represent the average of the symmetry unique enantiomers.

Amino Acid	Relative Conformational Energy (kJ/mol) of ASP Molecules
anhydrous L-ASP	0.00
L-ASP•H <sub>2</sub> O	-1.52
anhydrous DL-ASP	0.00
DL-ASP•H <sub>2</sub> O	+6.72
DL-ASP•0.5H <sub>2</sub> O	+7.01

Gibbs free energy differences can also be used to gauge the likelihood for these different hydrates to form. The  $\Delta G$  values for hydration were calculated using Gibbs energies of the anhydrous solids, an isolated water molecule, and the known and proposed crystalline hydrates. The Gibbs free energy difference between anhydrous L-ASP and the known L-ASP•H<sub>2</sub>O was -94.57 kJ/mol. This result is expected and confirms the creation of the monohydrated L-ASP crystal is energetically favorable and spontaneous. Conversely, since DL-ASP hydrates have never been observed, the  $\Delta G$  values should be positive. This is indeed the case for both the hemihydrate (+36.62 kJ/mol) and the monohydrate (+0.84 kJ/mol). The monohydrate Gibbs free energy is small enough to suggest that, perhaps under non-standard conditions, the hydrate could possibly be produced, while the large positive value for the hemihydrate is consistent with the total lack of amino acid hemihydrate structures in the literature. Thus, based on predictions of the

possible structures of hydrated DL-ASP and the energy components of these crystals, the DL-ASP hydrates will not form spontaneously under standard conditions, and this conclusion is largely rooted in the conformational energies of the amino acid molecules.

## 5.4 Conclusions

Homochiral and racemic crystals of L-aspartic acid exhibit very different abilities for incorporating co-crystallized water molecules. Solid-state density functional theory calculations, supported by terahertz spectroscopic measurements, have provided new insight as to why L-ASP•H<sub>2</sub>O exists, but DL-ASP•H<sub>2</sub>O does not. Two hydrates of DL-ASP have been proposed, a hemihydrate and a monohydrate, with both forms calculated to be at energetically stable minima. The possible formation of these hydrated species was considered in terms of solid-state conformational, cohesive, and Gibbs energies. The L-ASP•H<sub>2</sub>O solid was found to be spontaneously forming as expected from experimental observations. Neither DL-ASP hydrate was found to be energetically preferred over the anhydrous parent, thus its formation is unlikely. The origins of this behavior are found to be strongly connected to the conformational energies of the aspartic acid molecules in the solids, with the addition of water to the DL-ASP crystal significantly disrupting its molecular stability.

## 5.5 Supporting Information

Calculated IR-active mode frequencies and intensities for L-ASP•H<sub>2</sub>O, DL-ASP•0.5H<sub>2</sub>O, and DL-ASP•H<sub>2</sub>O. This material is available free of charge via the Internet at <http://pubs.acs.org>. This information is located in Appendix B.

## **5.6 Acknowledgements**

This research was funded by a grant from the National Science Foundation CAREER Program (CHE-0847405). The authors thank Syracuse University for its continued support.

## 5.7 References

- (1) Vippagunta, S. R.; Brittain, H. G.; Grant, D. J. W. Crystalline Solids. *Advanced Drug Delivery Reviews* **2001**, *48*, 3-26.
- (2) Clarke, H. D.; Arora, K. K.; Bass, H.; Kavuru, P.; Ong, T. T.; Pujari, T.; Wojtas, L.; Zaworotko, M. J. Structure–Stability Relationships in Cocrystal Hydrates: Does the Promiscuity of Water Make Crystalline Hydrates the Nemesis of Crystal Engineering? *Crystal Growth & Design* **2010**, *10*, 2152-2167.
- (3) Salameh, A. K.; Taylor, L. S. Physical Stability of Crystal Hydrates and Their Anhydrides in the Presence of Excipients. *J. Pharm. Sci.* **2006**, *95*, 446-461.
- (4) Li, Z. J.; Zell, M. T.; Munson, E. J.; Grant, D. J. W. Characterization of Racemic Species of Chiral Drugs Using Thermal Analysis, Thermodynamic Calculation, and Structural Studies. *J. Pharm. Sci.* **1999**, *88*, 337-346.
- (5) Jane Li, Z.; Ojala, W. H.; Grant, D. J. W. Molecular Modeling Study of Chiral Drug Crystals: Lattice Energy Calculations. *J. Pharm. Sci.* **2001**, *90*, 1523-1539.
- (6) Deng, Y.; Roux, B. Hydration of Amino Acid Side Chains: Nonpolar and Electrostatic Contributions Calculated from Staged Molecular Dynamics Free Energy Simulations with Explicit Water Molecules. *J. Phys. Chem. B* **2004**, *108*, 16567-16576.
- (7) Hamm, L. M.; Wallace, A. F.; Dove, P. M. Molecular Dynamics of Ion Hydration in the Presence of Small Carboxylated Molecules and Implications for Calcification. *J. Phys. Chem. B* **2010**, *114*, 10488-10495.
- (8) Hamm, L. M.; Wallace, A. F.; Dove, P. M. Molecular Dynamics of Cation Hydration in the Presence of Carboxylated Molecules: Implications for Calcification. *MRS Online Proceedings Library* **2011**, *1301*, null-null.
- (9) Kimura, T.; Matubayasi, N.; Sato, H.; Hirata, F.; Nakahara, M. Enthalpy and Entropy Decomposition of Free-Energy Changes for Side-Chain Conformations of Aspartic Acid and Asparagine in Acidic, Neutral, and Basic Aqueous Solutions. *J. Phys. Chem. B* **2002**, *106*, 12336-12343.
- (10) Matsuoka, D.; Nakasako, M. Probability Distributions of Hydration Water Molecules around Polar Protein Atoms Obtained by a Database Analysis. *J. Phys. Chem. B* **2009**, *113*, 11274-11292.
- (11) Paxton \*, A. T.; Harper, J. B. On the Solvation of L-Aspartic Acid. *Mol. Phys.* **2004**, *102*, 953-958.
- (12) Sang-aroon, W.; Ruangpornvisuti, V. Conformational Study of Cationic, Zwitterionic, Anionic Species of Aspartic Acid, Water-Added Forms and Their Protonation. A Dft Method. *Journal of Molecular Structure: THEOCHEM* **2006**, *758*, 181-187.
- (13) Silva, A. M.; Costa, S. N.; Silva, B. P.; Freire, V. N.; Fulco, U. L.; Albuquerque, E. L.; Caetano, E. W. S.; Maia, F. F. Assessing the Role of Water on the Electronic Structure and Vibrational Spectra of Monohydrated L-Aspartic Acid Crystals. *Crystal Growth & Design* **2013**, *13*, 4844-4851.
- (14) Silva, A. M.; Silva, B. P.; Sales, F. A. M.; Freire, V. N.; Moreira, E.; Fulco, U. L.; Albuquerque, E. L.; Maia, F. F.; Caetano, E. W. S. Optical Absorption and Dft Calculations in L-Aspartic Acid Anhydrous Crystals: Charge Carrier Effective Masses Point to Semiconducting Behavior. *Phys. Rev. B* **2012**, *86*, 195201.

- (15) Bendeif, E.-e.; Jelsch, C. The Experimental Library Multipolar Atom Model Refinement of L-Aspartic Acid. *Acta Crystallogr. Sect. C* **2007**, *63*, o361-o364.
- (16) Flaig, R.; Koritsanszky, T.; Zobel, D.; Luger, P. Topological Analysis of the Experimental Electron Densities of Amino Acids. 1. D,L-Aspartic Acid at 20 K. *J. Am. Chem. Soc.* **1998**, *120*, 2227-2238.
- (17) Umadevi, K.; Anitha, K.; Sridhar, B.; Srinivasan, N.; Rajaram, R. K. L-Aspartic Acid Monohydrate. *Acta Crystallogr. Sect. E* **2003**, *59*, o1073-o1075.
- (18) Hakey, P. M.; Allis, D. G.; Ouellette, W.; Korter, T. M. Cryogenic Terahertz Spectrum of (+)-Methamphetamine Hydrochloride and Assignment Using Solid-State Density Functional Theory. *J. Phys. Chem. A* **2009**, *113*, 5119-5127.
- (19) Wu, Q.; Litz, M.; Zhang, X. C. Broadband Detection Capability of ZnTe Electro-Optic Field Detectors. *Appl. Phys. Lett.* **1996**, *68*, 2924-2926.
- (20) Rice, A.; Jin, Y.; Ma, X. F.; Zhang, X. C.; Bliss, D.; Larkin, J.; Alexander, M. Terahertz Optical Rectification from <110> Zinc-Blende Crystals. *Appl. Phys. Lett.* **1994**, *64*, 1324-1326.
- (21) Shen, Y. C.; Taday, P. F.; Pepper, M. Elimination of Scattering Effects in Spectral Measurement of Granulated Materials Using Terahertz Pulsed Spectroscopy. *Appl. Phys. Lett.* **2008**, *92*, 051103-051103.
- (22) Dovesi, R.; Saunders, V. R.; Roetti, C.; Orlando, R.; Zicovich-Wilson, C. M.; Pascale, F.; Civalleri, B.; Doll, K.; Harrison, N. M.; Bush, I. J.; D'Arco, P.; Llunell, M.; Torino, U. o. T. *CRYSTAL09 User's Manual* **2009**.
- (23) Becke, A. D. A New Mixing of Hartree-Fock and Local Density-Functional Theories. *J. Chem. Phys.* **1993**, *98*, 1372-1377.
- (24) Hehre, W. J.; Ditchfield, R.; Pople, J. A. Self-Consistent Molecular Orbital Methods. XII. Further Extensions of Gaussian-Type Basis Sets for Use in Molecular Orbital Studies of Organic Molecules. *J. Chem. Phys.* **1972**, *56*, 2257-2261.
- (25) Civalleri, B.; Zicovich-Wilson, C. M.; Valenzano, L.; Ugliengo, P. B3LYP Augmented with an Empirical Dispersion Term (B3LYP-D\*) as Applied to Molecular Crystals. *CrystEngComm* **2008**, *10*, 405-410.
- (26) Monkhorst, H. J.; Pack, J. D. Special Points for Brillouin-Zone Integrations. *Phys. Rev. B: Condens. Matter* **1976**, *13*, 5188-5192.
- (27) Dall'Olio, S.; Dovesi, R.; Resta, R. Spontaneous Polarization as a Berry Phase of the Hartree-Fock Wave Function: The Case of KNbO<sub>3</sub>. *Phys. Rev. B: Condens. Matter* **1997**, *56*, 10105-10114.
- (28) Wang, W.-N. Correlations between Terahertz Spectra and Molecular Structures of 20 Standard A-Amino Acids. *Wuli huaxue xuebao* **2009**, *25*, 2074.
- (29) Nishizawa, J.; Sasaki, T.; Suto, K.; Tanabe, T.; Yoshida, T.; Kimura, T.; Saito, K. Frequency-Tunable Terahertz-Wave Generation from Gap Using Cr:Forsterite Lasers. *Int J Infrared Milli Waves* **2006**, *27*, 923-929.
- (30) Juliano, T. R., Jr.; King, M. D.; Korter, T. M. Evaluating London Dispersion Force Corrections in Crystalline Nitroguanidine by Terahertz Spectroscopy. *IEEE Trans. on THz. Sci. and Tech.* **2013**, *3*, 281-287.
- (31) Juliano, T. R.; Korter, T. M. Terahertz Vibrations of Crystalline Acyclic and Cyclic Diglycine: Benchmarks for London Force Correction Models. *J. Phys. Chem. A* **2013**, *117*, 10504-10512.



(32) Frey, M. N.; Lehmann, M. S.; Koetzle, T. F.; Hamilton, W. C. Precision Neutron Diffraction Structure Determination of Protein and Nucleic Acid Components. XI. Molecular Configuration and Hydrogen Bonding of Serine in the Crystalline Amino Acids L-Serine Monohydrate and Dl-Serine. *Acta Crystallogr. Sect. B* **1973**, *29*, 876-884.

(33) King, M. D.; Buchanan, W. D.; Korter, T. M. Investigating the Anharmonicity of Lattice Vibrations in Water-Containing Molecular Crystals through the Terahertz Spectroscopy of L-Serine Monohydrate. *J. Phys. Chem. A* **2010**, *114*, 9570-9578.

(34) Cambridge Structural Database; 1.16 ed.; Cambridge Crystallographic Data Centre: Cambridge, UK, 2014.

## **CHAPTER 6. Evaluating London Dispersion Force Corrections in Crystalline Nitroguanidine by Terahertz Spectroscopy**

The material contained within this chapter has been published in *IEEE Transactions on Terahertz Science and Technology*. (Juliano, T. R., Jr.; Korter, T. M. *IEEE Trans. THz. Sci. and Tech.*, **2013**, 3, 281-287. Invited.) This article has been reproduced with permission from IEEE.

### **Abstract**

The low-frequency vibrations of the crystalline explosive nitroguanidine have been investigated using pulsed terahertz spectroscopy (10 to 100  $\text{cm}^{-1}$ ) and analyzed with solid-state density functional theory simulations. The terahertz spectrum recorded at 78 K exhibited five distinct absorptions that have been successfully assigned using PBE/cc-pVTZ augmented with semi-empirical London force dispersion corrections. This computational investigation of the nitroguanidine structure and dynamics in the solid-state also included a study of the utilized dispersion force correction parameters, resulting in the development of new values for use in the analysis and prediction of the terahertz spectra of molecular solids. The applied models enabled the observed spectral absorptions to be assigned to external rigid rotations and translations of the molecules in the crystal. The assignments were further validated by a complementary study of perdeuterated nitroguanidine.

**Keywords:** explosive, far-infrared, intermolecular forces, low-frequency vibrations

## 6.1 Introduction

Terahertz (THz) spectroscopy provides a means for directly probing the intermolecular forces between molecules in the solid state by accessing the low-frequency vibrational motions that dominate the sub-100  $\text{cm}^{-1}$  spectral region. The investigation of lattice vibrations, specifically the translations and rotations of the molecular components within the crystalline arrangement, enables greater understanding of these forces to be achieved and also enables characteristic spectral signatures for various compounds to be identified.<sup>1,2</sup> Terahertz spectroscopy can be used to detect and identify a wide range of molecules including explosives<sup>3-6</sup>, narcotics<sup>7-9</sup>, and pharmaceuticals.<sup>10</sup> The experimental observation of these low-frequency vibrations is only one aspect of the effective utilization of THz spectroscopy for achieving new insights into intermolecular forces. A critical step in the process is proper interpretation of the spectroscopic data. Since the vibrations existing at these frequencies are either produced by the bulk or heavily influenced by the local environment, simulations of structure and dynamics need to integrate effects beyond the single molecule. Solid-state density functional theory (DFT), incorporating periodic boundary conditions, is able to efficiently calculate the internal and external structures of molecular solids, while simultaneously yielding the molecular and lattice vibrations of the crystalline material.<sup>11-13</sup> Such simulations allow the assignment of the observed THz absorption features to specific motions in the solid and permit the evaluation of the potential energy surfaces governing crystalline structures.

While solid-state DFT is a powerful technique, it often relies upon density functionals that generally are unable to accurately account for weak London dispersion forces. The neglect of weak forces can lead to significant structural errors in the simulations of solids, especially those substances lacking any strong intermolecular attractions such as hydrogen bonding or ion-

ion interactions. New density functionals are continuously being introduced to better treat London dispersion forces,<sup>14-17</sup> but the use of well-established density functionals, such as that devised by Perdew, Burke, and Ernzerhof (PBE) is far more common.<sup>18</sup> The performance of such density functionals has been improved with the implementation of semi-empirical London dispersion corrections to these existing standard formulations as proposed by Grimme (DFT-D2).<sup>19</sup> The general formula for the energy correction is

$$E_{disp} = -s_6 \sum_{i=1}^{N_{at}-1} \sum_{j=i+1}^{N_{at}} \frac{C_6^{ij}}{R_{ij}^6} f_{dmp}(R_{ij}) \quad (6.1)$$

$$f_{dmp}(R_{ij}) = \frac{1}{1 + e^{-d(\frac{R_{ij}}{R_r} - 1)}} \quad (6.2)$$

where  $N_{at}$  is the number of atoms in the system,  $C_6^{ij}$  is the dispersion coefficient for the atom pair  $ij$ ,  $s_6$  is the global scaling factor,  $R_{ij}$  is the interatomic distance, and  $R_r$  is the sum of the van der Waals radii (vdW). The vdW radii are derived from ROHF/TZV computations of atoms in the ground state.<sup>19</sup> The  $C_6^{ij}$  term is determined by the equation

$$C_6^a = 0.05NI_p^a\alpha^a \quad (6.3)$$

where  $N$  is 2, 10, 18, 36, or 54 based on the last element of rows 1-5 of the periodic table,  $I_p$  is the atomic ionization potential, and  $\alpha$  is the static dipole polarizability. The DFT-D2  $C_6$  component values are theoretically derived from the London formula for dispersion, based on DFT/PBE0 calculations of  $I_p$  and  $\alpha$ .<sup>19</sup> Since the parameters directly affect the total dispersion

energy correction, the success of the dispersion corrections is highly dependent on the values used for the variables found in the methodology. Even the form of the dispersion correction equations themselves have been the subject of continued study.<sup>20</sup>

The DFT-D2 model has subsequently been modified by Civalleri et. al. (DFT-D\*) and optimized for use in solid-state calculations.<sup>21</sup> The difference between the two is that DFT-D\* introduces scaling factors to the vdW radii. The DFT-D2 values for vdW radii are used as the basis, but the values are multiplied by 1.30 for hydrogen and 1.05 for all other elements. The DFT-D\* approach was found to provide a better model than DFT-D2 for the simulation of molecular solids in terms of lattice dimensions and cohesive energies.<sup>21</sup>

In this work, time-domain pulsed THz spectroscopy and solid-state DFT simulations, using the CRYSTAL09 software package,<sup>22</sup> have been used to investigate the structure and low-frequency vibrations of the crystalline explosive nitroguanidine (NG) at low temperature (78 K). In addition, isotopic substitution (deuteration) was utilized to test the efficacy of this common technique for the assignment of low-frequency motions. Nitroguanidine is a flammable solid used in explosive and propellant formulations, most notably, smokeless gunpowder.<sup>23</sup> Its vibrational character has been previously studied using room-temperature THz spectroscopy,<sup>24</sup> Raman spectroscopy,<sup>25</sup> and IR spectroscopy.<sup>26</sup> The absorption features in the THz spectrum have not been previously assigned.

Experimental spectra of NG and its fully deuterated form (d-NG) were collected from 10 to 100  $\text{cm}^{-1}$  (0.3 to 3 THz) at 78 K (liquid nitrogen). Solid-state DFT calculations using the general gradient approximation PBE<sup>18</sup> functional with the cc-pVTZ<sup>27</sup> basis set for both structural and spectral simulations were used in the data analysis. To correct for the poor modeling of weak intermolecular forces, London-type dispersion corrections were applied using the established

DFT-D2 and DFT-D\* approaches as well as with a reparameterization first reported here. For this third correction (termed DFT-DX), the parameters were redefined using values originating from experimental measurements (when available) for ionization potentials, polarizability volumes, and van der Waals radii.<sup>28-30</sup> As will be demonstrated, this modification resulted in the improvement of the quality of both the structural and spectral calculations, suggesting that DFT-DX may be a valuable variation of the DFT-D2 London force correction model.

## 6.2 Experimental

Nitroguanidine was purchased from Sigma Aldrich (lot #14321CDV) and was used as received with no further purification, but oven dried to remove residual water. Single crystals were grown for X-ray diffraction measurements by slow evaporation of a saturated aqueous solution. X-ray crystallographic data at 90 K was collected at Syracuse University and this structure was used as the standard structure for all comparisons. At 90 K, the NG crystal structure (**Figure 6-1**) is consistent with other reports<sup>31</sup> and exhibits space group symmetry of *Fdd2* with unit cell dimensions of  $a=17.5577 \text{ \AA}$ ,  $b=24.852 \text{ \AA}$ , and  $c=3.4964 \text{ \AA}$ , volume= $1525.6 \text{ \AA}^3$ , and  $Z=16$ . Deuterated NG was formed by dissolving NG in D<sub>2</sub>O and recrystallizing it by evaporation in a vacuum oven. This was repeated three successive times to ensure full deuterium substitution.

Experimental THz spectra were obtained using a time-domain pulsed THz spectrometer based on an amplified Ti:Sapphire femtosecond laser system. Zinc telluride crystals were used for both generation of THz radiation by optical rectification and detection by free-space electro-optic sampling.<sup>32,33</sup> A detailed description of the spectrometer has been previously reported.<sup>8</sup>

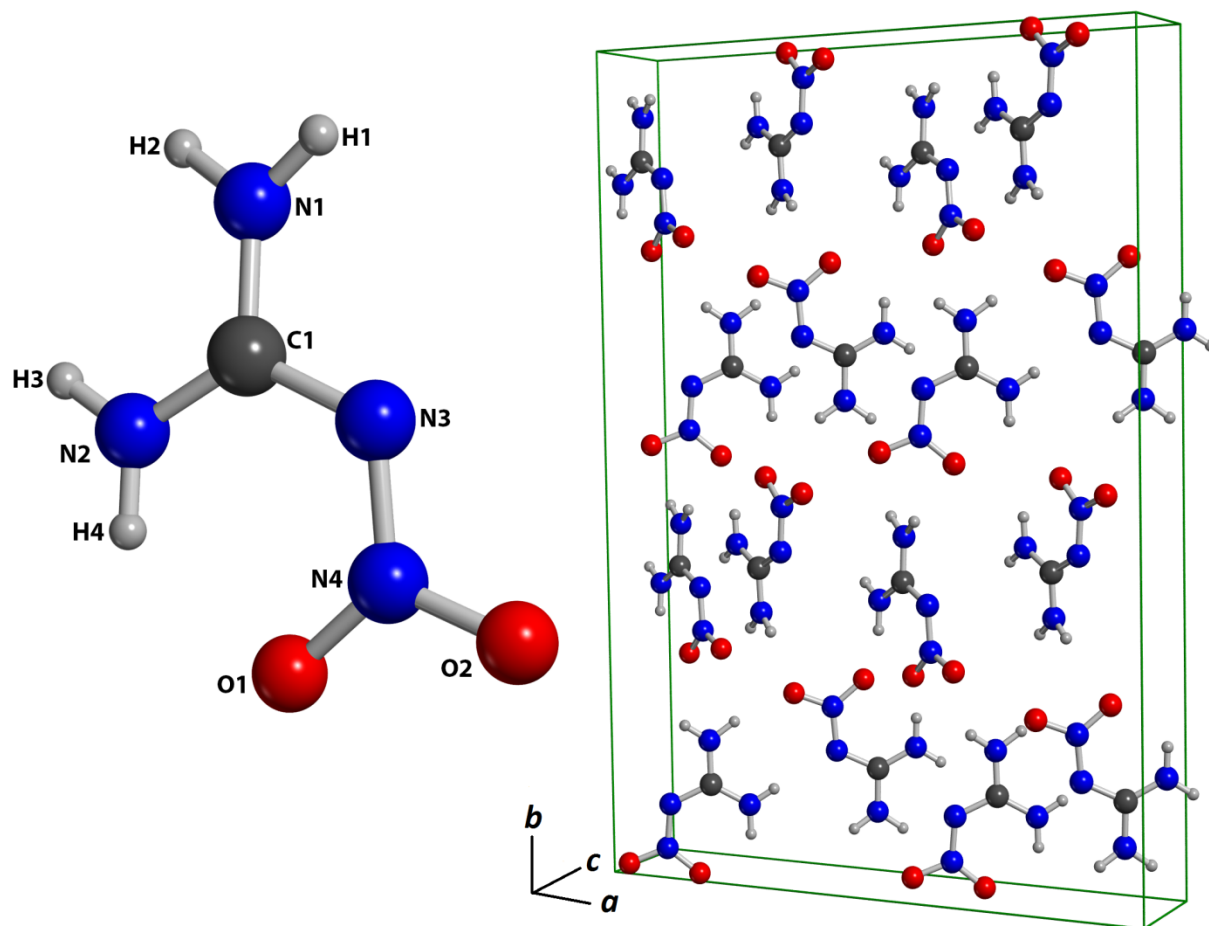


**Figure 6-1.** Labeled nitroguanidine molecule and nitroguanidine unit cell.

Samples of NG and d-NG were mixed with polytetrafluoroethylene (PTFE) powder to dilute the samples to a concentration of approximately 1% by mass. The sample/PTFE mixtures were then pulverized in a stainless steel ball mill (Dentsply Rinn 3110-3A) to minimize particle size and reduce the scattering of THz radiation<sup>34</sup> and other spectral feature issues associated with Kramers-Kronig<sup>35,36</sup> relations and the Christiansen effect.<sup>37</sup> After pulverization, approximately 0.55g of each mixture was pressed into separate pellets using a hydraulic press (ICL EZ-Press 12) under a measured pressure of 2000 psi. The press uses a 13-mm diameter stainless steel die, producing pellets of 13 x 2.2 mm thickness. The blank, a pure PTFE pellet, was produced using the same procedure. The samples and blank were held in a variable temperature cryostat under vacuum and data was acquired at 78 K. The time-domain THz waveform was captured using a 32 ps scan window consisting of 3200 data points. This data was then symmetrically zero-padded to 6000 total points before data transformation. Sample and blank pellets were scanned 32 times each and averaged for each individual set. Fourier transforms were performed using a Hanning window and a spectral resolution of approximately 1.0 cm<sup>-1</sup> resulted. The THz absorption spectra were obtained from the ratio of the power spectra (Fourier-transformed data) of the samples and blank. The final THz spectra presented in this work are the average of four individual THz spectra, each representing a complete set of sample and blank measurements.

### 6.3 Theoretical

Solid-state DFT calculations were performed using the CRYSTAL09 software package.<sup>22</sup> All calculations utilized the PBE density functional<sup>18</sup> with the atom-centered cc-pVTZ basis set.<sup>27</sup> Semi-empirical London type dispersion corrections of varying parameterizations were used throughout the calculations. Three variations of the corrections were used for both optimizations



and frequencies: DFT-D2, DFT-D\*, and DFT-DX. As described before, DFT-D2 and DFT-D\* use completely theoretical values for  $R_r$ ,  $I_p$ , and  $\alpha$ . When utilizing the new DFT-DX approach, the values of the dispersion parameters were changed to more accurately represent the atoms in the NG molecule by using standard experimental values (when available) for van der Waals radii, ionization potentials, and polarizabilities (**Table 6-1**).<sup>28-30</sup>

**Table 6-1.**  $C_6$  ( $\text{J nm}^6 \text{ mol}^{-1}$ ) and vdW radii ( $\text{\AA}$ ) values for DFT-D2, DFT-D\*, and DFT-DX.

Atom	DFT-D2		DFT-D*		DFT-DX	
	$C_6$	vdW radii	$C_6$	vdW radii	$C_6$	vdW radii
H	0.14	1.001	0.14	1.301	0.03	1.10
C	1.75	1.452	1.75	1.525	0.91	1.70
N	1.23	1.397	1.23	1.467	0.59	1.55
O	0.70	1.342	0.70	1.409	0.34	1.52

Simulations of the solid-state structure used initial atomic positions and lattice dimensions taken from the 90 K X-ray crystallographic data. These geometry optimizations allowed for full relaxation of all lattice dimensions and atomic positions, so long as the *Fdd2* space group symmetry was preserved.

Total energy convergence criteria for geometry optimizations and normal mode calculations were set to  $\Delta E < 10^{-8}$  hartree and  $\Delta E < 10^{-11}$  hartree, respectively. A shrinking factor of 8 (125  $k$  points in the irreducible Brillouin zone) was used in the NG calculations, based on the sampling and monitoring of the total energy convergence as a function of  $k$ -point count in reciprocal space according to the Pack-Monkhorst method.<sup>38</sup> The radial and angular distributions were defined by a (75,794) DFT integration grid. Truncation tolerances used for Coulomb and HF exchange integral series were set to the default values of  $10^{-6}$ ,  $10^{-6}$ ,  $10^{-6}$ ,  $10^{-6}$ , and  $10^{-12}$  hartree. Frequencies of normal modes were calculated within the harmonic approximation by numerical differentiation of the analytical gradient of the potential energy with respect to atomic

position. Infrared intensities for normal modes were calculated from the dipole moment derivatives ( $d\mu/dQ$ ) determined using the Berry phase approach to calculate the Born charge tensor.<sup>22,39</sup>

## 6.4 Results and Discussion

### 6.4.1 Experimental Section

The experimental THz spectrum of NG from 10 to 100  $\text{cm}^{-1}$  at 78 K is shown in **Figure 6-2** and the observed features are listed in **Table 6-2**. Room-temperature spectral data has been reported by Chen et. al.<sup>24</sup> and the cold spectrum shown here is consistent with their data. As compared to room temperature, when cooled to liquid-nitrogen temperature, the absorptions narrow and shift to higher energy. This sharpening is due to fewer vibrational states being thermally populated at the colder temperature. Also at the lower temperature, the unit cell volume is reduced due to anharmonicity effects, leading to the observed higher-energy shifting of the peaks.

**Table 6-2.** Comparison of experimental frequencies ( $\text{cm}^{-1}$ ) and intensities ( $\text{M}^{-1} \text{cm}^{-1}$ ) of nitroguanidine (NG) and its deuterated analogue (d-NG) and the percent frequency shift due to deuteration.

NG		d-NG		% frequency shift on deuteration
freq	$\epsilon$	freq	$\epsilon$	
43.9	23.29	43.0	34.68	-0.7
50.9	99.39	50.4	108.91	-1.0
69.5	80.04	69.2	88.35	-0.4
86.0	390.58	85.3	342.32	-0.8
96.1	200.31	93.3	194.62	-2.9
-	-	97.2	205.47	-

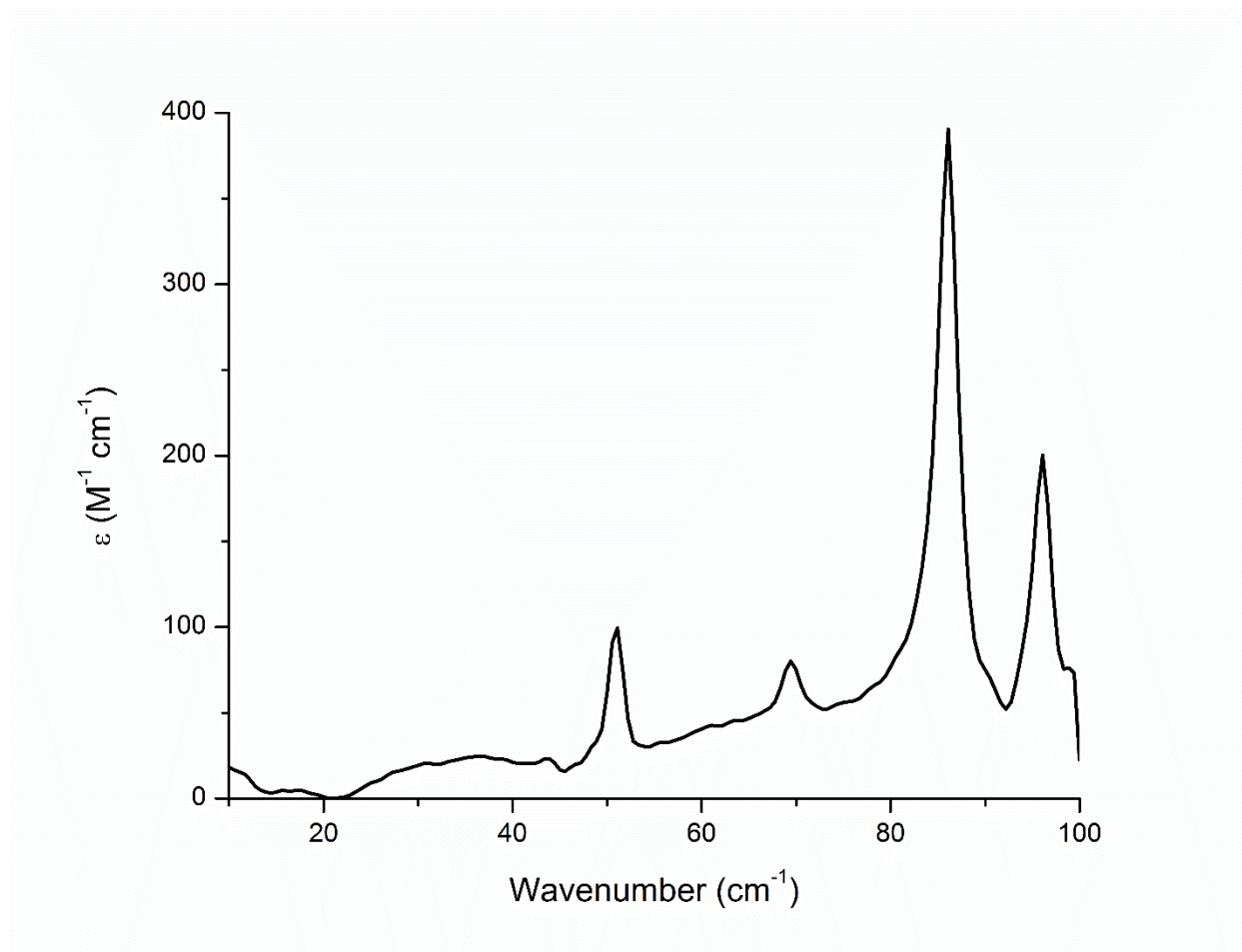


**Figure 6-2.** Terahertz spectrum of solid nitroguanidine at 78 K.

In an attempt to aid in the assignment of the absorptions to specific motions, the NG sample was perdeuterated and its THz spectrum recorded. The 78 K d-NG spectrum (**Figure 6-3**) showed essentially the same features as normal NG, except for a general shift of all vibrations to slightly lower energy. A sixth absorption feature at  $97.2\text{ cm}^{-1}$  appears in the d-NG spectrum that seems to not have a counterpart in the NG spectrum, however this peak is most likely present in the NG spectrum, just slightly outside the experimental bandwidth of the spectrometer. The infrared intensities of the absorptions do not change significantly. The frequency differences are listed in **Table 6-2** and are consistent with the increased mass of the deuterated compound. While the magnitudes of the shifts are small, they do vary from peak to peak and therefore may be useful in identifying the underlying molecular motions. These experimental mass-induced frequency shifts can be coupled with theoretical predictions to clarify the spectral assignments.

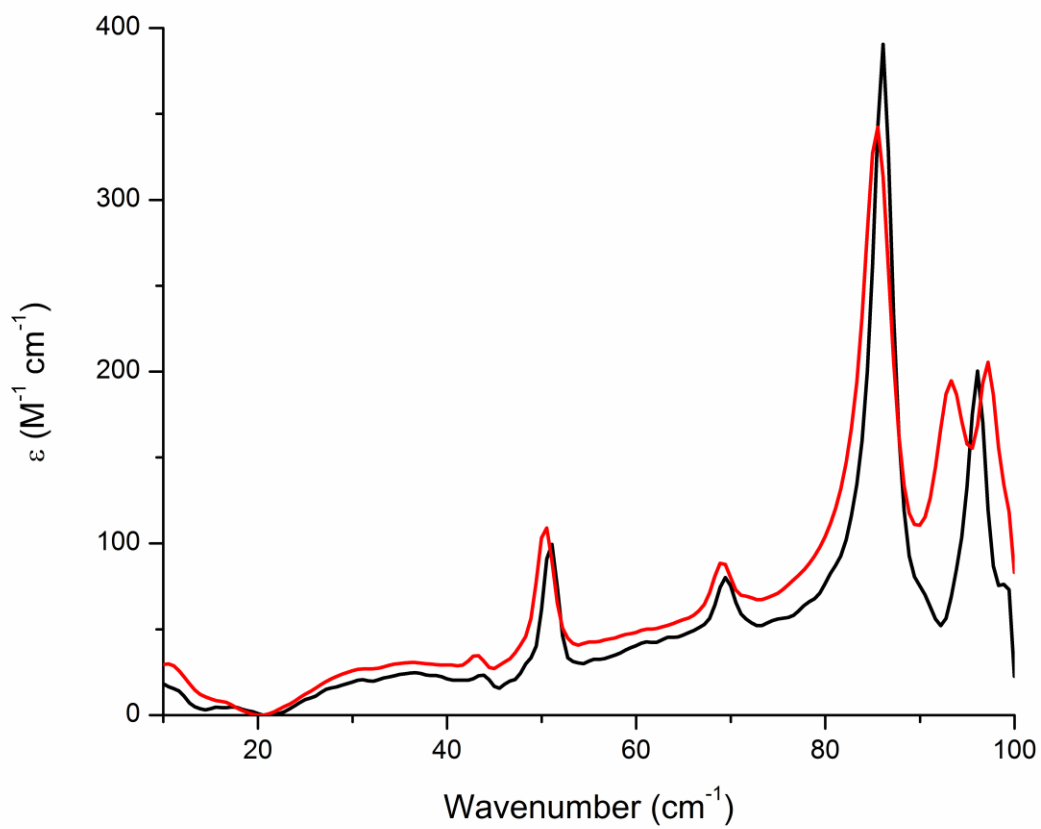


**Figure 6-3.** Terahertz spectra of solid nitroguanidine (black) and fully-deuterium substituted nitroguanidine (red) at 78 K.

## 6.4.2 Theoretical Section

### 6.4.2.1 Structural Analysis

The importance of including dispersion corrections in the calculations was evaluated by first performing simulations without these corrections. The resulting structure showed a large increase in unit cell volume of over 15%. This result is typical for calculations of structures of molecular solids that ignore London dispersion forces.<sup>21</sup> Given the physically unrealistic dimensions arrived at by the simulations without London force corrections, the need for their consideration is clear. Even though a meaningful THz spectrum could not be calculated using this structure (a representative THz spectrum based on this structure is provided in the Supplementary Information), these calculations do have some value. They demonstrate that weak London dispersion forces are important for the physically accurate simulation of the solid-state structure of NG despite the presence of numerous strong intermolecular hydrogen bonds.

London-type dispersion corrections were added to the calculations using three approaches, DFT-D2, DFT-D\* and the newly modified approach, DFT-DX, proposed here. These dispersion corrections were added in order to generate the best possible theoretical structures for NG from the full optimization of all atomic positions and lattice parameters (with preservation of space group symmetry). In order to ensure that the dispersion corrections were properly applied in the full optimization calculations, the global  $s_6$  scalar was optimized to minimize the absolute differences in the calculated lattice dimensions ( $a$ ,  $b$ ,  $c$ , and volume) when compared to the 90 K X-ray structure. The optimal  $s_6$  value for both DFT-D2 and DFT-D\* was found to be 0.60, less than the suggested value of 0.75 when using the PBE functional,<sup>19</sup> but similar to that found in other studies.<sup>40</sup> When using the DFT-DX corrections, an increase to 0.95 was necessary to produce the best structure. **Table 6-3** summarizes the errors in the unit cell

parameters generated by the calculations with optimal  $s_6$  values as compared to the experimental X-ray structure.

**Table 6-3.** Percent errors in unit cell parameters of calculated structures compared to X-ray data using different dispersion correction methods.

Parameter	No Dispersion Correction	DFT-D2 $s_6 = 0.60$	DFT-D* $s_6 = 0.60$	DFT-DX $s_6 = 0.95$
Volume ( $\text{\AA}^3$ )	15.66	-2.84	-2.18	1.44
A ( $\text{\AA}$ )	-6.29	-1.47	-0.92	0.56
B ( $\text{\AA}$ )	-0.14	-3.52	-3.48	-1.59
C ( $\text{\AA}$ )	23.60	2.20	2.28	2.50
Abs. Ave. Error	11.42	2.51	2.21	1.52

Overall, all of the resulting structures were similar to the experimental structure, but that generated using DFT-DX showed significantly better agreement versus the other simulations. Based on this evaluation, DFT-DX generated a unit cell with an absolute average dimensional error of 1.52%, while DFT-D\* yielded 2.21%, and the DFT-D2 approach, 2.51%.

It is important to evaluate the atomic-level accuracy of the DFT calculated structures to ensure that high quality reproductions of the crystal structures, and the vibrational spectra derived from them, have been achieved. For this, the calculated structures were compared to the 90 K X-ray crystallographic structure by calculation of the root-mean-squared deviations (RMSDs) of the bond lengths, bond angles, and bond dihedral angles (**Table 6-4**).

**Table 6-4.** Evaluation of RMSDs of calculated bond lengths, bond angles, and dihedral angles for nitroguanidine.

Dispersion Correction Method	Bond Length $\text{\AA}$	Bond Angle $^\circ$	Dihedral Angle $^\circ$
DFT-D	0.0292	0.3457	1.4701
DFT-D*	0.0293	0.3207	1.1077
DFT-DX	0.0292	0.3439	0.8337

The quality of the molecular packing of the calculated unit cell was assessed by comparing the intermolecular (plus one intramolecular) hydrogen bond heavy-atom separations to those from the experimental structure (**Table 6-5**).

**Table 6-5.** Comparison of the theoretical and experimental hydrogen bond heavy-atom distances (Å) in crystalline nitroguanidine.

Hydrogen Bond	Experimental	DFT-D2	DFT-D*	DFT-DX
<u>Intermolecular</u>				
N <sub>1</sub> H <sub>1</sub> ...O <sub>1</sub>	3.254	3.027	3.038	3.157
N <sub>1</sub> H <sub>2</sub> ...O <sub>2</sub>	2.937	2.901	2.907	2.929
N <sub>2</sub> H <sub>3</sub> ...N <sub>3</sub>	3.107	3.056	3.075	3.131
N <sub>2</sub> H <sub>4</sub> ...O <sub>1</sub>	2.991	2.935	2.934	2.993
<u>Intramolecular</u>				
N <sub>2</sub> H <sub>4</sub> ...O <sub>1</sub>	2.596	2.604	2.613	2.622
Absolute Ave. Error	-	2.544	2.389	1.159

The hydrogen-bond evaluation utilized only heavy atoms because of the uncertain hydrogen atom positions as determined by X-ray crystallography.

All three calculations provided very similar results for bond lengths with RMSD values of 0.0292 Å, 0.0293 Å, and 0.0292 Å for the DFT-D2, DFT-D\*, and DFT-DX methods, respectively. In a similar fashion, little variation is seen in the bond angle RMSD analysis with 0.3457°, 0.3207°, and 0.3439° for the DFT-D2, DFT-D\*, and DFT-DX methods, respectively. These results are expected because the application of long-range dispersion corrections should have little influence on the intramolecular covalent bond lengths and angles. The bond dihedral angles are where the changes are expected to be larger, due to the dispersion corrections having a significant effect on the packing of the molecules within the unit cell and therefore possibly an



influence on the overall molecular structure. A clear improvement was found in the RMSD for the dihedral angles when utilizing DFT-DX, achieving  $0.834^\circ$ , versus the DFT-D2 approach yielding  $1.470^\circ$  and DFT-D\* giving  $1.108^\circ$ .

The packing of the molecules in the unit cell is very important when analyzing the THz spectrum of a crystalline solid and the quality of this spatial arrangement in the simulations can be evaluated through inspection of the heavy atom positions in hydrogen bonds. Nitroguanidine exhibits one intramolecular and four intermolecular hydrogen bonds, listed in **Table 6-5** with atomic labels as shown in **Figure 6-1**. The intramolecular hydrogen bond,  $N_2-H_4 \cdots O_1$ , has an experimental  $N_2 \cdots O_1$  distance of 2.596 Å. All three of the calculations overestimate this interatomic separation, yielding 2.604 Å, 2.613 Å, and 2.622 Å for DFT-D2, DFT-D\*, and DFT-DX, respectively. The intermolecular hydrogen bonds correspond to the four amine hydrogens, bonded to  $N_1$  and  $N_2$ , interacting with neighboring NG molecules. The hydrogen bonds are as follows:  $N_1-H_1 \cdots O_1$ ,  $N_1-H_2 \cdots O_2$ ,  $N_2-H_3 \cdots N_3$ , and  $N_2-H_4 \cdots O_1$ . The absolute average error in the hydrogen bonds in the DFT-D2 calculation was 2.54%, in the DFT-D\* calculation it was 2.39%, and when using the DFT-DX approach, it is reduced to 1.16%. Using both the DFT-D2 and DFT-D\* approaches, all four of the hydrogen bond heavy atom distances are underestimated. When the DFT-DX approach is used, the two hydrogen bonds involving  $N_1$  are underestimated, while the two hydrogen bonds involving  $N_2$  are overestimated.

All three of the dispersion correction methods provide good reproductions of the internal (bond lengths, bond angles, and dihedral angles) and external (crystal axes) measurements. The use of dispersion corrections in the DFT simulations is crucial in the case of NG so that the unit cell dimensions and molecular contents can be accurately reproduced. The standard DFT-D2 and DFT-D\* corrections led to acceptable structures, showing deviations in

the unit cell parameters ( $a$ ,  $b$ ,  $c$ , and volume) of less than 3.5%. However, use of the DFT-DX approach produced a structure in which none of the errors exceeded 2.5%. DFT-DX also resulted in superior RMSD values for both the dihedral angles and heavy-atom hydrogen bond distances. These two structural parameters are particularly important because they influence the way in which the molecules are packed into the unit cells. Since THz spectroscopy focuses on the interactions between components in the unit cells, having the best possible intermolecular structure is clearly relevant to achieving accurate spectral simulations.

#### 6.4.2.2 Simulated Terahertz Spectra and Mode Assignments

The quality of the DFT calculated THz spectra (10 to 100  $\text{cm}^{-1}$ ) are compared to the 78 K experimental spectrum of NG in **Figure 6-4**. The calculated frequencies and intensities of the IR-active modes are listed in **Table 6-6** and descriptions of the vibrational mode characters assigned to the experimental features are listed in **Table 6-7**. The calculated intensities are generated and reported in units of  $\text{km mol}^{-1}$ , but these values are then converted into spectral absorption units ( $\text{M}^{-1} \text{cm}^{-1}$ ) using a Lorentzian line shape with a full width half-maximum (FWHM) determined empirically by least-squares fitting of the experimental spectra. The FWHM value of the features in the 78 K NG THz spectrum was found to be  $3.0 \text{ cm}^{-1}$ . When converting intensity units, the molarity refers to the molarity of primitive unit cells, noting that NG has a  $Z'=4$  asymmetric unit cell.

**Table 6-6.** Calculated IR-active mode frequencies ( $\text{cm}^{-1}$ ) and intensities ( $\text{km/mol}$ ) for nitroguanidine below  $150 \text{ cm}^{-1}$  using different dispersion correction parameterizations.

DFT-D2			DFT-D*			DFT-DX		
freq	intens	symm	freq	intens	symm	freq	intens	symm
52.5	3.70	B2	48.7	3.82	B2	50.6	2.98	B2
53.4	8.36	B1	50.7	2.18	A1	51.8	1.48	A1
57.4	1.69	A1	52.5	1.61	B1	55.7	1.07	B1
66.9	1.50	B2	63.6	4.66	B2	67.5	4.77	B2
87.5	1.69	B1	75.7	1.33	B1	79.1	1.91	B1
96.6	14.96	A1	91.6	26.22	A1	91.5	21.66	A1
97.7	24.20	B1	94.7	46.16	B2	95.4	53.31	B2
99.3	9.05	B2	100.4	4.04	A1	103.0	11.04	A1
106.9	24.45	A1	105.9	46.43	B1	104.8	50.47	B1
112.7	12.99	B1	112.8	17.37	B2	116.6	11.64	B2
123.7	62.17	B2	114.3	4.41	B1	117.3	1.56	B1
125.4	14.10	A1	119.3	9.57	A1	120.2	7.08	A1
141.8	27.32	A1	129.5	1.42	B1	128.1	1.02	B1
142.2	1.72	B1	134.4	22.27	A1	133.0	23.02	A1

**Table 6-7.** Vibrational character of the sub- $100 \text{ cm}^{-1}$  IR-active modes in nitroguanidine.

Experimental freq ( $\text{cm}^{-1}$ )	DFT-DX freq ( $\text{cm}^{-1}$ )	symm	mode description
50.9	50.6 <sup>a</sup>	B2	ET along <i>c</i>
	51.8 <sup>a</sup>	A1	ET along <i>b</i>
69.5	67.5	B2	ER about <i>b</i>
86.0	91.5	B2	ER about <i>c</i>
96.1	95.4	A1	ER about <i>c</i>

<sup>a</sup>The two calculated modes both contribute to the experimental mode.

<sup>b</sup>ET = external translation, ER = external rotation

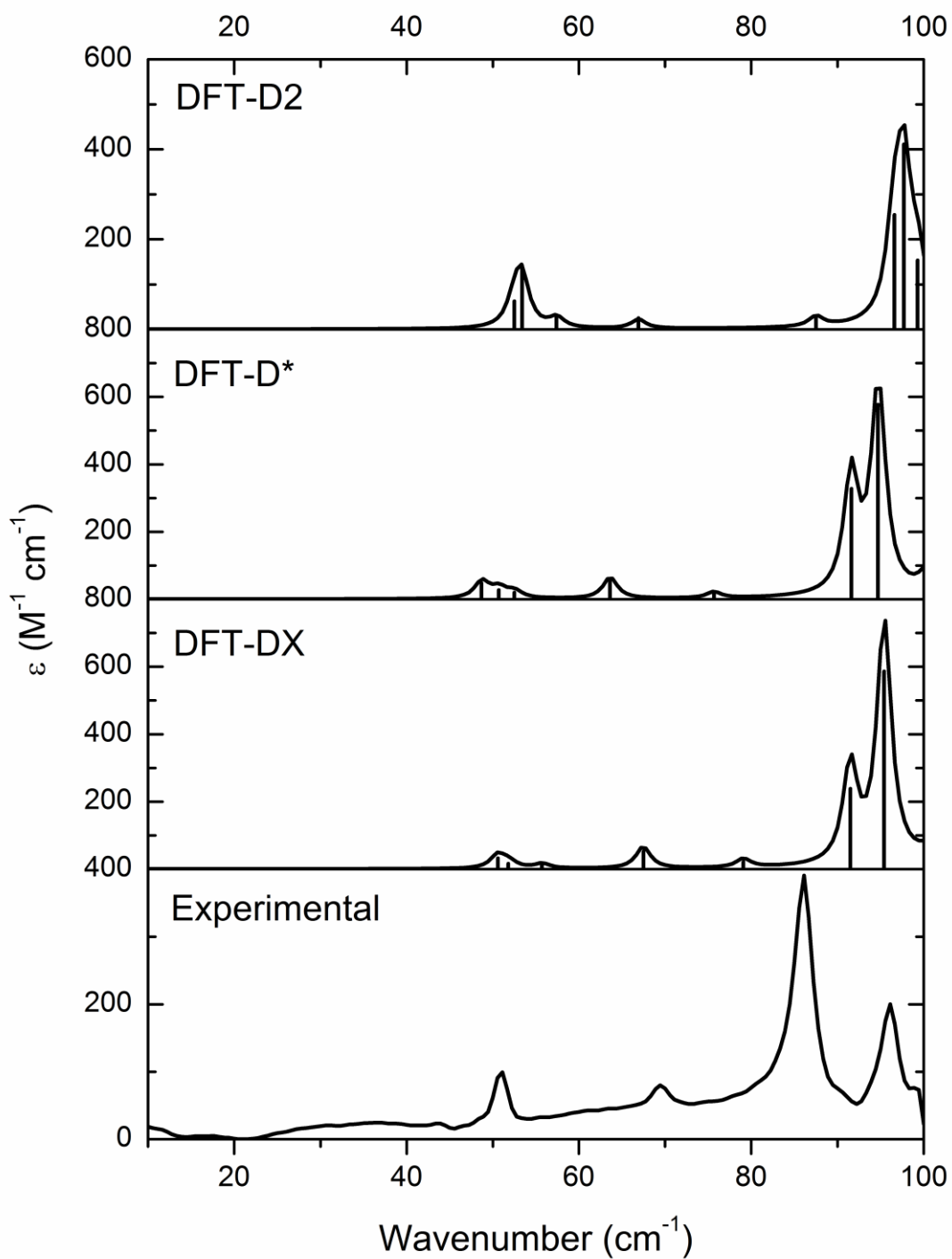


**Figure 6-4.** 78 K terahertz spectrum of nitroguanidine compared to the theoretical spectra generated using PBE/cc-pVTZ with DFT-D2, DFT-D\*, and DFT-DX London force corrections.

While all of the spectral simulations are qualitatively similar, certain aspects of the DFT-DX simulation identified it as the most successful reproduction of the experiment. These aspects include the positioning of the  $69.5\text{ cm}^{-1}$  peak and the splitting of the features at  $50.9\text{ cm}^{-1}$  and above  $\sim 80\text{ cm}^{-1}$ . This visual inspection led to the adopted mode assignments (**Table 6-7**) being based on the DFT-DX calculated spectrum. The first peak at  $50.9\text{ cm}^{-1}$  is represented by a combination of two modes,  $50.6$  and  $51.8\text{ cm}^{-1}$ , in the calculated spectrum. These modes are better aligned than the ones generated by DFT-D2 and DFT-D\*. In the experimental spectrum, the next mode is located at  $69.5\text{ cm}^{-1}$  and the corresponding peak in the calculated spectrum is at  $67.5\text{ cm}^{-1}$ . In all three of the theoretical approaches, the highest energy peaks have a reversed order of intensities as compared to the experiment. This indicates that either the ordering of the absorption features is incorrect in the simulations or the calculated intensities are incorrect. The issue can be resolved by utilizing the frequency shifts observed between the NG and the d-NG THz spectra, both experimentally and computationally. The percent shifts of the two highest frequency peaks for the experimental data are  $-0.8\%$  and  $-2.9\%$ . For the calculated spectra, the shift percentages for the same two peaks are  $-1.9\%$  and  $-4.1\%$ . These mass-induced frequency shifts enabled the ordering of these two peaks to be determined as being correct in the simulations, despite the infrared intensities suggesting the reverse assignment. Therefore, the simulated peaks actually do correspond to the ordering seen in the experimental spectrum and the experimental peaks at  $86.0\text{ cm}^{-1}$  and  $96.1\text{ cm}^{-1}$  correspond to the DFT-DX theoretical peaks at  $91.5\text{ cm}^{-1}$  and  $95.4\text{ cm}^{-1}$ , respectively. The origin of the intensity discrepancies for these features is unknown. Given these assignments, the frequency RMSD from the DFT-DX theoretical representation is  $1.5\text{ cm}^{-1}$ , significantly smaller than the RMSDs from DFT-D\* ( $2.1\text{ cm}^{-1}$ ) and DFT-D2 ( $2.8\text{ cm}^{-1}$ ). While most features are clearly assignable, there are some ambiguities. The

peak at  $43.3\text{ cm}^{-1}$  in the experimental spectrum is weak, and has no clear correspondence to any features found in the calculated spectra. The  $43.3\text{ cm}^{-1}$  feature does shift upon deuteration and remains even after re-crystallization of the sample, indicating that it is a vibration intrinsic to NG. Similarly, there is a peak seen in the calculated spectrum at  $79.1\text{ cm}^{-1}$ , that is not obvious in the experimental spectrum. This peak is likely under the base of the large peak located at  $86.0\text{ cm}^{-1}$ , as the left side of that peak is slightly asymmetric. It should be noted that the infrared intensities generated by the DFT-DX approach were approximately twice as intense as the experimental intensities, while the DFT-D\* modes are about one and a half times more intense, and the DFT-D2 predictions have only slightly higher intensities.

Overall, the DFT-DX method based on experimental  $C_6$  and vdW radii parameterizations produced a better theoretical structure and THz spectrum than the other London force corrections. Based on these results, this new dispersion correction parameterization shows promise, but needs further investigation by applying it in the simulation of the structure and dynamics of additional molecular solids to gauge its efficacy and transferability.

## 6.5 Conclusions

The THz spectrum of NG was measured from  $10$  to  $100\text{ cm}^{-1}$  at  $78\text{ K}$ , revealing sharp spectral features. Solid-state DFT simulations were performed on crystalline NG and their performance evaluated for both the reproduction of the measured crystal structure and observed THz vibrational frequencies. These calculations utilized three London force dispersion correction parameterizations, DFT-D2, DFT-D\*, and the newly modified DFT-DX approach. The use of all three corrections generated reasonable crystal structures and THz spectra as compared to experimental observations. However, the use of the DFT-DX correction, based on experimental

vdW radii and  $C_6$  parameters generally showed a more accurate prediction of the crystalline structure of NG and the lattice vibrations forming the basis of the THz spectrum. This suggests that basing London force correction parameters on empirical values can lead to superior results in molecular crystals. The validity of this idea will need to be tested against a variety of solid samples and this work is currently underway.

## **6.6 Acknowledgements**

Financial support by the National Science Foundation CAREER Program (CHE-0847405) is gratefully acknowledged. We thank Dr. Ewelina Witko and Sean Delaney for their aid in preliminary measurements and simulations, and Tiffany Smith for the collection of X-ray crystallographic data. We also thank Syracuse University for its continued support.

## 6.7 References

- (1) Beard, M. C.; Turner, G. M.; Schmuttenmaer, C. A. Terahertz Spectroscopy. *J. Phys. Chem. B* **2002**, *106*, 7146-7159.
- (2) Jepsen, P. U.; Cooke, D. G.; Koch, M. Terahertz Spectroscopy and Imaging – Modern Techniques and Applications. *Laser Photonics Rev* **2011**, *5*, 124-166.
- (3) Allis, D. G.; Prokhorova, D. A.; Korter, T. M. Solid-State Modeling of the Terahertz Spectrum of the High Explosive Hmx. *J. Phys. Chem. A* **2006**, *110*, 1951-1959.
- (4) Hu, Y.; Huang, P.; Guo, L.; Wang, X.; Zhang, C. Terahertz Spectroscopic Investigations of Explosives. *Phys. Lett. A* **2006**, *359*, 728-732.
- (5) Leahy-Hoppa, M. R.; Fitch, M. J.; Zheng, X.; Hayden, L. M.; Osiander, R. Wideband Terahertz Spectroscopy of Explosives. *Chem. Phys. Lett.* **2007**, *434*, 227-230.
- (6) Wilkinson, J.; Konek, C. T.; Moran, J. S.; Witko, E. M.; Korter, T. M. Terahertz Absorption Spectrum of Triacetone Triperoxide (Tatp). *Chem. Phys. Lett.* **2009**, *478*, 172-174.
- (7) Dobroiu, A.; Sasaki, Y.; Shibuya, T.; Otani, C.; Kawase, K. Thz-Wave Spectroscopy Applied to the Detection of Illicit Drugs in Mail. *Proceedings of the IEEE* **2007**, *95*, 1566-1575.
- (8) Hakey, P. M.; Allis, D. G.; Ouellette, W.; Korter, T. M. Cryogenic Terahertz Spectrum of (+)-Methamphetamine Hydrochloride and Assignment Using Solid-State Density Functional Theory. *J. Phys. Chem. A* **2009**, *113*, 5119-5127.
- (9) Wang, G.; Shen, J.; Jia, Y. Vibrational Spectra of Ketamine Hydrochloride and 3, 4-Methylenedioxymethamphetamine in Terahertz Range. *J. Appl. Phys.* **2007**, *102*, 013106-013104.
- (10) Zeitler, J. A.; Taday, P. F.; Gordon, K. C.; Pepper, M.; Rades, T. Solid-State Transition Mechanism in Carbamazepine Polymorphs by Time-Resolved Terahertz Spectroscopy. *ChemPhysChem* **2007**, *8*, 1924-1927.
- (11) Allis, D. G.; Zeitler, J. A.; Taday, P. F.; Korter, T. M. Theoretical Analysis of the Solid-State Terahertz Spectrum of the High Explosive Rdx. *Chem. Phys. Lett.* **2008**, *463*, 84-89.
- (12) King, M. D.; Korter, T. M. Effect of Waters of Crystallization on Terahertz Spectra: Anhydrous Oxalic Acid and Its Dihydrate. *J. Phys. Chem. A* **2010**, *114*, 7127-7138.
- (13) Hakey, P. M.; Allis, D. G.; Hudson, M. R.; Ouellette, W.; Korter, T. M. Investigation of (1r,2s)-(-)-Ephedrine by Cryogenic Terahertz Spectroscopy and Solid-State Density Functional Theory. *ChemPhysChem* **2009**, *10*, 2434-2444.
- (14) Vydrov, O. A.; Van Voorhis, T. Nonlocal van der Waals Density Functional Made Simple. *Phys. Rev. Lett.* **2009**, *103*, 063004/063001-063004.
- (15) Vydrov, O. A.; Van Voorhis, T. Nonlocal van der Waals Density Functional: The Simpler the Better. *J. Chem. Phys.* **2010**, *133*, 244103-244109.
- (16) Zhao, Y.; Truhlar, D. G. Density Functionals with Broad Applicability in Chemistry. *Acc. Chem. Res.* **2008**, *41*, 157-167.
- (17) Lee, K.; Murray, É. D.; Kong, L.; Lundqvist, B. I.; Langreth, D. C. Higher-Accuracy van der Waals Density Functional. *Phys. Rev. B: Condens. Matter* **2010**, *82*, 081101.
- (18) Perdew, J. P.; Burke, K.; Ernzerhof, M. Generalized Gradient Approximation Made Simple [Phys. Rev. Lett. *77*, 3865 (1996)]. *Phys. Rev. Lett.* **1997**, *78*, 1396-1396.



- (19) Grimme, S. Semiempirical Gga-Type Density Functional Constructed with a Long-Range Dispersion Correction. *J. Comput. Chem.* **2006**, *27*, 1787-1799.
- (20) Grimme, S.; Antony, J.; Ehrlich, S.; Krieg, H. A Consistent and Accurate Ab Initio Parametrization of Density Functional Dispersion Correction (DFT-D) for the 94 Elements H-Pu. *J. Chem. Phys.* **2010**, *132*, 154104-154119.
- (21) Civalleri, B.; Zicovich-Wilson, C. M.; Valenzano, L.; Ugliengo, P. B3LYP Augmented with an Empirical Dispersion Term (B3LYP-D\*) as Applied to Molecular Crystals. *CrystEngComm* **2008**, *10*, 405-410.
- (22) Dovesi, R.; Saunders, V. R.; Roetti, C.; Orlando, R.; Zicovich-Wilson, C. M.; Pascale, F.; Civalleri, B.; Doll, K.; Harrison, N. M.; Bush, I. J.; D'Arco, P.; Llunell, M.; Torino, U. o. T. *CRYSTAL09 User's Manual* **2009**.
- (23) Astakhov, A. M.; Dyugaev, K. P.; Kuzubov, A. A.; Nasluzov, V. A.; Vasiliev, A. D.; Buka, E. S. Theoretical Studies of the Structure of Nitrimes. I. Structure of 2-Nitroguanidine and Its Alkyl Derivatives. *Journal of Structural Chemistry* **2009**, *50*, 201-211.
- (24) Chen, J.; Chen, Y.; Zhao, H.; Bastiaans, G. J.; Zhang, X. C. Absorption Coefficients of Selected Explosives and Related Compounds in the Range of 0.1-2.8 Thz. *Opt. Express* **2007**, *15*, 12060-12067.
- (25) Fell, N. F.; Widder, J. M.; Medlin, S. V.; Morris, J. B.; Pesce-Rodriguez, R. A.; McNesby, K. L. Fourier Transform Raman Spectroscopy of Some Energetic Materials and Propellant Formulations II. *Journal of Raman Spectroscopy* **1996**, *27*, 97-104.
- (26) Oyumi, Y.; Rheingold, A. L.; Brill, T. B. Thermal Decomposition of Energetic Materials XXIV.
- A Comparison of the Crystal Structures, Ir Spectra, Thermolysis and Impact Sensitivities of Nitroguanidine and Trinitroethylnitroguanidine. *Propellants, Explosives, Pyrotechnics* **1987**, *12*, 46-52.
- (27) Dunning, T. H. Gaussian Basis Sets for Use in Correlated Molecular Calculations. I. The Atoms Boron through Neon and Hydrogen. *J. Chem. Phys.* **1989**, *90*, 1007-1024.
- (28) Miller, T. M.; Bederson, B. Atomic and Molecular Polarizabilities-a Review of Recent Advances. In *Advances in Atomic and Molecular Physics*; Bates, D. R., Benjamin, B., Eds.; Academic Press, 1978; Vol. Volume 13; pp 1-55.
- (29) *Crc Handbook of Chemistry and Physics*, 93 ed.; CRC Press/Taylor and Francis: Boca Raton, FL.
- (30) Sansonetti, J. E.; Martin, W. C. Handbook of Basic Atomic Spectroscopic Data. *J. Phys. Chem. Ref. Data* **2005**, *34*, 1559-2259.
- (31) Bracuti, A. J. Crystal Structure Refinement of Nitroguanidine. *J. Chem. Crystallogr.* **1999**, *29*, 671-676.
- (32) Wu, Q.; Litz, M.; Zhang, X. C. Broadband Detection Capability of ZnTe Electro-Optic Field Detectors. *Appl. Phys. Lett.* **1996**, *68*, 2924-2926.
- (33) Rice, A.; Jin, Y.; Ma, X. F.; Zhang, X. C.; Bliss, D.; Larkin, J.; Alexander, M. Terahertz Optical Rectification from <110> Zinc-Blende Crystals. *Appl. Phys. Lett.* **1994**, *64*, 1324-1326.
- (34) Shen, Y. C.; Taday, P. F.; Pepper, M. Elimination of Scattering Effects in Spectral Measurement of Granulated Materials Using Terahertz Pulsed Spectroscopy. *Appl. Phys. Lett.* **2008**, *92*, 051103-051103.

- (35) Herrmann, M.; Platte, F.; Nalpantidis, K.; Beigang, R.; Heise, H. M. Combination of Kramers–Kronig Transform and Time-Domain Methods for the Determination of Optical Constants in Thz Spectroscopy. *Vib. Spectrosc* **2012**, *60*, 107-112.
- (36) Peiponen, K. E.; Saarinen, J. J. Generalized Kramers–Kronig Relations in Nonlinear Optical- and Thz-Spectroscopy. *Rep. Prog. Phys.* **2009**, *72*, 056401.
- (37) Franz, M.; Fischer, B. M.; Walther, M. The Christiansen Effect in Terahertz Time-Domain Spectra of Coarse-Grained Powders. *Appl. Phys. Lett.* **2008**, *92*, 021107.
- (38) Monkhorst, H. J.; Pack, J. D. Special Points for Brillouin-Zone Integrations. *Phys. Rev. B: Condens. Matter* **1976**, *13*, 5188-5192.
- (39) Dall’Olio, S.; Dovesi, R.; Resta, R. Spontaneous Polarization as a Berry Phase of the Hartree-Fock Wave Function: The Case of KNbO<sub>3</sub>. *Phys. Rev. B: Condens. Matter* **1997**, *56*, 10105-10114.
- (40) King, M. D.; Ouellette, W.; Korter, T. M. Noncovalent Interactions in Paired DNA Nucleobases Investigated by Terahertz Spectroscopy and Solid-State Density Functional Theory. *J. Phys. Chem. A* **2011**, *115*, 9467-9478.

## CHAPTER 7. Terahertz Vibrations of Crystalline Acyclic and Cyclic Diglycine: Benchmarks for London Force Correction Models

The material contained within this chapter has been published in *The Journal of Physical Chemistry A*. (Juliano, T. R.; Korter, T. M. *J. Phys. Chem. A*. **2013**, *117*, 10504-10512.) This article has been reproduced with permission from the American Chemical Society.

### Abstract

Terahertz spectroscopy provides direct information concerning weak intermolecular forces in crystalline molecular solids and therefore acts as an excellent method for calibrating and evaluating computational models for non-covalent interactions. In this study, the low-frequency vibrations of two dipeptides were compared, acyclic diglycine and cyclic diglycine, as benchmark systems for gauging the performance of semi-empirical London force correction approaches. The diglycine samples were investigated using pulsed terahertz spectroscopy from 10 to 100  $\text{cm}^{-1}$  and then analyzed using solid-state density functional theory (DFT) augmented with existing London force corrections, as well as a new parameterization (DFT-DX) based on known experimental values. The two diglycine molecules provide a useful test for the applied models given their similarities, but more importantly the differences in the intermolecular forces displayed by each. It was found that all of the considered London force correction models were able to generate diglycine crystal structures of similar accuracy, but considerable variation occurred in their abilities to predict terahertz frequency vibrations. The DFT-DX parameterization was particularly successful in this investigation and shows promise for the improved analysis of low-frequency spectra.

Keywords: far-infrared, dipeptide, hydrogen bonding, lattice vibrations

## 7.1 Introduction

Weak, non-covalent intermolecular forces are the critical driving factors in the formation of specific crystalline arrangements of molecules in the solid state. Despite the low energies associated with such forces, understanding these interactions is of the utmost importance in elucidating the crystallization mechanisms in molecular solids such as pharmaceuticals and biomolecules. Our understanding of weak forces can be enhanced through the application of spectroscopic methods that directly access intermolecular interactions and the utilization of robust computational models that can simultaneously address both the covalent and non-covalent aspects of solid-state molecules.

Terahertz spectroscopy provides unique insights into the fundamental cohesive forces contained within condensed-phase materials. Intermolecular forces between solid-state molecules are readily explored by terahertz spectroscopy, since they directly impact the low-frequency vibrational modes seen in the sub-100  $\text{cm}^{-1}$  spectral region. This phenomenon gives powerful analytical capabilities to THz spectroscopy and it has been used to study and characterize a wide range of molecular solids, including explosives,<sup>1-4</sup> narcotics,<sup>5-7</sup> and pharmaceuticals.<sup>8,9</sup> On its own, terahertz spectroscopy provides measurement of the characteristic and identifying sub-100  $\text{cm}^{-1}$  vibrational features of various compounds, but it does not provide details of the specific nature of the vibrations.<sup>10,11</sup> To understand the chemical origins of the vibrations and extract out meaningful information concerning intermolecular forces, proper interpretation of the data is crucial. Since the vibrations in this region originate from the bulk material, or if intramolecular, are heavily influenced from the local environment, the method chosen for simulations must incorporate effects beyond single molecules. Solid-state density functional theory (DFT), utilizing periodic boundary conditions, is one method that is

able to calculate both the internal and external structures of molecular solids, while also simulating the molecular and lattice vibrations of crystalline materials.<sup>12-14</sup> Using DFT simulations, the assignment of the observed THz absorptions to specific atomic motions in the solid is possible and thus the intermolecular forces within the sample can be detailed.

Solid-state DFT is a powerful technique; however, the most common density functionals still fall short when the inclusion of weak London dispersion forces is necessary. In the cases of substances lacking significant intermolecular bonding, such as hydrogen bonding or ion-ion interactions, the neglect of weak forces can lead to large structural errors in the solid simulations.<sup>15</sup> To address these issues, new density functionals are continuously being developed,<sup>16-19</sup> as well as completely different approaches being pursued, such as explicit electron correlation with periodic MP2 in solids.<sup>20</sup> However, the use of well-established density functionals, such as that devised by Perdew, Burke, and Ernzerhof (PBE)<sup>21</sup>, is still commonplace given their widespread accessibility and computational efficiency. To improve the performance of these density functionals, semi-empirical London dispersion corrections, as proposed by Grimme,<sup>22</sup> have been incorporated into the calculations.

In this paper, the implementation of such corrections has been investigated in the study of two crystalline glycine dipeptides (Gly-Gly) using the unaltered Grimme approach (DFT-D2),<sup>23</sup> a modification of the Grimme method (DFT-D\*),<sup>15</sup> and a new approach that is parameterized with known experimental values (DFT-DX).<sup>24</sup> Acyclic diglycine (ADG) and cyclic diglycine (CDG) were chosen as the focus of this work because of their relative simplicities, yet they maintain their relevance to larger, more complex biological molecules. While both compounds are linkages of two glycine molecules, the different molecular structures create important variations in the intermolecular forces exhibited by each. For example, the ADG dipeptide can

accommodate eight intermolecular hydrogen bonds, while CDG has a maximum of four. This modification in the possible molecule-molecule interactions presents a test for the application of semi-empirical dispersion force corrections in DFT calculations. The theory must be robust enough to handle environments rich in hydrogen bonding, as well as those lacking strong van der Waals forces. These glycine dipeptides provide benchmarks for successful simulations and thus serve as a means for evaluating and improving London force correction models.

## 7.2 Methods

### 7.2.1 Experimental

Acyclic (lot #025K5440) and cyclic (lot #011M5420V) diglycine were purchased from Sigma Aldrich and used with no further purification, but were desiccator-dried to remove any residual water. The X-ray diffraction data for ADG has been reported at 100 K by Drebuschak, *et al.*<sup>25</sup> The space group of ADG is  $P2_1/c$  with unit cell dimensions of  $a=7.992 \text{ \AA}$ ,  $b=9.536 \text{ \AA}$ , and  $c=7.773 \text{ \AA}$ , volume= $569.016 \text{ \AA}^3$ , and  $Z=4$ .<sup>25</sup> Single crystals of CDG were grown from saturated aqueous solution and used to obtain X-ray diffraction measurements at 90 K at Syracuse University. The 90 K CDG crystal structure is consistent with the reported 120 K structure.<sup>26</sup> The space group of 90 K CDG is  $P2_1/c$  with unit cell dimensions of  $a=3.8995 \text{ \AA}$ ,  $b=11.556 \text{ \AA}$ , and  $c=5.1613 \text{ \AA}$ , volume= $231.13 \text{ \AA}^3$ , and  $Z=2$ . Single molecules and unit cells for ADG and CDG are shown in **Figures 7-1 and 7-2**, respectively. These two sets of data were used as the standards for all structural comparisons.

A detailed description of the time-domain pulsed THz spectrometer, based on an amplified Ti:Sapphire femtosecond laser system, has been previously reported in detail elsewhere.<sup>6</sup> Zinc telluride crystals were used for both generation of THz radiation by optical rectification and detection by free-space electro-optic sampling.<sup>27,28</sup> Samples of ADG and CDG

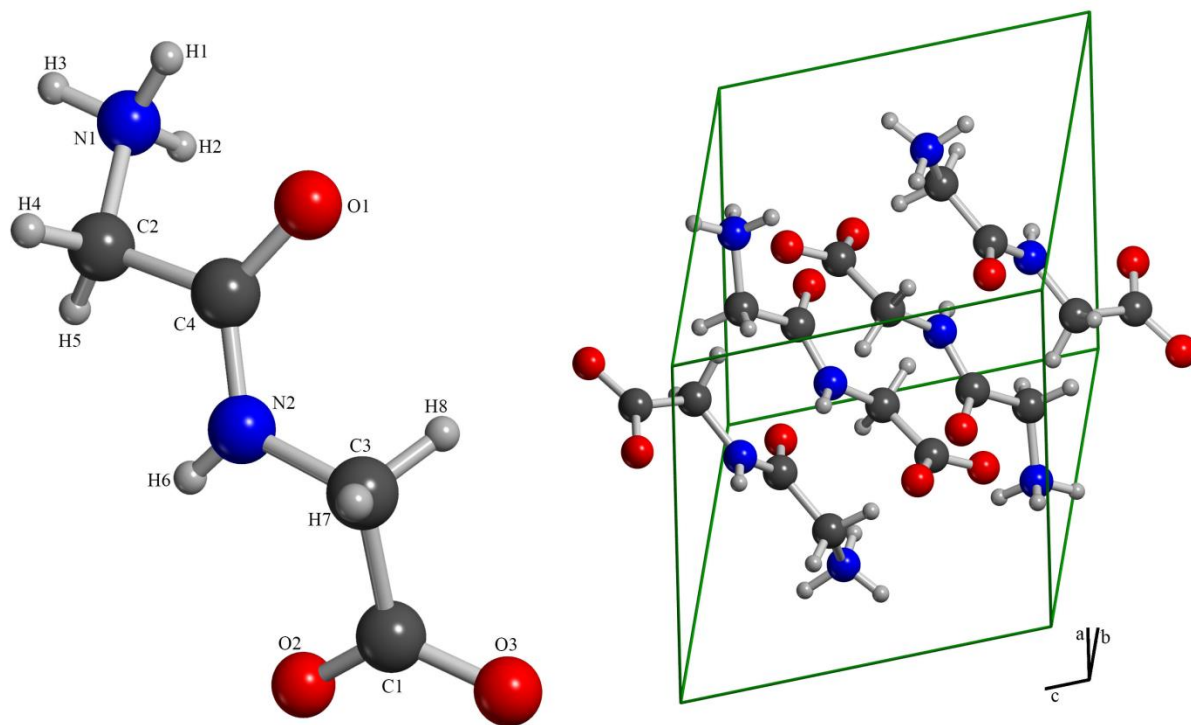


**Figure 7-1.** Labeled acyclic diglycine molecule and unit cell.

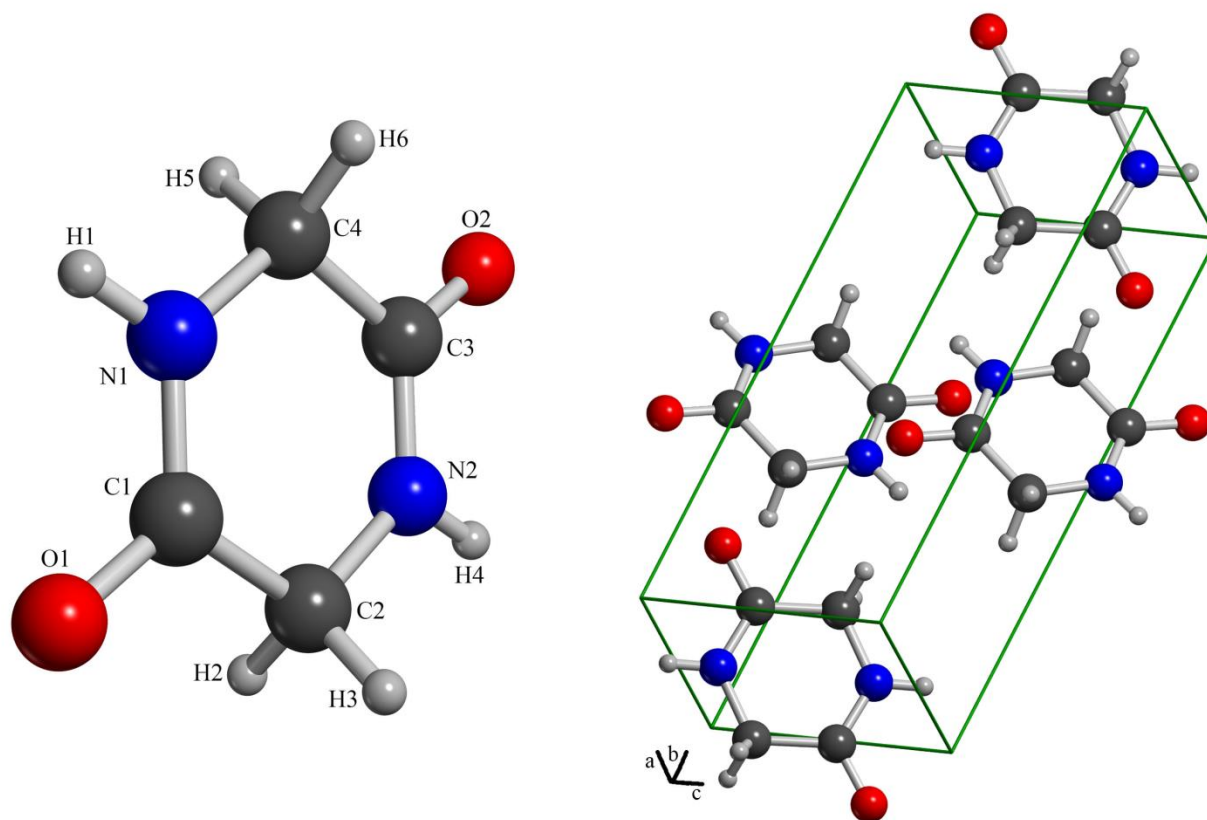


**Figure 7-2.** Labeled cyclic diglycine molecule and unit cell.



were mixed with polytetrafluoroethylene (PTFE) powder to dilute the samples to 1.0% and 7.4% by mass, respectively, due to significant differences in THz absorption strength. The mixtures were then pulverized in a stainless steel ball mill to reduce the scattering of THz radiation by ensuring small particle size.<sup>29</sup> Approximately 0.55 g of each pulverized sample was then taken and pressed into a pellet using a hydraulic press under a measured pressure of 2000 psi, producing pellets of 13 mm diameter and 2.2 mm thickness. A pure PTFE pellet was made in the same manner and used as a blank. A variable-temperature cryostat was used to hold the samples and blank under vacuum for both room-temperature (293 K) and cryogenic (78 K) data collection. A 32 ps scan window consisting of 3200 data points was used to capture the time-domain THz waveform with subsequent symmetrical zero-padding to 6000 points. Sample and blank pellets were scanned 32 times each and averaged for each individual set. Using a Hanning window, Fourier transforms were performed on the waveforms, resulting in a spectral resolution of approximately  $1.0 \text{ cm}^{-1}$ . Terahertz absorption spectra resulted from the ratio of the power spectra (Fourier transformed data) of the samples and blank. All THz spectra shown here are the averages of four separate THz absorption spectra, each representing a complete set of sample and blank measurements. Cubic spline interpolation has been applied for visual clarity.

### 7.2.2 Theoretical

The CRYSTAL09 software package<sup>30</sup> was used to perform all solid-state DFT calculations utilizing the PBE density functional<sup>21</sup> with the atom-centered cc-pVTZ basis set.<sup>31</sup> Calculations included semi-empirical London type dispersion corrections with varying parameterizations. The general formula<sup>23</sup> for the correction ( $E_{disp}$ ) is

$$E_{disp} = -s_6 \sum_{i=1}^{N_{at}-1} \sum_{j=i+1}^{N_{at}} \frac{C_6^{ij}}{R_{ij}^6} f_{dmp}(R_{ij}) \quad (7.1)$$

$$f_{dmp}(R_{ij}) = \frac{1}{1 + e^{-d(\frac{R_{ij}}{R_r-1})}} \quad (7.2)$$

where  $N_{at}$  is the number of atoms in the system,  $C_6^{ij}$  is the dispersion coefficient for the atom pair  $ij$ , defined by  $C_6^{ij} = \sqrt{C_6^i - C_6^j}$ ,  $s_6$  is the global scaling factor,  $R_{ij}$  is the interatomic distance, and  $R_r$  is the sum of the van der Waals radii. The  $C_6^a$  term is determined by the equation

$$C_6^a = 0.05 N I_p^a \alpha^a \quad (7.3)$$

where  $N$  is 2, 10, 18, 36, or 54 based on the last element of rows 1-5 of the periodic table,  $I_p$  is the atomic ionization potential, and  $\alpha$  is the static dipole polarizability.<sup>23</sup> The performance of the dispersion corrections is highly dependent on the values used for the variables found in the implementation. Three approaches were considered in this work, the regular DFT-D2, the modified DFT-D\*, and a newly developed, experimentally-based version, DFT-DX. DFT-D2 uses completely theoretical values for  $R_r$ ,  $I_p$ , and  $\alpha$ . DFT-D\* uses arbitrary scalars to modify the van der Waals radii of the original DFT-D2 method. DFT-DX introduces experimentally based values (whenever available) for the van der Waals radii, ionization potentials, and polarizabilities (**Appendix C, Table C1**).<sup>32-34</sup>

Initial atomic positions used in all calculations were taken from the X-ray crystallographic data mentioned above. All lattice dimensions and atomic positions were allowed to fully relax, so long as the space group symmetry ( $P2_1/c$ ) was preserved. Total energy convergence criteria for geometry optimizations and normal mode calculations were set to  $\Delta E <$

$10^{-8}$  hartree and  $\Delta E < 10^{-11}$  hartree, respectively. A shrinking factor of 8 (125  $k$  points in the irreducible Brillouin zone) was used in all calculations, based on the sampling and monitoring of the total energy convergence as a function of  $k$ -point count in reciprocal space according to the Pack-Monkhorst method.<sup>35</sup> Truncation tolerances used for Coulomb and HF exchange integral series were set to values of  $10^{-8}$ ,  $10^{-8}$ ,  $10^{-8}$ ,  $10^{-8}$ , and  $10^{-16}$  hartree. The radial and angular distributions were defined by a (75,794) DFT integration grid. Solid-state binding energies were calculated using the differences in the total solid-state energy as compared to isolated molecule energies and were corrected for basis set superposition error by the counterpoise method.<sup>36</sup> Normal mode frequencies were calculated within the harmonic approximation by numerical differentiation of the potential energy gradient with respect to atomic position. Infrared intensities for the normal modes were calculated from the dipole moment derivatives ( $d\mu/dQ$ ) determined using the Berry phase approach to calculate the Born charge tensor.<sup>30,37</sup> Spectral intensities are reported in units of  $\epsilon$  ( $M^{-1} \text{ cm}^{-1}$ ) where molarity is expressed in terms of the concentration of crystallographic unit cells ( $Z$ ).

## 7.3 Results and Discussion

### 7.3.1 Experimental

Experimental THz spectra of ADG and CDG are shown in **Figure 7-3**, from 10 to 100  $\text{cm}^{-1}$  at both 78 K and 293 K, with the observed frequencies listed in **Table 7-1**. The ADG spectra presented here are consistent with previously reported data.<sup>38,39</sup> When cooled to liquid-nitrogen temperature, from room temperature, the absorptions narrow and shift to higher energy. The narrowing of the features is due to fewer vibrational states being populated at 78 K.

Anharmonicity effects reduce the unit cell volume at low temperature, leading to the shifting of the vibrational absorptions to higher frequency for the majority of molecular solids.

The room-temperature spectrum of ADG showed one distinct peak at  $65.8\text{ cm}^{-1}$ , and a broad absorption from approximately  $80$  to  $95\text{ cm}^{-1}$ . When cooled, four distinct absorptions

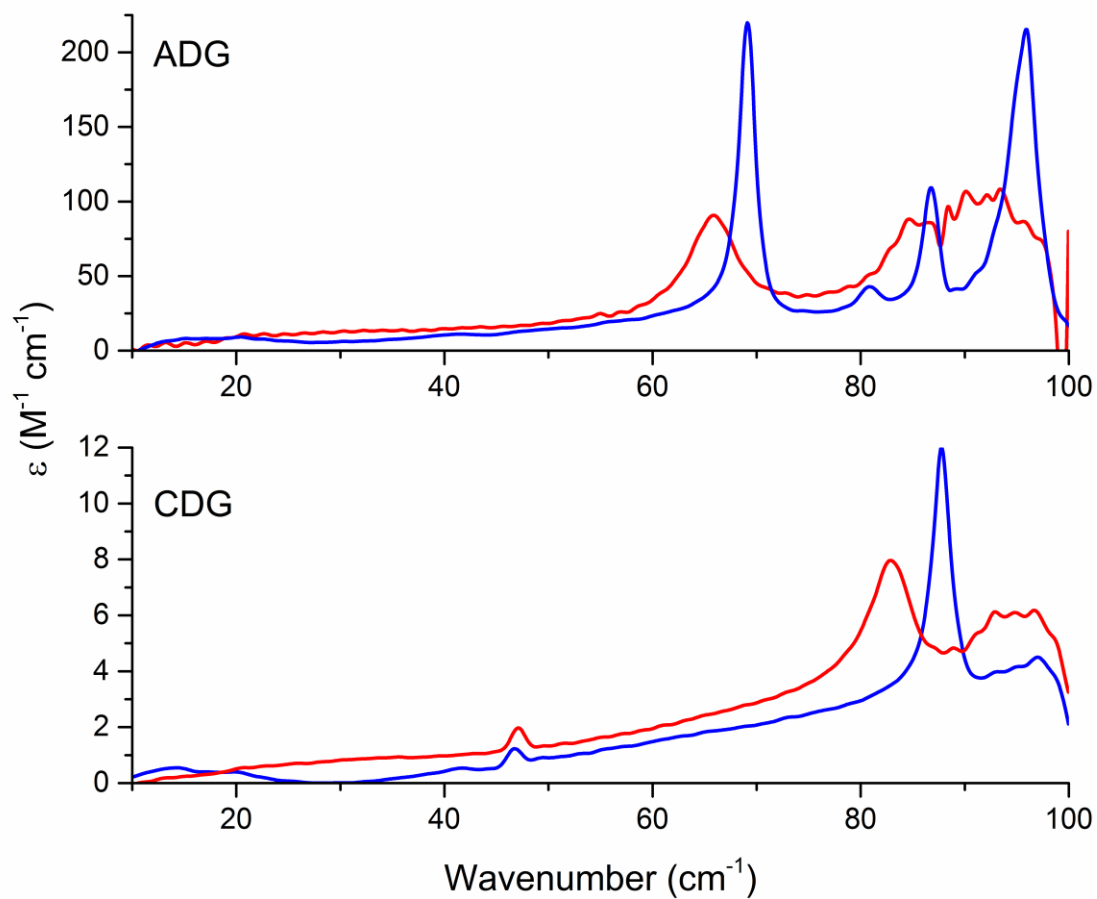


**Figure 7-3.** Terahertz spectra of acyclic diglycine (top panel) and cyclic diglycine (bottom panel) at 293 K (red) and 78 K (blue).

**Table 7-1.** Experimental frequencies ( $\text{cm}^{-1}$ ) and intensities ( $\text{M}^{-1} \text{cm}^{-1}$ ) of ADG and CDG.

ADG		CDG	
freq	$\epsilon$	freq	$\epsilon$
69.0	208.71	41.4	0.33
80.9	43.19	46.8	1.28
86.7	108.35	87.7	12.00
95.8	213.50	-	-

became visible in the spectrum centered at 69.0, 80.9, 86.7, and 95.8  $\text{cm}^{-1}$ , with the last three features resolving from the broad unstructured absorption seen at room temperature.

The CDG spectrum showed two apparent peaks in the 293 K spectrum centered at 47.0 and 82.7  $\text{cm}^{-1}$ . There was also a broad, unstructured absorption above 90  $\text{cm}^{-1}$ , near the edge of the spectral range. When cooled, these two absorptions sharpened and moved slightly, with the higher-energy peak shifting to higher frequency (87.7  $\text{cm}^{-1}$ ) and the lower-energy peak shifting to lower frequency (46.8  $\text{cm}^{-1}$ ). The red-shifting of a THz absorption feature on cooling is unusual, but there are a few reported observations.<sup>40,41</sup> A third absorption also became evident at 41.8  $\text{cm}^{-1}$ . The validity of this weak feature was confirmed using a second, high-concentration (50% w/w) CDG sample, and will be a focus of the discussion to follow.

## 7.3.2 Theoretical

### 7.3.2.1 Structural Analysis

Initial structural simulations for ADG and CDG were performed without the inclusion of dispersion corrections. These were carried out in order to gauge the general importance of such corrections in these particular solids. The ADG structural simulation with no dispersion force corrections produced an increase in unit cell volume of 11%, a large, but not unusual change.<sup>15</sup> In contrast, the structural simulation for CDG was never able to fully converge due to very large

deviations in the volume, unit cell axes, and  $\beta$ -angle. For example, the last generated structure of the optimization process showed an increase in unit cell volume of over 39%, significantly larger than most simulated solid-state structures.<sup>15</sup> Given the large deviations from experimental measurements in the solid-state structures without London force corrections, it is clear their presence is necessary to obtain physically reasonable crystal structures.

London-type dispersion corrections were added to the calculations using three different approaches, DFT-D2, DFT-D\*, and DFT-DX. The goal in using these corrections is to obtain the best possible structures for ADG and CDG, and ultimately, the closest reproduction of the experimental THz spectra. Combined, such observables show that the applied theory is able to successfully model the potential energy minima (structure) and the potential energy surface curvature (frequencies). The structural evaluation was performed by allowing the full optimization of all atom positions and lattice dimensions in these crystals, so long as space group symmetry was preserved. The global  $s_6$  scalar was optimized specifically for each correction/molecule combination, with the aim being to minimize the absolute differences in the calculated lattice dimensions ( $a$ ,  $b$ ,  $c$ , and volume) as compared to the cryogenic X-ray crystallographic data. **Table 7-2** lists the signed percent errors in the unit cell dimensions and the overall absolute average percent error achieved by using the optimized  $s_6$  values. The optimal  $s_6$  values found for ADG were 0.56, 0.75, and 2.06, using DFT-D2, DFT-D\*, and DFT-DX, respectively. The  $s_6$  value used with the DFT-D2 calculation was lower than the suggested value of 0.75.<sup>23</sup> When using DFT-D\*, the  $s_6$  value matched the suggested value for use with the PBE functional. The  $s_6$  for DFT-DX differentiates itself as being nearly three times larger than the standard scalar and twice as large as the  $s_6$  found for the DFT-DX model in the related study of crystalline nitroguanidine.<sup>24</sup> The larger magnitude of  $s_6$  in the DFT-DX approach is expected due

to a decrease in the  $C_6$  values used in it versus those utilized in DFT-D2 and DFT-D\* (**Table C1**). For CDG, the optimal  $s_6$  values found were 1.25, 0.69, and 1.93, using DFT-D2, DFT-D\*, and DFT-DX, respectively. The DFT-D2  $s_6$  value used was considerably higher than the suggested 0.75 value,<sup>23</sup> and more than twice its value found for the ADG solid. The DFT-D\*  $s_6$  value of 0.69 is fairly consistent with its value for ADG. Again, DFT-DX required a larger  $s_6$  value than the other models, yet the two DFT-DX  $s_6$  values for ADG and CDG (2.06 and 1.93, respectively) were very similar to each other. The DFT-D\* and DFT-DX results indicate at least some stability in the  $s_6$  scalar between systems.

**Table 7-2.** Percent errors in the unit cell parameters of the calculated structures of CDG and ADG as compared to experimental X-ray data, using the DFT-D2, DFT-D\*, and DFT-DX parameterizations.

Parameters	ADG			CDG		
	DFT-D2	DFT-D*	DFT-DX	DFT-D2	DFT-D*	DFT-DX
	$s_6 = 0.56$	$s_6 = 0.75$	$s_6 = 2.06$	$s_6 = 1.25$	$s_6 = 0.69$	$s_6 = 1.93$
Volume ( $\text{\AA}^3$ )	-0.02	0.04	-0.23	0.07	0.04	-0.03
$a$ ( $\text{\AA}$ )	0.55	1.14	1.05	-0.21	0.38	0.25
$b$ ( $\text{\AA}$ )	-0.30	-0.26	-0.33	0.99	0.76	0.53
$c$ ( $\text{\AA}$ )	-0.29	-0.96	-1.00	-0.67	-1.14	-0.72
Abs. Ave. Error	0.29	0.60	0.65	0.48	0.58	0.38

Despite the large differences in  $s_6$  magnitude, the amount of London force energy correction is similar between the models. **Table 7-3** lists the results for each model and includes the total binding energy per molecule in the solid state, the applied London force energy, and the percent contribution of this correction to the total. While the binding energy for ADG has not been previously reported, the binding energy calculated for CDG is comparable to the total intermolecular energy reported by Brady and Sharp ( $113.8 \text{ kJ mol}^{-1}$ ).<sup>42</sup> As expected, the corrections contribute a greater portion of the total binding energy in the CDG solid as compared



to the ADG, since the former has half as many hydrogen bonds holding the crystal together. Thus the importance of the London force corrections is magnified in the CDG sample. The differences in the intermolecular interactions found in the ADG and CDG crystals are apparent in the total binding energies. The significantly larger binding energy of the ADG molecules versus the CDG arises from the already noted additional hydrogen bonds, but also from the zwitterionic/dipolar nature of ADG as opposed to the nonpolar CDG molecules. It is useful to note that the DFT-D\* and DFT-DX models produce similar energies, but the DFT-D2 approach deviates from the general pattern by generating a binding energy twice as large as the other models for solid CDG. This result is particularly concerning because it is in precisely this kind of solid where a proper London force correction model is most needed. It is important to emphasize that both the DFT-D\* and DFT-DX parameterizations yielded relatively consistent values for the optimum  $s_6$  scalar, but the standard DFT-D2 method required surprisingly different  $s_6$  values between the two diglycines. These observations suggest a lack of transferability of the DFT-D2 model between different solids.

**Table 7-3.** Calculated ( $\text{kJ mol}^{-1}$ , per molecule) binding energies and London force corrections for crystalline ADG and CDG using the DFT-D2, DFT-D\*, and DFT-DX parameterizations.

ADG				
Correction Model	$s_6$	Total Binding Energy <sup>†</sup>	London Correction	Percent Contribution
DFT-D2	0.56	-398.27	-56.26	14%
DFT-D*	0.75	-408.73	-66.56	16%
DFT-DX	2.06	-414.25	-72.31	17%
CDG				
DFT-D2	1.25	-205.44	-123.40	60%
DFT-D*	0.69	-141.89	-60.21	42%
DFT-DX	1.93	-151.31	-68.93	46%

<sup>†</sup>corrected for basis set superposition error

The resulting structures for each of the calculations utilizing the optimized scalars were very good, with no absolute average error being above 0.65%. The DFT-D2 method resulted in the lowest absolute average dimensional error for ADG and DFT-DX was the best performer for CDG. It should be noted that there were no large differences in the performances of the various parameterizations once the  $s_6$  scalar was optimized. Thus from the standpoint of unit cell reproduction, the three approaches are effectively equal, with similar abilities for simulating the general crystallographic packing arrangements of the ADG and CDG molecules.

Reproduction of observed crystallographic parameters is a clear indicator of the quality of a solid-state simulation, but the atomic-level accuracy of the DFT-derived structures is also important in the evaluation of the calculated crystal structures. Root-mean-squared deviations (RMSDs) of the calculated bond lengths, bond angles, and bond dihedral angles were determined by comparison to the X-ray crystallographic data (**Table C2**). Additionally, to aid in the investigation of the quality of the molecular packing of the theoretical unit cell, the hydrogen bond heavy-atom separations were compared to those from the experimental structures and the RMSDs were used to gauge the accuracy. Hydrogen bond evaluation utilized only heavy atoms because of the uncertainty in the hydrogen atom positions as determined by X-ray diffraction. Little variation is seen between the three correction parameterizations, with all of the internal geometric parameters of the molecules reproduced very well by the models. The average RMSDs across both solids were 0.0024 Å in bond length, 0.13° in bond angles, 0.46° in dihedral angles, and 0.013 Å in the hydrogen bond lengths. The most variation is found in the dihedral angles, but even that is too small to classify any one model as being obviously superior. Based on these results, the use of DFT-D2, DFT-D\*, and DFT-DX resulted in very similar structures for both CDG and ADG and all three approaches yielded structures that compare well with experiment in

terms of both the internal (bonds, angles) and external (unit cell dimensions, hydrogen bonding) measurements

### 7.3.2.2 Simulated Terahertz Spectra

For both ADG (**Figure 7-4**) and CDG (**Figure 7-5**), the simulated THz spectra (no frequency scalars applied) were compared to the 78 K experimental spectra to explore the quality of the reproductions. The IR-active mode frequencies, intensities, and symmetries are listed in **Table 7-4** for ADG and CDG. Spectral absorption units ( $M^{-1} \text{ cm}^{-1}$ ) are calculated from the theoretical units ( $\text{km mol}^{-1}$ ) using Lorentzian line shapes with full width half-maximum (FWHM) values empirically determined by least-squares fitting of the experimental spectra. The FWHM values were  $2.7 \text{ cm}^{-1}$  for ADG and  $2.6 \text{ cm}^{-1}$  for CDG. The calculated frequencies are sensitive to the parameterization model, especially when considering the low-frequency vibrations. This sensitivity is shown graphically in **Figure 7-6**, where the percent variation of the mode frequencies between models is plotted for all normal modes (IR allowed and forbidden) of the two diglycine crystals. For both solids it is clear that the variation in the predicted frequencies is much greater at lower frequencies, averaging  $\sim 5\%$  variation in the terahertz region motions, but only  $\sim 0.5\%$  variation in the higher-frequency intramolecular modes. The low-frequency vibrations are more dependent on the applied London force correction because of the nature of these vibrations. In this spectral region, the vibrations correspond to motions of the molecules with respect to one another, such as translations and rotations. These intermolecular coordinates are the primary

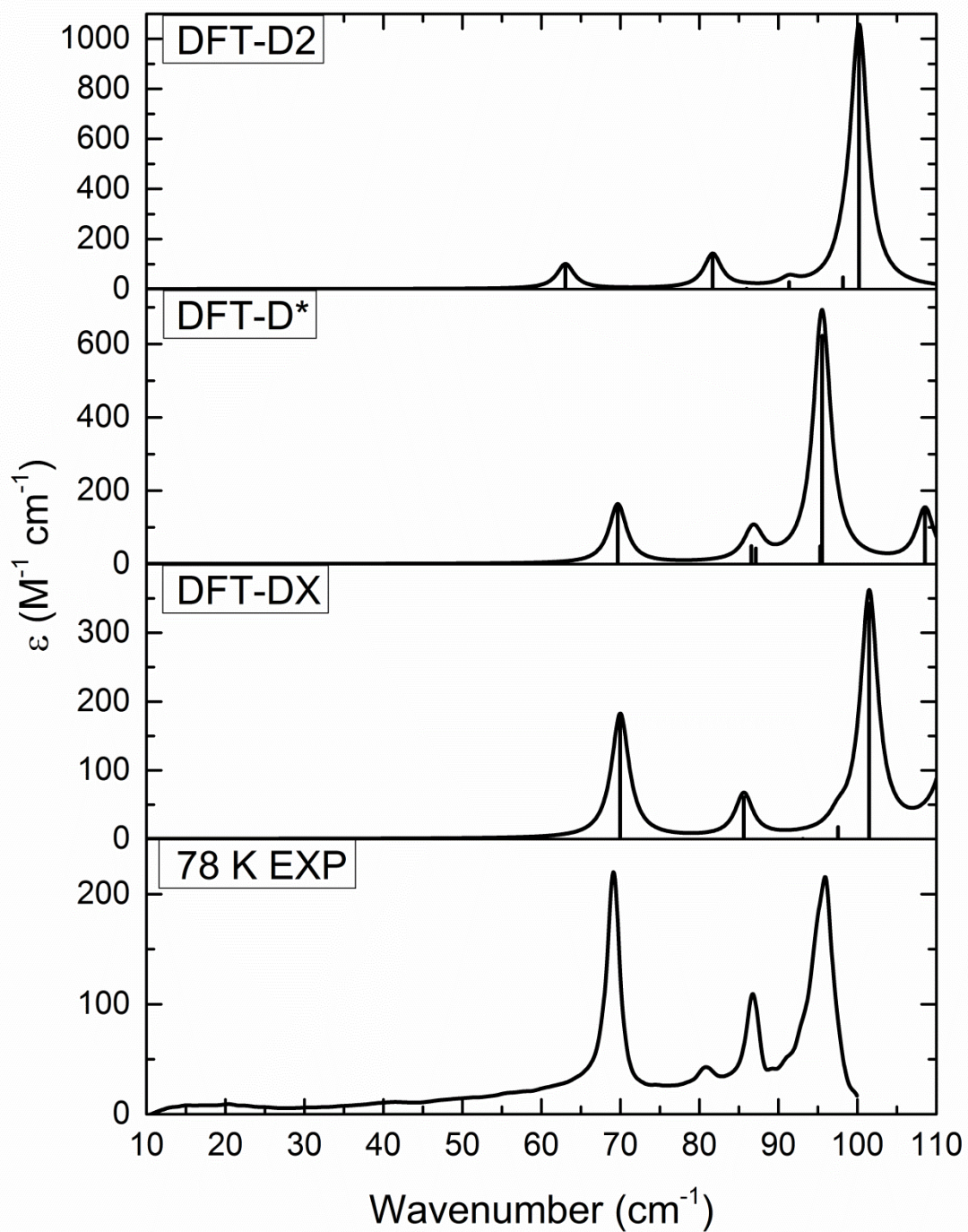


**Figure 7-4.** Terahertz spectrum of acyclic diglycine at 78 K compared to the theoretical spectra generated using PBE/cc-pVTZ with three different London force corrections applied. Note the differences in absorption unit scales.

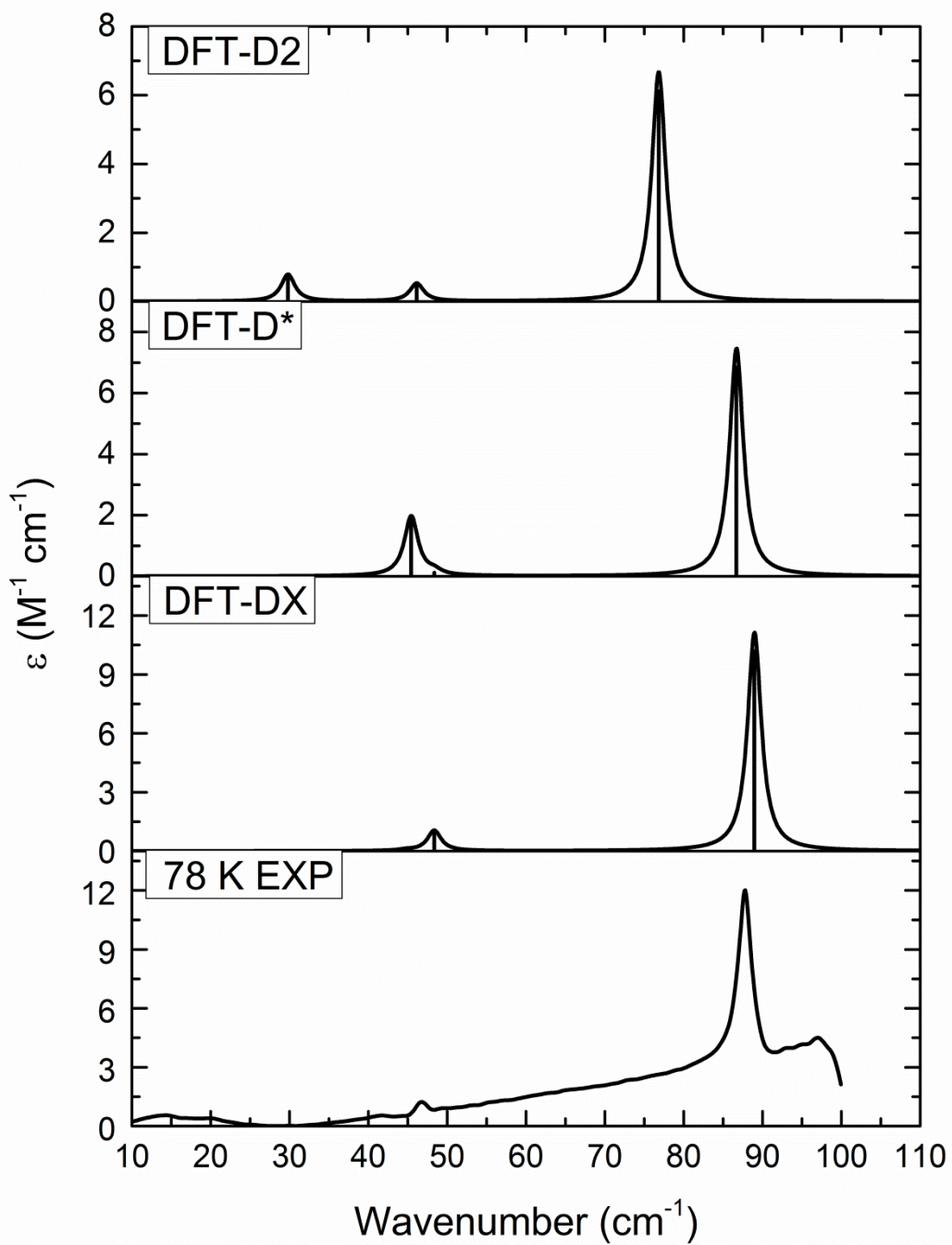


**Figure 7-5.** Terahertz spectrum of cyclic diglycine at 78 K compared to the theoretical spectra generated using PBE/cc-pVTZ with three different London force corrections applied.

**Table 7-4.** Calculated IR-active mode frequencies ( $\text{cm}^{-1}$ ), intensities ( $\text{km mol}^{-1}$ ), and symmetries for ADG and CDG below  $115 \text{ cm}^{-1}$  using DFT-D2, DFT-D\*, and DFT-DX corrections.

ADG								
DFT-D2			DFT-D*			DFT-DX		
freq.	inten.	symm.	freq.	inten.	symm.	freq.	inten.	symm.
63.0	9.59	A <sub>u</sub>	69.7	15.69	A <sub>u</sub>	70.0	17.6	A <sub>u</sub>
81.7	13.17	A <sub>u</sub>	86.6	4.90	A <sub>u</sub>	85.6	6.05	A <sub>u</sub>
86.0	0.21	A <sub>u</sub>	87.1	4.29	A <sub>u</sub>	93.1	0.02	A <sub>u</sub>
91.4	2.83	A <sub>u</sub>	95.3	4.87	A <sub>u</sub>	97.6	1.74	A <sub>u</sub>
98.2	4.72	B <sub>u</sub>	95.5	62.29	B <sub>u</sub>	101.5	34.25	B <sub>u</sub>
100.2	101.32	B <sub>u</sub>	108.6	14.33	B <sub>u</sub>	113.5	57.7	B <sub>u</sub>
CDG								
DFT-D2			DFT-D*			DFT-DX		
freq.	inten.	symm.	freq.	inten.	symm.	freq.	inten.	symm.
29.8	0.06	A <sub>u</sub>	45.4	0.15	A <sub>u</sub>	44.8	0.004	A <sub>u</sub>
46.1	0.04	A <sub>u</sub>	48.4	0.01	A <sub>u</sub>	48.4	0.08	A <sub>u</sub>
76.8	0.51	B <sub>u</sub>	86.7	0.57	B <sub>u</sub>	89.0	0.85	B <sub>u</sub>

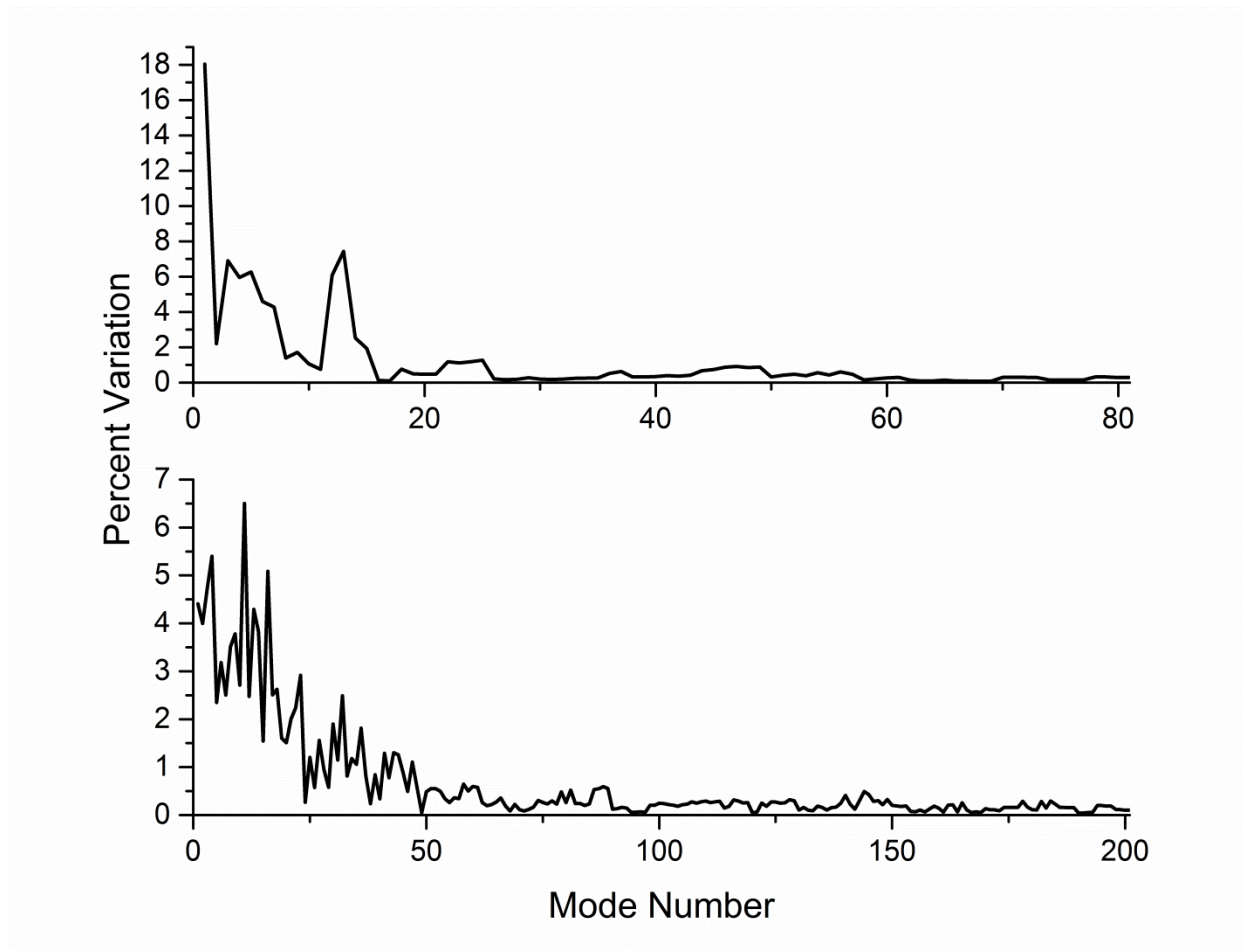


**Figure 7-6.** Percent variation across the DFT-D2, DFT-D\*, and DFT-DX models in the prediction of the frequencies of all normal modes of vibration for acyclic diglycine (bottom) and cyclic diglycine (top).

recipients of the corrections and react strongly to any correction-induced modifications to the potential energy surface, particularly those modifications that alter the distance dependence of the dispersion forces. These results demonstrate that low-frequency ( $<200\text{ cm}^{-1}$ ) vibrational spectroscopy is an ideal method for evaluating London force correction parameterizations.

Considering first ADG, **Figure 7-4** shows that all of the simulations share similarities, each with three main features that match the general pattern seen in the experimental spectrum. The DFT-D2 calculation has the poorest correlation to the experiment with a predicted vibrational frequency of the first mode being too low by  $6.0\text{ cm}^{-1}$ . It also has a greatly overestimated IR absorption for the highest-frequency absorption in the terahertz region, with it being  $\sim 5$  times stronger than actually measured. The DFT-D\* and DFT-DX based THz spectra are clearly better than DFT-D2 in terms of both frequency positions and absorption strengths. Identification of the superior parameterization between DFT-D\* and DFT-DX is not possible since, while both are able to well reproduce the experimental peaks at  $69.0\text{ cm}^{-1}$  and  $95.8\text{ cm}^{-1}$ , they both have difficulty predicting the features at  $80.9\text{ cm}^{-1}$  and  $86.7\text{ cm}^{-1}$ . Overall for ADG, it appears that DFT-D\* has slightly better frequency positions, but DFT-DX has slightly better IR intensities. The intensity differences become clearer by looking at the relative intensities. The experimental peaks at  $69.0\text{ cm}^{-1}$  and  $95.8\text{ cm}^{-1}$  have an intensity ratio of 1.02. The ratio of the peak intensities for DFT-D2, DFT-D\*, and DFT-DX are 10.57, 3.97, and 1.95, respectively.

The spectral simulations for CDG are qualitatively similar based upon the two peaks easily seen at  $46.8\text{ cm}^{-1}$  and  $87.7\text{ cm}^{-1}$  in the experiment. Considering only these two absorptions, the spectral reproductions from all three dispersion corrections are acceptable because each generates features that correlate with observation reasonably well. Some indication of better and worse performance can be seen in the predicted intensity ratios of these two clear absorptions



(87.7  $\text{cm}^{-1}$ :46.8  $\text{cm}^{-1}$ ). The experimental intensity ratio is 9.4, whereas the DFT-D2 is 12.8, DFT-D\* is 3.8, and DFT-DX is 10.6. However, when the theories are further evaluated, it is seen that all three approaches produce a third, weaker absorption that is not obvious in the original experimental spectrum. This third peak was predicted at 29.8  $\text{cm}^{-1}$  in DFT-D2, 48.4  $\text{cm}^{-1}$  in DFT-D\*, and 44.8  $\text{cm}^{-1}$  in DFT-DX. Based on these findings an additional high-concentration (50% w/w) sample of CDG was made and THz data collected at 78 K to better reveal the location of the third peak (**Figure 7-7**). Upon inspection of the new high-concentration data, a third low-intensity peak was resolved at 41.4  $\text{cm}^{-1}$  in the experimental spectrum. Using the three peak locations and intensities, the theories can now be more thoroughly appraised. Since the more intense features can be assigned using any of the models, the weak experimental peak becomes extremely important in the evaluation of the THz simulations. Focusing on this feature, the DFT-DX simulation provided the most accurate representation of the experimental data as shown in **Figure 7-7**. DFT-D2 yielded a very poor frequency for this mode, underestimating it by 11.6  $\text{cm}^{-1}$  and with inaccurate intensity. The DFT-D\* model significantly improves over DFT-D2, but it was unable to produce the correct frequency ordering of the peaks. Only DFT-DX correctly positioned this weak feature with respect to the nearby intense features.

Calculations using the DFT-DX parameterization have provided simulated THz spectra that are in good agreement with the observed experimental spectra for both ADG and CDG. These results indicate that the DFT-DX parameterization is able to accurately represent both the energetic minima on the potential energy surface, as well as its curvature. The quality of the DFT-DX simulations enables spectral assignments to be made to specific atomic motions with confidence for both ADG and CDG and these are provided in **Table 7-5**.

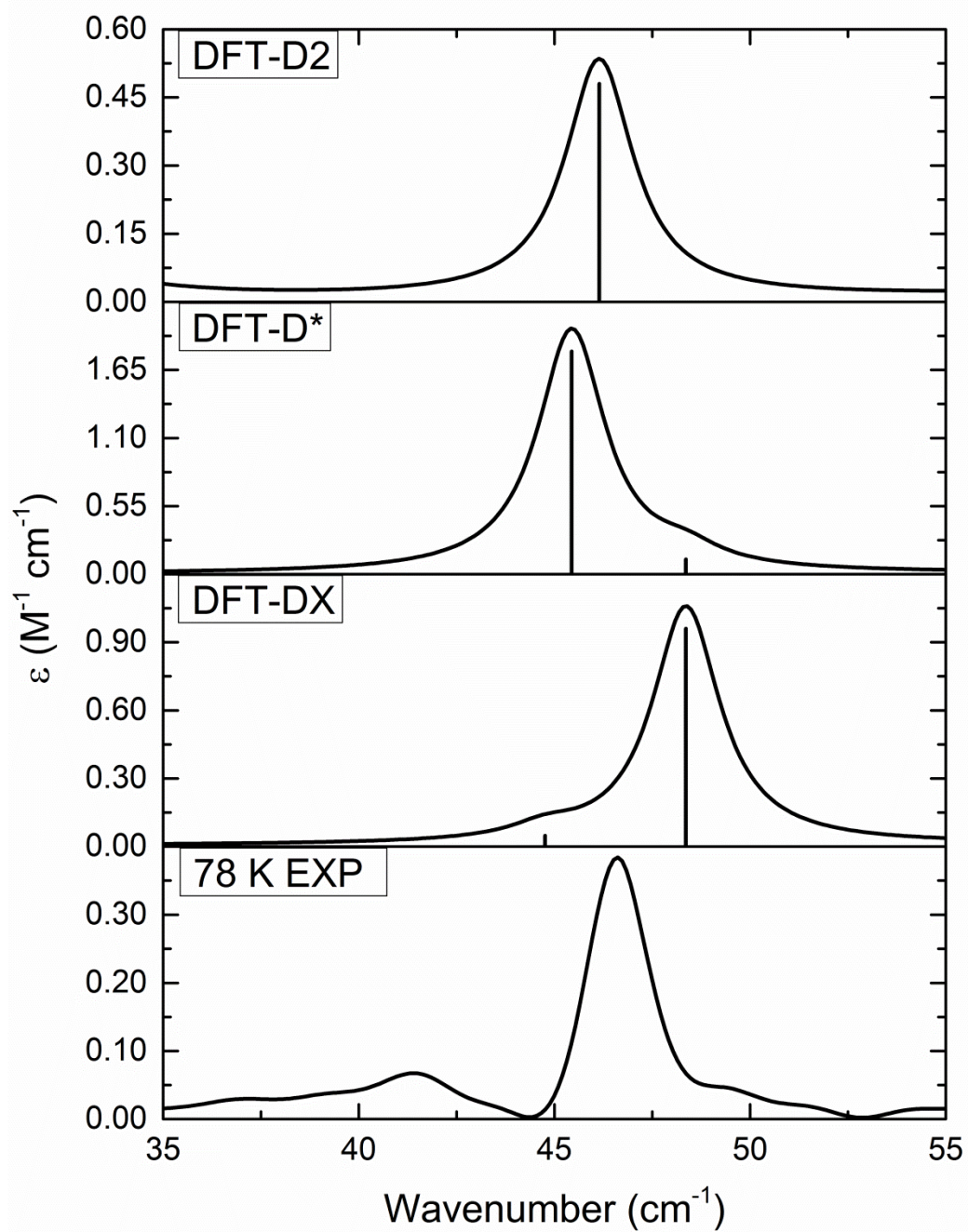


**Figure 7-7.** A portion of the 78 K terahertz spectrum of cyclic diglycine from 35 to 55  $cm^{-1}$  with baseline correction compared to the theoretical spectra generated using PBE/cc-pVTZ with three different London force corrections applied.

**Table 7-5.** Vibrational character of the IR-active modes ( $\text{cm}^{-1}$ ) in ADG ( $<115 \text{ cm}^{-1}$ ) and CDG ( $<115 \text{ cm}^{-1}$ ) using DFT-DX corrected PBE/cc-pVTZ simulations.

ADG			CDG		
Exp.	DFT-DX	description	Exp.	DFT-DX	description
69.0	70.0	ER about a	41.4	44.8	ET along c
80.9	-	-	46.8	48.4	ET along a
86.7	85.6	ER about c	87.7	89.0	ET along b
-	93.1	CH <sub>2</sub> torsion at C3			
-	97.6	CO/NH torsion at C4/N2			
95.8	101.5	CH <sub>2</sub> torsion at C3			
-	113.5	CH <sub>2</sub> torsion at C3			

ER = External Rotation, ET = External Translation

## 7.4 Conclusions

The terahertz spectra of ADG and CDG were measured from 10 to 100  $\text{cm}^{-1}$  at 293 K and 78 K, revealing sharp spectral features to be used for evaluation of London dispersion force corrections in solid-state DFT simulations. To evaluate the necessity, influence, and effectiveness of London dispersion corrections, three approaches were used: DFT-D2, DFT-D\*, and DFT-DX. The need for dispersion corrections was made clear by the results from the uncorrected calculations, and the use of DFT-D2, DFT-D\*, and DFT-DX all provided acceptable structures for both ADG and CDG, when compared to experimental crystallographic data. While structurally the various parameterizations were equivalent, in terms of vibrational motions, significantly more variation was seen between the models. The DFT-D2 approach was consistently underperforming in the reproduction of the observed terahertz spectra. DFT-D\* and DFT-DX provided greatly improved results and both could serve as acceptable semi-empirical corrections in solid-state DFT simulations. While DFT-D\* and DFT-DX are similar in performance, the simulated terahertz spectra of CDG suggest that the DFT-DX approach may perform better in solids that exhibit fewer strong intermolecular interactions. The use of the new

DFT-DX dispersion correction parameterization shows excellent promise based on these results, but must still be tested for its applicability across a wider range of molecular solids.

### **7.5 Supporting Information**

Values for  $C_6$  and van der Waals radii used in the London force dispersion corrections; RMSD values for intramolecular and intermolecular structural parameters. This material is available free of charge via the Internet at <http://pubs.acs.org>. This information is located in Appendix C.

### **7.6 Acknowledgements**

This research was funded by a grant from the National Science Foundation CAREER Program (CHE-0847405). The authors thank Tiffany M. Smith for the collection of X-ray crystallographic data. They also thank Syracuse University for its continued support.

## 7.7 References

- (1) Allis, D. G.; Prokhorova, D. A.; Korter, T. M. Solid-State Modeling of the Terahertz Spectrum of the High Explosive HMX. *J. Phys. Chem. A* **2006**, *110*, 1951-1959.
- (2) Hu, Y.; Huang, P.; Guo, L.; Wang, X.; Zhang, C. Terahertz Spectroscopic Investigations of Explosives. *Phys. Lett. A* **2006**, *359*, 728-732.
- (3) Leahy-Hoppa, M. R.; Fitch, M. J.; Zheng, X.; Hayden, L. M.; Osiander, R. Wideband Terahertz Spectroscopy of Explosives. *Chem. Phys. Lett.* **2007**, *434*, 227-230.
- (4) Wilkinson, J.; Konek, C. T.; Moran, J. S.; Witko, E. M.; Korter, T. M. Terahertz Absorption Spectrum of Triacetone Triperoxide (TATP). *Chem. Phys. Lett.* **2009**, *478*, 172-174.
- (5) Dobroiu, A.; Sasaki, Y.; Shibuya, T.; Otani, C.; Kawase, K. Thz-Wave Spectroscopy Applied to the Detection of Illicit Drugs in Mail. *Proceedings of the IEEE* **2007**, *95*, 1566-1575.
- (6) Hakey, P. M.; Allis, D. G.; Ouellette, W.; Korter, T. M. Cryogenic Terahertz Spectrum of (+)-Methamphetamine Hydrochloride and Assignment Using Solid-State Density Functional Theory. *J. Phys. Chem. A* **2009**, *113*, 5119-5127.
- (7) Wang, G.; Shen, J.; Jia, Y. Vibrational Spectra of Ketamine Hydrochloride and 3, 4-Methylenedioxymethamphetamine in Terahertz Range. *J. Appl. Phys.* **2007**, *102*, 013106-013104.
- (8) Zeitler, J. A.; Taday, P. F.; Gordon, K. C.; Pepper, M.; Rades, T. Solid-State Transition Mechanism in Carbamazepine Polymorphs by Time-Resolved Terahertz Spectroscopy. *ChemPhysChem* **2007**, *8*, 1924-1927.
- (9) Delaney, S. P.; Pan, D.; Yin, S. X.; Smith, T. M.; Korter, T. M. Evaluating the Roles of Conformational Strain and Cohesive Binding in Crystalline Polymorphs of Aripiprazole. *Cryst. Growth Des.* **2013**, *13*, 2943-2952.
- (10) Beard, M. C.; Turner, G. M.; Schmuttenmaer, C. A. Terahertz Spectroscopy. *J. Phys. Chem. B* **2002**, *106*, 7146-7159.
- (11) Jepsen, P. U.; Cooke, D. G.; Koch, M. Terahertz Spectroscopy and Imaging – Modern Techniques and Applications. *Laser Photonics Rev* **2011**, *5*, 124-166.
- (12) Allis, D. G.; Zeitler, J. A.; Taday, P. F.; Korter, T. M. Theoretical Analysis of the Solid-State Terahertz Spectrum of the High Explosive RDX. *Chem. Phys. Lett.* **2008**, *463*, 84-89.
- (13) King, M. D.; Korter, T. M. Effect of Waters of Crystallization on Terahertz Spectra: Anhydrous Oxalic Acid and Its Dihydrate. *J. Phys. Chem. A* **2010**, *114*, 7127-7138.
- (14) Hakey, P. M.; Allis, D. G.; Hudson, M. R.; Ouellette, W.; Korter, T. M. Investigation of (1r,2s)-(-)-Ephedrine by Cryogenic Terahertz Spectroscopy and Solid-State Density Functional Theory. *ChemPhysChem* **2009**, *10*, 2434-2444.
- (15) Civalleri, B.; Zicovich-Wilson, C. M.; Valenzano, L.; Ugliengo, P. B3LYP Augmented with an Empirical Dispersion Term (B3LYP-D\*) as Applied to Molecular Crystals. *CrystEngComm* **2008**, *10*, 405-410.
- (16) Zhao, Y.; Truhlar, D. G. Density Functionals with Broad Applicability in Chemistry. *Acc. Chem. Res.* **2008**, *41*, 157-167.
- (17) Vydrov, O. A.; Van Voorhis, T. Nonlocal van der Waals Density Functional Made Simple. *Phys. Rev. Lett.* **2009**, *103*, 063004/063001-063004.
- (18) Vydrov, O. A.; Van Voorhis, T. Nonlocal van der Waals Density Functional: The Simpler the Better. *J. Chem. Phys.* **2010**, *133*, 244103-244109.

- (19) Lee, K.; Murray, É. D.; Kong, L.; Lundqvist, B. I.; Langreth, D. C. Higher-Accuracy van der Waals Density Functional. *Phys. Rev. B: Condens. Matter* **2010**, *82*, 081101.
- (20) Pisani, C.; Casassa, S.; Maschio, L.; Shutz, M.; Usvyat, D. *CRYSCOR09 User's Manual* **2009**.
- (21) Perdew, J. P.; Burke, K.; Ernzerhof, M. Generalized Gradient Approximation Made Simple [Phys. Rev. Lett. 77, 3865 (1996)]. *Phys. Rev. Lett.* **1997**, *78*, 1396-1396.
- (22) Grimme, S.; Antony, J.; Ehrlich, S.; Krieg, H. A Consistent and Accurate Ab Initio Parametrization of Density Functional Dispersion Correction (DFT-D) for the 94 Elements H-Pu. *J. Chem. Phys.* **2010**, *132*, 154104-154119.
- (23) Grimme, S. Semiempirical GGA-Type Density Functional Constructed with a Long-Range Dispersion Correction. *J. Comput. Chem.* **2006**, *27*, 1787-1799.
- (24) Juliano, T. R., Jr.; King, M. D.; Korter, T. M. Evaluating London Dispersion Force Corrections in Crystalline Nitroguanidine by Terahertz Spectroscopy. *IEEE Trans. on THz. Sci. and Tech.* **2013**, *3*, 281-287.
- (25) Drebuschak, T. N.; Kolesnik, E. N.; Boldyreva, E. V. Variable Temperature (100-295 K) Single-Crystal X-Ray Diffraction Study of the  $\alpha$ -Polymorph of Glycylglycine and a Glycylglycine Hydrate. *Z. Kristallogr.* **2006**, *221*, 128-138.
- (26) Sarangarajan, T. R.; Panchanatheswaran, K.; Low, J. N.; Glidewell, C. Piperazine-2,5-Dione-Oxalic Acid-Water (1/1/2) and a Redetermination of Piperazine-2,5-Dione, Both at 120 K: Hydrogen-Bonded Sheets Containing multiple Ring Types. *Acta Crystallogr. Sect. C: Cryst. Struct. Commun.* **2005**, *61*, 118-121.
- (27) Wu, Q.; Litz, M.; Zhang, X. C. Broadband Detection Capability of ZnTe Electro-Optic Field Detectors. *Appl. Phys. Lett.* **1996**, *68*, 2924-2926.
- (28) Rice, A.; Jin, Y.; Ma, X. F.; Zhang, X. C.; Bliss, D.; Larkin, J.; Alexander, M. Terahertz Optical Rectification from  $\langle 110 \rangle$  Zinc-Blende Crystals. *Appl. Phys. Lett.* **1994**, *64*, 1324-1326.
- (29) Shen, Y. C.; Taday, P. F.; Pepper, M. Elimination of Scattering Effects in Spectral Measurement of Granulated Materials Using Terahertz Pulsed Spectroscopy. *Appl. Phys. Lett.* **2008**, *92*, 051103-051103.
- (30) Dovesi, R.; Saunders, V. R.; Roetti, C.; Orlando, R.; Zicovich-Wilson, C. M.; Pascale, F.; Civalieri, B.; Doll, K.; Harrison, N. M.; Bush, I. J.; D'Arco, P.; Llunell, M.; Torino, U. o. T. *CRYSTAL09 User's Manual* **2009**.
- (31) Dunning, T. H. Gaussian Basis Sets for Use in Correlated Molecular Calculations. I. The Atoms Boron through Neon and Hydrogen. *J. Chem. Phys.* **1989**, *90*, 1007-1024.
- (32) Miller, T. M.; Bederson, B. Atomic and Molecular Polarizabilities-a Review of Recent Advances. In *Advances in Atomic and Molecular Physics*; Bates, D. R., Benjamin, B., Eds.; Academic Press, 1978; Vol. Volume 13; pp 1-55.
- (33) *Crc Handbook of Chemistry and Physics*, 93 ed.; CRC Press/Taylor and Francis: Boca Raton, FL.
- (34) Sansonetti, J. E.; Martin, W. C. Handbook of Basic Atomic Spectroscopic Data. *J. Phys. Chem. Ref. Data* **2005**, *34*, 1559-2259.
- (35) Monkhorst, H. J.; Pack, J. D. Special Points for Brillouin-Zone Integrations. *Phys. Rev. B: Condens. Matter* **1976**, *13*, 5188-5192.
- (36) Boys, S. F.; Bernardi, F. The Calculation of Small Molecular Interactions by the Differences of Separate Total Energies. Some Procedures with Reduced Errors. *Mol. Phys.* **1970**, *19*, 553-566.

- (37) Dall'Olio, S.; Dovesi, R.; Resta, R. Spontaneous Polarization as a Berry Phase of the Hartree-Fock Wave Function: The Case of KNbO<sub>3</sub>. *Phys. Rev. B: Condens. Matter* **1997**, *56*, 10105-10114.
- (38) Kutteruf, M. R.; Brown, C. M.; Iwaki, L. K.; Campbell, M. B.; Korter, T. M.; Heilweil, E. J. Terahertz Spectroscopy of Short-Chain Polypeptides. *Chem. Phys. Lett.* **2003**, *375*, 337-343.
- (39) Ponseca, C. S.; Kambara, O.; Kawaguchi, S.; Yamamoto, K.; Tominaga, K. Low-Frequency Spectra of Amino Acids and Short-Chain Peptides Studied by Terahertz Time-Domain Spectroscopy. *J. of IR, mm, and THz Waves* **2010**, *31*, 799-809.
- (40) King, M. D.; Blanton, T. N.; Misture, S. T.; Korter, T. M. Prediction of the Unknown Crystal Structure of Creatine Using Fully Quantum Mechanical Methods. *Cryst. Growth Des.* **2011**, *11*, 5733-5740.
- (41) Walther, M.; Fischer, B. M.; Uhd Jepsen, P. Noncovalent Intermolecular Forces in Polycrystalline and Amorphous Saccharides in the Far Infrared. *Chem. Phys.* **2003**, *288*, 261-268.
- (42) Brady, G. P.; Sharp, K. A. Energetics of Cyclic Dipeptide Crystal Packing and Solvation. *Biophys. J.* **1997**, *72*, 913-927.

## CHAPTER 8. Applications to Future Work

### 8.1 Glutamic Acid

This work is inspired by the work done on the aspartic acid series of amino acids and hydrates in Chapter 5. Building on the knowledge gained from aspartic acid, the glutamic acid (GLU) series of L-GLU, DL-GLU, and DL-GLU monohydrate were evaluated using terahertz spectroscopy and solid-state density functional theory. The effects of the application of the semi-empirical London dispersion force correction known as DFT-D\*<sup>1</sup> were also investigated in terms of their influence on hydrated systems. After compiling the results from the glutamic acid systems with known X-ray crystallographic data, a prediction of the unknown L-glutamic acid monohydrate crystal structure was proposed.

Much like in the case of aspartic acid (**Chapter 5**), the experimental THz data collected on the known structures of GLU was used to evaluate the performance of the solid-state DFT calculations. In Chapter 5 the use of a single  $s_6$  value was shown to be effective in both the anhydrous aspartic acid molecules and the aspartic acid hydrates. When GLU was investigated, it was determined that the  $s_6$  value for the hydrates was different than that of the anhydrates. This was a very important finding, especially when trying to predict reasonable structures for unknown hydrates, seeing as the amount of dispersion correction in the calculation plays a significant role in the intermolecular bonding scheme.

Solid-state DFT calculations were conducted using the CRYSTAL09 software package<sup>2</sup> using the procedure outlined in Chapter 3. The hybrid B3LYP functional<sup>3,4</sup> and the atom-centered 6-31G (d,p) basis set<sup>5</sup> were chosen. Non-covalent London dispersion force corrections were added into the calculations following the model developed by Civalleri, DFT-D\*. The



suggested  $s_6$  value to be used with B3LYP is 1.05,<sup>1</sup> however in the study of GLU species, this was proven to be much too large.

Using the experimental X-ray crystallographic data as a reference (L-GLU taken at Syracuse University, DL-GLU,<sup>6</sup> and DL-GLU monohydrate<sup>7</sup>), the best  $s_6$  value for the anhydrous GLUs was determined to be 0.64 (molecules of L-GLU and DL-GLU are shown in **Figure 8-1.**), which was used for all of the final geometry optimizations and frequency simulations. The anhydrous GLUs were evaluated based on their relative energies in order to determine which structure was lower in energy and to shed light on the formation of only one hydrate (DL). Based on the relative energies, DL-GLU was found to be 8.04 kJ/mol higher in energy than the L-GLU, which suggested that the L-GLU was more tightly packed together. This is a contributing factor to the formation of the monohydrate for only DL-GLU, since it would be more willing to accept water molecules. To further validate this idea, the structures were used to calculate the vibrational frequencies of the molecules. Once the frequencies were finished, thermodynamic data could be extracted to help explain the formation of the DL-monohydrate. When the thermodynamic data was evaluated, the difference in energy between the two anhydrous structures increased to 11.12 kJ/mol, which supported the earlier claims. In order to further understand the hydrate formation, the DL-GLU monohydrate structure was evaluated.

Using the same procedure from above, DL-GLU monohydrate was investigated using solid-state DFT. The  $s_6$  value was determined to be 0.48, 25% lower than the  $s_6$  used for the anhydrous versions. Based on the trend from the anhydrous GLUs, the  $s_6$  value determined here was applied to the prediction of the unknown L-GLU monohydrate structure. Once the fully optimized structure was determined, the frequencies were simulated and compared to the experimental THz data to ensure accuracy.

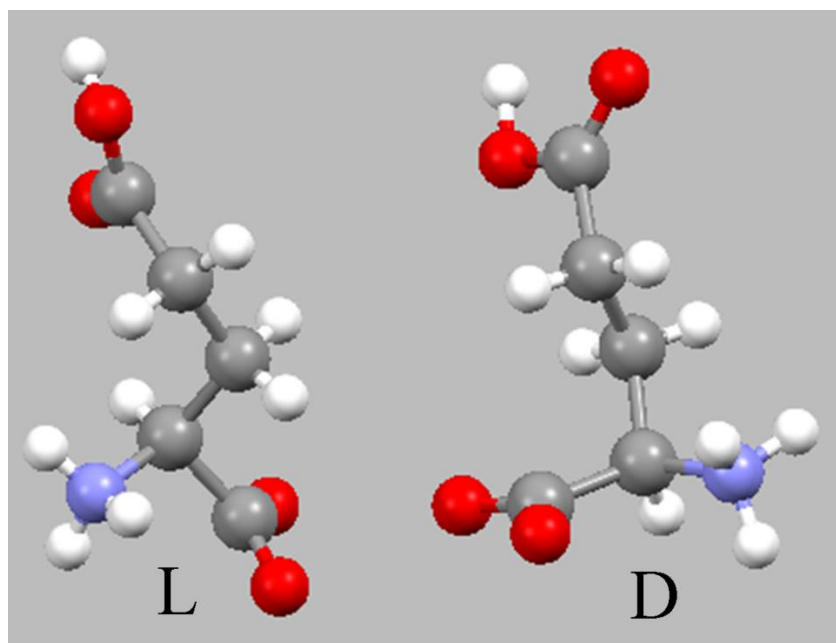


**Figure 8-1.** Images of molecules of L-GLU (extracted from L-GLU crystal) and D-GLU(extracted from DL-GLU crystal) to show the L- and DL- orientations.

With the hydrate  $s_6$  value in hand, the prediction of an L-GLU monohydrate could be made. This structural prediction was attempted from two starting points. First, the necessary water molecules were added to the known L-GLU anhydrous structure in order to form a monohydrate. These attempts failed to produce a reasonable hydrate prediction. The second attempted started with the known L-ASP monohydrate structure. Since ASP and GLU differ only by a methylene group, this was a reasonable starting choice. With the majority of the molecule in place, a methylene group was simply added to the structure, thereby forming GLU molecules. After the GLU molecules were set, the water molecules were arranged in the crystal structure to form a monohydrate. This structure was then subjected to an optimization using P1 symmetry to allow for full relaxation of all atoms and unit cell parameters. Once the P1 optimization reached completion, the structure was extracted from the output and evaluated for symmetry. This led to two options: P21 and P212121. Both of these structures were considered, but ultimately the P212121 version was chosen to continue on to the frequency calculations.

Once a viable structure for the L-GLU monohydrate was obtained, the thermodynamic data for all four species were compared. In the case of the DL-GLU/hydrate series, the Gibbs free energy difference between the anhydrate and the monohydrate was -119.26 kJ/mol, proving the formation of this hydrate to be a favorable process. When the L-GLU/hydrate series was compared, the Gibbs free energy difference was found to be +75.99 kJ/mol, proving this hydrate formation to be an unfavorable process. The Gibbs free energy calculations provided the defining numbers in the investigation of the formation or non-formation of hydrates of amino acids.

This work needs to be continued to extend the experimental THz data collection to the DL-GLU anhydrate. Thus far, all attempts to obtain the anhydrous DL-GLU have failed, and therefore the frequency simulations are not able to be fully evaluated.

## 8.2 Serine and Proline

In line with most of the work done described in this thesis, the amino acids serine (SER) and proline (PRO) are also under investigation. Proline was chosen due to its unique hydrate formation. It is the only amino acid with known structures for both an L-PRO<sup>8</sup> and DL-PRO<sup>9</sup> monohydrate. Proline also has published structures for both anhydrous versions (DL-PRO<sup>7</sup> and L-PRO<sup>10</sup>). The formation of both hydrated forms is very interesting because of the rarity of this occurrence. All of the other amino acids with hydrates that are in the Cambridge Database only show the presence of either an L- or DL- hydrate version. By using proline, predictions on the likelihood of the formation of amino acid hydrates (and even any hydrate) could be made. Serine was used as a comparison model since it has published structures for the L-SER<sup>11</sup>, DL-SER<sup>12</sup>, and L-SER monohydrate<sup>13</sup> versions. **Figure 8-2** illustrates L-PRO, L-PRO monohydrate, L-SER, and L-SER monohydrate.

This work consists of theoretical results only. All of the computations were carried out using the CRYSTAL14 software package<sup>14</sup> and followed the procedure described in Chapter 3. Two approaches were used to obtain the theoretical data, PBESOL<sup>15</sup> and PBE<sup>16</sup> with DFT-D\*<sup>1</sup> corrections (PBE-D\*). All calculations utilized the atom-centered 6-311G (d,p)<sup>5</sup> basis set. PBESOL was chosen because it is a functional that has been optimized for use in the solid state and does not require the addition of any correction terms in order to account for non-covalent dispersion interactions. This is at least true to the extent that PBESOL has been utilized to optimize unit cell dimensions that are close to experiment. The widely used PBE functional was chosen as a comparison to the PBESOL functional. When using the PBE functional for solid-state simulations, it is necessary to use a correction model to account for dispersion interactions. The dispersion model chosen here was the DFT-D\* method. It is based on Grimme's DFT-D2<sup>17</sup>

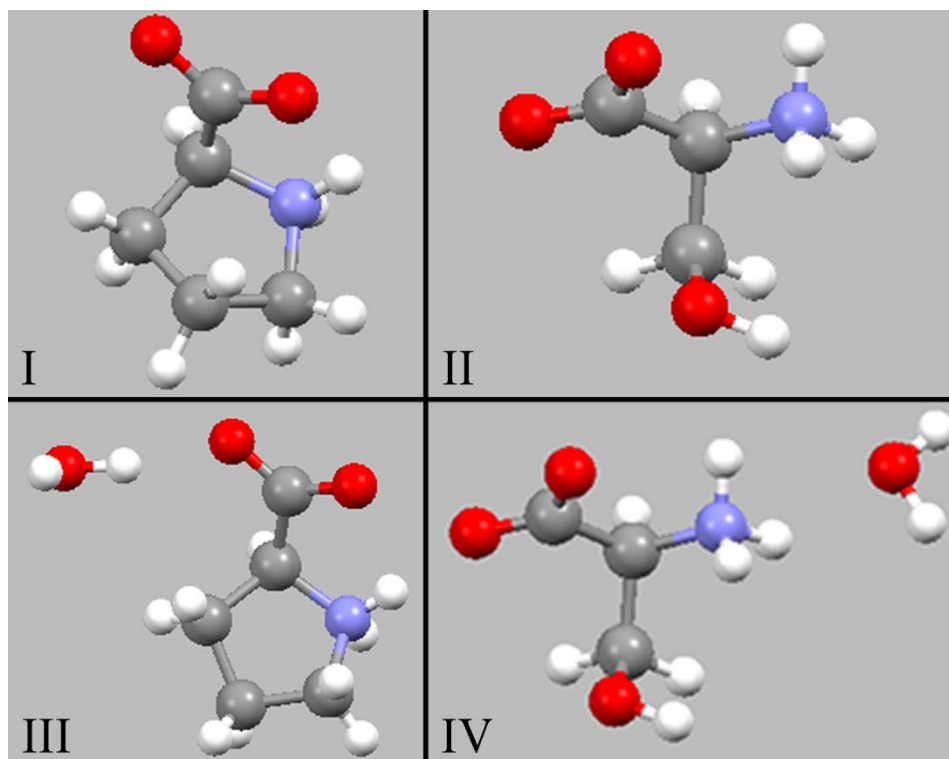


**Figure 8-2.** Single molecule (molecule pairs for hydrates) for the crystalline amino acids L-PRO (I), L-SER (II), L-PRO monohydrate (III), and L-SER monohydrate (IV). All molecules were extracted from their respective crystal structures.

model, but has scaled coefficients to make it more applicable to solid-state work. When using DFT-D\* with PBE, the suggested global scaling value is 0.75,<sup>17</sup> which was adopted in this particular study.

All four of the anhydrous amino acids studied here used experimental X-ray crystallographic data to obtain the initial atomic positions for calculations. Each crystalline structure was fully optimized within space group symmetry restraints. The energies between the L- and DL- versions of PRO and SER were compared to determine if the homochiral or racemic crystal had the lowest solid-state energy. In all cases, using both theoretical approaches, the lowest energy solids were determined to be the DL-amino acids. The total electronic (DFT) energies of the anhydrous amino acids are listed in **Table 8-1**.

**Table 8-1.** Total energies and energy differences of L- and DL- proline and serine. The total energies are reported in hartree and the energy differences are reported in kJ/mol. All of these values are based on the total energy present in one unit cell with a Z value of 2.

Amino Acid	PBESOL	PBE-D* 0.75
L-PRO	-1597.2275	-1603.4568
DL-PRO	-1597.2282	-1603.4585
(L-PRO)-(DL-PRO)	1.87	4.62
L-SER	-1589.0047	-1594.8540
DL-SER	-1589.0392	-1594.8763
(L-SER)-(DL-SER)	90.64	58.42

Once the total energies were determined, the relative energies for each set of amino acids were determined (also listed in **Table 8-1**). Relative energies were used in order to directly compare the stability of the homochiral and heterochiral solids to each other. The DL-amino acids had the lowest energies in all cases, which may be expected due to the better packing that may be achieved by the enantiomer pairs. When the proline structures were compared, the

relative energies of the L-PRO were found to be 1.87 kJ/mol and 4.62 kJ/mol higher than DL-PRO from calculations using PBESOL and PBE-D\*, respectively. The L-SER series showed much larger differences in the relative energies, 90.64 kJ/mol from PBESOL and 58.42 kJ/mol from PBE-D\* as compared to the more stable DL-SER crystal. While the magnitude of the energy differences may change based on the theory applied, the energetic ordering is unchanged. The difference in the relative energies of these chiral solids has provided some insight into the formation of the known hydrate structures because in order for any crystalline hydrate to form, the original anhydrous form must first be disrupted.

The results from the geometry optimizations of these anhydrous amino acids show promise in helping us understand the formation (or non-formation) of amino acid hydrates. When proline is considered, the relative energies of the L- and DL- forms are very close to one another. This indicates that the packing forces within the solids are very similar. This is consistent with the structures of both L-PRO•H<sub>2</sub>O and DL-PRO•H<sub>2</sub>O being known and published. The existence of both hydrates is due to the small difference in the relative energies of the anhydrous solids allowing each solid to form hydrates without energetic penalties. The serine series was used to further prove this finding. Since the only known serine hydrate is L-SER monohydrate, the comparison of the relative energies of the anhydrides can be used to provide information about the hydrate formation. In this case, the relative energies of the L- and DL- versions were considerably different. The calculations indicate that the DL-SER structure is more tightly held together than that of L-SER. Due to the increased cohesive energy; it is unfavorable for the DL-SER crystal to rearrange and accommodate water molecules into its solid-state structure. Since the L-SER exhibits much weaker packing interactions, water molecules can more easily be

integrated into the crystal structure, producing the monohydrate that has been seen experimentally.

These preliminary results are very promising, but more work is needed to quantify the claims of this project. Further work will focus on a more complete understanding of the hydration mechanisms in these amino acids. For example, the simulations of the vibrational frequencies still must be done using both theoretical approaches. This will allow for the calculation of thermodynamic data that can be used to further determine the favorability of hydrate formation. Further it is also necessary to perform calculations to obtain the cohesive binding energies and internal conformational energies in order to determine how much energy must be overcome to allow for water molecules to enter into the crystalline structures.



### 8.3 References

- (1) Civalleri, B.; Zicovich-Wilson, C. M.; Valenzano, L.; Ugliengo, P. B3LYP Augmented with an Empirical Dispersion Term (B3LYP-D\*) as Applied to Molecular Crystals. *CrystEngComm* **2008**, *10*, 405-410.
- (2) Dovesi, R.; Saunders, V. R.; Roetti, C.; Orlando, R.; Zicovich-Wilson, C. M.; Pascale, F.; Civalleri, B.; Doll, K.; Harrison, N. M.; Bush, I. J.; D'Arco, P.; Llunell, M.; Torino, U. o. T. *CRYSTAL09 User's Manual* **2009**.
- (3) Becke, A. D. Density-Functional Exchange-Energy Approximation with Correct Asymptotic Behavior. *Phys. Rev. A* **1988**, *38*, 3098.
- (4) Lee, C.; Yang, W.; Parr, R. G. Development of the Colle-Salvetti Correlation-Energy Formula into a Functional of the Electron Density. *Phys. Rev. B* **1988**, *37*, 785-789.
- (5) Hehre, W. J.; Ditchfield, R.; Pople, J. A. Self-Consistent Molecular Orbital Methods. XII. Further Extensions of Gaussian-Type Basis Sets for Use in Molecular Orbital Studies of Organic Molecules. *J. Chem. Phys.* **1972**, *56*, 2257-2261.
- (6) Dunitz, J. D.; Schweizer, W. B. Anhydrous DL-Glutamic Acid. *Acta Crystallogr. Sect. C* **1995**, *51*, 1377-1379.
- (7) Flaig, R.; Koritsanszky, T.; Dittrich, B.; Wagner, A.; Luger, P. Intra- and Intermolecular Topological Properties of Amino Acids: A Comparative Study of Experimental and Theoretical Results. *J. Am. Chem. Soc.* **2002**, *124*, 3407-3417.
- (8) Kayushina, R. L.; Vainshtein, B. K. Structure Determination of L-Proline by X-Ray Diffraction. *Kristallografiya* **1965**, *10*, 834-844.
- (9) Myung, S.; Pink, M.; Baik, M.-H.; Clemmer, D. E. DL-Proline. *Acta Crystallogr. Sect. C* **2005**, *61*, 506-508.
- (10) Janczak, J.; Luger, P. L-Proline Monohydrate at 100 K. *Acta Crystallogr. Sect. C* **1997**, *53*, 1954-1956.
- (11) Benedetti, E.; Pedrone, C.; Sirigu, A. Crystal Structure of L-(-)Serine. *Gazz. Chim. Ital.* **1973**, *103*, 555.
- (12) Kistenmacher, T. J.; Rand, G. A.; Marsh, R. E. Refinements of the Crystal Structures of DL-Serine and Anhydrous L-Serine. *Acta Crystallogr. Sect. B* **1974**, *30*, 2573-2578.
- (13) Frey, M. N.; Lehmann, M. S.; Koetzle, T. F.; Hamilton, W. C. Precision Neutron Diffraction Structure Determination of Protein and Nucleic Acid Components. XI. Molecular Configuration and Hydrogen Bonding of Serine in the Crystalline Amino Acids L-Serine Monohydrate and DL-Serine. *Acta Crystallogr. Sect. B* **1973**, *29*, 876-884.
- (14) Dovesi, R.; Saunders, V. R.; Roetti, C.; Orlando, R.; Zicovich-Wilson, C. M.; Pascale, F.; Civalleri, B.; Doll, K.; Harrison, N. M.; Bush, I. J.; D'Arco, P.; Llunell, M.; Torino, U. o. T. *CRYSTAL14 User's Manual* **2014**.
- (15) Perdew, J. P.; Ruzsinszky, A.; Csonka, G. I.; Vydrov, O. A.; Scuseria, G. E.; Constantin, L. A.; Zhou, X.; Burke, K. Restoring the Density-Gradient Expansion for Exchange in Solids and Surfaces. *Phys. Rev. Lett.* **2008**, *100*, 136406.
- (16) Perdew, J. P.; Chevary, J. A.; Vosko, S. H.; Jackson, K. A.; Pederson, M. R.; Singh, D. J.; Fiolhais, C. Atoms, Molecules, Solids, and Surfaces: Applications of the Generalized Gradient Approximation for Exchange and Correlation. *Phys. Rev. B* **1992**, *46*, 6671-6687.
- (17) Grimme, S. Semiempirical Gga-Type Density Functional Constructed with a Long-Range Dispersion Correction. *J. Comput. Chem.* **2006**, *27*, 1787-1799.

## CHAPTER 9. Conclusions

Molecular crystals are a very important class of materials that continue to draw much attention in research areas. To better understand these materials, computational methods such as solid-state density functional theory, can be employed to reveal both structural and vibrational properties of solids. Terahertz spectroscopy is used to evaluate the vibrational frequency simulations that are generated by solid-state density functional theory calculations. When using density functional theory, some of the most popular strategies are not able to accurately account for the presence of London dispersion forces. In order to model these interactions, semi-empirical dispersion force corrections can be added into the calculations. The use of the suggested models of these corrections often leads to simulations that yield less-than-ideal structures and vibrational spectra. By modifying the global scaling factor within the formulation of the corrections, the accuracy of the calculations can be increased. A majority of this research has investigated the modifications to the standard implementations of the correction models. A number of small organic molecules were investigated in order to judge the effectiveness of modifications to the semi-empirical dispersion force corrections.

Interest in biologically relevant substances led to research on several amino acids. Closely related amino acids, such as L-glutamine and L-asparagine (**Chapter 4**), were chosen to evaluate the magnitudes of the necessary corrections. Since these amino acids only differ by a methylene, it was expected that the scaling factor values would be very similar, if not identical. However, this was not the case, the scaling factors ultimately differed by over 40%. Once the need for different scaling values was identified, the resulting simulated terahertz spectra were compared to experimental data, revealing accurate reproductions. With such a large difference in

the scaling factors necessary for such similar molecules, the next study focused on chirality in amino acids to check on their computational equivalence.

Chiral amino acids can exist in homochiral and racemic forms; one example of this is aspartic acid. Aspartic acid has known structures for both the pure L- and racemic DL- crystals (**Chapter 5**). The effect of the global scaling factor was investigated for these solids. When solid-state density functional theory calculations were conducted on L-aspartic acid and DL-aspartic acid, the unsurprising result was an equal global scalar. To further investigate aspartic acid, the L-aspartic acid monohydrate, the only known aspartic acid hydrate, was considered. In this case, the global scalar used for the anhydrous versions worked well for the hydrate as well. Once all of this data was collected, interest grew into the reasons behind the fact that there are no known DL-hydrates in the literature. Using the same global scalar for solid-state density functional theory calculations, the structures of two potential DL-aspartic acid hydrates were proposed. Further investigation into this series of amino acids led to several energy calculations in order to determine the energetic reasons behind the spontaneous formation of only an L-aspartic acid monohydrate.

The testing conducted on the standard dispersion force correction model proved the need for a system-dependent global scaling factor. Additionally, the need for a better representative model has been identified through this work. In an attempt to improve the accuracy of solid-state calculations, a new parameterization to the dispersion correction model has been proposed in **Chapters 6 and 7**. This parameterization, known as DFT-DX, uses experimentally obtained (where available) values in place of the theoretically obtained values used by the standard approach. DFT-DX still has the need for the global scaling value, which has proven to be system-dependent as well.

The first test of the DFT-DX parameterization was that of the crystalline explosive nitroguanidine (**Chapter 6**). In order to determine if DFT-DX was a viable correction model, its performance was compared to the performance of two standard correction implementations, DFT-D2 and DFT-D\*. The first test of performance was geometry optimizations. The results from these calculations showed that DFT-DX generated the lowest overall error in the external crystallographic parameters, as well as in the heavy-atom hydrogen bond distances. Errors in the internal parameters were similar across all three methods, although DFT-DX performed considerably better when handling dihedral angles. Once the optimizations were completed, the structures were used to simulate terahertz spectra. All three methods provided spectra that were, arguably, acceptable. The simulated spectrum generated by the DFT-DX method was considered to be the best reproduction based on peak positioning and the splitting of features. These results were very promising for the use of DFT-DX; however, more testing was needed and led to the study of diglycine molecules.

Two diglycine molecules, one cyclic and one acyclic, were chosen to further evaluate the potential of the DFT-DX correction model. These amino acid dimers were chosen for their small size, biological relevance, and their similarities. The performance of the DFT-DX model was once again tested against the established DFT-D2 and DFT-DX models. To first assess the performance of the models, the external crystallographic parameters were compared. In the case of the acyclic diglycine, DFT-D2 showed the best reproduction, but when the cyclic diglycine was considered, DFT-DX showed the best performance. The internal parameters of the simulated crystal structures proved to be equally well-modeled by each of the approaches. Up to this point, it was hard to decide if DFT-DX was doing a better job than the standard approaches, but once the vibrational frequencies were simulated, it became a clear winner. In the case of the acyclic

diglycine, the three simulated spectra were similar, but DFT-DX showed the best peak positions and relative intensities. The cyclic diglycine spectral analysis was the highlight of the DFT-DX performance. In the case of the low-frequency active modes, DFT-DX was the only model that was able to accurately simulate both the ordering and intensities of these peaks. The results from this work must continue to be tested on more systems in order to prove that DFT-DX is a worthy dispersion force correction model.

The research presented in this thesis has proven that through the use of terahertz spectroscopy, the accuracy of solid-state density functional theory calculations, particularly those including semi-empirical London dispersion force corrections, can be tested and evaluated. The use of modified London dispersion force corrections result in high-accuracy simulated vibrational spectra that can be used as an aid in the interpretation of experimental terahertz data. Future work will continue on similar molecular solids in order to further understand the impact of dispersion force correction models. The results presented in this work are valuable to future research in the Korter group, as well as the terahertz and computational communities.

## Appendix A. Chapter 4 Supporting Information

### Contents

**Figure A1.** Experimental cryogenic terahertz spectrum of asparagine monohydrate from 10 to 100  $\text{cm}^{-1}$ .

**Figure A2.** Experimental powder X-ray diffraction data of room-temperature ASN (black). The best fit X-ray data is shown in red. The calculated pattern based on 90 K single-crystal X-ray data (gray) is shown for reference.<sup>3</sup> Data was collected on a Bruker KAPPA APEX DUO using Cu radiation.

### References for Supporting Information

(1) Koetzle, T. F.; Frey, M. N.; Lehmann, M. S.; Hamilton, W. C. Precision Neutron Diffraction Structure Determination of Protein and Nucleic Acid Components. XIII. Molecular and Crystal Structure of the Amino Acid L-Glutamine. *Acta Crystallographica Section B* **1973**, *29*, 2571-2575.

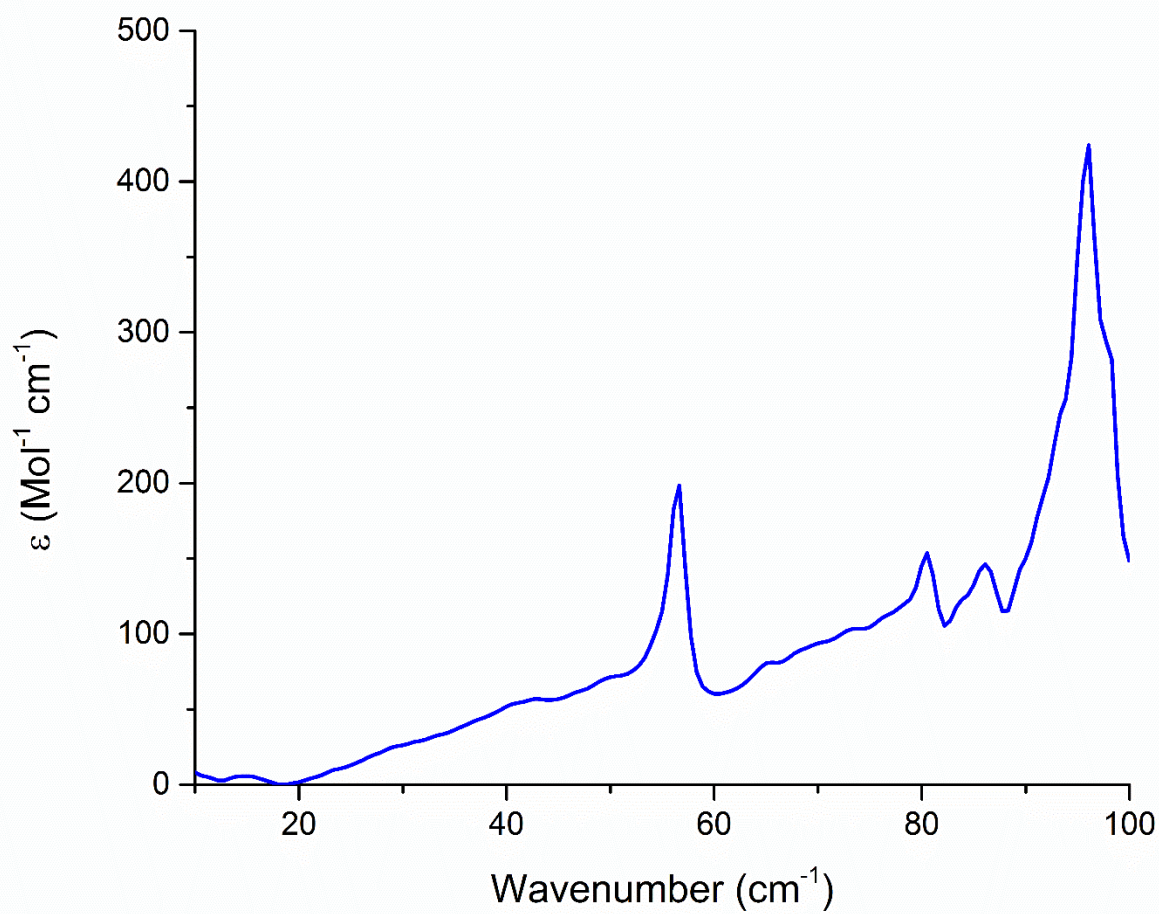


**Figure A1.** Experimental cryogenic terahertz spectrum of asparagine monohydrate from 10 to 100  $\text{cm}^{-1}$ .

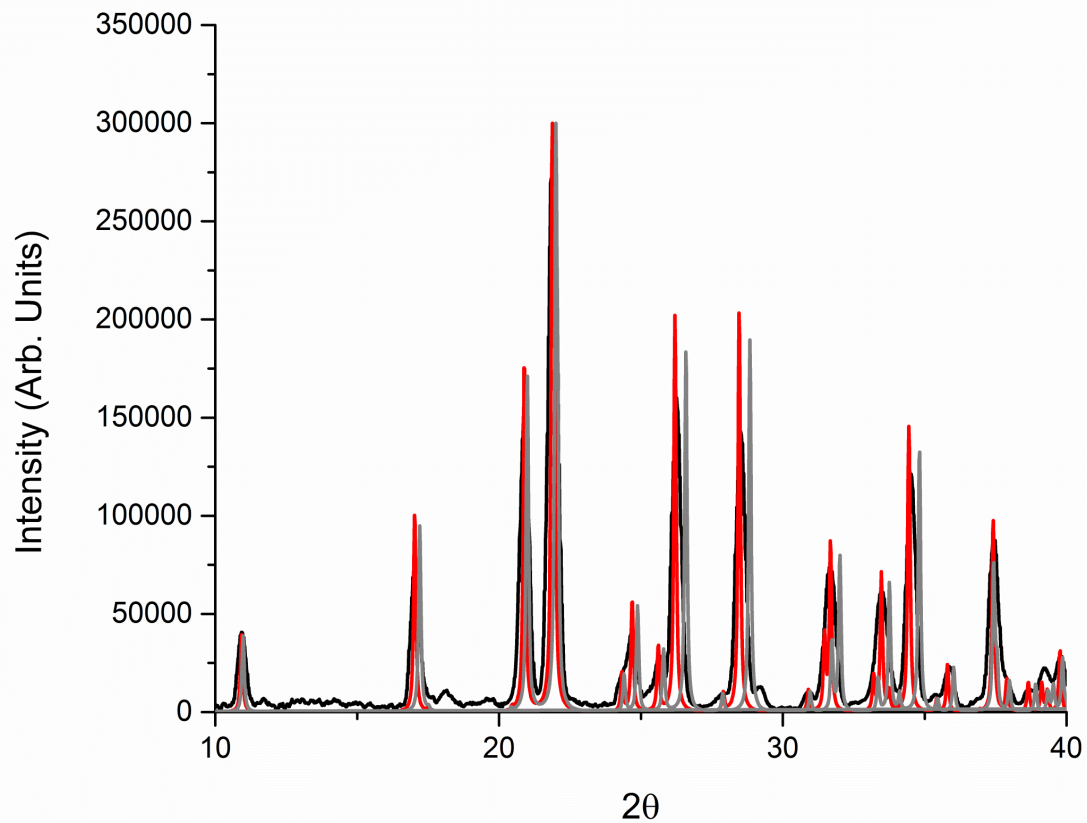


**Figure A2.** Experimental powder X-ray diffraction data of room-temperature ASN (black). The best fit X-ray data is shown in red. The calculated pattern based on 90 K single-crystal X-ray data (gray) is shown for reference.<sup>1</sup> Data was collected on a Bruker KAPPA APEX DUO using Cu radiation.



## Appendix B. Chapter 5 Supporting Information

### Contents

**Table B1.** Calculated IR-Active Mode Frequencies ( $\text{cm}^{-1}$ ), Intensities ( $\text{km mol}^{-1}$ ), and Symmetries for L-ASP  $\text{H}_2\text{O}$

**Table B2.** Calculated IR-Active Mode Frequencies ( $\text{cm}^{-1}$ ), Intensities ( $\text{km mol}^{-1}$ ), and Symmetries for DL-ASP  $\frac{1}{2} \text{H}_2\text{O}$

**Table B3.** Calculated IR-Active Mode Frequencies ( $\text{cm}^{-1}$ ), Intensities ( $\text{km mol}^{-1}$ ), and Symmetries for DL-ASP  $\text{H}_2\text{O}$

**Table S1.** Calculated IR-Active Mode Frequencies ( $\text{cm}^{-1}$ ), Intensities ( $\text{km mol}^{-1}$ ), and Symmetries for L-ASP  $\text{H}_2\text{O}$

L-ASP• $\text{H}_2\text{O}$		
freq.	intens.	symm.
44.1	5.33	B1
66.8	8.84	B3
84.4	9.90	B1
87.2	1.01	B2
87.4	8.17	B3
97.8	83.97	B3
98.7	11.42	B2

**Table S2.** Calculated IR-Active Mode Frequencies ( $\text{cm}^{-1}$ ), Intensities ( $\text{km mol}^{-1}$ ), and Symmetries for DL-ASP  $\frac{1}{2}$   $\text{H}_2\text{O}$

DL-ASP• $0.5\text{H}_2\text{O}$		
freq.	intens.	symm.
87.6	32.79	AU
92.2	17.47	AU
97.7	5.27	AU

**Table S3.** Calculated IR-Active Mode Frequencies ( $\text{cm}^{-1}$ ), Intensities ( $\text{km mol}^{-1}$ ), and Symmetries for DL-ASP  $\text{H}_2\text{O}$

DL-ASP• $\text{H}_2\text{O}$		
freq.	intens.	symm.
57.8	21.53	AU
62.8	33.30	AU
80.6	10.66	AU
88.9	11.67	AU
95.0	19.31	AU

## Appendix C. Chapter 7 Supporting Information

### Contents

**Table C1.**  $C_6$  ( $\text{J nm}^6 \text{mol}^{-1}$ ) and vdW radii ( $\text{\AA}$ ) values used in the DFT-D2, DFT-D\*, and DFT-DX dispersion correction parameterization.

**Table C2.** Evaluation of RMSDs in bond lengths, bond angles, bond dihedral angles, and hydrogen bond heavy-atom separations in the calculated structures of CDG and ADG as compared to X-ray diffraction data.

**Table C1.**  $C_6$  ( $\text{J nm}^6 \text{mol}^{-1}$ ) and vdW radii ( $\text{\AA}$ ) values used in the DFT-D2<sup>a</sup>, DFT-D\*<sup>b</sup>, and DFT-DX<sup>b-d</sup> dispersion correction parameterization.

Atom	DFT-D2		DFT-D*		DFT-DX	
	$C_6$	vdW radii	$C_6$	vdW radii	$C_6$	vdW radii
H	0.14	1.001	0.14	1.301	0.03	1.10
C	1.75	1.452	1.75	1.525	0.91	1.70
N	1.23	1.397	1.23	1.467	0.59	1.55
O	0.70	1.342	0.70	1.409	0.34	1.52

- a. Grimme, S. Semiempirical GGA-type density functional constructed with a long-range dispersion correction. *J. Comput. Chem.* **2006**, *27*, 1787-1799.
- b. Miller, T. M.; Bederson, B. Atomic and Molecular Polarizabilities-A Review of Recent Advances. In *Advances in Atomic and Molecular Physics*; Bates, D. R., Benjamin, B., Eds.; Academic Press, 1978; Vol. Volume 13; pp 1-55.
- c. *CRC Handbook of Chemistry and Physics*, 93 ed.; CRC Press/Taylor and Francis: Boca Raton, FL.
- d. Sansonetti, J. E.; Martin, W. C. Handbook of Basic Atomic Spectroscopic Data. *J. Phys. Chem. Ref. Data* **2005**, *34*, 1559-2259.

**Table C2.** Evaluation of RMSDs in bond lengths, bond angles, bond dihedral angles, and hydrogen bond heavy-atom separations in the calculated structures of CDG and ADG as compared to X-ray diffraction data.

	ADG			CDG		
	DFT-D2	DFT-D*	DFT-DX	DFT-D2	DFT-D*	DFT-DX
Bond Length ( $\text{\AA}$ )	0.0026	0.0024	0.0025	0.0023	0.0020	0.0022
Bond Angle ( $^\circ$ )	0.184	0.171	0.178	0.088	0.065	0.087
Dihedral Angle ( $^\circ$ )	0.794	0.865	0.956	0.065	0.027	0.042
Intermolecular Hydrogen Bond Length ( $\text{\AA}$ )	0.0077	0.0080	0.0088	0.017	0.018	0.020

## Curriculum Vitae

### Thomas R. Juliano Jr.

1240 Westmoreland Ave, Syracuse, NY 13210  
Cell: (716) 523-3975, Email: tjules1388@gmail.com

## Education

### Doctor of Philosophy in Physical Chemistry

Syracuse University, Syracuse, NY

December 2014

### Masters of Philosophy in Physical Chemistry

Department of Chemistry, Syracuse University, Syracuse, NY

May 2013

### Bachelor of Science in Chemistry

Department of Chemistry, State University of New York at Buffalo, Buffalo, NY

May 2011

## Research Experience

Dissertation Title: Evaluation of Non-Covalent Interaction Models in Molecular Crystals Using Terahertz Spectroscopy

Advisor: Professor Timothy M. Korter

Area 1: Evaluation of London Dispersion Force Corrections in Solid-State Density Functional Theory Simulations

- Performed sub-100  $\text{cm}^{-1}$  terahertz vibrational spectroscopy using an amplified femtosecond Ti:Sapphire laser system for radiation generation and detection
- Obtained and analyzed single-crystal and powder X-ray diffraction data
- Utilized solid-state density functional theory simulations to accurately reproduce both structural and spectral experimental data of complex molecular solids
- Investigated the effectiveness of several semi-empirical London dispersion force correction models, yielding a newly parameterized model (DFT-DX)
- Performed spectral analyses in order to characterize the vibrational nature of materials ranging from explosives (nitroguanidine) to amino acid dipeptides (acyclic and cyclic diglycine)

Area 2: *Ab Initio* Prediction of Unknown Crystal Structures for Amino Acid Hydrates

- Studied the hydration propensities of amino acids (proline and serine) using solid-state density functional theory simulations
- Discovered several previously unknown amino acid co-crystalline hydrates using solid-state density functional theory
- Evaluated the solid-state transformations and Gibbs free energy changes related to the formation of crystalline hydrates using both density functional theory and explicit electron correlation methods

## Publications

**Juliano, T. R., Jr.;** Korter, T. M. Hydration Mechanisms in Crystalline Glutamic Acid. In preparation.

**Juliano, T. R. Jr.;** Korter, T. M. *Ab Initio* Study of the Hydration Tendencies of the Amino Acids Proline and Serine. In Preparation.

**Juliano, T. R., Jr.;** Korter, T. M. Origins of Hydration Differences in Homochiral and Racemic Crystals of Aspartic Acid. In Preparation.

**Juliano, T. R., Jr.;** Korter, T. M. London Force Correction Disparity in the Modeling of Crystalline Asparagine and Glutamine, *Journal of Physical Chemistry A*, **2014**. Submitted.

**Juliano, T. R., Jr.;** Korter, T. M. Terahertz Vibrations of Crystalline Acyclic and Cyclic Diglycine: Benchmarks for London Force Correction Models. *Journal of Physical Chemistry A*, **2013**, *117*, 10504-10512. DOI: 10.2021/jp407112w.

**Juliano, T. R., Jr.;** King, M. D.; Korter, T. M. Evaluating London Dispersion Force Corrections in Crystalline Nitroguanidine by Terahertz Spectroscopy. (Invited Article). *IEEE Transactions on Terahertz Science and Technology*. **2013**, *3*, 281-287. DOI: 10.1109/TTHZ.2013.2254483.

## Conference Participation

**Juliano Jr., T. R.,** Korter, T. M. Utilizing Terahertz Spectroscopy in the Evaluation of London Dispersion Forces in Cyclic and Acyclic Dipeptides. Poster Presentation, 246<sup>th</sup> ACS National Meeting and Exposition, Indianapolis, IN, September 11, 2013, PHYS-348.

**Juliano Jr., T. R.,** Korter, T. M. Utilizing Terahertz Spectroscopy in the Evaluation of London Dispersion Forces in Cyclic and Acyclic Dipeptides. Poster Presentation, MSSC2013- *Ab Initio* Modeling in Solid State Chemistry, Turin, Italy, September 3, 2013.

**Juliano Jr., T. R.,** Korter, T. M. Terahertz Spectroscopy of the Crystalline Explosive Nitroguanidine. Poster Presentation, 244<sup>th</sup> ACS National Meeting & Exposition, Philadelphia, PA, August 22, 2012, PHYS-355.

## Teaching Experience (August 2011- present)

### **Chemistry in the Modern World Lab (CHE103)**

- Composed syllabi and quizzes, mentored and graded non-science major students in a laboratory setting, conducted pre-outlined experiments, assisted with homework assignments, graded homework and quizzes, responsible for 75 students in lab (3 classes of 25) and the grading of 125 students' homework and quizzes

### **Forensic Science Lab (CHE 113)**

- Monitored undergraduate forensic students while conducting pre-outlined laboratory experiments, assisted them with questions regarding procedures, homework, or quiz material,

composed syllabi and quizzes, graded quizzes and homework assignments, responsible for assisting 60 students in lab (3 classes of 20) and grading subsequent quizzes and homework

## **Teaching Experience Continued**

### **General Chemistry Lecture II Recitation (CHE 116)**

- Responsible for providing supplementary lecture material, assisted students with questions related to homework assignments and lecture material, conducted office hours to provide assistance outside of class and recitation, responsible for 50 students in two recitation sections

## **Awards**

Provost Scholarship, SUNY at Buffalo (August 2007- May 2011)

Wegmans Scholarship, Wegmans Food Markets (August 2009- May 2011)

## **Community Outreach**

Volunteer Assistant Hockey Coach (October 2013- May 2014)

Valley Youth Hockey Organization

- Coached a 15-player co-ed team of 11-12 year olds
- Regular weekend travel for games
- 15-20 hours per week
- Won division championship

Volunteer Assistant Hockey Coach (October 2012- May 2013)

Valley Youth Hockey Organization

- Coached a 12-player co-ed team of 13-14 year olds
- Regular weekend travel for games
- 15-20 hours per week